Hierarchical spatiotemporal analyses and the design of all-solid-state lithium-ion batteries

Seunghoon Yang

Hierarchical spatiotemporal analyses and the design of all-solid-state lithium-ion batteries

Seunghoon Yang

Graduate School of Human and Environmental Studies

Kyoto University

Supervised by

Prof. Dr. Yoshiharu Uchimoto

Contents

Chapter 1. General introduction

1.1. Background

Recently, the use of fossil-fuel-based energy sources for modern industrial civilization has frequently been considered to be a cause of serious environmental pollution issues[1,2]. In particular, climate change, caused by carbon dioxide from fossil fuels, has become a serious concern[1]. One of the major carbon dioxides originates from thermoelectric power plants and vehicles, which use fossil fuels. Unfortunately, these are deeply connected to the survival of civilization, and energy demands continue to increase over time. Thus, gradual reduction of carbon dioxide emissions would be preferable. Currently, major countries have been implementing the policies to reduce carbon dioxide emissions, replacing non-renewable energy (Fossil fuel) with renewable energy as shown in Figure 1. Among the green energies, application of electricity has been suggested as immediate utilization and alternative. As a result, various regulations for carbon dioxide reduction were emerged such as the policies for electric vehicles, which do not rely on fossil fuels but using green energy like electricity. Figure 2 summarizes the power sources for current and future mobile vehicles. Currently, most vehicles are powered by internal combustion engines, but electric vehicles and plug-in hybrid vehicles are expected to spread rapidly in the future, and fuel cell vehicles are also expected to increase gradually. Furthermore, as a source of electricity for electric and plug-in hybrid vehicles, international environmental associations have suggested that a new system based on environmentally friendly renewable energy sources is needed to replace fossil fuel-based sources. Based on these arguments, the concept of smart grids emerged and has been attracting attention in recent years. Smart grids are not only power grids, but also systems that can efficiently supply electricity anywhere it is consumed with minimal power and information technology[3-11]. Moreover, smart grids can provide sustainable energy regardless of the weather and store excess energy as chemical energy. Therefore, optimization of the production and distribution of energy can decrease carbon dioxide emissions[3]. To realize smart grid systems, it is essential to develop novel systems based not on fossil fuels, but on environmentally friendly energy sources, such as the sun, wind,

water, and hydrogen. In order to stably use these power sources, which fluctuate greatly over time, it is necessary to charge the storage batteries and then stably extract the current.

Among applications that need to reduce fossil fuel consumption, the reduction for vehicles is urgent. However, vehicles require large amounts of energy to achieve high power density and/or high energy density[11]. Therefore, various energy storage systems capable of this, such as supercapacitors, lead-acid batteries, fuel cells, and lithium-ion batteries (LIBs), have already been either installed or attempted[11–14]. A supercapacitor, which uses an electric double layer to store electricity, can charge and discharge faster than a battery using chemical reactions, but has a very low energy density.[12–15]. Lead-acid batteries are charged and discharged by the movement of sulfate ions between the electrodes and electrolyte and provide low cost per unit of electricity[14]. However, because of their poor specific energy (Wh/kg), they are ineffective as power sources for vehicles. For this reason, lead-acid batteries have been used as supplemental tools for vehicles. Meanwhile, fuel cells generating electricity based on the reaction of oxygen with hydrogen has received much attention because no emission gas is produced, long distances can be travelled with short charging times, and oxygen and hydrogen are abundant on Earth[11]. Because of these properties, applications into smart grid system are promising as to an environmentally friendly concept; however, there are critical issues obstructing their application that must be solved, such as expensive cells including platinum catalysts, insufficient facilities for hydrogen charging stations[16]. Fortunately, LIBs have sufficient energy density owing to the light weight of lithium and the high electromotive force of the electrodes[17–19]. They are charged and discharged by the movement of Li ions, generating electricity, which is stored in the electrodes[17]. Therefore, LIBs are suitable as power sources and energy storage devices for vehicles. Furthermore, they can enable the production of vehicles that do not rely on fossil fuels.

However, in order for LIBs to be utilized and for LIB-based vehicles to perform at the level of existing fossil-fuel-dependent vehicles, stricter standards than those for small electronic appliances currently in use must be met[16]. The application of LIBs should be considered for not only vehicles, but also large-scale energy storage systems. Environmentally friendly energy production systems that use solar cells, wind power, and hydrogen can produce enormous amounts of energy, but no storage system can

accommodate these amounts of produced energy thus far. Therefore, utilizing LIBs as energy storage systems can be a suitable approach owing to their ability to store energy.

1.2. Lithium-ion batteries and their limitations

Ever since LIBs were first commercialized in 1991 by Sony[3], they have played an important role in modern civilization. This section presents an overview of the basic aspects of LIBs, such as their mechanism and production using an organic solvent as the electrolyte. Figure 3 shows an illustration of existing LIBs. Representative key components are the cathode, anode, electrolyte, and separator[3]. Li-containing transition metal oxides such as $LiMO_2$, graphite, and organic solvents containing dissolved Li salt function as the cathode, anode, and electrolyte, respectively. Microporous polymer materials such as polyethylene (PE) or polypropylene (PP) have been applied as separators in LIBs. The charge-discharge reaction is presented below[3].

Cathode electrode：$Li_{1-x}MO_2 + xLi^+ + xe^- \Leftrightarrow LiMO_2$

Anode electrode： $Li_xC_6 \Leftrightarrow xLi^+ + xe^- + C_6$

Total reaction：$Li_{1-x}MO_2 + Li_xC_6 \Leftrightarrow LiMO_2 + C_6$

The Li ions within the crystalline structure of the cathode are extracted and transported through the electrolyte during charging, and then inserted into the inner parts of the anode (graphite edge site)[3]. At the same time, electrons are transferred from the cathode to the anode through an external circuit. During discharging, the opposite reaction occurs. The battery can store and extract power owing to the movement of Li ions and electrons from the anode to the cathode within the battery and through the external circuit, respectively.

Currently, the anode and cathode are being actively studied toward enhancing their capacities to improve energy density and power density for LIBs. These would be the next-generation electrodes for LIBs. Researchers have searched for an anode material

that can provide a higher capacity than graphite, which is currently widely used for the anode. Lithium metal and silicon have been considered promising anode candidates for the following reasons. Lithium metal has a significantly high theoretical capacity (3,840 $mAhg^{-1}$), low reduction potential (−3.045 V versus standard hydrogen electrode (SHE)), and low density (0.59 $g \cdot cm^{-3}$). Above all, because lithium is the main material in LIBs, there is no need to consider polarization due to intercalation and deintercalation. However, the critical problem for LIBs is lithium dendrite formation, which is directly connected to safety problems and obstructs their utilization. Thus, to avoid lithium dendrite formation in LIBs, silicon has been suggested for the anode[4,5]. Silicon also has a high theoretical capacity (4,200 $mAhg^{-1}$) and low reduction potential (0.4 V versus Li/Li^{+}) and is abundant on Earth. However, it undergoes significant volume expansion during cycling, which lowers the battery performance. Investigations of these two types of materials for the anodes of LIBs have concentrated on overcoming the aforementioned issues[5].

The studies on anode materials introduced earlier focused on battery safety concerns and improvements in electricity generation. In contrast, cathode materials have been more studied because they determine the amount of electricity that can be used after charging in a battery[4,6]. As a representative cathode, $LiCoO_2$ has a layered structure in which lithium ions are intercalated and deintercalated. There are many candidates for next-generation cathode materials, and most of them have this layered structure. In particular, both $LiNi_xCo_yMn_zO_2$ and $LiNi_xCo_yAl_zO_2$ with over 80% Ni have been utilized in LIBs because of their high capacity of approximately 280 $mAhg^{-1}$. To improve the capacities of cathode materials, they should be designed to operate at higher potentials; however, most currently used electrolytes are inadequate because they are oxidized at high potentials[17].

Existing LIBs that use organic solvents as electrolytes are unsafe owing to their ignitability, which has hindered their application to mid-to-large-sized batteries and energy storage systems. Furthermore, as shown in Figure 2, demands for better performance are being predicted, such as for higher energy density suitable for electric vehicles capable of long-distance driving with short charging times and perfect safety compared to existing LIBs[17–19]. However, performance enhancement is limited by safety concerns. First, fast charging is accompanied by lithium dendrite formation from a high

current density, which is why lithium metal cannot be used as an anode material, despite being the best anode material for LIB systems. This also prevents the improvement of the energy density of LIBs. Therefore, next-generation batteries must be developed with safety, energy density, power density, and operation environment taken into consideration. Among the candidates for next-generation batteries, all-solid-state batteries, in which organic liquid electrolytes are replaced with solid electrolytes, have attracted attention and are expected to be promising. The following section discusses all-solid-state batteries[8,9].

1.3. All-solid-state batteries

Shown in Figure 4[20], all-solid-state batteries (ASSBs), featuring solid electrolytes instead of organic liquid electrolytes, had been suggested because of their potential in the 1980s, but several drawbacks such as poor energy density and low ionic conductivity have prevented practical application[19]. Furthermore, the electrodes of ASSBs cannot be made to be as thick as those in LIBs. While a small amount of a liquid electrolyte can smoothly impregnate an electrode and act as an ionic conductor, the electrodes in ASSBs require a solid electrolyte to provide an ionic path. Therefore, the amount of electrode is reduced due to the addition of solid electrolyte within the electrode, leading to poor energy density of ASSBs. It makes difficult to the expectation of commercialization. In the late 20th and early 21st centuries, the development of solid electrolytes brought about renewed interest in ASSB technologies, particularly for electric vehicles since the 2010s[21]. Furthermore, ASSBs received widespread attention after Toyota demonstrated a prototype in the 2010s[22]. Although there are restrictions related to battery shape to prevent leakage and operating temperature and voltage because of the risks of ignition and explosion for organic liquid electrolytes, solid electrolytes theoretically have no risks of burning, leaking, or corroding[23–29], making ASSBs safer than existing LIBs.

Various types of ASSBs can be tailored, such as with flexible shapes or bipolar stacking, for different needs. The use of bipolar layers contributes to the increase of the energy density, and the high thermal stability of the solid electrolyte enables utilization in a variety of environments, such as in a wide range of temperatures. The solid electrolyte

is the most important component of ASSBs because battery performance depends on its characteristics, such as the potential window, temperature, and reactivity with active materials[30,31]. An ideal solid electrolyte should have (1) high ionic conductivity, (2) thermal stability, (3) electrochemical stability, (4) negligible electronic conductivity, and (5) chemical stability toward the electrodes[31]. Based on this, thus far, three types of solid electrolytes for ASSBs have been discovered and widely investigated from discovering to developing. In the following section, these solid electrolytes will be introduced along with their intrinsic characteristics, including the structures and ionic conduction mechanisms, and the expectations for each from a practical viewpoint.

1.3.1. Overview of solid electrolytes

1.3.1.1. Oxide solid electrolytes

Oxide-based materials used as solid electrolytes have a NASICON, garnet, or perovskite structure. NASICON-type solid electrolytes are composed of a phosphate compound with the chemical formula $L_{1+6x}M^{4+}{}_{2-x}M^{3+}{}_{x}(PO_4)_3$ in a rhombohedral unit cell, where L is Li or Na; M^{4+} is Ti, Ge, Sn, Hf, or Zr; and M^{3+} is Cr, Al, Ga, Sc, Y, In, or La[32–40]. The major frameworks comprise PO_4 tetrahedra and MO_6 octahedra sharing a corner, with Li ions occupying two different sites: the center of the six-coordinated structure with oxygen between the MO_6 octahedra and the central site of the eight-coordinated structure with oxygen between columns composed of the MO_6 octahedra (Figure 5). Li ions migrate through these two sites. $Li_{1+x}Al_xTi_{2-x}(PO_4)_3$ (LATP) exhibited the highest ionic conductivities (~10^{-3} S·cm^{-1}) at room temperature. However, the reduction of Ti^{4+} in contact with the Li metal anodes has restricted the application of LATP[37].

Perovskite-type solid electrolytes have the general formula ABO_3. The A atoms, B atoms, and oxygen atoms are found at the corners, center of the body, and centers of the faces, respectively, of the cubic unit cell (Figure 6). In perovskite-type solid electrolytes[41–44], Li ions diffuse through a square planar bottleneck consisting of oxygen. Moreover, the ionic conductivity has been reported to be significantly affected by the concentrations of the Li ions and vacancies, as well as the size of the bottleneck. This bottleneck can be controlled by replacing La and Ti ions with Al and Mg, producing materials that exhibit high ionic conductivities up to 10^{-3} S·cm^{-1} at room temperature[44]. Although perovskite materials are stable at high potentials, they are known to be reduced

at approximately 1.5 V versus Li/Li^+; hence, they are also unsuitable for use with Li and graphite anodes[41].

Garnet-type solid electrolytes possess cubic unit cells with the formula $A_3B_2(XO_4)_3$, where the A, B, and X sites correspond to an eight-coordinated structure, a six-coordinated structure, and a four-coordinated structure, respectively[45–49]. Li occupies the four-coordinated sites in a typical Li-conducting garnet-type solid electrolyte (Figure 7). However, the mobility of Li in the four-coordinated sites is low. $Li_3Ln_3Te_2O_{12}$, in which Li occupies four-coordinated sites, is known as a poor ionic conductor[49]. To improve the ionic conductivity, insertion of the Li ions into the structure has been attempted by modifying the valences of the cations in the A and B sites[48]. The introduction of pentavalent ions causes the Li ions to occupy some of the distorted octahedral sites in addition to the tetrahedral sites. The Li ions in the octahedral sites exhibit high mobility, owing to static repulsion caused by the short Li-Li distance. Consequently, garnet-type solid electrolytes such as $Li_7La_3Zr_2O_{12}$ (LLZO) with Li ions in octahedral sites exhibit relatively high ionic conductivity ($\sim 10^{-4}$ $S \cdot cm^{-1}$) at room temperature. However, these garnet-type solid electrolytes have been reported to be unstable toward water, as hydrogen-oxygen exchange can occur in the air, and the cathode, and exhibit high contact resistance with Li metal owing to its grain boundaries, which also play a role in lithium dendrite formation[50].

In addition, for all oxide solid electrolytes, high temperatures of approximately 1000 °C are required for high ionic conductivity. However, the grain boundary still affects the interface resistance[51].

1.3.1.2. Polymer solid electrolytes

The first ion-conducting polymeric material was discovered by Fenton et al. in 1973[52], and this was followed by the practical demonstration of the first ASSB based on polyethylene oxide (PEO)–Li salt[53]. To date, PEO-based electrolytes have been studied as the representative polymer-based solid electrolytes. These electrolytes can be divided into dry solid polymer electrolytes, consisting of thermoplastic polymers and Li salts, and gel polymer electrolytes with liquid electrolytes and lithium salts[54]. Herein, gel-type electrolytes will not be discussed because they feature organic liquids and theoretically

share an ion conduction mechanism with organic liquid electrolytes[54–56]. The advantages, disadvantages, properties of the structures, and ion conduction mechanisms of dry solid polymer electrolytes are described below.

Dry solid polymer electrolytes with lithium salts have excellent advantages of flexibility, light weight, low cost, and processability[56]. Most polymers have a crystalline phase, which leads to low ionic conductivity (10^{-5} to 10^{-6} S·cm^{-1}) at room temperature[57–60]. PEO-based materials require relatively high temperatures of over 60 °C to achieve ionic conductivities higher than 10^{-4} S·cm^{-1}. This means that ion conduction can occur under an amorphous phase in this temperature range, and the crankshaft torsional movement around C–C and C–O bonds in the –CH_2CH_2O (ethylene oxide) repeating unit leads to segmental movement in the polymer, enabling ion migration through the polymeric refractor (Figure 8), where a polar oxygen atom easily forms a coordination bond with an alkali metal ion[53–55]. However, the discovery that incompletely dissociated species in the polymer matrix contribute to ion conduction by providing hopping sites has led to debate[61]. Nevertheless, it is obvious that the mobility of lithium ions is strongly related to the movement of the polymer chains at different temperatures.

However, the mechanical properties, such as the thermal character and ability to suppress dendrite formation, of these electrolytes are inferior to those of inorganic solid electrolytes when it comes to producing safe and durable batteries[56]. Furthermore, they have poor electrochemical stability at high temperatures, even though a high operation temperature is recommended, and their ionic conductivity is insufficient for utilization in commercial batteries[60]. Thus, expectations for these solid electrolytes are low.

1.3.1.3. Sulfide solid electrolytes

Sulfide-based solid electrolytes can be either crystalline or amorphous. The structures, advantages, and disadvantages of the various types of sulfide solid electrolytes are discussed in this section. There are two types of crystalline sulfide solid electrolytes: LISICON and argyrodite. Since Taches et al.[62] reported a LISICON crystalline material in 1984, $Li_{10}GeP_2S_{12}$ (LGPS) has received much attention owing to its high Li ion conductivity, which is similar to those of liquid electrolytes, of 10^{-2} S·cm^{-1} at room temperature[27,63,64]. The crystal structure of LGPS has a tetragonal unit cell composed of

a PS_4 tetrahedron, a $(M/P)S_4$ tetrahedron, and a LiS_6 octahedron. In this structure, phosphorus atoms completely occupy the 2*b* sites, germanium and phosphorus atoms in a 1:1 ratio share the 4*d* sites, and Li occupies four crystal structure sites (4*c*, 4*d*, 8*f*, and 16*h*). The Li octahedra and the $(P/Ge)S_4$ tetrahedra in the 4*d* sites form a one-dimensional chain along the c-axis with shared edges (Figure 9)[27]. The Li octahedron in the 4*d* site also forms an a- and b-axis connected structure with the PS_4 tetrahedron in the 2*b* site by sharing corners. In the LGPS structure, Li ions are conducted through the one-dimensional chain along the c-axis formed by the shared edges of the 4*d*-site Li octahedra and the $(P/Ge)S_4$ tetrahedra[27]. The transfer energy for Li ion transport through this one-dimensional channel has been reported to be very low, resulting in high Li ion conductivity[64].

Argyrodite-type sulfide solid electrolytes with cubic unit cells were reported by Deiseroth et al. In these structures, phosphorus atoms form a network of isolated PS_4 tetrahedra, with halogen atoms at the 4*a* sites, sulfur atoms at the 4*c* sites, and Li ions randomly located at the 24*g* and 48*h* sites[65,66]; hexagonal cages are formed from the sulfur atoms at the 4*c* sites and the Li ions around them are connected through interstitial sites around the sulfur and halogen ions, and Li is conducted through this chain of hexagonal cages (Figure 10)[65]. However, despite excellent ionic conductivity, the commercial application of both LGPS and argyrodite sulfide electrolytes has been limited owing to inefficient synthesis (solid-state reactions) and low stability toward Li metal anodes at low voltages.

Unlike crystalline materials, amorphous materials do not have medium- to long-range ordered structures[66–71]. Binary Li_2S-P_2S_5 glass, a representative sulfide amorphous solid electrolyte, has been reported because of its short-range ordered structure composed of P_xS_y species such as PS_3^{3-}, $P_2S_7^{4-}$, $P_2S_6^{4-}$, and $P_2S_6^{2-}$. Li ion conductivity can be increased by adjusting the ratio of Li_2S to P_2S_5, which leads to transitions from $P_2S_7^{4-}$ icosahedra to PS_4^{3-} tetrahedra (Figure 11)[69]. Moreover, synthesis requires only a few raw materials such as Li_2S, P_2S_5, and other additional materials, unlike the complex synthesis systems of crystalline sulfide electrolytes.

1.3.2. Composite electrodes with solid electrolyte for ASSBs

Unlike the liquid electrolytes for LIBs, solid electrolytes cannot flow or infiltrate into gaps and voids, resulting in high interfacial resistance between them and the electrodes, which can lead to various interfacial problems. Therefore, the electrodes in ASSBs require a solid electrolyte for ion conduction[61,71,72] because conventional electrodes, made with conductive carbon for LIBs, cannot be used for ASSBs because of poor ion conduction paths. They are commonly called composite electrodes and are shown in Figure 4. Figure 14 shows the various interfacial factors for composite electrodes that should be considered. A solid electrolyte with good interfacial compatibility would be suitable as an ion conductor, and the choice of electrolyte is of utmost importance along with the electrode materials.

Oxide solid electrolytes have poor interfacial ductility with heterogeneity and require high-temperature sintering to obtain a high ionic conductivity and reduce the grain boundaries[50,51,60]. The sintering process is expensive, and poor ductility with heterogeneity is unfavorable for composite fabrication. Furthermore, the poor ductility of oxide materials leads to high interfacial resistance, which makes battery use difficult in ambient environments, and additional interfacial treatment on the electrolyte surface is required. In the case of polymer electrolytes, interfacial contact with the electrode materials is relatively favorable because of the flexibility of the polymer chain structure compared to those of oxide materials. However, a relatively high temperature (60–70 °C) is required to obtain a favorable interface and operate the battery, which can lead to the heat deterioration of the polymer and reduction of battery durability and safety[58,60,61]. Although the high-temperature deterioration of polymer electrolytes has been alleviated by compounding with ceramic materials, further study is still required[61]. However, sulfide solid electrolytes, which have thermal stability, no grain boundary, and high ionic conductivity, are relatively free from these problems[73,74]. Thus, sulfide solid electrolytes have been widely utilized to fabricate composite electrodes for ASSBs. They are considered to be close to commercialization owing to their superior chemical, mechanical, and electrochemical properties.

As discussed above, most sulfide solid electrolytes have relatively high ionic conductivity, because sulfur exhibits high polarization owing to its large ionic radius and

is less electronegative than oxygen[72,73]. Therefore, the interaction of lithium ions within the structure is relatively weak, resulting in wider ion transport paths than in oxide-based materials. Moreover, this leads to favorable ductility in sulfide solid electrolytes for contact with electrode materials. These properties are useful for achieving good contact between the electrode and the solid electrolyte simply through cold pressing because the sulfide materials have a relatively low elastic modulus[73], making the interface between the sulfide solid electrolyte and the electrode materials a favorable environment. Furthermore, because of this favorable approach to controlling the interface between the electrodes and the sulfide solid electrolytes, composite electrodes have been widely utilized to fabricate ASSBs. In addition, significant results have been reported for composite electrodes composed of existing electrode materials[74–76]. Therefore, ASSBs with sulfide solid electrolytes are considered to be the closest to commercialization, provided that several issues are overcome.

Most of the interfacial resistance problems related to the performances of ASSBs reported thus far come from the composites containing the solid electrolyte and electrode material. Various factors affect the interfacial resistance of ASSBs. Thus, in addition to simply manufacturing composite electrodes, the interfacial phenomena need to be investigated according to the sequential spatial scale of ASSBs within the systematic frame. From the interface between the electrolyte and electrode, where charge transfer is considered to occur first spatially, to the phase transition of the electrode due to the movement of lithium ions, these processes should be interpreted from a macroscopic point of view. The interfacial problems that occur in the composite electrodes for ASSBs are discussed below.

1.4 Electrochemical reaction with spatial temporal scale

ASSBs with sulfide electrolytes are expected to have potential for commercialization owing to their interface wettability and high ionic conductivity, enabling battery operation at ambient temperature. Even for these ASSBs, a clear solution for the interfacial resistance problem is required for commercialization[74]. To improve the performance of ASSBs, analysis of the interfacial phenomena occurring within them should concentrate on the sequential spatial scale, as shown in Figure 12[77]. A systematic study and approach for each element is required because it can be the key to solving interfacial resistance problems, and the application of this concept will be very useful for ASSBs and understanding complex interfacial phenomena.

Based on previous studies, the first triggered interfacial resistance phenomenon in ASSBs to consider is the charge transfer phenomenon by adjusting the electrochemical potential difference between the electrode and the electrolyte[77]. This might depend significantly on the ionic conductivity of the solid electrolyte and the interfacial contact state. After charge transfer at the interface between the solid electrolyte and electrode, interphases are formed through phase transition from the decomposition of the solid electrolyte due to the redox potential of the electrode, which is a significant problem because the decomposition products will show interfacial resistance. Unfortunately, this is inevitable because most sulfide solid electrolytes have a narrow potential window[77]. In other words, unwanted reactions occur at the interface between the solid electrolyte and the electrode before and after charge transfer. Furthermore, these decomposition products can disrupt the homogeneity of the reaction distribution in a composite electrode, which is the main reason that the thickness of the electrode cannot be increased. Unfortunately, a thin electrode cannot meet the energy density requirements of ASSBs. This inhomogeneous reaction distribution in a composite electrode is the main cause of high interfacial resistance, which leads to battery performance deterioration during cycling[79].

To address the various interface issues, comprehensive investigations based on the sequential spatial scale in ASSBs are required. The main focuses are (1) interfacial resistance caused by charge transfer originating from the difference in potential due to lithium ion transport from the solid electrolyte to the electrode, (2) phase transition

dynamics, affecting lithium ion diffusion, due to lithium ion insertion/extraction during cycling, and (3) macroscopic interpretation of internal phenomena. The following sections discuss the interfacial perspective for ASSBs according to sequential spatial scale and introduce previous studies related to each element to be solved.

1.4.1. Interface between solid electrolyte and electrode

For the alleviation of the interfacial resistance between the solid electrolyte and the electrode, both the ionic conductivity and the particle size of the solid electrolyte are important. Homogeneous particles are favorable for fabricating composite electrodes as well as for improving the energy density of ASSBs. However, thus far, almost all sulfide solid electrolytes have been prepared by mechanical milling, so-called solid-state reactions, in which additional thermal treatment is conducted in a vacuum-sealed quartz ampoule[27,78,79]. This process is not only unsuitable for commercialization, but also unfavorable for obtaining high-energy-density composite electrodes with a high weight percentage of active materials. Moreover, the particle size cannot be controlled with these conventional synthesis methods because of the naturally poor interaction between the solids. This lack of homogeneity in their particle properties, such as in their shape and size, result in low ionic conductivity, high interfacial resistance, and low energy density[78–81]. This is a major drawback for obtaining sulfide solid electrolytes with high ionic conductivity and favorable ductility. Moreover, as shown in Figure 13, it has been reported that significant interface problems arise from solid electrolytes in cells, a significant portion of which (voids between particles) is considered to be the result of inhomogeneous electrolyte particles. Furthermore, with mechanical milling, it is difficult to quickly synthesize materials in bulk and to commercialize ASSBs with sulfide-based solid electrolytes, because of their high cost[80,81].

With the high cost and long synthesis time, the amount of obtainable electrolyte powder is not satisfactory. In contrast to the solid-state reaction method, liquid-phase synthesis uses a solvent as a medium, enabling bulk synthesis[80–86]. This is beneficial because it not only leads to lower costs and shorter synthesis times than those of solid-state reaction methods, but also enables control of the particle size of the materials, which is difficult with solid phases. Furthermore, provided that this method can be utilized, it

would be more favorable for improving the energy density of ASSBs because nano-sized solid electrolyte particles can act as ionic conductors in composite electrodes[81–83,85]. For these reasons, ever since the synthesis of β-Li_3PS_4 with tetrahydrofuran (THF) as a solvent was first reported[79], sulfide electrolytes have been synthesized using various solvents and have shown different ionic conductivities depending on the solvent used; however, most of the sulfide solid electrolytes synthesized in liquid phase have significantly lower ionic conductivities than those synthesized using solid-state reaction methods. Moreover, the cause of the low ionic conductivity is difficult to determine because materials obtained through liquid-phase synthesis are amorphous and cannot be obtained for specific information analyzed using conventional analysis methods such as X-ray diffraction (XRD), Raman spectroscopy, or scanning electron microscopy (SEM). However, using pair distribution function (PDF) analysis, Yamamoto et al. found that Li_3PS_4 synthesized in the liquid phase shows significantly higher crystallinity than that prepared through a solid-state reaction; hence, the distance between each PS_4^{3-} tetrahedron was shorter, resulting in low ionic conductivity[85]. Later, Takahashi et al. reported that removing the solvent after synthesis increased the crystallinity of the materials[86]. However, it is still unclear how the solvent used for liquid-phase synthesis affects the ionic conductivity of the material[87-88]. Thus, the properties of solvents, such as the polarity, solubility, and molecular structure, should be investigated to determine their correlation with ionic conductivity.

1.4.2. Phase transition dynamics

Either the solid electrolyte or electrode will undergo a phase transition after interfacial transport. This is attributed to the electrochemical properties of the solid electrolytes. Figure 14 shows that the inherent electrochemical characteristics must be considered for the utilization of solid electrolytes as ionic conductors in the electrodes of ASSBs[89,90]. In the following sections, the causes of and solutions for undesirable reactions due to phase transition phenomena in ASSBs from previous studies are discussed.

1.4.2.1. Narrow potential windows of solid electrolytes

Almost all sulfide-based solid electrolytes possess a narrow potential window, and thus, redox decomposition reactions of the electrolyte occur outside of the potential window[88]. The decomposition products increase interfacial resistance, reducing battery life. Furthermore, this makes it difficult to apply to ASSBs equipped with electrode materials due to their over redox potential less/more than that of sulfide solid electrolyte. To suppress oxidative or reductive decomposition, it has been reported that the original potential range can be extended by applying materials with excellent potential stability[74,80,89]. First, electrolyte oxidation should be suppressed when the potential window is relatively high. For example, cathode materials such as $LiCoO_2$ and $LiNi_{1/3}Mn_{1/3}Co_{1/3}O_2$ operate at approximately 3.5–3.7 V (versus Li/Li^+), but most sulfide solid electrolytes have a potential window below 3.5 V (versus $Li\text{-}In/Li^+$) because of the use of lithium alloy to prevent decomposition. Thus, cathode materials were coated with $Li_4Ti_5O_{12}$, $LiNbO_3$, Li_2SiO_3, or Li_3PO_4, which are stable at potentials 2.0–4.0 V higher than the potential window of sulfide solid electrolytes, and it was confirmed that oxidative decomposition was suppressed and the resistance at the interface with the electrolyte was alleviated[89–91]. Likewise, solid electrolytes with low potential windows must be considered for the utilization of anode materials with low reduction potential windows. In particular, the Li metal anode is the ideal anode for LIBs and ASSBs. In previous studies, it was found that reductive decomposition products resulting from low potential affect lithium dendrite growth as interfacial resistance increases[91,92]. Meanwhile, Tatsumisago and Wang reported that lithium halides showed excellent stability at low potentials[93-96]. Lithium dendrite formation was significantly inhibited in sulfide solid electrolytes featuring lithium halides at critical current density (CCD)[95,98]. Takahashi et al. reported that LiI-incorporated Li_3PS_4 forms a stable interface with Li metal and that lithium dendrite suppression depends on ionic conductivity[96]. Therefore, surface modification of electrode materials by coating with stable materials at high/low potentials should be considered.

Interfacial phenomena in ASSBs have also been considered (Figure 13). Typically, the voids, chemical reactions, electrochemical reactions, and grain boundaries are considered[90]. In the case of LIBs, a small amount of a liquid electrolyte can easily infiltrate an electrode and act as an ionic conductor. In contrast, solid electrolytes cannot

by themselves. Therefore, a composite electrode must contain a certain amount of solid electrolyte to induce ionic conduction. Interestingly, according to previous studies on LIBs, battery performance depends significantly on the inherent porosity and anisotropic tortuosity of the cathode and anode materials, in terms of Li ion kinetics[99]. In other words, improper consideration of the anisotropic tortuosity of the electrode materials affects the homogeneous intercalation/deintercalation reactions of Li ions, leading to reduced battery safety and durability. For this reason, properties such as softness, ionic conductivity, and anisotropic tortuosity also significantly impact the performance of ASSBs. However, their correlations are not yet known. To the best of our knowledge, there have been no such studies for ASSBs, unlike for existing LIBs.

1.4.2.2. Reductive decomposition of solid electrolyte in composite anode for ASSBs

Thus far, the cathode and anode active materials used in existing LIBs have been considered for electrode active materials for ASSBs. Hence, there have been several studies on composite electrodes featuring $LiCoO_2$[76], $LiNi_{1/3}Co_{1/3}Mn_{1/3}O_2$[74], and Li_2S[97] as cathodes in combination with sulfide solid electrolytes. Although those all-solid-state cells showed relatively high specific capacities, the energy densities were insufficient and still lower than those of the existing LIBs[100–106]. One reason for this is the application of lithium-indium (Li-In) alloy to improve reversibility and suppress reactions between the sulfide-based electrolyte and pure lithium metal. Paradoxically, owing to the utilization of Li-In alloy (0.62 V versus Li^+), the average operation voltage of the all-solid-state cells is low[97]. Because a high operation voltage is favorable for obtaining battery systems with high energy density, this is not optimal. Moreover, it has been reported that lithium-based alloys undergo large volume expansion, leading to physical crumbling, accelerating battery degradation, within composites during alloying/dealloying[101]. This is the primary reason that lithium-based alloys are not used in rechargeable batteries. Fortunately, graphite anodes, which are lighter and have a lower reduction potential, can replace Li-In alloy in ASSBs with sulfide solid electrolytes. Graphite is a typical anode material in existing LIBs and has a low reduction potential range (0–0.01 V), relatively high theoretical capacity (372 $mAhg^{-1}$), and high reversibility after the first cycle. Despite this, there have only been a few studies on the use of graphite for ASSBs. To the best of our knowledge, the earliest studies related to graphite anodes for ASSBs were conducted by

Takada et al. and Seino et al., who reported full-cell-type ASSBs with a graphite anode and $LiCoO_2$ cathode and suggested the possibility of graphite as an anode for ASSBs[100,101]. Later, Takeuchi et al. reported an ASSB with Li_2S as the cathode and graphite as the anode, which showed considerably high charge and discharge capacities because of the high theoretical capacity of Li_2S (1166 $mAhg^{-1}$), but cyclability was not satisfactory[97]. In a recent study, Otoyama et al. showed that cracks and voids that form within graphite composite electrodes limit the movement of lithium ions into the electrode during lithiation and delithiation through *operando* confocal microscopy[102,103]. Höltchi et al. reported that control of sulfide solid electrolyte particles could improve the electrochemical performance of graphite composite electrodes; however, the interface between the electrolyte and graphite was unstable[103]. Most recently, Maresca et al. reported on the interface stability of graphite for sulfide solid electrolytes in graphite composite electrodes, examined using linear sweep voltammetry, and the improvement of the electronic conductivity through the conductive carbons of graphite composites with cell assembly optimization[105].

Most of the previous studies sufficiently show the potential of graphite as an anode for ASSBs; however, most of the charge and discharge capacities after several cycles are unfortunately lower than those of LIBs. Although this is probably the result of decomposition of the sulfide electrolyte due to the low reduction potential of graphite[89], the problem of performance degradation caused by electrolyte decomposition has not been addressed. Furthermore, because intercalation/deintercalation of lithium ions in a graphite anode occurs at a significantly low potential[89,100–106], which is almost identical to the potential of lithium metal deposition, the sulfide solid electrolyte can undergo reductive decomposition, according to theoretical research[89]. The decomposition products can increase the interfacial resistance between the graphite anode and sulfide solid electrolyte[91]. Otoyama et al. also demonstrated that the poor contact between the electrode material and the solid electrolyte during the lithiation process in a composite electrode leads to performance degradation[102]. This can also be attributed to the cracks chemically induced by the decomposition products. Therefore, to use graphite anodes in ASSBs for high energy and power densities, decomposition must be suppressed. To achieve a performance similar to the theoretical capacity of graphite, the solid electrolyte must not

decompose; this decomposition may be the main cause of the large polarization of the graphite anode, resulting from the high interfacial resistance in the composite electrode[102,105].

1.4.3. Reaction distribution inside composite electrode

Although the electrochemical and interfacial properties of the ASSB materials mentioned above are understood, some aspects of the phenomena occurring within the battery cannot be explained through these research results[90,106–108]. For example, where the decomposition begins when the battery operates and why lithium dendrites form even when a solid electrolyte is used are still debated. Furthermore, these investigations and studies focus mostly on modeling research, such as with density functional theory (DFT) calculations[19,64,93].

However, these computational studies are limited to microscopic views. For that reason, they cannot explain all of the phenomena in ASSBs, where various reactions occur. Therefore, the internal phenomena in solid-state cells should be explained based on direct observation at the overall scale of the ASSBs, rather than the microscopic scale. The best method would be the *operando* method, which examines how the interface in the solid state changes in real time through direct observation[108]. This method has already been conducted toward understanding the structural transitions of materials two-dimensionally[89]. Various visual analyses have been attempted to elucidate the mechanism of lithium dendrite formation in LIBs and ASSBs (Figure 15). Fortunately, this buried interface information can be obtained using X-ray computed tomography (X-ray CT) to probe lithium dendrite evolution, the reacted electrolyte, or the electrode. Although it is difficult to directly observe lithium dendrite evolution this way owing to the transmission of X-rays for lithium, information can be obtained directly or indirectly through changes in other areas in an ASSB. Thus, X-ray CT should also be applied to ASSB electrodes because interfacial phenomena in solid-state batteries are considered to be more complex than those in LIBs and lithium metal. Moreover, the scale of these phenomena is inhomogeneous, according to various experimental environments. Fortunately, X-ray CT can provide three-dimensional (3D) images by reconstructing solid-state cells from slices

of materials at the micrometer scale. Thus, this analysis technique is expected to provide more convincing evidence about internal phenomena that have been difficult to explain.

1.5. Objectives

As stated above, several problems must be solved for the commercialization of ASSBs. In this doctoral thesis, the author focused on the fabrication of ASSBs using sulfide-type solid electrolytes. In particular, it was focused on (1) the establishment of an inexpensive and industrially suitable method for the synthesis of solid electrolyte nanoparticles in the liquid phase, (2) the elucidation of the factors governing the properties of composite anodes, (3) the establishment of a method to achieve good contact at the interface between graphite anodes and solid electrolytes, and (4) the development of solid electrolytes for the realization of solid-state batteries with lithium metal anodes, which represent the next generation of anodes. The low ionic conductivity of sulfide solid electrolytes synthesized in the liquid phase, various interface issues originating from lithium dendrite formation, and decomposition within solid-state battery cells must be fully understood. Thus, it is essential to first investigate the effects of solvents on the ionic conductivity of sulfide solid electrolytes synthesized in the liquid phase and to understand the structures of the materials synthesized in various solvents. Furthermore, lithium dendrite evolution and decomposition in ASSBs should be investigated at the local scale to understand the fundamental origins toward suppressing them. In addition, a more in-depth understanding of the high polarization induced by the reductive decomposition of sulfide solid electrolytes in composite electrodes is required.

In the research conducted for this thesis, interfacial and microstructural phenomena of solid-state cells for ASSBs were investigated from the atomic scale to the bulk scale. Specific structural information for Li_3PS_4, which was synthesized using various solvents and incorporated lithium bromide, was obtained through PDF analysis. Information on the interface between the solid electrolyte and lithium metal or the electrode before and after electrochemical tests was gathered using X-ray absorption spectroscopy (XAS). Furthermore, to investigate the overall correlations on a larger scale for solid-state cells, X-ray CT was utilized to examine the structure at each interface and

the morphologies of the active materials and solid electrolytes in the solid-state cells, which are difficult to observe using conventional methods such as atomic force microscopy (AFM), SEM, and transmission electron microscopy (TEM). Then, the correlation between the electrochemical properties and the materials was extracted and explained for the kinetics of lithium ions in the composite electrode using various electrochemical methods.

1.6. Thesis outline

This thesis has six chapters, which give general discussions of the solvent used for the liquid-phase synthesis of sulfide solid electrolytes, the role of lithium halides in lithium dendrite suppression, the suppression ability of lithium iodide for the decomposition of Li_3PS_4, and the correlation between the anisotropic tortuosity of a material and electrochemical performance.

Chapter 2 discusses the synthesis of Li_3PS_4 with an acetate solvent system and the characterization of its structure using high-energy XRD coupled with PDF analysis. Butyl acetate, with high polarity, led to the highest ionic conductivity and lowest crystallinity. The correlation between the structural information and properties of the solvent is discussed.

Chapter 3 discusses the study of LiBr-doped Li_3PS_4 in terms of improvement of ionic conductivity, lithium dendrite suppression ability, and structure. The results for LiBr-doped Li_3PS_4 were compared with previously reported results for LiI-doped Li_3PS_4 toward discussing the structural and interfacial information obtained through PDF analysis, X-ray absorption fine structure (XAFS), and high-frequency impedance in the context of the factors affecting lithium dendrite suppression ability.

Chapter 4 discusses the suppression of the decomposition of Li_3PS_4 at the interface with graphite. We attempted to coat the surface of graphite with LiI to suppress decomposition through simple liquid-phase synthesis. XRD, SEM, and Raman results clearly showed that the graphite surface was coated with LiI. The effect of the coating

was revealed through the electrochemical performance. Interface investigations through XAFS and impedance measurements are also discussed.

Chapter 5 discusses the lithium dendrite evolution in the graphite composite electrode observed via *operando* X-ray CT measurements. Based on the obtained X-ray CT images, the starting point for reductive decomposition and lithium dendrite formation on the graphite surface was identified; the lithium filaments grew from the edge of graphite. Consequently, the decomposed layer and lithium filaments disrupt the homogeneous reaction distribution in the composite electrode.

Chapter 6, the correlation between the anisotropic tortuosity of all materials for ASSBs and the electrochemical properties is suggested. X-ray CT was applied to examine the internal morphological change, from which the tortuosity was extracted and calculated. The electrochemical properties were then compared with the obtained data. The relationship between anisotropic tortuosity and the ion kinetic mechanism is discussed.

In chapter 7, all conclusions drawn from experimental results are gathered and expectations of commercialization and directions of further study for ASSBs are suggested.

Reference

1. Worldwide Emission Standards and Related Regulations, *Power train*, 2021.
2. Global annual passenger vehicle sales by drivetrain, *Bloomberg New Energy Forecast.*
3. Dunn, B.; Kamath, H.; Tarascon, J. M., Electrical Energy Storage for the Grid: A Battery of Choices. *Science* **2011,** *334* (6058), 928-935.
4. Zubi, G.; Dufo-López, R.; Carvalho, M.; Pasaoglu, G., The lithium-ion battery: State of the art and future perspectives. *Renew. Sust. Energ. Rev.* **2018,** *89*, 292-308.
5. Wu, H.; Cui, Y., Designing nanostructured Si anodes for high energy lithium ion batteries. *Nano Today* **2012,** *7* (5), 414-429.
6. Islam, M. S.; Fisher, C. A. J., Lithium and sodium battery cathode materials: computational insights into voltage, diffusion and nanostructural properties. *Chem. Soc. Rev.* **2014,** *43* (1), 185-204.
7. Seh, Z. W.; Sun, Y.; Zhang, Q.; Cui, Y., Designing high-energy lithium–sulfur batteries. *Chem. Soc. Rev.* **2016,** *45* (20), 5605-5634.
8. Wang, C.; Nehrir, M. H., Power management of a stand-alone wind/photovoltaic/fuel cell energy system. *IEEE Trans. Energy Convers.* **2008,** *23* (3), 957-967.
9. Bai, W.; Abedi, M. R.; Lee, K. Y., Distributed generation system control strategies with PV and fuel cell in microgrid operation. *Control. Eng. Pract.* **2016,** *53*, 184-193.
10. Bigdeli, N., Optimal management of hybrid PV/fuel cell/battery power system: A comparison of optimal hybrid approaches. *Renew. Sust. Energ. Rev.* **2015**, *42*, 377-393.
11. Frackowiak, E., Carbon materials for supercapacitor application. *Phys. Chem. Chem. Phys.* **2007,** *9* (15), 1774-1785.
12. Conway, B. E., Transition from Supercapacitor to Battery Behavior in Electrochemical Energy-Storage. *J. Electrochem. Soc.* **1991,** *138* (6), 1539-1548.
13. Kathryn R. B., Lead/acid batteries. *J. Power Sources,* **1994**, 51, 1-17.
14. Simon, P.; Gogotsi, Y., Materials for electrochemical capacitors. *Nat. Mater.* **2008,** *7* (11), 845-854.
15. Pasupathi, S.; Gomez, C. C. J.; Su, H.; Reddy, H.; Bujlo, P.; Sita, C., Chapter 5-Stationary HT-PEMFC-Based Systems—Combined Heat and Power Generation,

Hydrogen Energy and Fuel Cells Primers, **2016**, 55-77.

16. Goodenough, J. B.; Kim, Y., Challenges for Rechargeable Li Batteries. *Chem. Mater.* **2010,** *22* (3), 587-603.
17. Goodenough, J. B.; Park, K. S., The Li-ion rechargeable battery: A perspective. *J. Am. Chem. Soc.* **2013,** *135* (4), 1167-1176.
18. Whittingham, M. S., Lithium Batteries and Cathode Materials. *Chem. Rev.* **2004,** *104* (10), 4271-4302.
19. Reisch, Marc S., Solid-state batteries inch their way toward commercialization, *C&EN*, **2017**, 95, 19-21.
20. Nolan, A.M.; Zhu, Y.; He, X.; Bai, Q.; Mo, Y.; Computation-Accelerated Design of Materials and Interfaces for All Solid State Lithium Ion Batteries, Joule, **2018**, 2, 2016-2046.
21. Weppner. W., Engineering of solid state ionic devices, Ionics, **2003**, 9, 444-464.
22. Buckland, K.; Sagiike, H., Toyota Deepens Panasonic Battery Ties in Electric-Car Rush, *Bloomberg Technology*, **2017**.
23. Tatsumisago, M.; Nagao, M.; Hayashi, A., Recent development of sulfide solid electrolytes and interfacial modification for all-solid-state rechargeable lithium batteries. *J. Asian Ceram. Soc.* **2013,** *1* (1), 17-25.
24. Hayashi, A.; Sakuda, A.; Tatsumisago, M., Development of Sulfide Solid Electrolytes and Interface Formation Processes for Bulk-Type All-Solid-State Li and Na Batteries. *Front. Energy Res.* **2016,** *4*, 25-25.
25. Inaguma, Y.; Liquan, C.; Itoh, M.; Nakamura, T.; Uchida, T.; Ikuta, H.; Wakihara, M., High ionic conductivity in lithium lanthanum titanate. *Solid State Commun.* **1993,** *86* (10), 689-693.
26. Murugan, R.; Thangadurai, V.; Weppner, W., Fast Lithium Ion Conduction in Garnet-Type $Li_7La_3Zr_2O_{12}$. *Angew. Chem., Int. Ed.* **2007,** *46* (41), 7778-7781.
27. Kamaya, N.; Homma, K.; Yamakawa, Y.; Hirayama, M.; Kanno, R.; Yonemura, M.; Kamiyama, T.; Kato, Y.; Hama, S.; Kawamoto, K.; Mitsui, A., A lithium superionic conductor. *Nat. Mater.* **2011,** *10* (9), 682-686.
28. Rangasamy, E.; Liu, Z.; Gobet, M.; Pilar, K.; Sahu, G.; Zhou, W.; Wu, H.; Greenbaum, S.; Liang, C., An Iodide-Based $Li_7P_2S_8I$ Superionic Conductor. *J. Am. Chem. Soc.* **2015,** *137* (4), 1384-1387.

29. Nagao, M.; Kitaura, H.; Hayashi, A.; Tatsumisago, M., High Rate Performance, Wide Temperature Operation and Long Cyclability of All-Solid-State Rechargeable Lithium Batteries Using Mo-S Chevrel-Phase Compound. *J. Electrochem. Soc.* **2013,** *160* (6), A819-A823.
30. Braga, M. H.; Grundish, N. S.; Murchison, A. J.; Goodenough, J.B., Alternative strategy for a safe rechareable battery, *Energy Environ. Sci.*, **2017**, 10, 331-336.
31. Miura, A.; Rosero-Navarro, N. C.; Sakuda, A.; Tadanaga, K.; Phuc, N. H. H.; Matsuda, A.; Machida, N.; Hayashi, A.; Tatsumisago, M., Liquid-phase syntheses of sulfide electrolytes for all-solid-state lithium battery. *Nat. Rev. Chem.* **2019,** *3* (3), 189-198.
32. Gromov, O. G.; Kunshina, G. B.; Kuz'min, A. P.; Kalinnikov, V. T., Ionic conductivity of solid electrolytes based on $Li_{1.3}Al_{0.3}Ti_{1.7}(PO_4)_3$. *Russ. J. Appl. Chem.* **1996,** *69*, 385-388.
33. Kubanska, A.; Castro, L.; Tortet, L.; Schäf, O.; Dollé, M.; Bouchet, R., Elaboration of controlled size $Li_{1.5}Al_{0.5}Ge_{1.5}(PO_4)_3$ crystallites from glass-ceramics. *Solid State Ionics* **2014,** *266*, 44-50.
34. Ortiz, G. F.; López, M. C.; Lavela, P.; Vidal-Abarca, C.; Tirado, J. L., Improved lithium-ion transport in NASICON-type lithium titanium phosphate by calcium and iron doping. *Solid State Ionics* **2014,** *262*, 573-577.
35. Subramanian, M. A.; Subramanian, R.; Clearfield, A., Lithium ion conductors in the system $AB(IV)_2(PO_4)_3$ (B = Ti, Zr and Hf). *Solid State Ionics* **1986,** *18-19*, 562-569.
36. Thangadurai, V.; Shukla, A. K.; Gopalakrishnan, J., New lithium-ion conductors based on the NASICON structure. *J. Mater. Chem.* **1999,** *9*, 739-741.
37. Breuer, S.; Prutsch, D.; Ma, Q.; Epp, V.; Preishuber-Pflügl, F.; Tietz, F.; Wilkening, M., Separating bulk from grain boundary Li ion conductivity in the sol-gel prepared solid electrolyte $Li_{1.5}Al_{0.5}Ti_{1.5}(PO_4)_3$. *J. Mater. Chem. A* **2015,** *3*, 21343-21350.
38. Fu, J., Superionic conductivity of glass-ceramics in the system Li_2O-Al_2O_3-TiO_2-P_2O_5. *Solid State Ionics* **1997,** *96*, 195-200.
39. Pershina, S. V.; Antonov, B. D.; Farlenkov, A. S.; Vovkotrub, E. G., Glass-ceramics in $Li_{1+x}Al_xGe_{2-x}(PO_4)_3$ system: The effect of Al_2O_3 addition on microstructure, structure and electrical properties. *J. Alloys Compound.* **2020,** *835*, 155281.
40. Xu, X.; Wen, Z.; Yang, X.; Zhang, J.; Gu, Z., High lithium ion conductivity glass-

ceramics in Li_2O-Al_2O_3-TiO_2-P_2O_5 from nanoscaled glassy powders by mechanical milling. *Solid State Ionics* **2006,** *177*, 2611-2615.

41. Bohnke, O.; Bohnke, C.; Fourquet, J. L., Mechanism of ionic conduction and electrochemical intercalation of lithium into the perovskite lanthanum lithium titanate. *Solid State Ionics* **1996,** *91*, 21-31.
42. Harada, Y.; Ishigaki, T.; Kawai, H.; Kuwano, J., Lithium ion conductivity of polycrystalline perovskite $La_{0.67-x}Li_{3x}TiO_3$ with ordered and disordered arrangements of the A-site ions. *Solid State Ionics* **1998,** *108*, 407-413.
43. Stramare, S.; Thangadurai, V.; Weppner, W., Lithium Lanthanum Titanates: A Review. *Chem. Mater.* **2003,** *15*, 3974-3990.
44. Inaguma, Y.; Liquan, C.; Itoh, M.; Nakamura, T.; Uchida, T.; Ikuta, H.; Wakihara, M., High ionic conductivity in lithium lanthanum titanate. *Solid State Commun.* **1993,** *86*, 689-693.
45. Murugan, R.; Thangadurai, V.; Weppner, W., Fast Lithium Ion Conduction in Garnet-Type $Li_7La_3Zr_2O_{12}$, *Angew. Chem. Int. Ed.*, **2007**, 46, 7778-7781.
46. Awaka, J.; Kijima, N.; Hayakawa, H.; Akimoto, J., Synthesis and structure analysis of tetragonal $Li_7La_3Zr_2O_{12}$ with the garnet-related type structure. *J Solid State Chem* **2009,** *182*, 2046-2052.
47. O'Callaghan, M. P.; Lynham, D. R.; Cussen, E. J.; Chen, G. Z., Structure and ionic-transport properties of lithium-containing garnets $Li_3Ln_3Te_2O_{12}$ (Ln = Y, Pr, Nd, Sm-Lu). *Chem. Mater.* **2006,** *18*, 4681-4689.
48. Thangadurai, V.; Narayanan, S.; Pinzaru, D., Garnet-type solid-state fast Li ion conductors for Li batteries: Critical review. *Chem. Soc. Rev.* **2014,** *43*, 4714-4727.
49. Thangadurai, V.; Weppner, W., $Li_6ALa_2Ta_2O_{12}$ (A=Sr, Ba): Novel garnet-like oxides for fast lithium ion conduction. *Adv. Funct. Mater.* **2005,** *15*, 107-112.
50. Sharafi, A.; Yu, S.; Naguib, M.; Lee, M.; Ma, C.; Meyer, M. H.; Nanda, J.; Chi, M.; Siegel, J. D.; Sakamoto, J., Impact of air exposure and surface chemistry on Li-$Li_7La_3Zr_2O_{12}$ interfacial resistance, *J.Mater.Chem.A*, **2017**, 5, 13475-13487.
51. Jiang, Z.; Han, Q.; Wang, S.; Wang, H., Reducing the Interfacial Resistance in All-Solid-State Lithium Batteries Based on Oxide Ceramic Electrolytes, *ChemElectroChem*, **2019**, 6, 2970-2983.
52. Fenton, D.E.; Parker, J.M.; Wright, P.V., Complexes of alkali metal ions with

poly(ethylene oxide), *Polymer*, **1973**, 589.

53. Farrington, G.C.; Briant, J.L., Fast Ionic Transport in Solids: Crystalline solids with liquid-like ionic conductivities are revolutionizing solid-state electrochemistry, *SCIENCE*, **1979**, 204, 1371-1379.
54. Murata, K.; Izushi, S.; Yoshihisa, Y., An overview of the research and development of solid polymer electrolyte batteries, *Electrochemica Acta*, **2000**, 45, 1501-1508.
55. Xu, K.; Nonaqueous Liquid Electrolytes for Lithium-Based Rechareable Batteries, *Chem. Rev.*, **2004**, 104, 4304-4417.
56. Yao, P.; Yu, H.; Ding, Z.; Liu, Y.; Lu, J.; Lavorgna, M.; Wu, J.; Liu, X., Review on Polymer-Based Composite Electrolytes for Lithium Batteries, *Front. Chem.*, **2019**.
57. Park, S.; Han, A.; Shin, J., Kim, Kim., Influence of crystallinity on ion conductivity of PEO-based solid electrolytes for lithium batteries, *Macromol. Res.*, **2010**, 18, 336-340.
58. Hasan, N.; Pulst, M.; Samiullah, M.H.; Kressler, J., Comparison of Li^+ ion conductivity in linear and crosslinked poly(ethylene oxide), *J Poly Sci Poly Phys.*, **2019**, 57, 21-28.
59. Guo, H.; Sun, H.; Jiang, Z.; Luo, C.; Gao, M.; Wei, M.; Hu, J.; Shi, W.; Cheng, J.; Zhou H., A new type of composite electrolyte with high performance for room-temperature solid-state lithium battery, *J Mater Sci*, **2019**, 54, 4874-4884.
60. Zha, W.; Chen, F.; Yang, D.; Shen, D.; Zhang, L., High performance $Li_{6.4}La_3Zr_{1.4}Ta_{0.6}O_{12}$/Poly(ethylene oxide)/Succinonitrile composite electrolyte for solid-state lithium batteries, *J. Power Sources*, **2018**, 397, 87-94.
61. Agrawal, R.C.; Pandey, G.P., Solid polymer electroytes: materials designing and all-solid-state battery application: an overview., *J. Phys. D: Appl. Phys.*, **2008**, 41, 223001-223019.
62. Tachez, M.; Malugani, J.; Mercier, R.; Robert, G., Ionic conductivity of and phase transition in lithium thiophosphate Li_3PS_4. *Solid State Ionics* **1984,** *14* (3), 181-185.
63. Kuhn, A.; Gerbig, O.; Zhu, C.; Falkenberg, F.; Maier, J.; Lotsch, B. V., A new ultrafast superionic Li-conductor: Ion dynamics in $Li_{11}Si_2PS_{12}$ and comparison with other tetragonal LGPS-type electrolytes. *Phys. Chem. Chem. Phys.* **2014,** *16*, 14669-14674.
64. Mo, Y.; Ping Ong, S.; Ceder, G., First Principles Study of the $Li_{10}GeP_2S_{12}$ Lithium Super Ionic Conductor Material. *Chem. Mater.* **2011,** *24*, 15-17.

65. Deiseroth, H.-J.; Kong, S.-T.; Eckert, H.; Vannahme, J.; Reiner, C.; Zaiß, T.; Schlosser, M., Li_6PS_5X: A Class of Crystalline Li-Rich Solids With an Unusually High Li^+ Mobility. *Angew. Chem., Int. Ed.* **2008,** *120* (4), 767-770.

66. Kraft, M. A.; Culver, S. P.; Calderon, M.; Bocher, F.; Krauskopf, T.; Senyshyn, A.; Dietrich, C.; Zevalkink, A.; Janek, J.; Zeier, W. G., Influence of Lattice Polarizability on the Ionic Conductivity in the Lithium Superionic Argyrodites Li_6PS_5X (X = Cl, Br, I). *J. Am. Chem. Soc.* **2017,** *139* (31), 10909-10918.

67. Dietrich, C.; Weber, D.A.; Culver, S.; Senyshyn, A.; J. Sedlmaier, S.; Indris, S.; Janek, J.; G. Zeier, W., Synthesis, Structural Characterization, and Lithium Ion Conductivity of the Lithium Thiophosphate $Li_2P_2S_6$. *Inorg. Chem.* **2017,** *56*, 6681-6687.

68. Dietrich, C.; Koerver, R.; Gaultois, M. W.; Kieslich, G.; Cibin, G.; Janek, J.; Zeier, W. G., Spectroscopic characterization of lithium thiophosphates by XPS and XAS-a model to help monitor interfacial reactions in all-solid-state batteries. *Phys. Chem. Chem. Phys.* **2018,** *20*, 20088-20095.

69. Dietrich, C.; Weber, D.A.; Sedlmaier, S.J.; Indris, S.; Culver, P.S.; Walter, D.; Janek, J.; Zeier, W.G., Lithium ion conductivity in Li_2S-P_2S_5 glasses-building units and local structure evolution during the crystallization of superionic conductors Li_3PS_4, $Li_7P_3S_{11}$ and $Li_4P_2S_7$, *J.Mater.Chem.A*, 2017, 5, 18111-18119.

70. Ohara, K.; Mitsui, A.; Mori, M.; Onodera, Y.; Shiotani, S.; Koyama, Y.; Orikasa, Y.; Murakami, M.; Shimoda, K.; Mori, K.; Fukunaga, T.; Arai, H.; Uchimoto, Y.; Ogumi, Z., Structural and electronic features of binary Li_2S-P_2S_5 glasses. *Sci. Rep.* **2016,** *6* (1), 1-9.

71. Ohtomo, T.; Hayashi, A.; Tatsumisago, M.; Tsuchida, Y.; Hama, S.; Kawamoto, K., All-solid-state lithium secondary batteries using the $75Li_2S{\cdot}25P_2S_5$ glass and the $70Li_2S{\cdot}30P_2S_5$ glass-ceramic as solid electrolytes. *J. Power Sources* **2013,** *233*, 231-235.

72. Nam, Y. J.; Cho, S.-J.; Oh, D. Y.; Lim, J.-M.; Kim, S. Y.; Song, J. H.; Lee, Y.-G.; Lee, S.-Y.; Jung, Y. S., Bendable and Thin Sulfide Solid Electrolyte Film: A New Electrolyte Opportunity for Free-Standing and Stackable High-Energy All-Solid-State Lithium-Ion Batteries., *Nano Letters*, **2015**, *15*, 3317-3323.

73. Sakuda, A.; Hayashi, A.; Tatsumisago, M., Sulfide Solid Electrolyte with Favorable Mechanical Property for All-Solid-State Lithium Battery. *Sci. Rep.* **2013,** *3* (1), 2261-

2261.

74. Auvergniot, J.; Cassel, A.; Ledeuil, J.-B.; Viallet, V.; Seznec, V.; Dedryvère, R., Interface Stability of Argyrodite Li_6PS_5Cl toward $LiCoO_2$, $LiNi_{1/3}Co_{1/3}Mn_{1/3}O_2$, and $LiMn_2O_4$ in Bulk All-Solid-State Batteries. *Chem. Mater.* **2017,** *29* (9), 3883-3890.
75. Murayama, M.; Kanno, R., Synthesis of New Lithium Ionic Conductor Thio-LISICON—Lithium Silicon Sulfides System. *J. Solid State Chem.* **2002,** *168* (1), 140-148.
76. Sakuda, A.; Hayashi, A.; Ohtomo, T.; Hama, S.; Tatsumisago, M., All-solid-state lithium secondary batteries using $LiCoO_2$ particles with pulsed laser deposition coatings of Li_2S-P_2S_5 solid electrolytes. *J. Power Sources* **2011,** *196* (16), 6735-6741.
77. Orikasa Y., Hierarchical Spatiotemporal Analyses of Reaction Using Synchrotron Radiation and the Design of Next-Generation Energy Conversion Devices, *Electrochemistry*, **2015**, 83(9), 695-700.
78. Hayashi, A.; Hama, S.; Morimoto, H.; Tatsumisago, M.; Minami, T., Preparation of Li_2S-P_2S_5 Amorphous Solid Electrolytes by Mechanical Milling. *J. Am. Ceram. Soc.* **2004,** *84* (2), 477-479.
79. Boulineau, S.; Courty, M.; Tarascon, J.-M.; Viallet, V., Mechanochemical synthesis of Li-argyrodite Li_6PS_5X (X=Cl, Br, I) as sulfur-based solid electrolytes for all solid state batteries application. *Solid State Ionics* **2012,** *221*, 1-5.
80. Liu, Z.; Fu, W.; Payzant, E. A.; Yu, X.; Wu, Z.; Dudney, N. J.; Kiggans, J.; Hong, K.; Rondinone, A. J.; Liang, C., Anomalous High Ionic Conductivity of Nanoporous β-Li_3PS_4. *J. Am. Chem. Soc.* **2013,** *135* (3), 975-978.
81. Choi, S.; Lee, S.; Park, J.; Nichols, W. T.; Shin, D., Facile synthesis of Li_2S-P_2S_5 glass-ceramics electrolyte with micron range particles for all-solid-state batteries via a low-temperature solution technique (LTST). *Appl. Surf. Sci.* **2018,** *444*, 10-14.
82. Wang, H.; Hood, Z. D.; Xia, Y.; Liang, C., Fabrication of ultrathin solid electrolyte membranes of β-Li_3PS_4 nanoflakes by evaporation-induced self-assembly for all-solid-state batteries. *J. Mater. Chem. A* **2016,** *4* (21), 8091-8096.
83. Teragawa, S.; Aso, K.; Tadanaga, K.; Hayashi, A.; Tatsumisago, M., Liquid-phase synthesis of a Li_3PS_4 solid electrolyte using N-methylformamide for all-solid-state lithium batteries. *J. Mater. Chem. A* **2014,** *2* (14), 5095-5099.
84. Matsuda, A.; Muto, H.; H.H. Phuc, N., Preparation of Li_3PS_4 Solid Electrolyte by

Liquid-Phase Shaking Using Organic Solvents with Carbonyl Group as Complex Forming Medium. *J. Jpn. Soc. Powder and Powder Metallurgy* **2016,** *63* (11), 976-980.

85. Phuc, N. H. H.; Morikawa, K.; Totani, M.; Muto, H.; Matsuda, A., Chemical synthesis of Li_3PS_4 precursor suspension by liquid-phase shaking. *Solid State Ionics* **2016,** *285*, 2-5.
86. Lim, H.-D.; Yue, X.; Xing, X.; Petrova, V.; Gonzalez, M.; Liu, H.; Liu, P., Designing solution chemistries for the low-temperature synthesis of sulfide-based solid electrolytes. *J. Mate. Chem. A,* **2018,** *6* (17), 7370-7374.
87. Yamamoto, K.; Takahashi, M.; Ohara, K.; Phuc, N.H.H.; Yang, S; Watanabe, T.; Uchiyama, T.; Sakuda, A.; Hayashi, A.; Tatsumisago, M; Muto, H.; Matsuda, A.; Uchimoto, Y.; Synthesis of Sulfide Solid Electrolytes through the Liquid phase: Optimization of the Preparation Conditions, *ACS Omega*, **2020**. 5, 26287-26294.
88. Takahashi, M.; Yang, S; Yamamoto, K.; Ohara, K.; Phuc, N.H.H.; Watanabe, T.; Uchiyama, T.; Sakuda, A.; Hayashi, A.; Tatsumisago, M; Muto, H.; Matsuda, A.; Uchimoto, Y.; Improved of lithium ionic conductivity of Li_3PS_4 through suppression of crystallization using low-boiling point solvent in liquid-phase synthesis, *Solid State Ionics*, **2021**, 361, 115568-115573.
89. Zhu, Y.; He, X.; Mo, Y.; Origin of Outstanding Stability in the Lithium Solid Electrolyte Materials: Insights from Thermodynmic Analyses Based on First-Principles Calculations, *ACS Appl. Mater. Interfaces*, **2015**, 7, 23682-23693.
90. Banerjee, A.; Wang, X.; Fang, C.; Wu, A. E,; Meng, S. Y.; Interfaces and Interphases in All-Solid-State Batteries with Inorganic Solid Electrolytes, *Chem. Rev.*, **2020**, 120, 6878-693387. Zhu, Y.; He, X.; Mo, Y.; Origin of Outstanding Stability in the Lithium Solid Electrolyte Materials: Insights from Thermodynmic Analyses Based on First-Principles Calculations, *ACS Appl. Mater. Interfaces*, **2015**, 7, 23682-23693.
91. Otoyama, M.; Suyama, M.; Hotehama, C.; Kowada, H.; Takeda, Y.; Ito, K.; Sakuda, A.; Tatsumisago, M.; Hayashi, A.; Visulization and Control of Chemically induced Crack Formation in All-Solid-State Lithium-Metal Batteries with Sulfide Electrolyte, *ACS Appl. Mater. Interfaces*, **2021**, 13, 5000-5007.
92. Lewis, J. A.; Cortes, F. J. Q.; Liu, Y.; Miers, J. C.; Verma, A.; Vishnugopi, B. S.; Tippens, J.; Prakash, D.; Marches, T. S.; Han, S.Y.; Lee, C.; Shetty, P. P.; Lee, H-W.;

Shevchenko, P.; Carlo, F. D.; Saldana, C.; Mukherjee. P. P.; McDowell, M. T.; Linking void and interphase elvolution to electrochemistry in solid-state batteries using operando X-ray tomography, *Nature Materials*, **2021**, 20, 503-510.

93. Kato, A.; Yamamoto, M.; Sakuda, A.; Hayashi, A.; Tatsumisago, M.; Mechanical Properties of Li_2S-P_2S_5 Glasses with Lithium Halides and Application in All-Solid-State Batteries, *ACS Appl. Energy Mater.*, **2018**, 1, 1002-1007.
94. Ji, X.; Hou, S.; Wang, P.; He, X.; Piao, N.; Chen, J.; Fan, X.; Wang, C.; Solid-State Electrolyte Design for Lithium Dendrite Suppression, *Adv. Mater.*, **2020**, 32, 2002741-2002750.
95. Han, F.; Yue, J.; Zhu, X.; Wang, C.; Suppressing Li Dendrite Formation in Li_2S-P_2S_5 Solid Electrolyte by LiI Incorporation, *Adv. Energy Mater.*, **2018**, 8, 1703644-1703650.
96. Takahashi, M.; Watanabe, T.; Yamamoto, K.; Ohara, K.; Sakuda, A.; Kimura, T.; Yang, S.; Nakanishi, K.; Uchiyama, T.; Kimura, M.; Hayashi, A.; Tatsumisago, M.; Uchimoto, Y.; Investigation of the Suppression of Dendritic Lithium Growth with a Lithium-Iodide-Containing Solid Electrolyte, *Chem. Mater.*, **2021**, 33, 4907-4914.
97. Takeuchi, T.; Kageyama, H.; Nakanishi, K.; Ohta, T.; Sakuda, A.; Sakai, T.; Kobayashi, H.; Sakaebe, H.; Ogumi, Z.; Application of graphite-solid electrolyte composite anode in all-solid-state lithium secondary battery with Li_2S positive electrode, *Solid State Ionics*, **2014**, 262, 138-142.
98. Suyama, M.; Kato, A.; Sakuda, A.; Hayashi, A.; Tatsumisago, M., Lithium dissolution/deposition behavior with Li_3PS_4-LiI electrolyte for all-solid-state batteries operating at high temperatures. *Electrochim. Acta* **2018,** *286*, 158-162.
99. Ebner, M.; Chung, D-W.; Garcia, R. W.; Wood, V.; Tortuosity Anisotropic in Lithium-Ion Battery Electrodes, *Adv. Energy Mater.*, **2014**, 4, 1301278-1301284.
100. K. Takada, T. Inada, A. Kajiyama, H. Sasaki, S. Kondo, M. Watanabe, M. Murayama, R. Kanno, Solid-state lithium battery with graphite anode, *Solid State Ionics*, **2003**, 158, 269 – 274.
101. Y. Seino, K. Takada, B-C Kim, L. Zhang, N. Ohta, H. Wada, M. Osada, T. Sasaki, Synthesis of phosphorous sulfide solid electrolyte and all-solid-state lithium batteries with graphite electrode, *Solid State Ionics*, **2005**, 176, 2389–2293.
102. M. Otoyama, H. Kowada, A. Sakuda, M. Tatsumisago, A. Hayashi, *Operando*

Confocal Microscopy for Dynamic Changes of Li^+ Ion Conduction Path in Graphite Electrode Layers of All-Solid-State Batteries, *J. Phys. Chem. Lett.* **2020**, 11, 990 – 904.

103. M. Otoyama, A. Sakuda, A. Hayashi, M. Tatsumisago, Optical microscopic observation of graphite composite negative electrodes in all-solid-state lithium batteries, *Solid State Ionics*, **2018**, 323, 123–129.
104. L. Höltchi, F. Jud, C. Borca, T. Huthwelker, C. Villevieille, V. Pelé, C. Jordy, M. E. Kazzi, P. Nvák, Study of Graphite Cycling in Sulfide Solid Electrolytes, *J. Electrochem. Soc.*, **2020**, 167, 110558–1105568.
105. G. Maresca, A. Tsurumaki, N. Suzuki, T. Tsujimura, Y. Aihara, M. A. Navarra, Improvement of Graphite Interfacial Stability in All-Solid-State Cells Adopting Sulfide Glassy Electrolytes, *ChemElectroChem*, **2021**, 8, 689–696.
106. L. Höltchi, C. Borca, T. Huthwelker, F. Marone, C. schlepütz, V. Pelé, C. Jordy, C. Villevieille, M. E. Kazzi, P. Nvák, Performance-limiting factors of graphite in sulfide-based all-solid-state lithium-ion batteries, *Electrochem. Acta*, **2021**, 389, 138735-138745.
107. Hatzell, K.B.; Chen, X.C.; Cobb, C.L; Dasgupta N.P.; Dixit, M.B; Marbella, L.E.; McDowell. M.T.; Mukherjee, P.P.; Verma, A.; Viswanathan, V.; Westover, A.S.; Zeier, W.G.; Challenges in Lithium Metal Anodes for Solid-State Batteries, *ACS Energy Lett.*, **2020**, 5, 922-934.
108. Liu, H.; Cheng, X.B.; Huang, J.Q.; Yuan, H.; Lu, Y.; Yan, C.; Zhu, G.L.; Xu, R.; Zhao, C.Z.; Hou, L.P.; He, C.; Kaskel, S.; Zhang, Q.; Controlling Dendrite Growth in Solid-State Electrolytes, *ACS Energy Lett.*, **2020**, 5, 833-843.
109. Lewis, J.A.; Cortes, F.J.Q.; Liu, Y.; Miers, J.C.; Verma, A.; Vishinugopi, B.S.; Tippens, J.; Prakash, D.; Marchese, T.S.; Han, S.Y.; Lee, C.; Shetty, P.P.; Lee, H-W.; Shevchenko, P.; Carlo, F.D.; Saldana, C.; Mukherjee, P.P.; McDowell M.T.; Linking void and interphase evolution to electrochemistry in solid state batteries using operando X-ray tomography, *Nature materials*, **2021**, 20, 503-510.

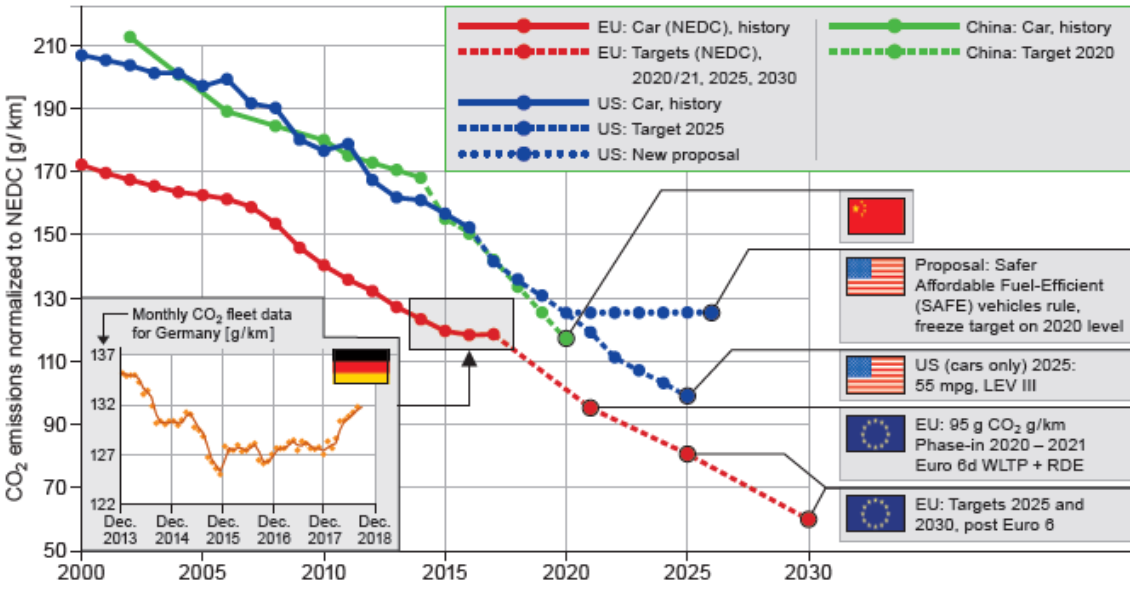

Figure 1. Historic carbon dioxide emissions and reduction target for different regions in the world[1]

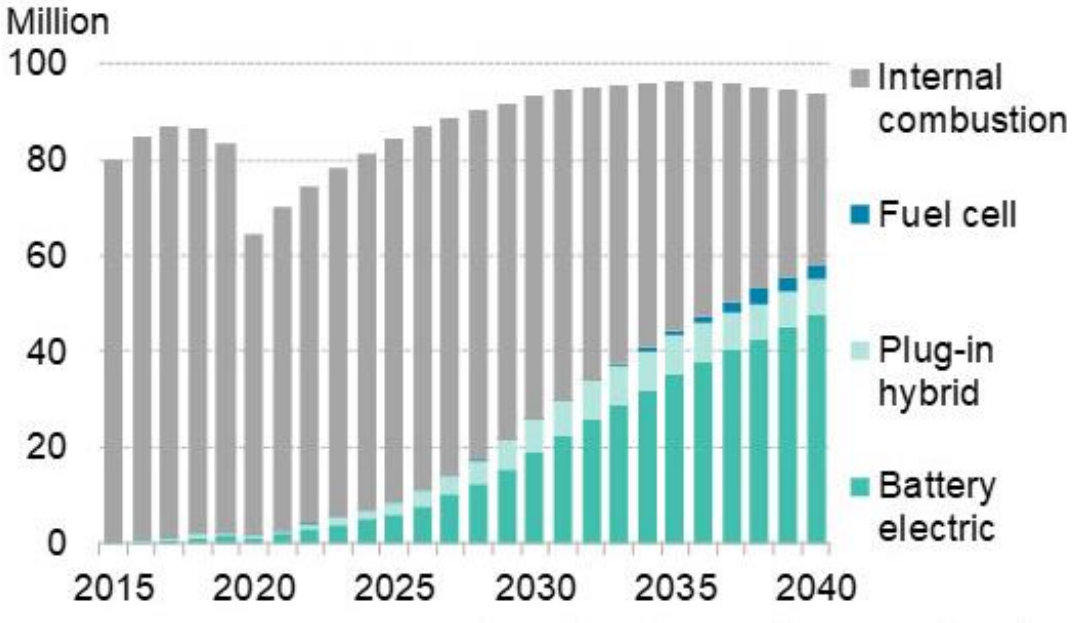

Figure 2. Global annual passenger vehicle sales by drivetrain[2]

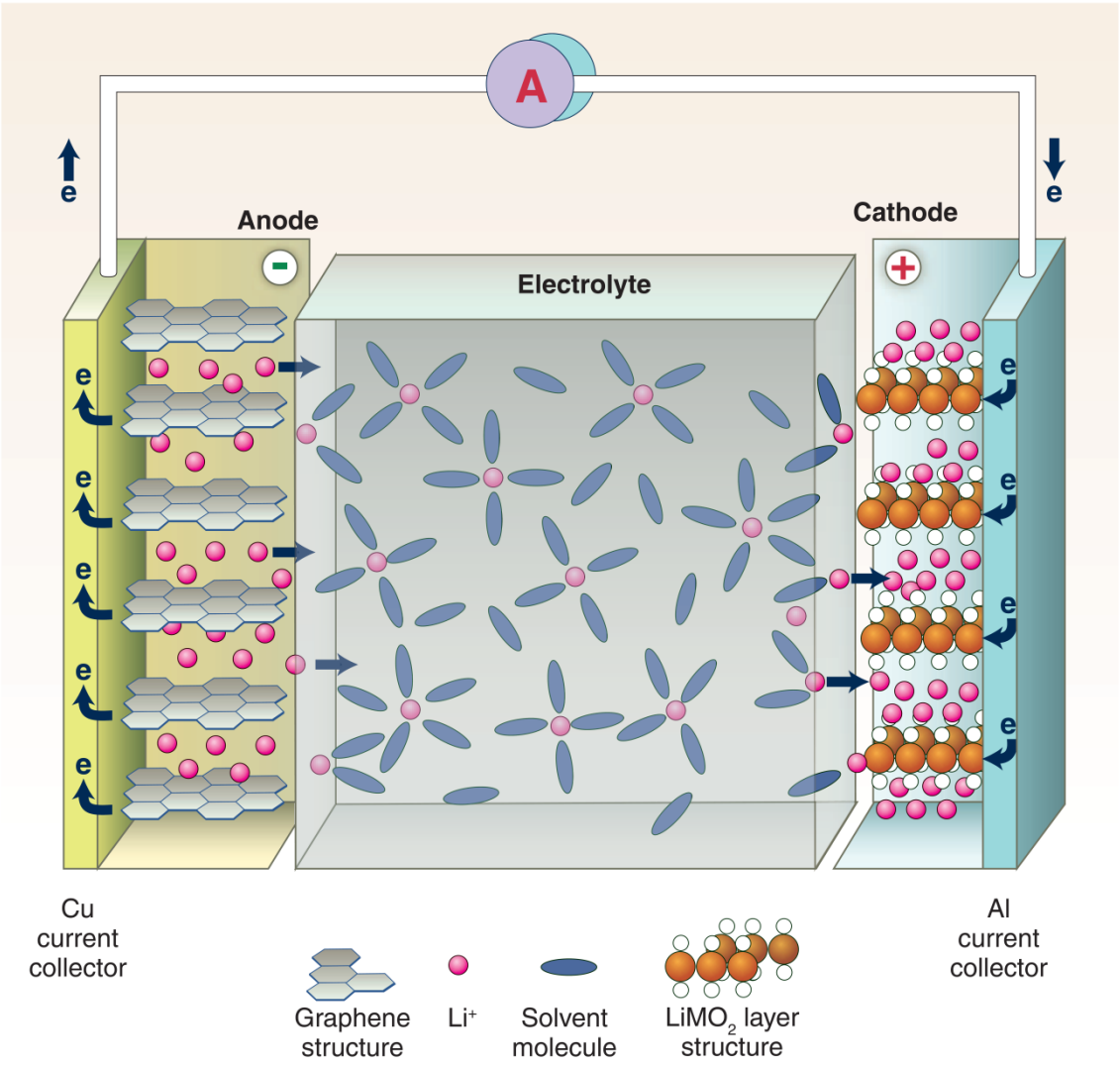

Figure 3. Schematic figure of rechargeable lithium-ion battery[3]

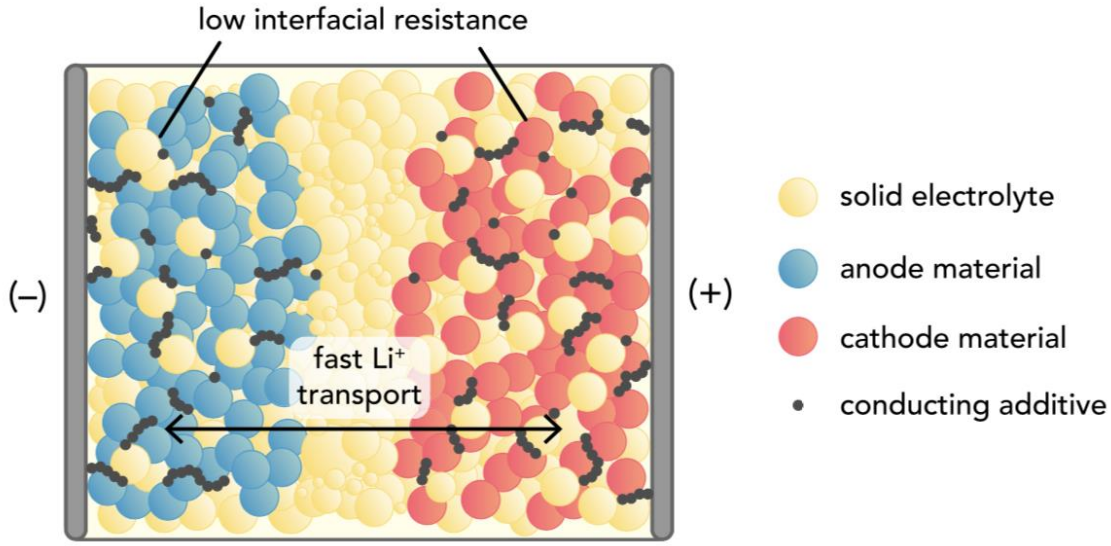

Figure 4. Illustration for the configuration of all-solid-state batteries[20]

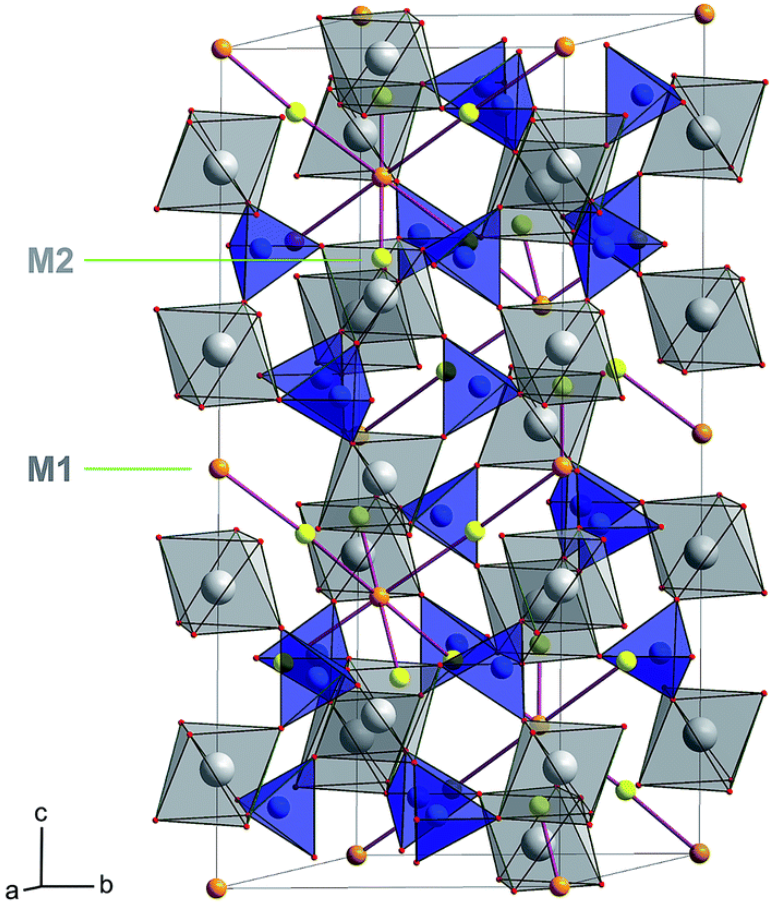

Figure 5. Crystal structure of NASICON-type solid electrolyte, using LATP as an example[36]

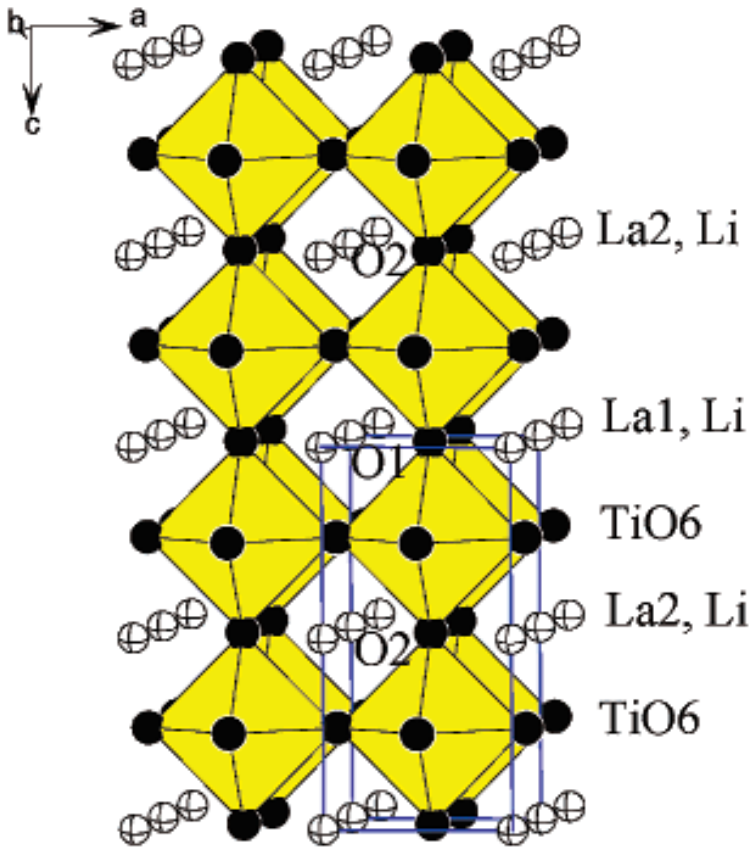

Figure 6. Crystal structure of perovskite-type solid electrolyte, using $Li_{3x}La_{(2/3)-x}\square_{(1/3)-2x}TiO_3$ (x = 0.11) as an example[67]

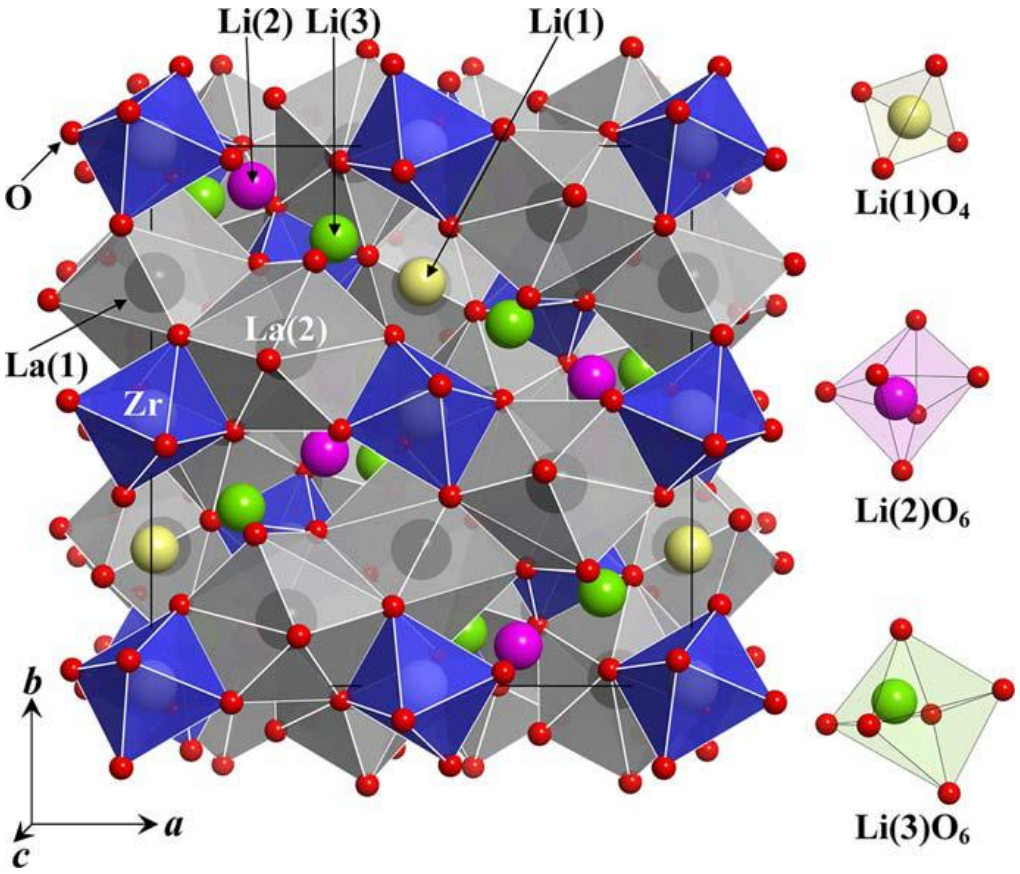

Figure 7. Crystal structure of garnet-type solid electrolyte, using $Li_7La_3Zr_2O_{12}$ as an example [44]

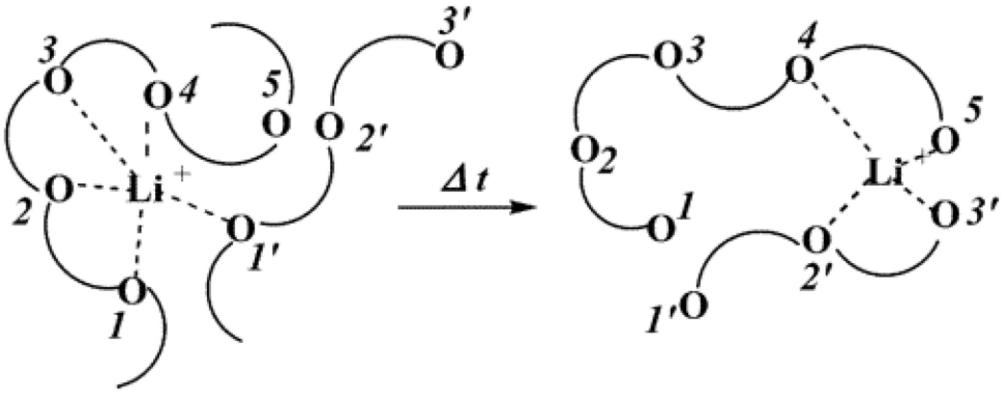

Figure 8. Schematic illustration of lithium-ion conduction mechanism for PEO-based polymer electrolyte[54]

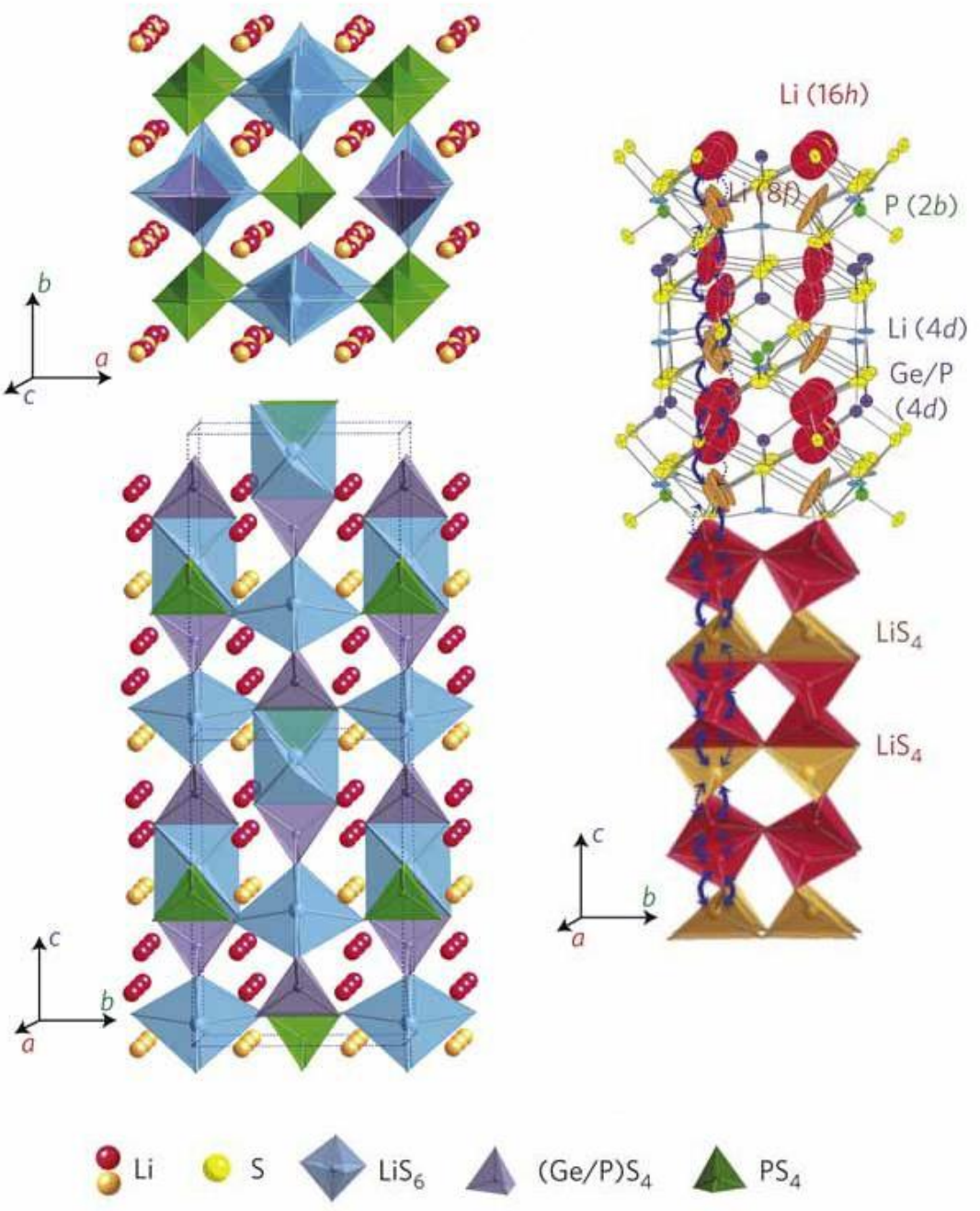

Figure 9. (a) Framework structure of $Li_{10}GeP_2S_{12}$ and lithium ions that participate in ionic conduction. (b) Conduction pathways of lithium ions[26]

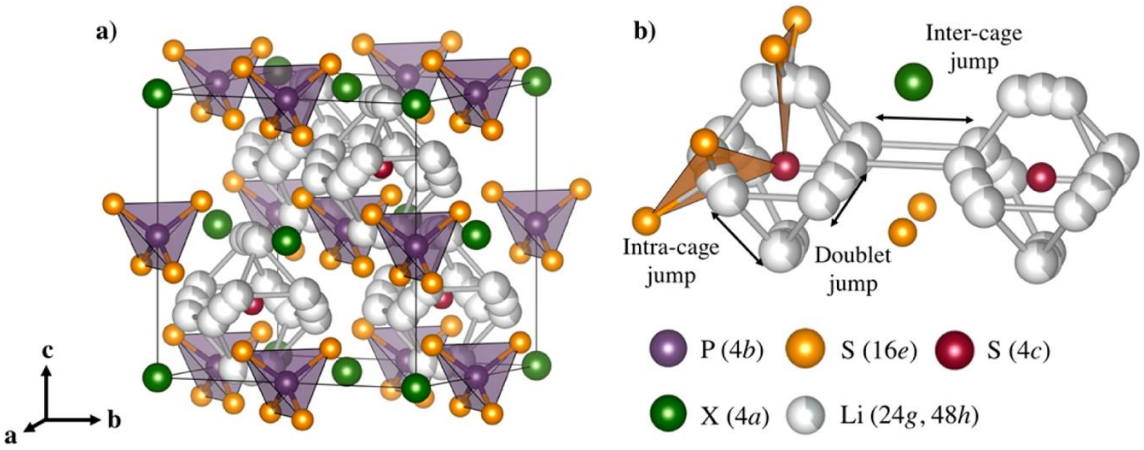

Figure 10. (a) Ordered crystal structure of Li_6PS_5X where X = Cl, Br, I and (b) scheme of inter-cage jumps[64]

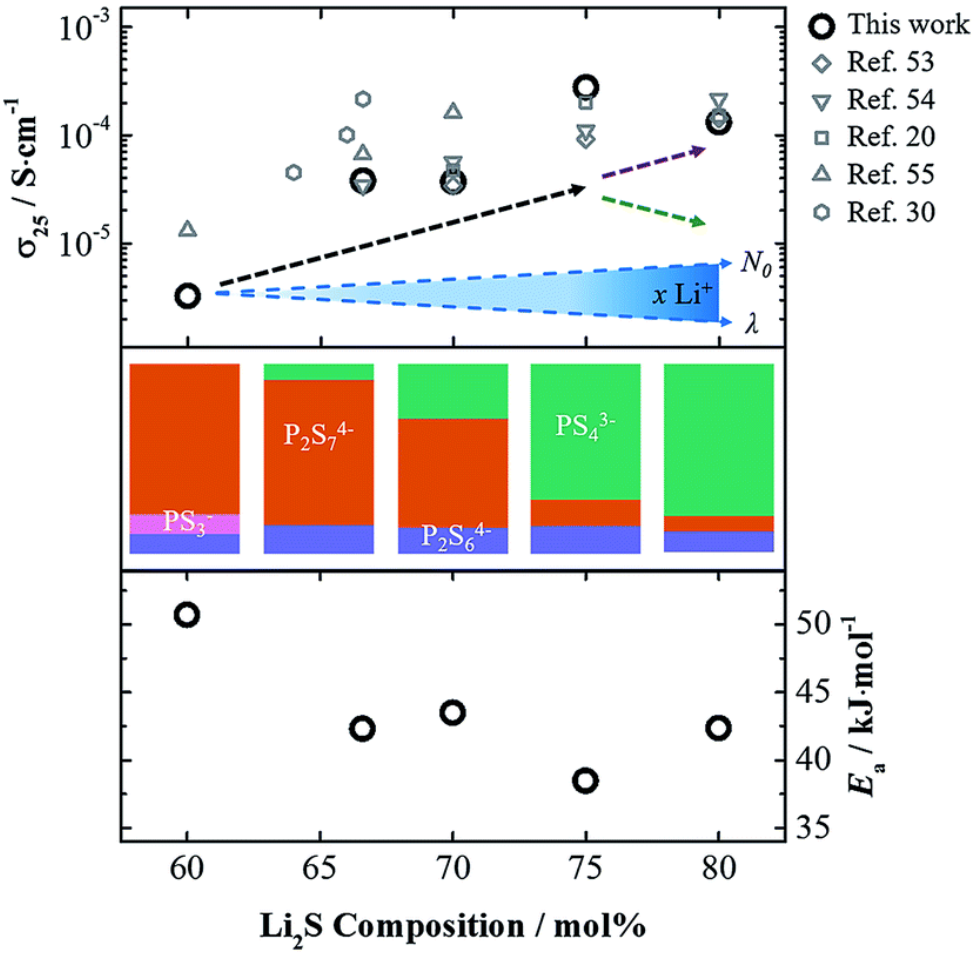

Figure 11. (Top) Variation of isothermal conductivity of LPS glass with x at room temperature and literature data. The arrows show the general trend with composition; at x > 75, there were two different trends (green and purple arrows). (Middle) Colored bar graphs depicting the percentages of various thiophosphate anions that affect transport properties. (Bottom) Activation energies at various Li_2S compositions[68]

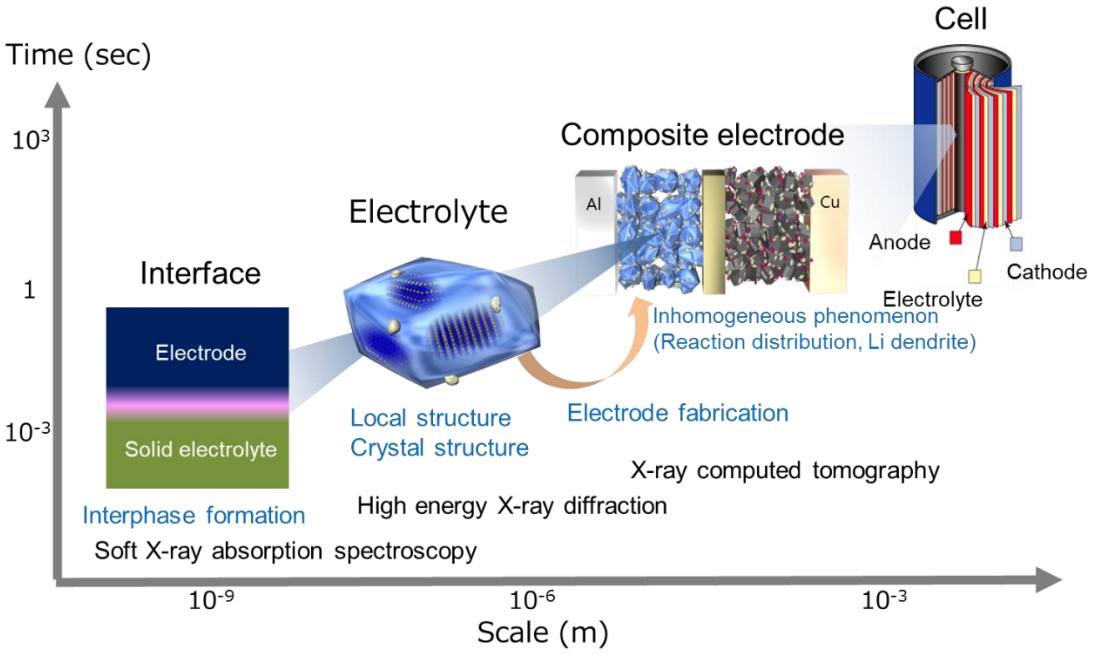

Figure 12. Schematic plot for spatiotemporal analysis according to the reaction processes in batteries[77]

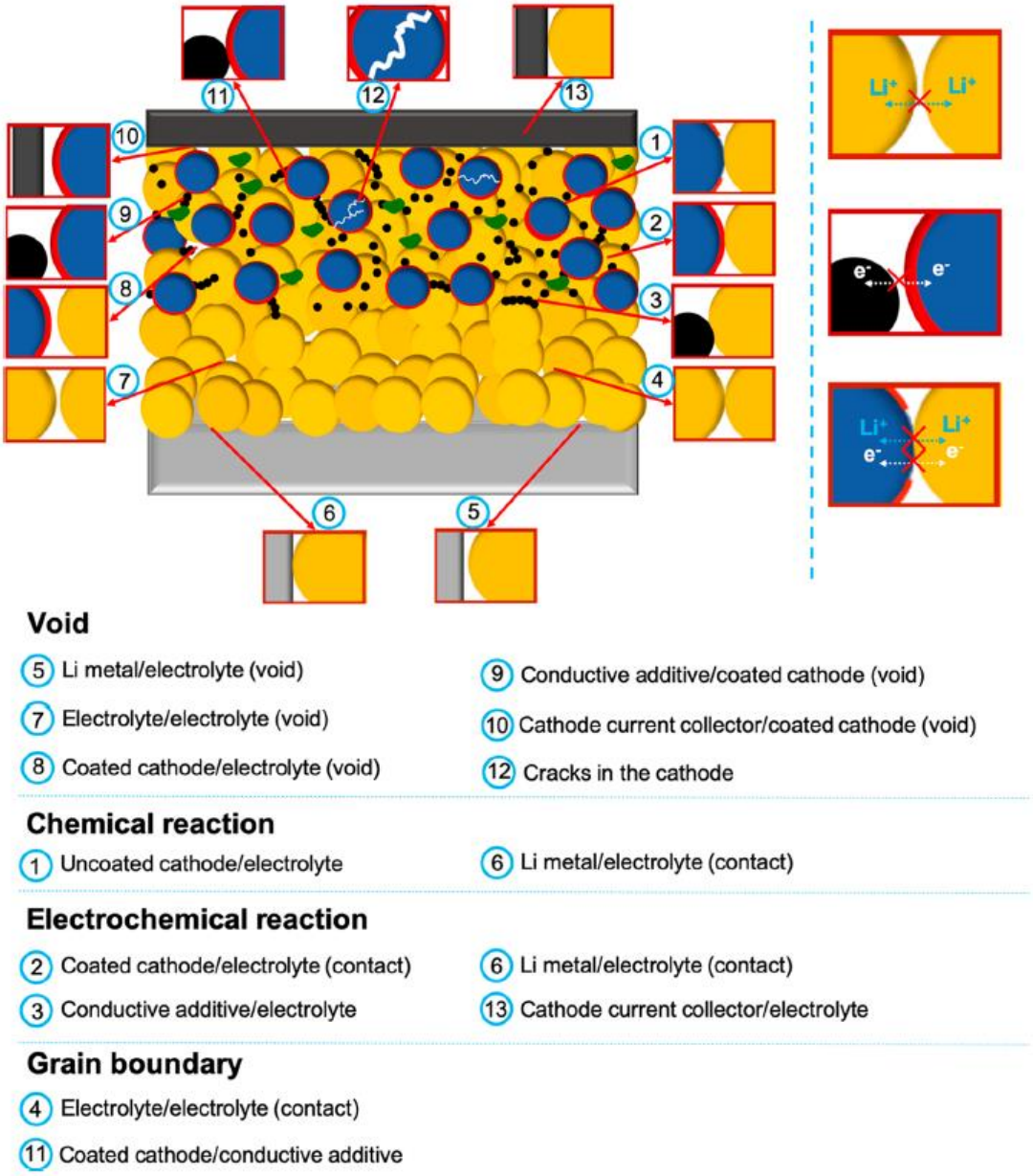

Figure 13. Schematic illustration of interfacial phenomena experienced in ASSBs[89]

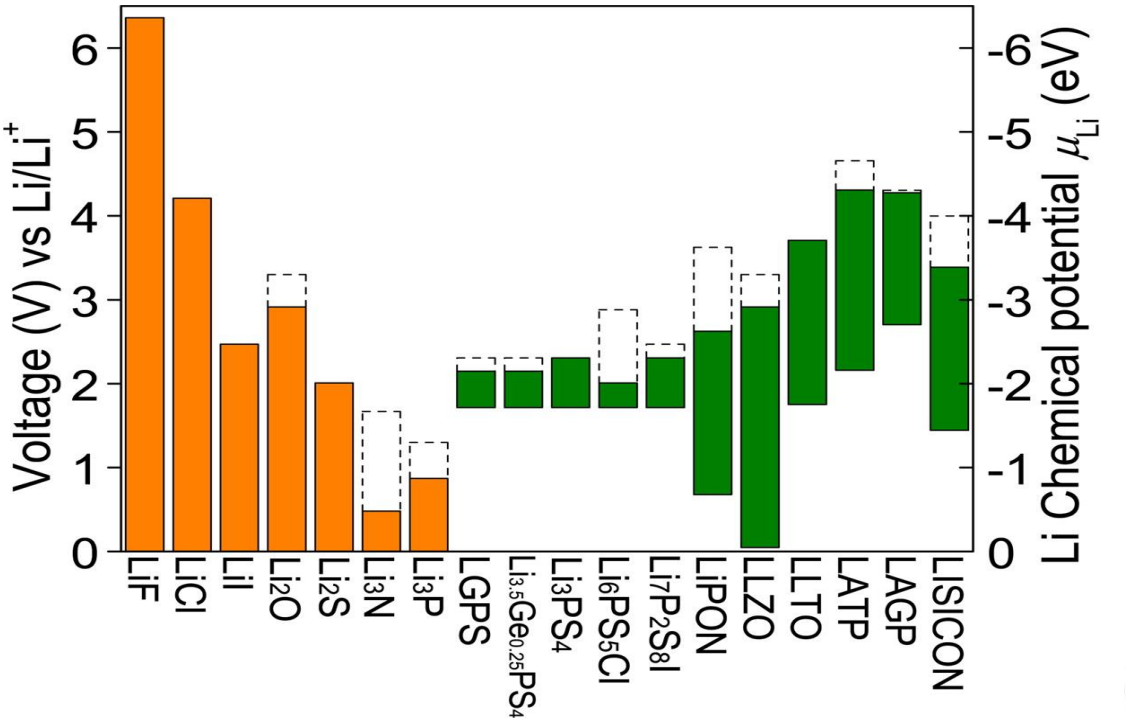

Figure 14. Electrochemical potential window of solid electrolytes and other materials[88]

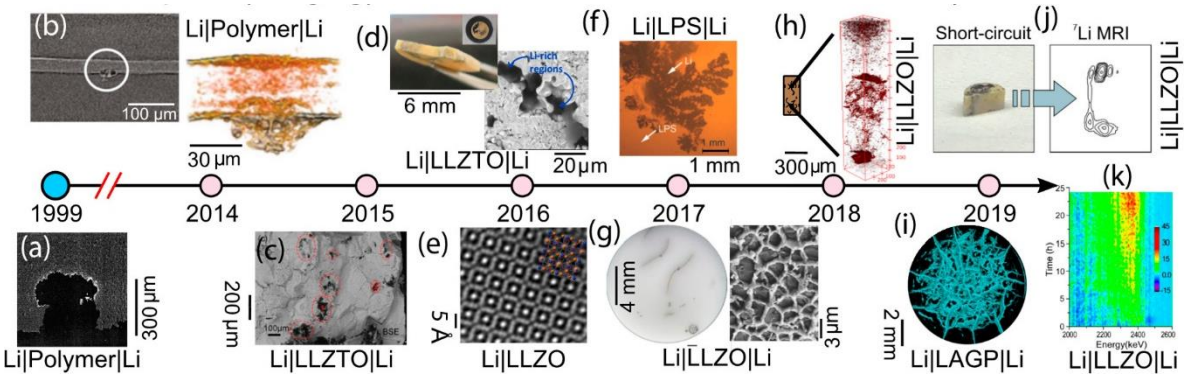

Figure 15. Timeline of visual analyses for the mechanism of lithium dendrite formation at the interface between lithium metal and electrolytes[105]

Chapter 2. High Ionic Conductivity of Liquid-Phase-Synthesized Li_3PS_4 Solid Electrolyte, Comparable to That Obtained *via* Ball Milling

Recently, several sulfide solid electrolytes have been synthesized by liquid-phase synthesis for the commercialization of all-solid-state batteries. Unfortunately, the ionic conductivity for most of these solid electrolytes is unsatisfactory compared to that of solid electrolytes synthesized by conventional ball milling. This problem is attributed to different mechanisms between the liquid phase and the solid phase in reaction and formation. However, to the best of our knowledge, the effect of the solvent on the ionic conductivity of solid electrolytes has not been extensively investigated, although the identification of these properties is a key point in understanding the liquid-phase synthesis. Herein, the correlation between ionic conductivity and crystallinity originating from the solvents used has been investigated. As a result, the ionic conductivity of the electrolyte was found to be strongly dependent on polarity (δ_p) with low crystallinity. The highest ionic conductivity (5.09 x 10^{-4} Scm^{-1} at 25 ºC) was obtained using butyl acetate, which exhibited the lowest δ_p. Moreover, the highest ionic conductivity of Li_3PS_4 produced by liquid-phase synthesis using butyl acetate was very comparable to that obtained by ball milling (5.14 x 10^{-4} Scm^{-1}).

2.1. Introduction

Lithium-ion secondary batteries are expected to be applied in electrical vehicles and smart grid systems. However, the existing LIBs have a safety concern because of the use of flammable organic liquid electrolytes. All-solid-state batteries, which use inorganic solid electrolyte, are the most promising next-generation energy storage devices to achieve high safety[1]. The key component in the all-solid-state battery is the solid electrolyte, which is typically synthesized by mechanical milling or by a solid-state reaction at high temperature[1-2]. Unfortunately, this conventional synthesis method limits

the commercial application of all-solid-state batteries because of the difficulty in upscaling the synthesis process and high cost[1-2]. One of the alternatives to overcome this limitation is the liquid-phase synthesis using organic solvents[3]. The liquid–phase synthesis of sulfide solid electrolytes has several advantages with respect to the conventional ball milling method in terms of synthesis time, controlling morphology, and scalability[3–5]. In addition, the liquid–phase is useful to prepare a composite between electrolyte and electrode. Composite electrodes prepared by the mechanical milling method typically need to be mixed with 30–60 wt% solid electrolyte to maintain lithium–ion conduction pathways in the composite electrode[6–7]. However, liquid phase processes can cover active materials with solid electrolyte more easily than mechanical milling. This is useful to minimize the amount of solid electrolyte needed for preparation of the composite, leading to an improved energy density of all–solid–state batteries

So far, the thiosulfates Li_3PS_4[5-8], $Li_7P_3S_{11}$[9-12], $Li_7P_2S_8I$[12-14], Li_4PS_4I[14], argyrodites Li_6PS_5X (X = Cl, Br, and I)[15-17], and the thio-LISICON $Li_{10}GeP_2S_{12}$ family ($Li_{3.25}Ge_{0.25}P_{0.75}S_4$)[18] have been synthesized and reported. Among these electrolytes, the argyrodite-type solid electrolyte exhibits high ionic conductivity ~10^{-2}–10^{-3} S cm^{-1}, however, it has critical threshold such as the multi-step synthesis using two different solvents, which is not suitable for commercialization[17]. Conversely, Among the Li_2S-P_2S_5 systems, Li_3PS_4 is the most stable compound and requires only a one-step synthesis process[4,18-20]. Despite its advantages, another critical limitation of Li_3PS_4 produced by liquid-phase synthesis is its lower ionic conductivity than that produced by the ball milling process[1,3-7]. Most of the previous studies have not only successfully accomplished improving the Li_3PS_4 ionic conductivity by using organic solvents such as ethyl propionate[21], ethyl acetate[5], dimethyl carbonate[22-23], acetonitrile[6], and tetrahydrofuran[4,7] but also suggested the model of interaction between the functional group of solvents and raw materials (Li_2S, P_2S_5) in liquid media[22-23]. However, the ionic conductivity (1.6–2.0 × 10^{-4} S cm^{-1}) still remains unsatisfactory compared to that of ball milling.

Among a lot of efforts to clarify the origin of low ionic conductivity of Li_3PS_4, we had previously investigated the causes of the low ionic conductivity of solid electrolytes prepared by liquid-phase synthesis through the Pair distribution functions (PDF) analysis, which was known as a suitable analysis tool for amorphous materials[24-27]. In there, thermal treatment to remove the remaining solvents in vacuum mood led to

an increase in crystallinity with a decrease in ionic conductivity. Furthermore, we demonstrated that ionic conductivity can be improved by modifying the annealing conditions for the electrolyte synthesized by the liquid-phase synthesis. However, the improved ionic conductivity (1.68×10^{-4} S cm^{-1}) was not satisfactory compared to that of the electrolyte synthesized by ball milling, and the solvent effects on the ionic conductivity remain unclear.

In this study, we investigated the effects of solvents, namely, ethyl acetate (EA), isopropyl acetate (IPA), propyl acetate (PA), and butyl acetate (BA) on the ionic conductivity of Li_3PS_4 prepared by liquid-phase synthesis, and confirmed how the characterization of materials vary from solvent to solvent. After the synthesis with mentioned solvents above, the composites (hereafter referred to precursors) were measured by X-ray diffraction (XRD) to confirm the structure, and thermogravimetry analysis (TGA) to obtain appropriate annealing temperatures in terms of the thermal dynamic behavior before annealing. The annealed materials were also analyzed by electrochemical impedance spectroscopy (EIS), XRD, Raman, and scanning electron microscopy (SEM) to investigate their electrochemical and chemical properties and microstructures, accompanying with PDF analysis based on high energy X-ray diffraction. To gain insight on the relationship between ionic conductivity of the materials prepared by liquid-phase synthesis and solvent properties, the correlation between the Hansen solubility parameter[29-30] of the solvent and ionic conductivity was evaluated for each solvent.

2.2. Experimental Section

2.2.1. Liquid phase synthesis with each acetate solvent

Li_3PS_4 was synthesized by mixing Li_2S (Sigma Aldrich, 99%) with P_2S_5 (Sigma Aldrich, 99%) in a molar ratio of 3:1) and adding a zirconia ball of 4 mm in the solvents such as ethyl acetate (hereafter referred to EA), propyl acetate (hereafter referred to PA), isopropyl acetate (hereafter referred to IPA), and butyl acetate (hereafter referred to BA). All solvents were purchased from Sigma-Aldrich. The reaction times were optimized according to the solvent used (6 h for BA, and 12 h for EA, IPA, and PA), and the reactions

were performed at 30 °C. The white precipitates were obtained and extracted into centrifugation tube, followed by centrifugation (Sigma, 3-30K) under 10,000 rpm for 5 min and drying under vacuum. Annealing of the as-dried powders was performed at 100 °C from 1 h to 24 h. The final product yields were ~85–90% in a 1.0 g scale. Additionally, as a reference material for comparison, Li_3PS_4 was prepared by mechanical milling of Li_2S and P_2S_5 with 600 rpm rotation speed for 10 h, using 45 mL of zirconia. All processes were performed in an air-filled glove box.

2.2.2. TGA, XRD, and Raman measurements

TGA of the precursors was performed using a Thermo plus EVO 02 (Rigaku) system, in which the argon gas was purged to the TGA chamber after transferring the alumina pan loaded with the precursor powder in the glove box. The weight loss of the precursor was monitored over 25–250 °C. XRD measurements were performed using a RINT-Ultima III (Rigaku) system with CuKα radiation at 40 kV and 40 mA. Raman spectra were collected using a DXR3 (Thermo scientific) device with 532 nm laser. All samples were prepared on a special holder fabricated to prevent the reaction of the compounds with air in the glove box. SEM measurements were performed using a SU8220 (Hitachi High-Technologies) system in order to evaluate the microstructure of each material.

2.2.3. High-Energy X-ray diffraction coupled with Pair distribution function (PDF) analysis

The high-energy XRD experiments for Li_3PS_4 prepared with each solvent were performed at room temperature by a SPring-8 high-energy XRD beamline BL04B2 system using a two-axis diffractometer[28]. The incident X-ray energy obtained using Si 220 crystal monochromator was 61.4 keV[24-25]. The scattering X-ray was detected by a flat panel detector. The scattering data were collected in terms of background, absorption, multiple scattering, and inelastic scattering. The calculations were performed according to previous studies[27], as follows. The structure factor, $S(Q)$, was obtained from the standardization of the collected scattering data using the number of atoms and scattering intensity of one atom. Moreover, the reduced PDF, $G(r)$, was calculated using the Fourier transform of $S(Q)$. $G(r)$ was defined by the equation $G(r) = 4\pi r\rho_0[\rho(r)/\rho_0 - 1]$, where r, ρ_0,

and $\rho(r)$ are the real-space distances, average atomic number density, and local atomic number density, respectively. Therefore, the data for the existing probability of the real distance were obtained using high-energy XRD measurements correlated to PDF analysis. Additionally, the crystallinity of the materials was calculated using the obtained PDF results, according to a previous study[25], by the following equation (1):

$$G_{\text{experimental data}}(r) = (1-\chi)\, G_{\text{ball milling}}(r) + \chi\, G_{\text{crystal}}(r) \quad (1)$$

where $G_{\text{experimental data}}(r)$, $G_{\text{ball milling}}(r)$, and $G_{\text{crystal}}(r)$ are the experimental data for the synthesized materials in each solvent, ball milling, and Li_3PS_4 annealed at 270 ℃, which was obtained from the previous study[25] owing to the Li_3PS_4 crystallinity of nearly 100%, respectively. Lastly, the fraction of the crystalline phase *(χ)* was determined. Equation (1) also provides the error of the experimental result, $G_{experimental\ data}(r)$, by comparing the calculated value with the obtained the fraction of the crystalline phase, χ.

2.2.4. Ionic conductivity

Individual Li_3PS_4 samples prepared with each solvent were added to the electrochemical cell with 10 mm diameter and pressed with two stainless-steel rods on both sides at 360 MPa in an argon-filled glove box. The ionic conductivity measurements were performed by alternating current impedance at 25 °C in the frequency range between 1 MHz and 0.1 Hz with an amplitude of 100 mV^4 using a ModuLab XM ECS (Solartron Analytical) system. The Nyquist plots exhibited a semi-arc pattern at high frequencies and a straight line at low frequencies. The total conductivity was determined using the intercept between the semi-arc and straight line as the total resistance obtained in the Nyquist plots.

2.3. Results and discussion

The weight loss due to heating of the precursors synthesized using each solvent was measured by TGA, as shown in Figure 1. Interestingly, the weight loss behavior is not compatible with inherent solvent's boiling point (EA: 77 °C, IPA: 89 °C, PA: 102 °C, and BA: 127 °C). This implies that the chemical interaction between the sulfur

compounds and the solvent in precursor structure must be different. Moreover, the weight loss for each solvent at 150 °C was also different, 30 wt% of EA, 36 wt% of IPA, 38 wt% of PA, and 45 wt% of BA. DTA (Figure 1b) shows that endothermic peaks for all precursors were observed at around 100 °C, in the order of BA (100 °C) < PA (104 °C) < IPA (106 °C) < EA (112 °C). Moreover, the calculated numbers of coordinated solvent molecules for the precursors, based on TGA at 150 °C, followed the order BA < PA < IPA < EA (Figure 2). These results imply that the strength of the chemical interaction between the sulfur compounds and the solvent in the precursor structure increases in the order BA < PA < IPA < EA. This is attributed to each solvent's polarity, which will be discussed later with respect to the Hansen's solubility parameter. The XRD patterns were studied to verify the presence of raw materials (Figure 3). Both Li_2S and P_2S_5 must react completely in the liquid phase for the optimization of the liquid-phase synthesis; if these materials are remained, their ionic conductivity would be lower because of remained Li_2S with low ionic conductivity (10^{-5} Scm^{-1})[27]. The peaks corresponding to Li_2S and P_2S_5 were not detected in all XRD patterns. Thus, the liquid-phase synthesis using each solvent proceeded satisfactorily and different precursor structures, which might be related to the solvent molecular structures, were observed depending on the solvent used.

The annealing of the synthesized precursors was carried out at 100 °C; this condition was determined because all solvent molecules were decomposed at around 100 °C (Figure 1). Next, the ionic conductivities for all materials were measured by EIS (Figure 4 and Figures 5 and 6). The ionic conductivity of Li_3PS_4 synthesized with BA was higher than those of other materials, and the ionic conductivity decreased after reaching the highest value regardless of used solvent. The highest ionic conductivity followed the order BA > PA > IPA > EA, and the specific values were as follows, BA: 5.09×10^{-4} S cm^{-1}, PA: 2.52×10^{-4} S cm^{-1}, IPA: 2.11×10^{-4} S cm^{-1}, and EA: 1.42×10^{-4} S cm^{-1}. It is interesting to note that the ionic conductivity of Li_3PS_4 synthesized with BA was similar to that with ball milling (5.14×10^{-4} S cm^{-1}). To the best of our knowledge, this is the first time that a solid electrolyte prepared by liquid-phase synthesis exhibits an ionic conductivity comparable to that prepared by ball milling. The tendency for the ionic conductivity to first increase and then decrease with annealing time is attributed to the fact that the

decrease of the intermediate and the increase of the crystallinity occurred simultaneously as the annealing time increased[27]. The increase of the crystallinity of the Li_3PS_4 from 1 to 24 h annealing time was confirmed by XRD (Figure 7).

In the next step, to determine the factors governing the ionic conductivity of the solid electrolyte prepared by liquid-phase synthesis, SEM and XRD analyses were performed for the samples that showed the highest ionic conductivity in each solvent group. The Li_3PS_4 prepared by mechanical milling and that prepared by liquid-phase synthesis with different solvents have different particle morphologies (Figure 8). Figure 9 shows the pressure dependency of the ionic conductivity of Li_3PS_4 prepared by mechanical milling and liquid-phase synthesis with BA. The ionic conductivities of both Li_3PS_4 products increased greatly in the pressure from 0 to 100 MPa, and they remained almost constant in the pressure range from 100 to 460 MPa. This result implies that the morphology of the sulfide solid electrolyte does not affect the ionic conductivity under high pressure. Therefore, although the solvent can be selected according to the target particle shape, it might be not a crucial factor affecting the ionic conductivity.

Figure 10a shows the XRD patterns for the samples that showed the highest ionic conductivity in each solvent in comparison with the one prepared by ball milling; it can be seen that the phase corresponds to a typical amorphous structure of Li_3PS_4[1]. The evident peaks corresponding to crystalline Li_3PS_4 can be seen in the XRD patterns of EA and IPA with similar intensity; however, the peak intensity of PA is lower than those of EA and IPA. Moreover, the peak intensity of BA is the lowest, and a broad peak profile is shown. The XRD results not only suggest that BA is closer to the amorphous phase rather than the crystalline phase, but also indicates that the other materials synthesized with EA, IPA and PA have higher crystallinity than BA and ball milling. Moreover, the XRD results agree with the Raman spectra (Figure 10b); the strong peak at 423 cm^{-1} is attributed to the PS_4^{3-} tetrahedral anion species and is detected in all samples[31]. In the Raman spectra, the crystallinity of the materials was confirmed by the full width at half maximum (FWHM) of the peak, which reflects the structural distribution; for example, the crystalline materials show sharper and narrower peaks than amorphous materials[32]. The peaks at 423 cm^{-1} have different FWHM, and the results are summarized in Table 1. The BA-based Li_3PS_4 showed the broadest FWHM with a wider area among the liquid-phase-synthesized materials, but it was lower than that that of ball milling. This is the

most important factor contributing to the lower ionic conductivity of the BA-based Li_3PS_4 than that of the ball milling.

The results of PDF analysis based on the high-energy XRD patterns not only supported our findings based on the above XRD and Raman data but also confirmed the differences from the structural and crystallographic viewpoints, which could not be confirmed using conventional analysis. After analyzing the data and assignment of each peak, the detailed results are discussed below. According to previous studies[25-27], the peak at 2.0 Å, which is maintained regardless of crystallization, is associated to the P-S bond in the PS_4^{3-} tetrahedral anions, and the peaks at 3.3 Å and 4.1 Å indicate the S–S bonds in PS_4^{3-} and between PS_4^{3-} tetrahedral structures, respectively. The peak at 3.3 Å is detected regardless of crystallization, whereas the intensity of the peak at 4.1 Å increases upon crystallization. Thus, the ratio of these peaks enables us to determine the crystallinity of the material and confirms the existence of an intermediate, which is composed of a mixture of the solvent and solid electrolyte[27]. Lastly, the peak at 6.6 Å is associated to the P–P bond and its intensity increases upon crystallization, which indicates the formation of ordered PS_4^{3-} tetrahedral anions.

Along with the data for the peaks described above, the PDF results (Figure 11) show the characteristic PDF patterns corresponding to Li_3PS_4 for all samples, in which a constant peak intensity is observed at 2.0 Å, whereas intensity differences are observed in the peaks ranging from 3.0 to 5.0 Å and those in the 6.6 Å region. Compared that of ball milling with those of liquid-phase synthesized, the intensity of the peaks ranging of 3.0 to 5.0 Å and the peaks at 6.6 Å shows evident differences, suggesting that the liquid-phase-synthesized samples, IPA, EA, have predominant higher crystalline characteristics than non-crystalline characteristics, which is in agreement with the XRD and Raman results. Crystallinity was increased when the intensity of peak at 4.1 Å was higher[27]. Comparing the peaks at 4.1 Å, the peak intensities for the ball milling and BA-based sample were almost equal, and the other solvents-based materials exhibited relatively higher peak intensities. That is, the materials prepared by ball milling and BA exhibit low peak intensities and low crystallinity and their ionic conductivity is higher than the others; these findings agreed with the aforementioned XRD and Raman results as well as with previous studies[25, 27]. Based on the PDF results, the author investigated the crystallinity

ratio of the samples using equation (1), in which the crystallinity ratio of the ball-milling sample was designated to be 0% and was considered as the reference (See experimental section). The specific crystallinity percent ratios for each sample were as follows, BA-based Li_3PS_4: 3.9%, PA-based Li_3PS_4: 36.7%, IPA-based Li_3PS_4: 56.8%, and EA-based Li_3PS_4: 77.2%, and its relationship with ionic conductivity was plotted for each solvent as shown in Figure 11b. Furthermore, to determine the error of the calculated crystallinity ratio, the author compared the $G_{\text{experimental data}}(r)$ values with the calculated $G(r)$ and the fraction of the crystalline phase, χ. As shown in Figure 12, both $G_{\text{experimental data}}(r)$ and calculated $G(r)$ for each sample show identical patterns, indicating that the errors between them were negligible. Therefore, the fraction of the crystalline phase obtained by PDF analysis clearly explained the reason for the higher ionic conductivity of BA-based Li_3PS_4 than those prepared using other solvents and also for the lower ionic conductivity of BA-based Li_3PS_4 compared to that of the ball milling. Because of the fine crystallinity of BA-based Li_3PS_4, it exhibits lower ionic conductivity than that of ball milling. Thus, crystallinity is an extremely critical factor to the ionic conductivity of Li_3PS_4.

Moreover, the author investigated the key factor, which is employed from Hansen's solubility parameter components, on the ionic conductivity of Li_3PS_4 prepared by liquid-phase synthesis by correlating the TGA results. These results were also plotted using the components of the Hansen solubility parameter from the following equation:

$$\delta^2 = \delta_D^2 + \delta_P^2 + \delta_H^2 \qquad (2)$$

Hansen solubility parameter δ is obtained by the sum of the energy from dispersion forces δ_D, polarity δ_P, and hydrogen bonds δ_H among molecules, and it is a useful approach to predict if one material will dissolve in another and form a solution suggested by Charles M. Hansen[30-31].

Table 2 summarizes δ, δ_P, δ_H, and δ_D for each solvent, which were plotted against ionic conductivity in Figure 13. The results revealed the correlation of Hansen's solubility parameter components, in particular, ionic conductivity has a strong correlation with δ_P. The crystallinity obtained from PDF is combined with the data shown in Figure 14, in which lower δ_P led to a decrease in the crystallinity ratio, thereby improving the ionic conductivity. This clearly demonstrates that δp is the major factor contributing to the

crystallinity and ionic conductivity of the electrolyte prepared through the liquid-phase synthesis method. Because of the low δ_P of BA, it was favorably eliminated than other solvents, as observed in the TGA result, (Figure 1), while EA which has high δ_P is difficult to be eliminated.

2.4. Conclusion

Acetate solvent systems were used in liquid-phase synthesis, which was completely optimized under each condition. Among the prepared materials, Li_3PS_4 synthesized with BA showed the highest ionic conductivity (5.09×10^{-4} S cm^{-1}), which is comparable to that of the same material obtained via ball milling (5.14×10^{-4} S cm^{-1}). This is the highest value of ionic conductivity obtained among the solid electrolytes prepared by liquid-phase synthesis. Structural and crystallographic data obtained by XRD, Raman spectral, and PDF analyses were collected. Compared to samples prepared from other solvents, BA-based Li_3PS_4 demonstrated a more amorphous phase according to the XRD and PDF results and lower crystallinity based on the fwhm of the Raman spectra. Moreover, the relationship between ionic conductivity and crystallinity ratio was obtained by PDF analysis, from which BA had the lowest crystallinity ratio (3.9%). Despite its low value, that fine crystallinity ratio might affect the ionic conductivity. To further investigate the reason for the BA-based compound having the highest ionic conductivity and to determine the key factor of the solvent, the Hansen solubility parameter was used to identify the effect of solubility parameters on ionic conductivity. It was determined that the lower the polarity, the higher was the ionic conductivity. That is, solvent polarity had the most significant effect on ionic conductivity, which possibly affects the formation of the complex during liquid-phase synthesis and the thermodynamic behavior during annealing. However, elucidation of the kinetic correlation between the molecular structure of the solvent and complex formation requires further investigation. the author believes that the results of this study clarify the reason for the high ionic conductivity in electrolytes prepared through liquid-phase synthesis and will provide insights into development of efficient sulfide solid electrolytes.

Reference

1. Hayashi, S. Hama, H. Morimoto, M. c, T. Minami, *J.Am.Ceram. Soc.* **2001**, 84, 477-479.
2. S. Boulineau, C. Matthieu, J.-M. Tarascon, V. Viallet, *Solid state Ionics.* **2012**, 221, 1-5.
3. A. Miura, N. C. Rosero-Navarro, A. Sakuda, T. Kiyoharu, N. H. H. Phuc, A. Mastuda, N. Machida, A. Hayashi, M. Tatsumisago, *Nat. Rev. Chem.* **2019,** 3**,** 189–198.
4. Z. Liu, W. Fu, E. A. Payzant, X. Yu, Z. Wu, N. J. Dudney, J. Kiggans, K. Hong, A. J. Rondinone, C. Liang, *J. Am. Chem. Soc.*, **2013,** 135, 975– 978.
5. N. H. H. Phuc, M. Totani, K. Morikawa, H. Muto, A. Matsuda, *Solid State Ionics.* **2016**, 288, 240–243.
6. H. Wang, Z. D. Hood, Y. Xia, C. Liang, *J. Mater. Chem. A.* **2016**, 4, 8091–8096
7. H.D Lim, X. Yue, X. Xing, V. Petrova, M. Gonzalez, H. Liu, P. Liu, *J. Mater. Chem. A.*, **2018**, 6, 7370–7374.
8. M. Calpa, N. C. Rosero-Navarro, A. Miura, K.Tadanaga, *RSC Adv.* 2017, 7, 46499–46504.
9. S. Ito, M. Nakakita, Y. Aihara, T. Uehara, N. Machida, *J. Power Sources*, **2017,** 271, 342–345.
10. R.C. Xu, X.H. Xia, J.L. Yao, X.L. Wang., C.D. Gu, J.P. Tu, *Electrochimca. Acta.*, **2016**, 219, 235–240.
11. X. Yue, D. Liu, C. Wang, P. Long, G. Peng, Y. Hu, H. Li, L. Chen, X. Xu, *Nano Lett.*, **2016**, 16, 7148–7154.
12. N. H. H. Phuc, T. Yamamoto, H. Muto, A. Matsuda, *Inorg. Chem. Front.*, **2017**, 4, 1660–1664.
13. E. Rangasamy, Z. Liu, M. Gobet, K. Pilar, G. Sahu, W. Zhou, H. Wu, S. Greenbaum, C. Liang, *J. Am. Chem. Soc.*, **2015**, 137, 1384-1387.
14. S. J. Sedlmaier, S. Indris, C. Dietrich, M. Yavuz, C. Drager, F. V. Seggern, H. Sommer, J. Janek. *Chem. Mater.*, **2017**, 29, 1830–1835.
15. H. J. Deiseroth, S.T. Kong, H. Eckert, J. Vannahme, C. Reiner, T. Zaiβ, M. Schlosser, *Angew. Chem. Int. Ed.*, **2008**, 47, 755–758.

16. L. Zhou, K. H. Park, X. Sun, F. Lalere, T. Adermann, P. Hartmann, L. F. Nazar, *ACS Energy Lett.*, **2019**, 4, 265–270.
17. S. Yubuchi, M. Uematsu, C. Hotehama, A. Sakuda, A. Hayashi, M. Tatsumisago, *J. Mater. Chem. A*, **2018**, 7, 558–566.
18. Y. Wang, Z. Liu, X. Zhu, Y. Tang, F. Huang, *J. Power Sources*, **2013**, 224, 225–229.
19. M. Tachez, J. P. Malugani, R. Mercier, G. Robert, *Solid state ionics*, **1984**, 14, 181-185.
20. K. Homma, M. Yonemura, T. Kobayashi, M. Nagao, M. Hirayama, R. Kanno, *Solid State ionics*, **2011,** 182, 53-58.
21. N. H. H. Phuc, K. Morikawa, T. Mitsuhiro, H. Muto, A. Matsuda, *Ionics*, **2017**, 23, 2061-2067.
22. N. H. H. Phuc, K. Morikawa, T. Mitsuhiro, H. Muto, A. Matsuda, *Solid state ionics*, **2016**, 285, 2-5.
23. A. Matsuda, H. Muto, N. H. H. Phuc, *J. Jpn. Soc. Power Powder Metallurgy*, **2016**, 63, 976 - 980.
24. K. Ohara, A. Mitsui, M. Mori, Y. Onodera, S. Shiotani, Y. Koyama, Y. Orikasa, M. Murakami, K. Shimoda, K. Mori, T. Fukunaga, H. Arai, Y. Uchimoto, Z. Ogumi, *Sci. Rep.*, **2016**, 6, 21302.
25. S. Shiotani, K. Ohara, H. Tsukasaki, S. Mori, R. Kanno, *Sci. Rep.*, **2017**, 7, 6972.
26. C. Dietrich, D. A. Weber, S. J. Sedlmaier, S. Indris, S. P. Culver, D. Walter, J. Janek, W. G. Zeier, *J. Mater. Chem. A*, **2017**, 5, 18111.
27. K. Yamamoto, M. Takahashi, K. Ohara, N. H. H. Phuc, S. Yang, T. Watanabe, T. Uchiyama, A. Sakuda, A. Hayashi, M. Tatsumisago, H. Muto, A. Matsuda, Y. Uchimoto, *ACS Omega*, **2020**, DOI:10.1021/acsomega.0c04307.
28. S. Kohara, M. Itou, K. Suzuya, Y. Inamura, Y. Sakurai, Y. Ohishi, M. Takata, *J.Phys.: Condens. Matter*, **2007**, 19, 506101.
29. C. M. Hansen, *The Three Dimensional Solubility Parameter and Solvent Diffusion Coefficient and Their Importance in Surface Coating Formulation*, Copenhagen: Danish Technical Press, **1968**.
30. C. M. Hansen, *Hansen Solubility Parameters a User's Handbook*, Second Edition, 2007

31. Y. Aoki, K. Ogawa, T. Nakagawa, Y. Hasegawa, Y. Sakiyama, T. Kojima, M. Tabuchi, *Solid state ionics*, **2017**, 310, 50-55
32. Z. Xu, Z. He, Y. Song, X. Fu, M. Rommel, X. Luo, A. Hartmaier, J. Zhang, F. Fang, *Micromachines*, **2018**, 9, 361

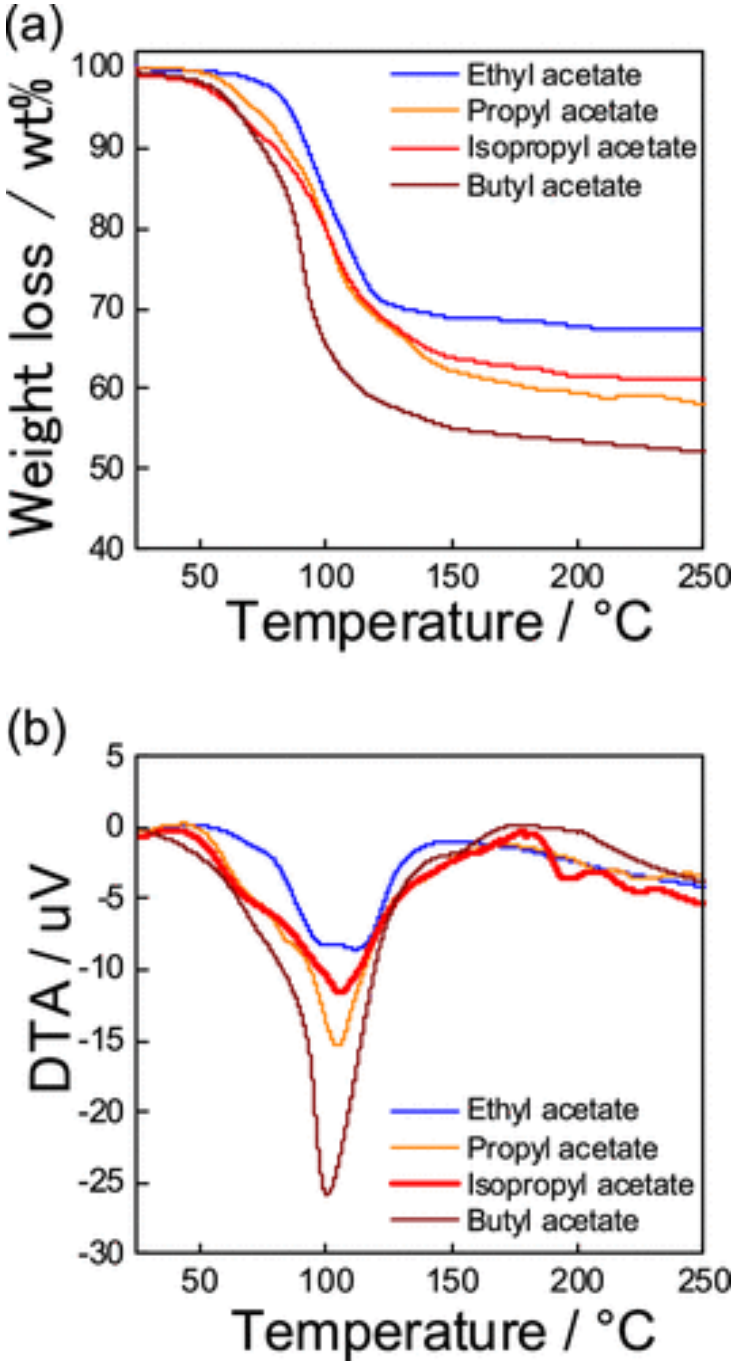

Figure 1. (a) TGA and (b) DTA from 25 to 250 °C for the precursors synthesized with ethyl acetate (blue), propyl acetate (orange), isopropyl acetate (red), and butyl acetate (brown).

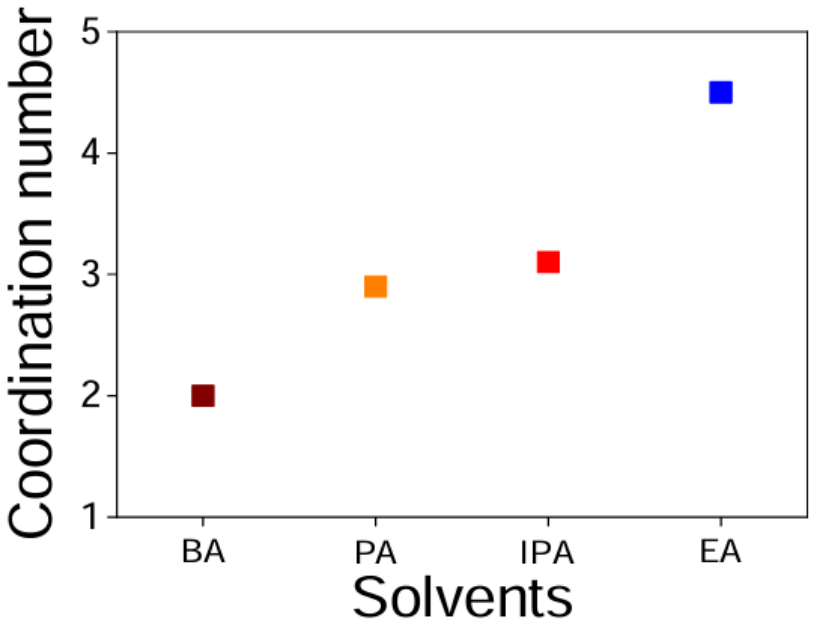

Figure 2. Coordination number of solvents with sulfur compounds calculated based on TGA at 150 ºC.

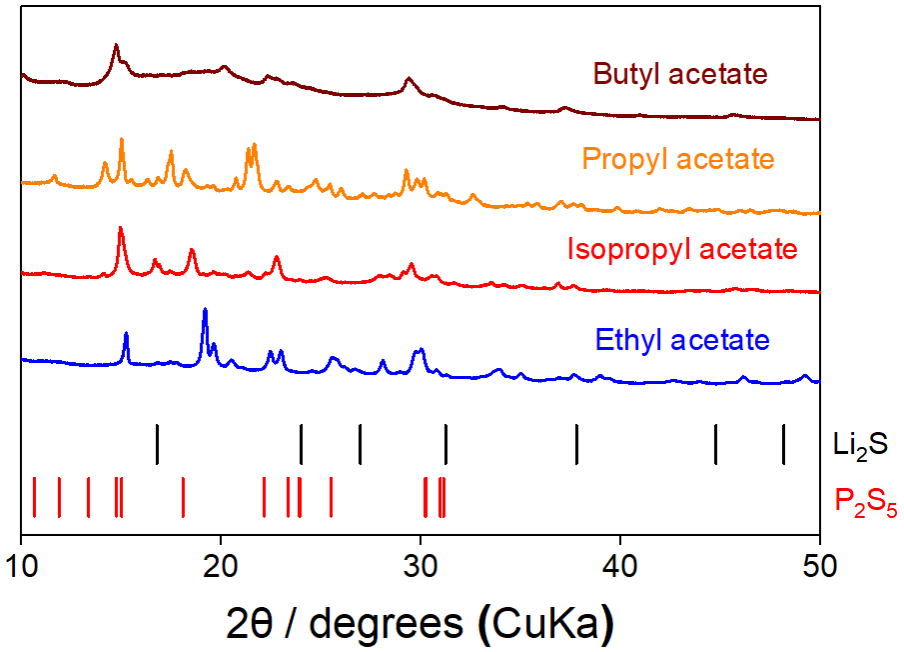

Figure 3. XRD patterns of precursor complex synthesized using different solvents.

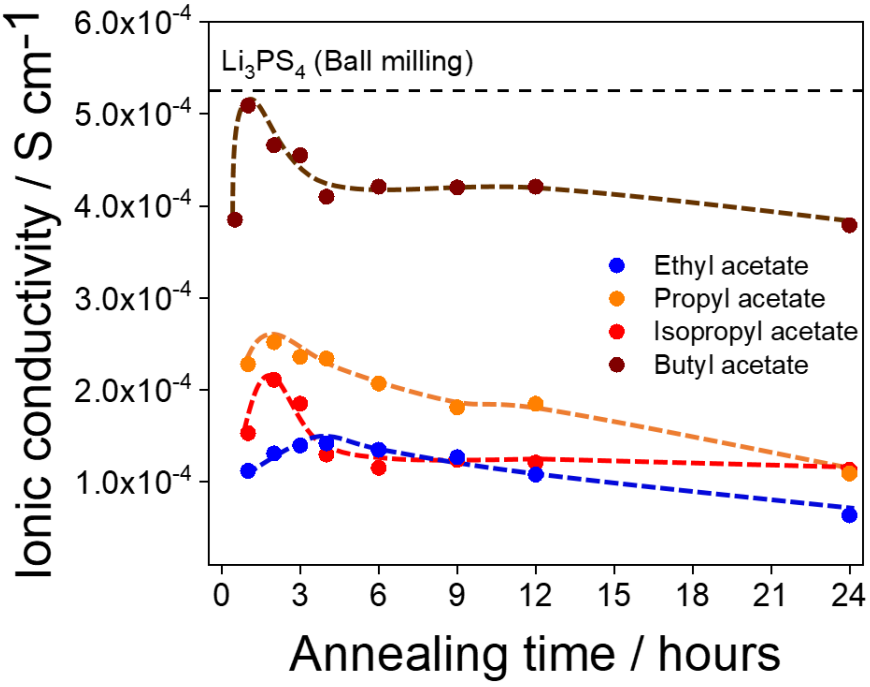

Figure 4. Ionic conductivity for Li_3PS_4 synthesized with different solvents, annealed at 100 °C according to the determined duration time, and with ball milling (5.14×10^{-4} S cm^{-1}).

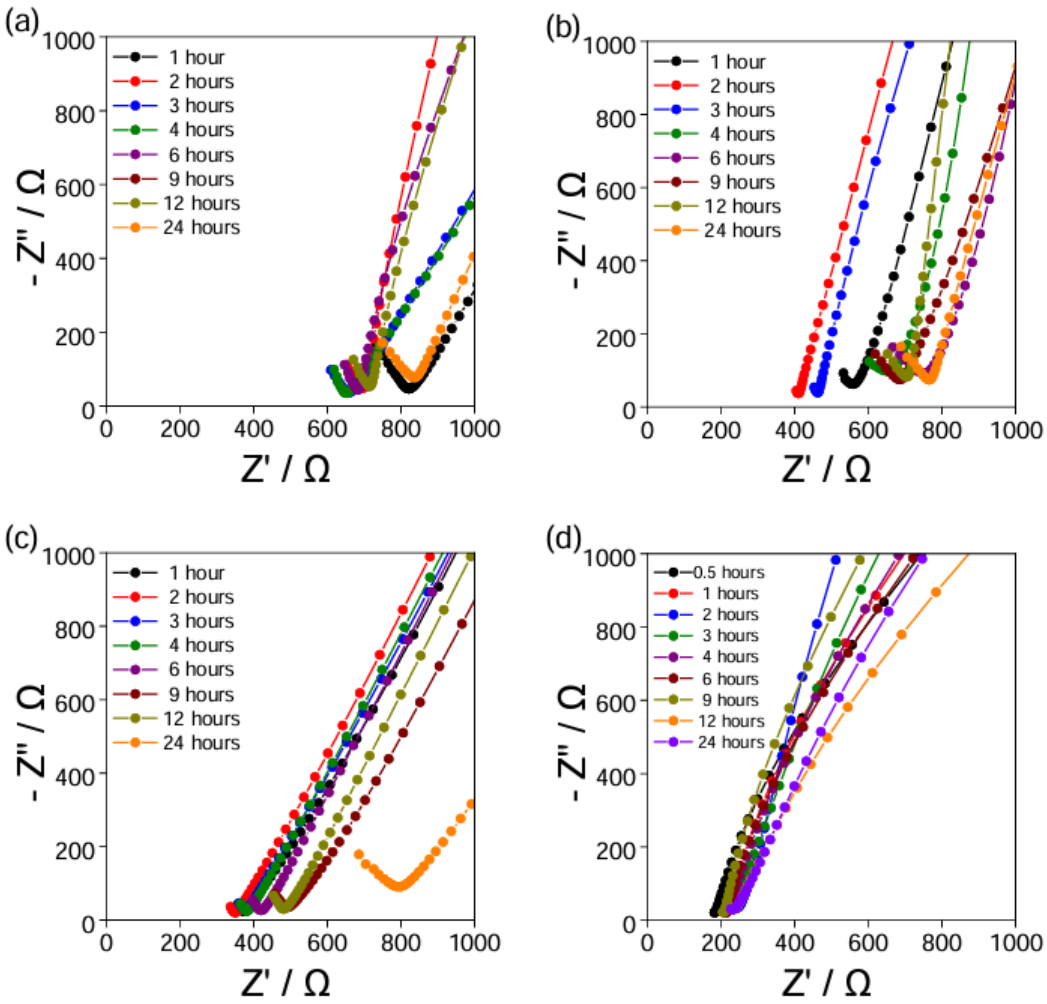

Figure 5. Nyquist plots at 25 ºC for Li_3PS_4 synthesized using different solvents after the annealing process at 100 ºC, ethyl acetate (a), isopropyl acetate (b), propyl acetate (c), and butyl acetate (d).

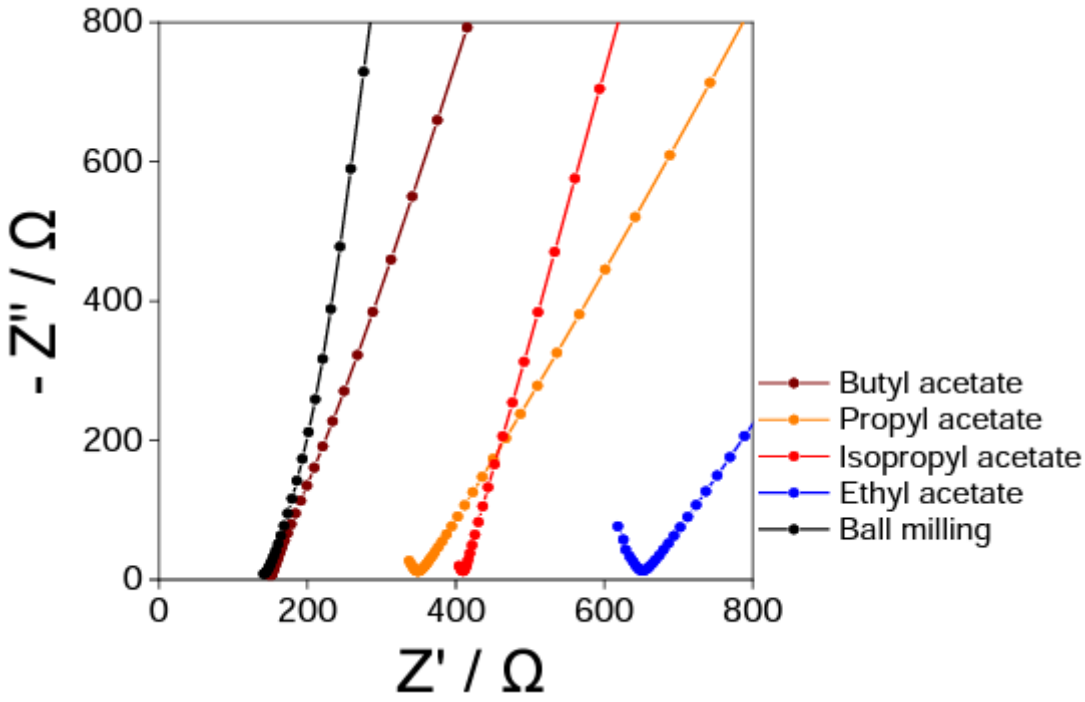

Figure 6. Nyquist plots corresponding to the highest ionic conductivity of the different solvents.

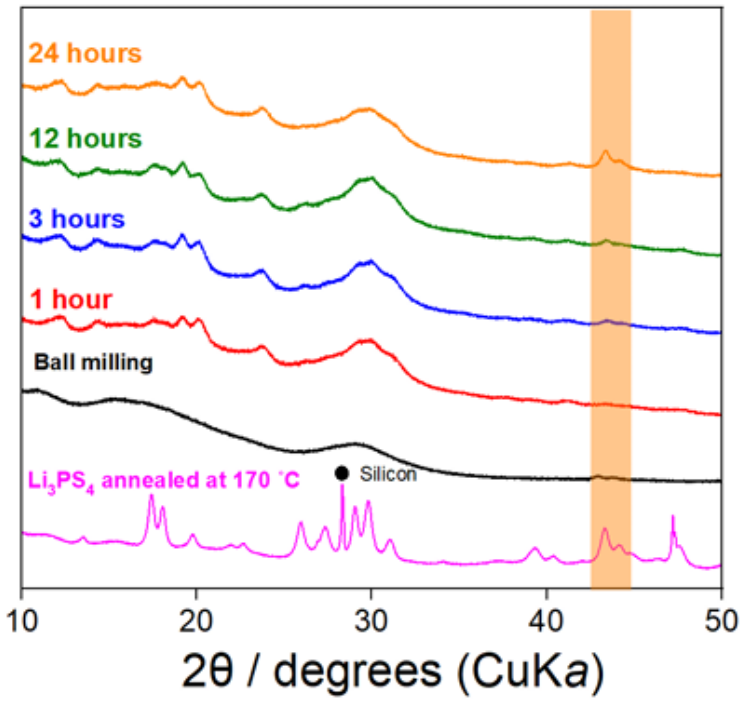

Figure 7. The XRD pattern corresponding to the Li_3PS_4 synthesized with butyl acetate as the annealing time at 100 ºC.

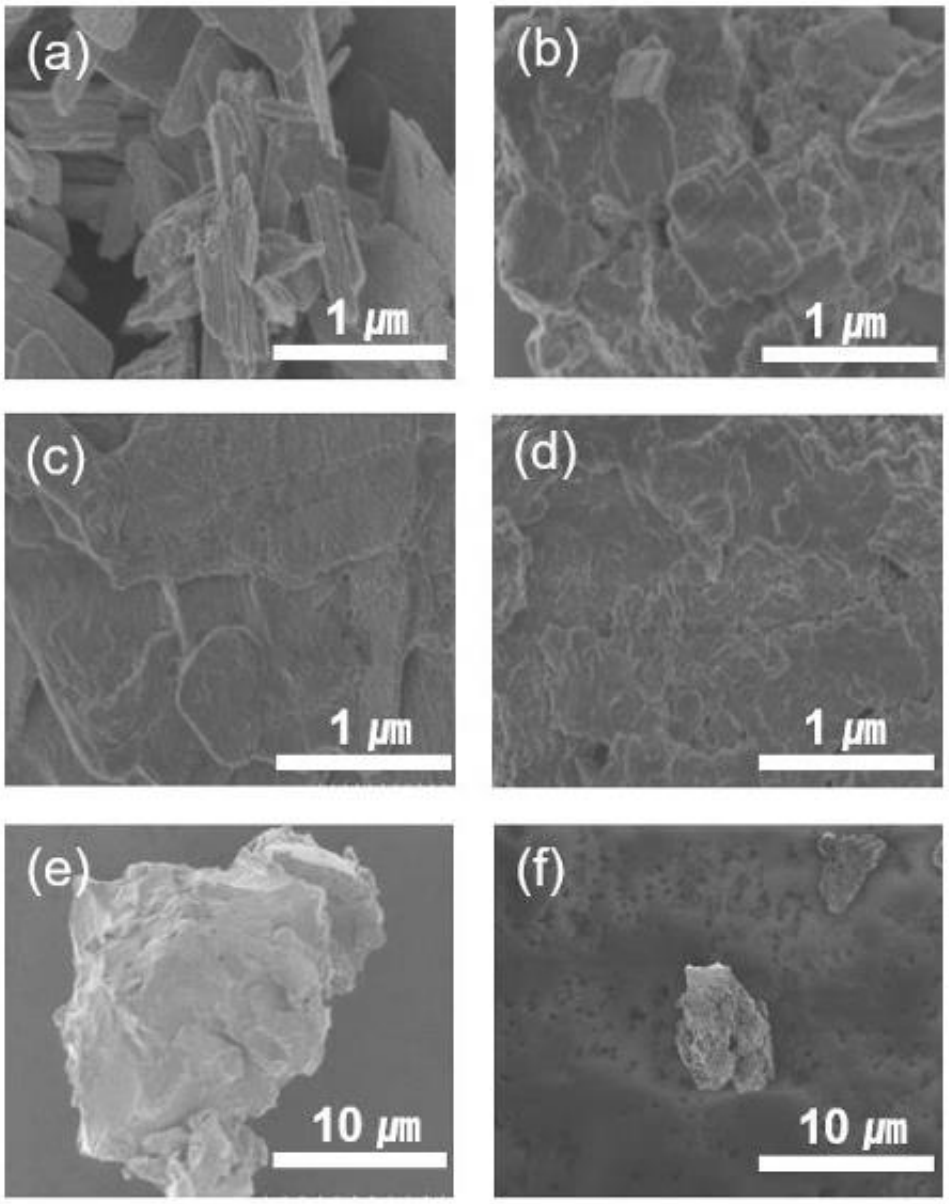

Figure 8. SEM images of Li_3PS_4 synthesised using ethyl acetate (a), isopropyl acetate (b), propyl acetate (c), and butyl acetate (d) after the annealing process at 100 °C. SEM images at different magnification of Li_3PS_4 prepared by (e) the ball milling method and (f) the liquid phase synthesis with butyl acetate.

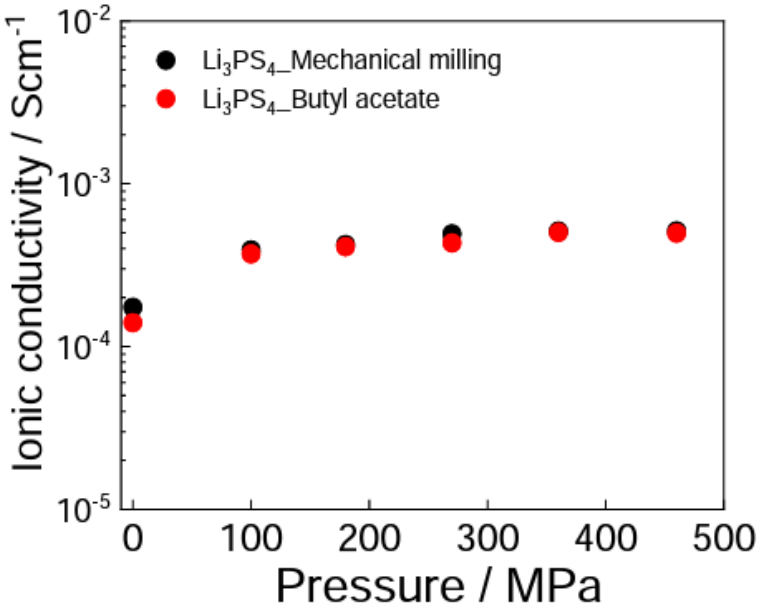

Figure 9. The ionic conductivity according to the pressure the fabricate the pellet with powder corresponding to each synthesis process.

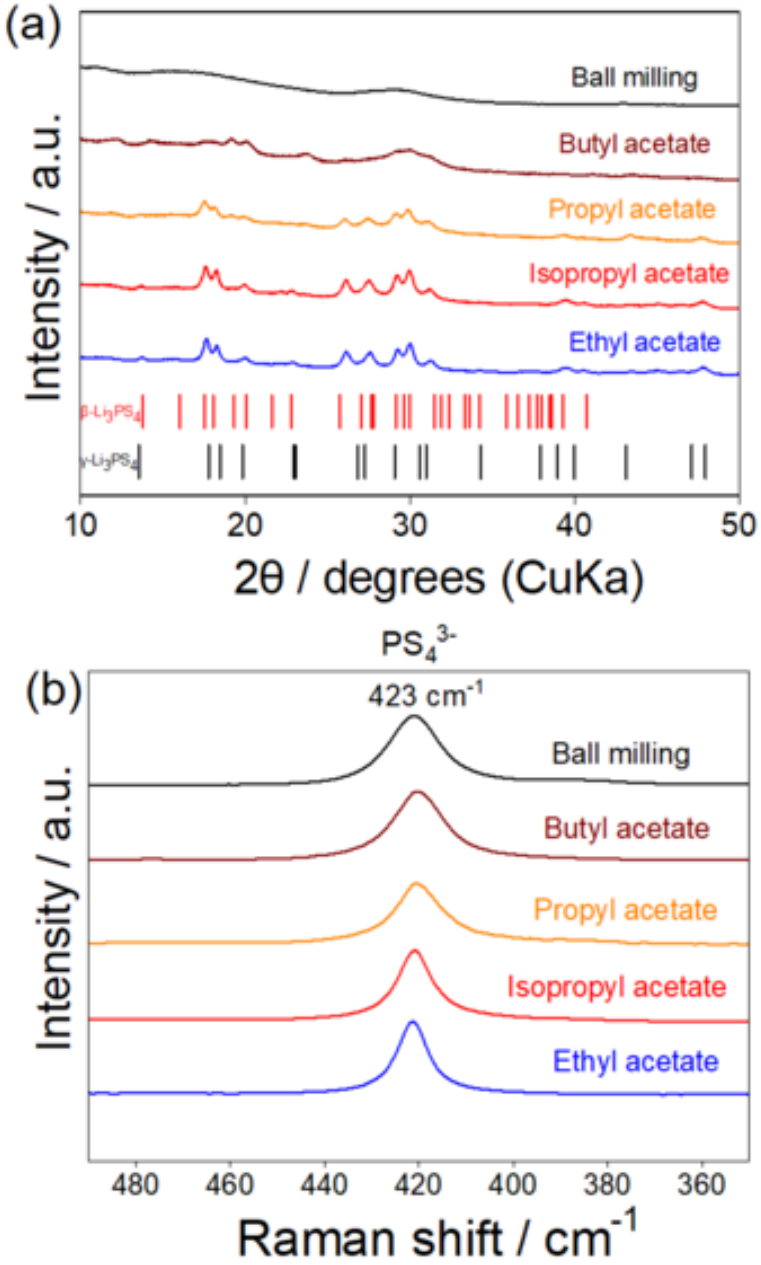

Figure 10. XRD patterns (a) and Raman spectra (b) for the samples that showed the highest ionic conductivity in each solvent group, including Li_3PS_4 prepared by ball milling.

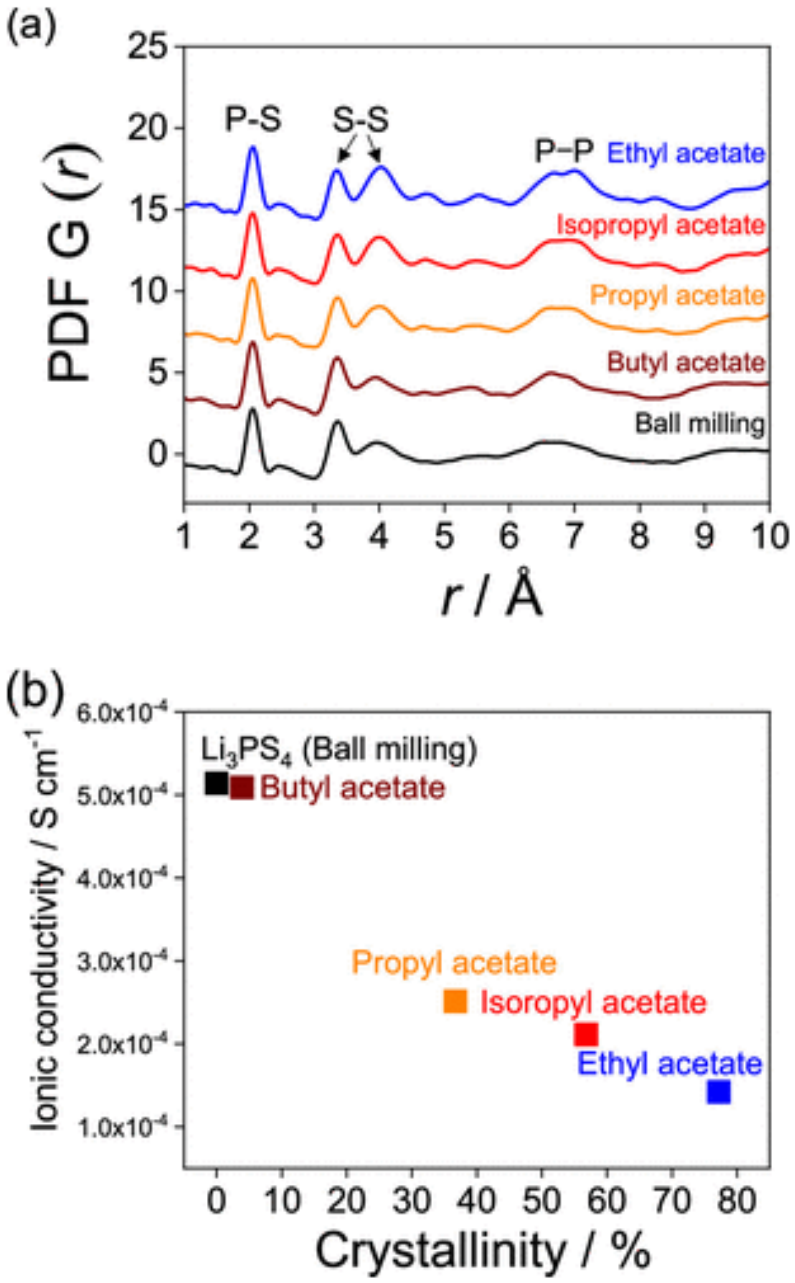

Figure 11. PDF analysis of samples prepared by mechanical milling and by using ethyl acetate, isopropyl acetate, propyl acetate, or butyl acetate with the highest ionic conductivity (a) and correlation of crystallinity calculated from PDF using equation (1) for each solvent with ionic conductivity (b).

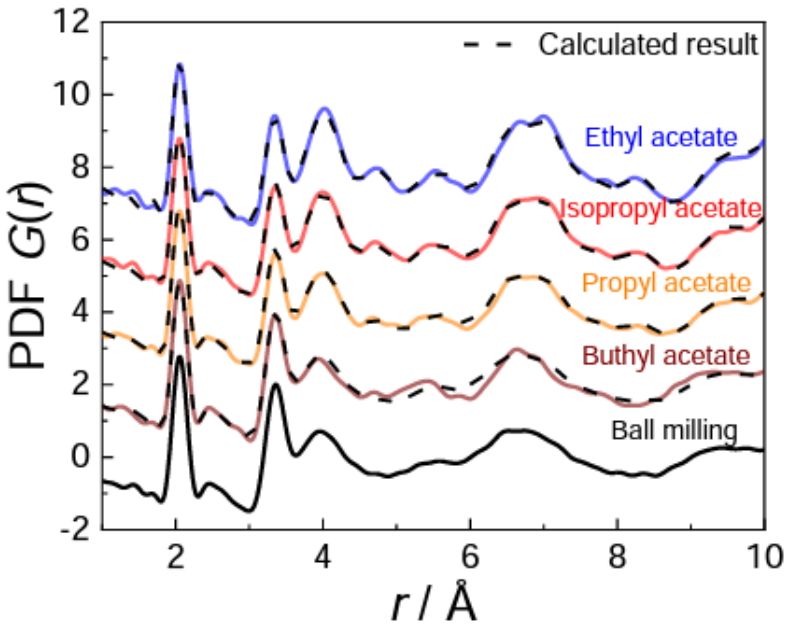

Figure 12. PDF fitting results for the confirmation of errors between experimental and calculated data of the fraction of the crystalline phase obtained by equation (1).

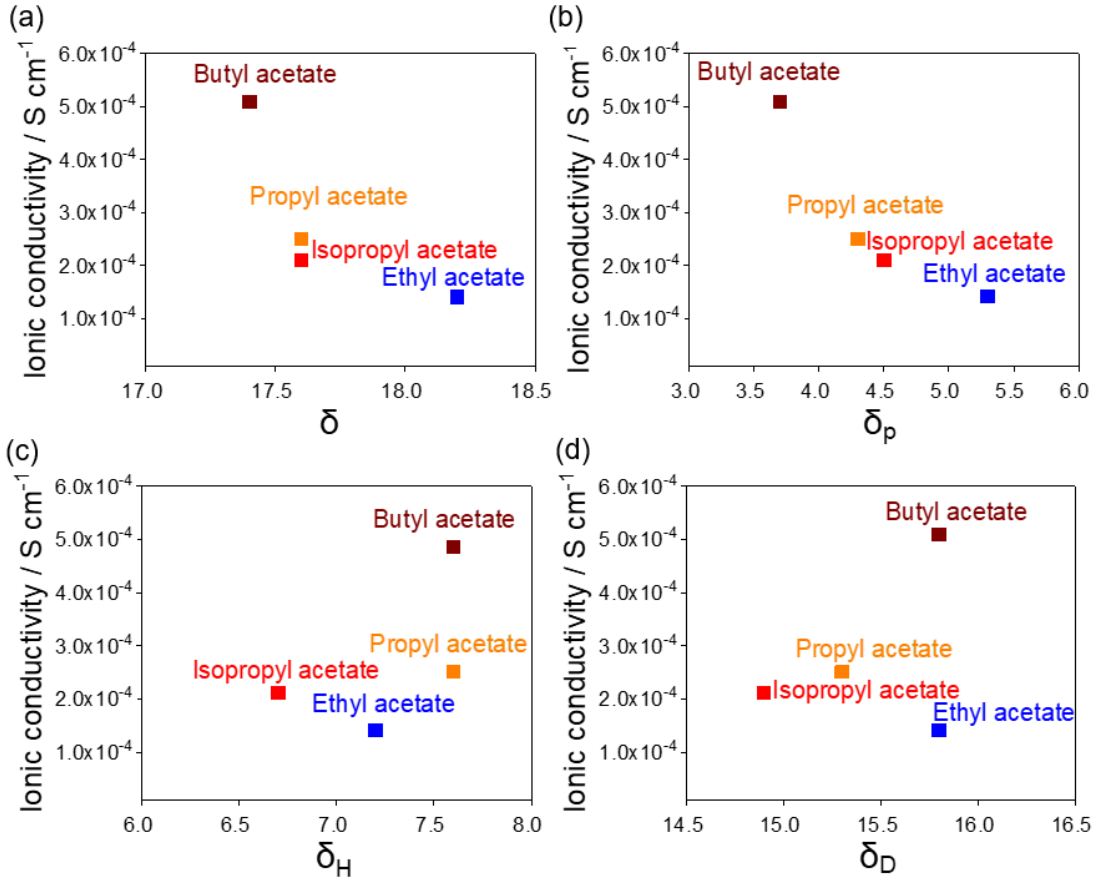

Figure 13. Ionic conductivity as a function of the Hansen solubility parameter (a), polarity (b), hydrogen bonding (c), and dispersion force (d).

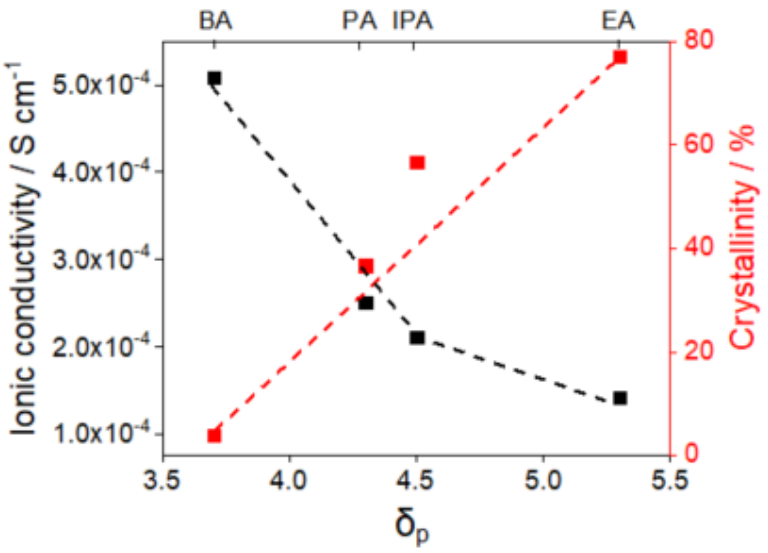

Figure 14. Relationship between solvent polarity (δ_P) and ionic conductivity and crystallinity. Solvents are as follows, BA: butyl acetate, PA: propyl acetate, IPA: Isopropyl acetate, EA: Ethyl acetate.

Table 1. Full width at half maximum (FWHM) and peak area obtained from the Raman spectra in the range from 350 to 490 cm^{-1}

Samples	FWHM	Area
Ball milling	13.56	20.56
Butyl acetate	13.09	19.74
Propyl acetate	12.01	15.16
Isopropyl acetate	9.36	13.69
Ethyl acetate	8.40	9.35

Table 2. Hansen's solubility parameter components for solvents used in this study

	Ethyl acetate	Isopropyl acetate	Propyl acetate	Butyl acetate
δ_D	15.8[1)]	14.9[1)]	15.3[1)]	15.8[1)]
δ_P	5.3[1)]	4.5[1)]	4.3[1)]	3.7[1)]
δ_H	7.2[1)]	8.2[1)]	7.6[1)]	6.3[1)]
δ	18.2	17.6	17.6	17.4

1) Charles M. Hansen - Hansen Solubility Parameters_ A User's Handbook, Second Edition, 2007

Solubility (δ) was calculated using the data shown in Table S2 by the following equation:

$$\delta^2 = \delta_D^2 + \delta_P^2 + \delta_H$$

Chapter 3. Studies on the Inhibition of Lithium Dendrite Formation in Sulfide Solid Electrolytes Doped with LiX (X = Br, I)

A promising method to increase the energy density of all-solid-state batteries (ASSBs) featuring lithium ions as carriers is to employ Li metal as the anode. However, this has been accompanied by safety problems like flammable accidents associated with lithium dendrites originating from reactions with the solid electrolyte, leading to reduced battery performance. To overcome this issue toward the commercialization of ASSBs, various approaches have been proposed by many researchers. Among the suggested solutions, the use of lithium-halide-doped Li_3PS_4, to suppress lithium dendrite formation, has attracted attention. LiI-doped Li_3PS_4 has shown the highest lithium dendrite growth suppression among lithium-halide-doped systems, but the reason for this is unclear. Thus, the author attempted to clarify the cause of this suppression by comparing LiBr-doped Li_3PS_4 with LiI-doped Li_3PS_4. Investigation using various methods such as electrochemical evaluation, X-ray absorption spectroscopy, X-ray computed tomography, and pair distribution function analysis revealed that two factors affect the suppression of Li dendrite growth: the suppression of the current density distribution by improving the ionic conductivity and the stable interfacial layer. This is the main reason LiI-doped Li_3PS_4 shows excellent Li dendrite suppression.

3.1. Introduction

Currently, lithium-ion batteries (LIBs) are expected to be applied as a power source for electric vehicles and in load shifting in smart grids[1–3]. Therefore, the energy density and safety of LIBs must be improved[3]. However, with current LIBs, along with other safety issues, there is the risk of ignition of the organic solvents used as the electrolytes[4–6]. Thus, the use of Li metal as the anode has been limited because of the difficulty in suppressing dendrite formation[6]. However, lithium metal has great potential to be used as the anode and obtain batteries with high energy density because of its high

theoretical capacity (3860 mAh g^{-1}), low reduction potential (−3.04 V), and low density (0.59 g cm^{-3}).

In recent years, all-solid-state batteries (ASSBs), in which liquids have been replaced with solids, have received considerable attention[7–12]. Because inorganic solid electrolytes are far from the ignition possibility. they pose no risk of explosion[10,11]. Therefore, ASSBs can be safer than LIBs and exhibit high energy density. Among the solid electrolytes developed thus far, sulfide-based solid electrolytes are expected to find practical application owing to their advantages such as high ionic conductivity[9,13,14] and low modulus[15]. In particular, Li_2S–P_2S_5 glass electrolytes are expected to reduce Li dendrite formation because of the reduction in the number of voids and grain boundaries; simple pressing reduces these voids and grain boundaries owing to the low elastic modulus of the electrolytes[15]. However, Li dendrite formation can occur even if glass sulfide solid electrolytes are used[15,16]. The main cause is the reactivity between Li metal and the electrolyte owing to the decomposition of Li_3PS_4 into Li_2S and Li_3P when Li_3PS_4 is in contact with Li metal[16,17]. Recently, it was reported that the addition of LiI to a glass electrolyte improves the suppression of Li dendrite formation[17,18]. Although the exact mechanism of this significant improvement is not fully understood, it was considered that LiI acts as a protective layer against lithium growth. LiI on the surface suppresses the decomposition of Li_3PS_4 because LiI is thermodynamically stable in the presence of Li metal and maintains the good contact between Li metal and the electrolyte at the interface[17,18]. Based on these previous studies, we have reported that there is a linear correlation between ionic conductivity and not only critical current density performance, but also the reactivity with lithium metal, following comparison with Li_3PS_4. The author's result indicated that LiI addition improved the ionic conductivity of the solid electrolyte, leading to uniform current density distribution[19]. However, it has also been reported that a Li_2S–P_2S_5 glass electrolyte doped with LiBr, which is known to exhibit similar resistance to that of LiI against reduction by Li metal, incorporated into Li_3PS_4 is not significantly effective for suppressing lithium dendrites[18]. The reason LiI-doped Li_3PS_4 inhibits dendrite growth effectively is not clear at present; clarification of this will provide important design guidelines for solid electrolytes for Li dendrite suppression.

In this study, LiBr-doped Li_3PS_4 was synthesized through mechanical milling. The products were annealed at various temperatures to improve the ionic conductivity. The ionic conductivities of LiBr-doped Li_3PS_4 before and after annealing were measured, and the structures were evaluated. In addition, the lithium dendrite suppression capability of LiBr-doped Li_3PS_4 before and after annealing was investigated using galvanostatic cycling tests with Li/solid electrolyte/Li cells. By comparing the results for LiBr-doped Li_3PS_4 with previously reported results for LiI-doped Li_3PS_4, The author attempted to clarify the factors affecting lithium dendrite suppression ability[19].

3.2. Experimental section

3.2.1. Synthesis of (100-x)Li_3PS_4-xLiBr solid electrolyte

$(100-x)Li_3PS_4$–xLiBr (x = 0, 10, 20, 30, 40, 50, or 60) was synthesized through mechanical milling of the corresponding molar amounts of Li_2S (Sigma-Aldrich, >99.9%), P_2S_5 (Sigma-Aldrich, 99%), and LiBr (Sigma-Aldrich, >99.99%) with 90 g of 4 ϕ zirconia balls at 600 rpm for 10 h. The $(100-x)Li_3PS_4$–xLiBr products were shaped into 10 Φ pellets and then annealed at 160–270 °C for 2 h. All aforementioned processes were carried out in a glove box filled with argon gas.

3.2.2. Material characterization

X-ray diffraction (XRD) measurements in the 10°–80° range for all samples were performed using an RINT-Ultima III (Rigaku) with CuKα radiation as the X-ray source. The measurements were performed using a non-exposed cell to prevent air exposure. Raman measurements in the 50–1800 cm^{-1} range were performed using a DXR3 Smart Raman spectrometer (Thermo Fisher Scientific) with a 532 nm diode-pumped solid-state laser at room temperature. All samples were sealed in glass tubes to prevent reaction with air. High-energy XRD was carried out at beamline BL04B2 at SPring-8 (Japan). Samples sealed in 2 ϕ quartz capillary tubes were irradiated with 61.2 keV synchrotron radiation energy, and the scattered X-rays were detected using seven point-type detectors. The structure factor, $S(Q)$, was obtained by normalizing the scattering data to the number of atoms and the scattering intensity from one atom. Moreover, the reduced pair distribution

function (PDF), $G(r)$, was calculated using the Fourier transform of $S(Q)$[19–21]. X-ray computed tomography (CT) measurements were conducted at beamline BL20XU at SPring-8 (Japan). Laminate cells containing the samples were irradiated with 30 keV synchrotron radiation, and transmission images were acquired at various angles. Laboratory-based X-ray CT measurements were performed using an Xradia 520 Versa (Carl Zeiss Co., Ltd., USA). X-ray absorption spectroscopy (XAS) spectra of the samples before and after galvanostatic cycling tests in the sulfur *K*-edge and phosphorus *K*-edge energy regions were measured using the partial fluorescence yield method at beamline BL27SU at SPring-8 (Japan). The samples before and after the galvanostatic cycling tests were sealed in a glove box filled with argon to prevent exposure to air after the stainless–steel foil was removed from both sides of the samples.

3.2.3. Electrochemical measurement

Dense pellets approximately 0.7 mm in thickness and 10 mm in diameter were prepared for all samples by pressing them at 360 MPa with stainless steel rods on each side in an argon-filled glove box. The alternating current impedance at 25–100 °C in the 1.0 MHz to 0.1 Hz frequency range with an amplitude of 100 mV was measured using a ModuLab XM ECS (Solartron Analytical). The impedance at a high frequency range of 120 MHz to 0.1 Hz, which was maintained for 1 h after heating to 100 °C, was measured to determine the interphase layer resistance using a high-frequency impedance measurement system (Toyo Tech.). The obtained Nyquist plots were used to determine the total conductivity. The critical current density (CCD) was measured to obtain the short-circuit current density. The cell preparation and measurement conditions were as follows. Pellets of the solid electrolyte were prepared by pressing at 360 MPa in an argon-filled glove box. The thickness and diameter of the pellets were approximately 1.0 and 10 mm, respectively. The pellets were attached to 8 ϕ Li metal on both sides and then, also covered with 10 ϕ stainless steel (SUS) foil on the other. In addition, the pellets were placed in a laminate cell and sealed under vacuum. The laminate cell was subjected to cold isostatic pressing at 80 MPa to effect good contact between Li and the solid electrolyte at the interface. The Li/solid electrolyte/Li cell was tested via galvanostatic cycling with the current density increasing by 0.04 mA cm^{-2} after charging and discharging for 1 h at 100 °C to evaluate the CCD.

3.3. Results and discussion

The XRD patterns of (100−x) Li_3PS_4–xLiBr prepared via mechanical milling are shown in Figure 1(a). The XRD pattern of the sample without LiBr doping (x = 0) showed a broad peak at around 30°, which was also observed in the XRD pattern of Li_3PS_4 in previous reports[11,16,18–22]. The broad peak at around 30° was also observed for the LiBr-doped samples; it shifted to a lower angle as the amount of LiBr increased. In the LiBr-doped samples with $x \geq 40$, peaks attributed to LiBr (JCPDS No. 06-0319) were observed. These results show that the lattice constant of Li_3PS_4 increased with the introduction of bromide ions because a bromide ion has a larger ionic radius than a sulfide ion[23,24]. The appearance of the LiBr peak for samples with $x \geq 40$ indicates that the solid solution limit of bromide ions was exceeded. The ionic conductivities of the prepared (100−x) Li_3PS_4–xLiBr samples are shown in Figure 1(b). All Nyquist plots are shown in Figure 2. The ionic conductivity increased as the amount of LiBr was increased up to 40 mol%, and then decreased with further LiBr incorporation. This behavior is consistent with the results from previous reports[17–19]. Figure 1(c) shows the correlation between the ionic conductivity and the position of the peak near 30° in the XRD patterns of (100−x)Li_3PS_4–xLiBr (x = 0, 10, 20, 30). As the ionic conductivity increased, the peak shifted to a lower angle, indicating that the increase in ionic conductivity is attributed to the expansion of diffusion paths caused by an increase in the lattice constant of Li_3PS_4 due to bromide ion incorporation. The decrease in ionic conductivity when $x > 40$ is caused by high crystalline LiBr, which has low conductivity.

The presence of bromide ions in the solid electrolyte changes the local structure of Li_3PS_4, which influences the formation of a lithium-halide-containing film at the interface through the reaction between lithium metal and the halide-doped solid electrolyte[17–19]. However, it is difficult to obtain information on the local structure of LiBr-doped Li_3PS_4 from the XRD patterns. Therefore, high-energy XRD and PDF analysis were performed for LiBr-doped Li_3PS_4 because crystalline LiBr complicates the structural elucidation of LiBr-doped Li_3PS_4 through PDF analysis, Li_3PS_4 doped with 40, 50 mol% LiBr was not considered.

The obtained PDF patterns of (100−x) Li_3PS_4–xLiBr (x = 0, 10, 20, 30) are presented in Figure 3, which shows representative peaks at 2.0, 2.5, 3.3, 4.1, 5.3, and 6.6 Å. For Li_3PS_4, these peaks corresponded to the P-S bond in the PS_4^{3-} units, the Li-S correlation between PS_4^{3-} unit, the S-S correlation in the PS_4^{3-} units, the S-S correlation between the PS_4^{3-} units, P-S correlation between the PS_4^{3-} units, and the P-P bond between the PS_4^{3-} units, respectively[19–22,25]. As the amount of LiBr increased, the peak at 3.3 Å reduced, whereas the intensity of the peak at 4.1 Å including shoulder peak increased. This result indicates that the local structure around 4.1 Å expands with increasing x value, corresponding to XRD results. As shown in Figure 3, LiBr-doped Li_3PS_4 demonstrated a peak at a similar position to that of Li_3PS_4. This result suggested that the correlation within the PS_4^{3-} anions were unaffected by the addition of LiBr. Furthermore, to investigate the structure in detail, the author simulated the G(r) of model structures by using the similar method in the previous report[19] and compared it with that of 70 Li_3PS_4–30LiBr as shown in Figure 4. The simulation was conducted by using both bromine is inserted model between the PS_4^{3-} anions and bromine is exchanged model into sulfur site in the PS_4^{3-} anions. The blue and green lines in Figure 4 show the simulated PDFs from the inserted and exchanged models, respectively. The G(r) of the exchange model showed a characteristic peak at around 2.3 Å whereas the G(r) of the insertion model showed a characteristic peak at around 4.0 Å. In the PDF pattern of the LiBr-doped Li_3PS_4, there is no peak at around 2.3 Å and is at 4.0 Å, which corresponds to the insertion model. The simulation results indicate that the bromide ions did not replace the sulfur ions in the PS_4^{3-} units but were inserted between the PS_4^{3-} units. This behavior is similar to those of (100−x) Li_3PS_4–xLiI[19].

To compare its electrochemical properties with those of 70 Li_3PS_4–30LiI from our previous work[19], we investigated 70Li_3PS_4–30LiBr and attempted to control its ionic conductivity by annealing. The XRD patterns and ionic conductivity of 70 Li_3PS_4–30LiBr after annealing at different temperatures are shown in Figure 5 (see Figure 6 for each annealing temperature). Figure 5(a) shows that the XRD patterns of 70 Li_3PS_4–30LiBr did not change after annealing below 180 °C. New peaks, which were attributed to thio-LISICON II and crystalline β- Li_3PS_4[26,27], were observed after annealing at 200 and 210 °C. Upon further increasing the annealing temperature to 270 °C, the peaks attributed

to the thio-LISICON II phase disappeared, while the peak intensity for the crystalline β-Li_3PS_4 phase increased and new peaks indexed to LiBr appeared. The ionic conductivity of 70 Li_3PS_4–30LiBr increased gradually with increasing annealing temperature up to 180 °C, and then increased drastically at 200 °C (Figure 5(b)). The ionic conductivity decreased at 210 °C, decreased drastically at 220 °C, and decreased slightly as the temperature was increased from 220 to 270 °C. The gradual increase in the ionic conductivity may be due to a progression of nucleation for thio-LISICON II phase[21] as shown in Figure 7, where the intensity of peak at 3.3, 4.1 Å is decreased/increased as the higher temperature. It implies that the free volume was expanded by changing volume of PS_4^{3-} tetrahedrons in the 70 Li_3PS_4–30LiBr. Later the drastic increase at 200 °C is attributed to clear formation of the thio-LISICON II phase, which has high ionic conductivity[26]. By contrast, the decrease in the ionic conductivity at 210 °C is caused by the formation of the crystalline β- Li_3PS_4 phase, which has low ionic conductivity[20–22,26]. The drastic decrease is caused by the disappearance of the thio-LISICON II phase and the formation of the crystalline β- Li_3PS_4 phase and LiBr.

The dendrite suppression ability of 70 Li_3PS_4–30LiBr before and after annealing was evaluated through galvanostatic cycling tests using Li/solid electrolyte/Li cells with stepwise increases in current density at 100 °C. The results are shown in Figure 8. A voltage drop due to the internal short circuit caused by the formation of lithium dendrites in the solid electrolyte is shown in Figure 8, based on previous studies[17–19]. The current density leading to the short circuit that caused this voltage drop was defined as the CCD[19]. The CCD was used to evaluate the dendrite suppression ability of the LiBr-doped Li_3PS_4 electrolyte. The CCDs of Li_3PS_4 and 70 Li_3PS_4–30LiBr before annealing and after annealing at various temperatures are shown in Figure 9(a). The CCD of 70 Li_3PS_4–30LiBr before annealing was higher than that of Li_3PS_4. For annealed 70 Li_3PS_4–30LiBr, the CCD increased with annealing temperature up to 200 °C and then decreased at higher temperatures. Furthermore, the linear relationship between the enhanced ionic conductivity after annealing and the CCD was confirmed, as shown in Figure 9(b), and compared to the results from our previous study on LiI-doped Li_3PS_4[19]. For 70 Li_3PS_4–30LiBr, the CCD increased with increasing ionic conductivity and was higher than that of Li_3PS_4 for the same ionic conductivity. Although this trend is consistent with LiI-doped

Li_3PS_4, LiBr-doped Li_3PS_4 shows lower CCDs[19]. Meanwhile, higher CCDs are noticeable in LiI and LiBr-doped Li_3PS_4 despite lower ionic conductivity than that of Li_3PS_4. According to previous studies, this is attributed to stabilized interface with lithium metal by thermodynamically stable LiI. LiBr, which has thermodynamic stability similar to that of LiI[31-32], will stabilize the interface with lithium metal. To explain this with interface morphology, we conducted an X-ray CT and XAS analysis on the interface.

X-ray CT and XAS were performed to examine the differences in the CCDs of Li_3PS_4, 70 Li_3PS_4–30LiBr, and 70 Li_3PS_4–30LiI. X-ray CT measurements were performed on 70 Li_3PS_4–30LiBr and Li_3PS_4 without annealing after galvanostatic cycling tests; an internal short circuit occurred at 0.72 $mAcm^{-2}$ in Li_3PS_4 while, it was not occurred even at 1.20 $mAcm^{-2}$, at which Li_3PS_4 sample was collected, in 30LiBr-doped Li_3PS_4, as shown in Figure 10. Additionally, in order to compare with the interface state of LiI-doped Li_3PS_4, unannealed 30LiBr-doped 70 Li_3PS_4 was also employed. Before the CCD tests, there is no morphological difference between Li/LiI-doped Li_3PS_4 and Li/LiBr-doped Li_3PS_4 interfaces, which was confirmed by X-ray CT (Figure 11). After the cycling test shown in Figure 10(a), the X-ray CT images were recorded as three–dimension in Figures 10(b) and (c), in which the terms for Li_3PS_4 and lithium metal were marked based on our previous study[19]. Then, the cross-sections for blue and red dash lines are listed next to each three–dimension images as the direction of X—Y, and Z—Y. Li_3PS_4 showed enormous cracks and an unstable interface state, whereas 70 Li_3PS_4–30LiBr showed a stable interface without cracks. It clearly demonstrates the stable interface state suppressed by LiBr unlike Li_3PS_4. Moreover, the difference before and after the cycle is also subtle as shown in Figure 11. To investigate decomposition products during galvanostatic cycling, the P *K*-edge and S *K*-edge XAS spectra were obtained about a partial fluorescence yield (PFY), reflecting information that can understand the depth about 1 um of the samples (Figure 12). In the P *K*-edge XAS spectrum of Li_3PS_4, the peak intensity at around 2148 eV decreased, while a shoulder peak attributed to Li_3P was also observed at around 2145 eV after the galvanostatic cycling test (Figure 12(a)). In the S *K*-edge XAS spectrum of Li_3PS_4, the peak intensity at around 2471 eV decreased, while a peak attributed to Li_2S was observed at around 2472 eV after the galvanostatic cycling test. By contrast, in the P *K*-edge and S *K*-edge XAS spectra of 70 Li_3PS_4–30LiBr,

slightly changes attributed to decomposition of the solid electrolyte were observed after the galvanostatic cycling test (Figure 13). The slightly changes compared to the Li_3PS_4 changes indicated that the addition of LiBr suppressed largely the decomposition of the solid electrolyte. These results show that the addition of LiBr to Li_3PS_4 suppresses the formation of cracks at the lithium/solid electrolyte interface and the reduction reaction between the electrolyte and lithium metal, similar to the addition of LiI to Li_3PS_4[18–20]. From these results, we were able to clearly identify the cause of the interfacial stability that prevented the formation of the decomposition products, Li_3P and Li_2S. However, the differences between LiI and LiBr could not be explained. Thus, we used high-frequency impedances (120 MHz to 10 Hz) for a deeper analysis of the interphase of LiI- and LiBr-doped Li_3PS_4 systems.

To analyze the resistance of the interface for each solid electrolyte, we attempted to measure the time-dependent impedance at high frequencies; the results are shown in Figure 14, Figure 15, and Table 1. Two semicircles were observed for each electrolyte, which is consistent with the results of previous studies[33–35]. The impedance spectra were fitted with an equivalent circuit[31], shown in Figure 16. The higher and lower semicircles are attributed to an interfacial layer and grain boundary, respectively. In the case of Li_3PS_4, the resistances of the interfacial layer and grain boundary largely increased as the time increased as shown Figure 15. On the other hand, in the cases of LiBr-doped Li_3PS_4 and LiI-doped Li_3PS_4, the resistances of the interfacial layer and grain boundary slightly increased with the time increased. The resistances of the interfacial layer and grain boundary decreased in the order Li_3PS_4 > LiBr-doped Li_3PS_4 > LiI-doped Li_3PS_4. The increasing resistance of the Li_3PS_4 is due to the Li_2S and Li_3P generated by the reaction between Li and Li_3PS_4[34–36]. The lithium–ion conductivity of Li_2S is poor and that of Li_3P is relatively low, causing non-uniform current density. In addition, the decomposition product, Li_3P, has been reported to have relatively high electronic conductivity of more than 10^{-4} S cm^{-1}.[37] These properties of the decomposition products accelerate lithium dendrite formation, leading to low CCDs in bare Li_3PS_4. Although the increase of the resistance is suppressed in LiBr-doped Li_3PS_4 and LiI-doped Li_3PS_4, the interfacial and grain boundary resistances of the LiBr-doped Li_3PS_4 were higher than those of LiI-doped Li_3PS_4. These differences are may be caused by the ionic conductivity and density of the

formed interfacial layer because the ionic conductivity of LiBr is lower than that of LiI[37] and the Young's Modulus of LiBr (38 GPa) is higher than that of LiI (27 GPa)[39]. Therefore, high resistance by grain boundary of formed LiBr layer with low density might induce slow lithium-ion transport, leading to inhomogeneous current distribution at the interface. Thereby the lithium dendrite growth would be favorable in the formed LiBr layer at interface more than at the formed LiI layer with high density. However, in the case of the formed LiI layer, it would be formed with homogeneous current density distribution, leading to alleviated lithium dendrite formation, due to its high density by low Young's modulus. In a previous study[19], it was also clarified that the suppression of electrolyte reduction and the improvement of the uniformity of the current density distribution through the improvement of the ionic conductivity are important factors for lithium dendrite suppression. In summary, both LiI and LiBr, as the lithium halides, could attribute to expand the free volume by the insertion of both iodine and bromide between PS_4^{3-} tetrahedrons in the Li_3PS_4, leading to improved ionic conductivity. Moreover, the change of phase behavior with the annealing temperatures was similar to that formed Thio-LISICON II phase from 180 to 200 ºC and crystalline phase of β-Li_3PS_4 with crystalline LiI and LiBr at over 220 ºC. However, the ionic conductivity of LiBr-doped Li_3PS_4 was lower than that of LiI-doped Li_3PS_4. It might be attributed to difference of expanded free volume due to smaller atomic radius of Br than that of LiI. In addition to the improved CCD, stable interfaces were confirmed by X-ray CT and XAS for both solid electrolytes, but there was a difference in interfacial resistance between them at high frequency impedance. In particular, in the case of LiBr, a behavior in which the grain boundary resistance was significantly increased than that of LiI was confirmed. This is due to the difference in elastic modulus higher than LiI (27 GPa) of LiBr (38 GPa).

3.4. Conclusion

In this study, the properties and lithium dendrite suppression capability of LiBr-doped Li_3PS_4 with and without annealing treatment were compared with those of Li_3PS_4 and LiI-doped Li_3PS_4. PDF analysis revealed that the LiBr-doped Li_3PS_4 solid electrolyte has a structure in which bromine is inserted between the PS_4^{3-} anions. The ionic

conductivity of LiBr-doped Li_3PS_4 increased with increasing annealing temperature, reaching approximately five times the value of the unannealed sample at 200 °C, and then tended to decrease. The change in ionic conductivity was found to be due to the formation of a high ionic conductivity thio-LISICON II phase and low ionic conductivity Li_3PS_4 and LiBr phases. The CCD and ionic conductivity of LiBr-doped Li_3PS_4 showed a linear relationship similar to that of LiI-doped Li_3PS_4. However, the CCD of LiBr-doped Li_3PS_4 was lower than that of LiI-doped Li_3PS_4, even though their ionic conductivities are almost equal. In the X-ray CT measurements after CCD tests, cracks at the lithium metal/solid electrolyte interface were observed in Li_3PS_4 whereas they were not observed in the LiBr-doped Li_3PS_4. In the XAS measurements after CCD tests, Li_2S and Li_3P, which are reductive decomposition product from Li_3PS_4, were observed in the Li_3PS_4 electrolyte whereas they were not observed in the LiBr-doped Li_3PS_4. Therese results are similar to the LiI-doped Li_3PS_4. The interfacial resistances of the three solid electrolytes decreased in the order Li_3PS_4 > LiBr-doped Li_3PS_4 > LiI-doped Li_3PS_4. These results indicate that lithium dendrite suppression is due to the suppression of electrolyte reduction, the improvement of the ionic conductivity, and the ionic conductivity of the stable interfacial layer between the solid electrolyte and lithium metal. This information will be useful for establishing design guidelines for materials for dendrite growth suppression.

Reference

1. Dunn, B.; Kamath, H.; Tarascon, J. M., Electrical Energy Storage for the Grid: A Battery of Choices. *Science* **2011,** *334* (6058), 928-935
2. Wu, H.; Cui, Y., Designing nanostructured Si anodes for high energy lithium ion batteries. *Nano Today* **2012,** *7* (5), 414-429
3. Seh, Z. W.; Sun, Y.; Zhang, Q.; Cui, Y., Designing high-energy lithium–sulfur batteries. *Chem. Soc. Rev.* **2016,** *45* (20), 5605-5634
4. Goodenough, J. B.; Kim, Y., Challenges for Rechargeable Li Batteries. *Chem. Mater.* **2010,** *22* (3), 587-603
5. Goodenough, J. B., Rechargeable batteries: challenges old and new. *J. Solid State Electrochem.* **2012,** *16* (6), 2019-2029
6. Goodenough, J. B.; Park, K. S., The Li-ion rechargeable battery: A perspective. *J. Am. Chem. Soc.* **2013,** *135* (4), 1167-1176
7. Inaguma, Y.; Liquan, C.; Itoh, M.; Nakamura, T.; Uchida, T.; Ikuta, H.; Wakihara, M., High ionic conductivity in lithium lanthanum titanate. *Solid State Commun.* **1993,** *86* (10), 689-693.
8. Murugan, R.; Thangadurai, V.; Weppner, W., Fast Lithium Ion Conduction in Garnet-Type $Li_7La_3Zr_2O_{12}$. *Angew. Chem. Int. Ed.* **2007,** *46* (41), 7778-7781.
9. Kamaya, N.; Homma, K.; Yamakawa, Y.; Hirayama, M.; Kanno, R.; Yonemura, M.; Kamiyama, T.; Kato, Y.; Hama, S.; Kawamoto, K.; Mitsui, A., A lithium superionic conductor. *Nat. Mater.* **2011,** *10* (9), 682-686
10. Tatsumisago, M.; Nagao, M.; Hayashi, A., Recent development of sulfide solid electrolytes and interfacial modification for all-solid-state rechargeable lithium batteries. *Journal of Asian Ceramic Societies* **2013,** *1* (1), 17-25

11. Hayashi, A.; Sakuda, A.; Tatsumisago, M., Development of Sulfide Solid Electrolytes and Interface Formation Processes for Bulk-Type All-Solid-State Li and Na Batteries. *Fron. Energy Res.,* **2016,** *4*, 25-25
12. Kato, Y.; Hori, S.; Saito, T.; Suzuki, K.; Hirayama, M.; Mitsui, A.; Yonemura, M.; Iba, H.; Kanno, R., High-power all-solid-state batteries using sulfide superionic conductors. *Nature Energy* **2016,** *1* (4), 16030-16030.
13. Deiseroth, H.-J.; Kong, S.-T.; Eckert, H.; Vannahme, J.; Reiner, C.; Zaiß, T.; Schlosser, M., Li_6PS_5X: A Class of Crystalline Li-Rich Solids With an Unusually High Li^+ Mobility. *Angew. Chem.,* **2008,** *120* (4), 767-770
14. Minami, K.; Hayashi, A.; Tatsumisago, M., Preparation and characterization of superionic conducting $Li_7P_3S_{11}$ crystal from glassy liquids. *Journal of the Ceramic Society of Japan* **2010,** *118* (1376), 305-308.
15. Sakuda, A.; Hayashi, A.; Tatsumisago, M., Sulfide Solid Electrolyte with Favorable Mechanical Property for All-Solid-State Lithium Battery. *Sci. Reports* **2013,** *3* (1), 2261-2261
16. Nagao, M.; Hayashi, A.; Tatsumisago, M.; Kanetsuku, T.; Tsuda, T.; Kuwabata, S., In situ SEM study of a lithium deposition and dissolution mechanism in a bulk-type solid-state cell with a Li_2S-P_2S_5 solid electrolyte. *Phys. Chem. Chem. Phys*. **2013,** *15* (42), 18600-18606.
17. Suyama, M.; Kato, A.; Sakuda, A.; Hayashi, A.; Tatsumisago, M., Lithium dissolution/deposition behavior with Li_3PS_4-LiI electrolyte for all-solid-state batteries operating at high temperatures. *Electrochimica Acta* **2018,** *286*, 158-162.
18. Han, F.; Yue, J.; Zhu, X.; Wang, C., Suppressing Li Dendrite Formation in Li_2S-P_2S_5 Solid Electrolyte by LiI Incorporation. *Adv. Energy Mater.,* **2018,** *8* (18), 2-7

19. Takahashi, M.; Watanabe, T.; Yamamoto, K.; Ohara, K.; Sakuda, A.; Kimura, T.; Yang, S.; Nakanishi, K.; Uchiyama, T.; Kimura, M.; Hayashi, A.; Tatsumisago, M.; Uchimoto, Y. Invetigation of the suppression of dendrite lithium growth with a lithium-iodide-containing solid electrolyte. *Chem. Mater.*, **2021**, 33, 4907-4914.
20. Ohara, K.; Mitsui, A.; Mori, M.; Onodera,Y.; Shiotani, S.; Koyama, Y.; Orikasa, Y.; Murakami, M.; Shimoda, K.; Mori, K.; Fukunaga, T.; Arai, H.; Uchimoto, Y.; Ogumi, Z., Structural and electronic feature of binary Li_2S-P_2S_5 glasses, *Sci. Rep.*, **2016**, 6, 21302
21. Shiotani, S.; Ohara, K.; Tsukasaki, H.; Mori, S.; Kanno, R., Pair distribution function analysis of sulfide glassy electrolytes for all-solid-state batteries: Understanding the improvement of ionic conductivity under annealing condition, *Sci. Rep.*, **2017**, 7, 6972.
22. Yamamoto. K.; Takahashi. M.; Ohara. k,; Phuc N. H. H.,; Yang. S.; Watanabe. T.; Uchiyama. T.; Sakuda. A.; Hayashi. A.; Tatsumisago. M.; Muto. H.; Matsuda. A.; Uchimoto. Y.; Synthesis of Sulfide Solid Electrolytes through the Liquid Phase: Optimization of the Preparation Conditions, *ACS Omega*, **2020**, 5, 40, 26287-26294.
23. Niek. J. J. K., Irek. R., Marnix W., Diffusion Mechanism of LI argyrodite Solid Electrolytes for Li-ion Batteries and Prediction of Optimized Halogen Doping : The effect of Li Vacancies, Halogens, and Halogen Disorder, *Chem. Mater.*, **2016**, 28, 7955-7963.
24. Marvin. A. K., Sean. P. C., Mario. C., Felix B., Thorben K., Anatoliy. S., Christian. D., Alexandra. Z., Jurgen. J., Wolfgang G. Z., Influence of Lattice Polarizability on the Ionic Conductivity in the Lithium Superionic Argyrodites Li_6PS_5X (X=Cl, Br, I), *J. Am. Chem. Soc.*, 2017, 139, 10909-10918.

25. Jeffrey. S. G.; Donald S. J., Low temperature paddlewheel effect in glassy solid electrolytes, *Nat. Commun.*, **2020**, 11, 1483-1494

26. Hayashi, A.; Hama, S.; Minami, T.; Tatsumisago, M. Formation of Superionic Crystals from Mechanically Milled Li_2S-P_2S_5 Glasses. *Electrochem. commun.* **2003**, *5* (2), 111–114.

27. Kanno, R.; Murayama, M. Lithium Ionic Conductor Thio-LISICON: The Li_2S-GeS_2-P_2S_5 System. *J. Electrochem. Soc.* **2001**, *148* (7), A742.

28. Deng. Y., Eames. C., Fleutot. B., David. R., Chotard. J., Suard. E., Masquelier. C., Islam. M., Enhancing the Lithium Ion Conductivity in Lithium Superionic Conductor (LISICON) Solid Electrolytes through a Mixed Polyanion Effect, *ACS Appl. Mater. Interfaces*, **2017**, 9, 7050-7058

29. Okumura. T., Taminato. S., Miyazaki. T., Kitamura. M., Saito. T., Takeuchi. T., Kobayashi. H.,LISICON-Based Amorphous Oxide for Bulk-Type All-Solid-State Lithium-Ion Battery, *ACS Appl. Energy Mater*., **2020**, 3, 3220-3229

30. Kanno. R., Murayama. M., Lithium Ionic Conductor Thio-LISICON: The Li_2S-GeS_2 -P_2S_5 System, J. *Electrochem. Soc.*, **2001**, 148, 742-746

31. Richard. W., Miara. L., Wang. Y., Kim. J., Ceder. G., Interface Stability in Solid-State Batteries, *Chem. Mater.*, **2016**, 28, 266-273.

32. William. A., Dominika. A. B., Yang. L., Mehendra. S., Thad. D., Hui. W., Halide doping effect on solvent-synthesized lithium argyrodites Li_6PS_5X (X = Cl, Br, I) superionic conductors, Journal of Power Sources, 2020, 464, 228158.

33. Sebastian. W.; Stefan. J. S.; Christain. D.; Wolfhang G. Z.; Jurgen. J., Interfacial reactivity and interphase growth of argyrodite solid electrolytes at lithium metal electrodes, *Solid State Ionics*. **2018**, 318, 102-112.

34. Sebastian. W.; Dominik. A. W.; Thomas. L.; Martin. R. B.; Joachim. S.; Jurgen. J., Interphase formation and degradation of charge transfer kinetics between a lithium metal anode and highly crystalline $Li_7P_3S_{11}$ solid electrolyte, *Solid State Ionics*, **2016**, 286, 24-33.

35. Sebastian. W.; Simon. R.; Thomas. L.; Dominik A. W.; Joachim. S.; Wolfhang G. Z.; Jurgen. J., Direct Observation of the Interfacial Instability of the Fast Ionic Conductor $Li_{10}GeP_2S_{12}$ at the Lithium Metal Anode, *Chem. Mater.*, **2016**, 28, 2400-2407.

36. Otoyama, M.; Suyama, M.; Hotehama, C.; Kowada, H.; Takeda, Y.; Ito, K.; Sakuda. A; Tatsumisago, M.; Hayashi, A. Visualization and Control of Chemically Induced Crack Formation in All-Solid-State Lithium-Metal Batteries with Sulfide Electrolyte. *ACS appl. Mater.* **2021**, 13, 4, 5000-5007.

37. Xiao. J,; Singyuk. H.; Pengfei. W.; Xinzi. H.; Nan. P.; Ji. C.; Xiulin. F.; Chunsheng. W.; Solid-State Electrolyte Design for Lithium Dendrite Suppression, *Adv. Mater.* **2020**, 32, 2002741.

38. Haven. Y, The ionic conductivity of Li-HALIDE CRYSTALS, *Recl. Trav. Chim. Pays-Bas.*, **1950**, 69, 1471–1489.

39. Atsuka. K., Mirai. Y., Atsushi. S., Akitoshi H., Masahiro T.,Mechncal Properties of Li_2S-P_2S_5 Glasses with Lithium Halides and Application in All-Solid-State Batteries, *ACS Appl. Energy Mater.*, **2018**, 1, 1002–1007.

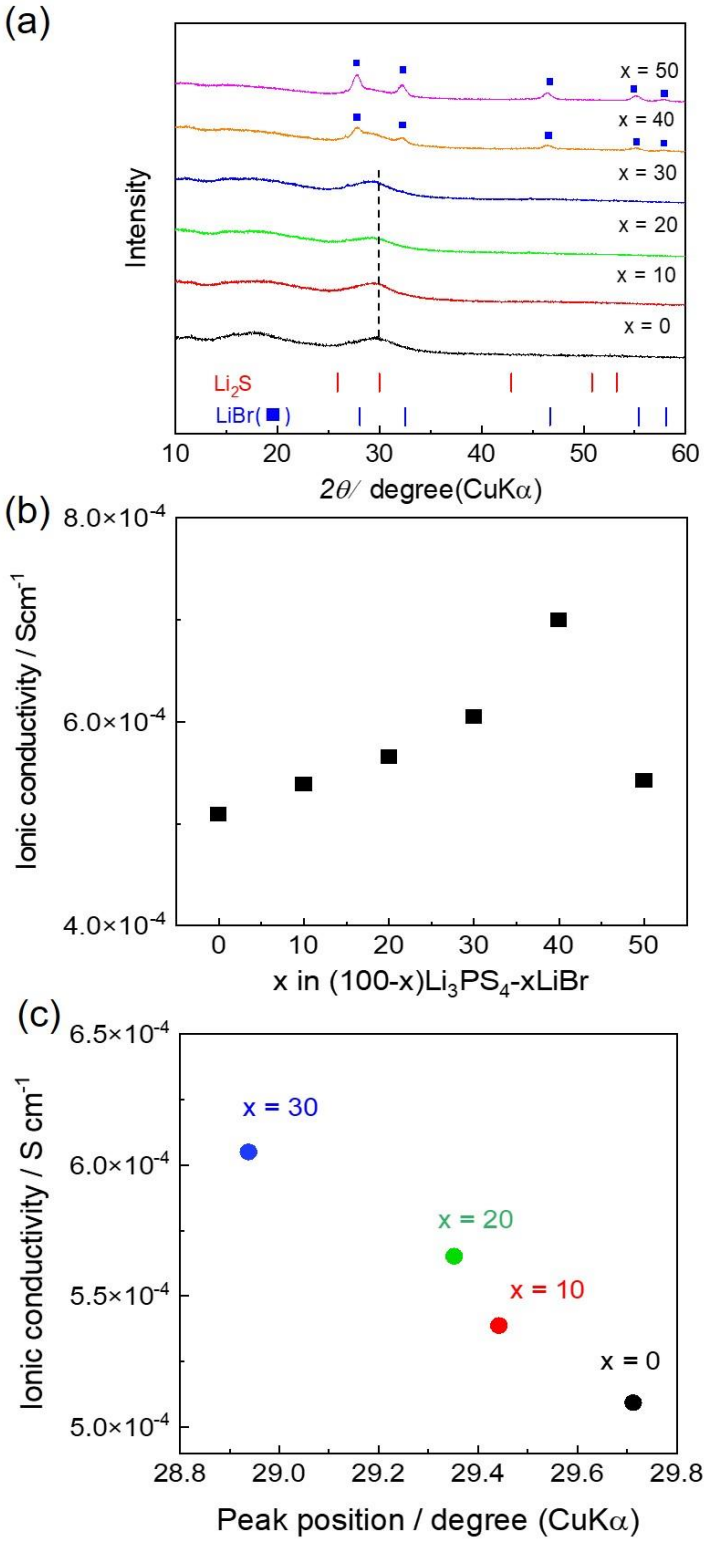

Figure 1. XRD patterns of (100−*x*)Li_3PS_4–*x*LiBr prepared via mechanical milling (a), Ionic conductivity at 25 °C (b), and correlation between the ionic conductivity at 25 °C and peak position in the XRD patterns of (100−*x*)Li_3PS_4–*x*LiBr (*x* = 0, 10, 20, 30) (c).

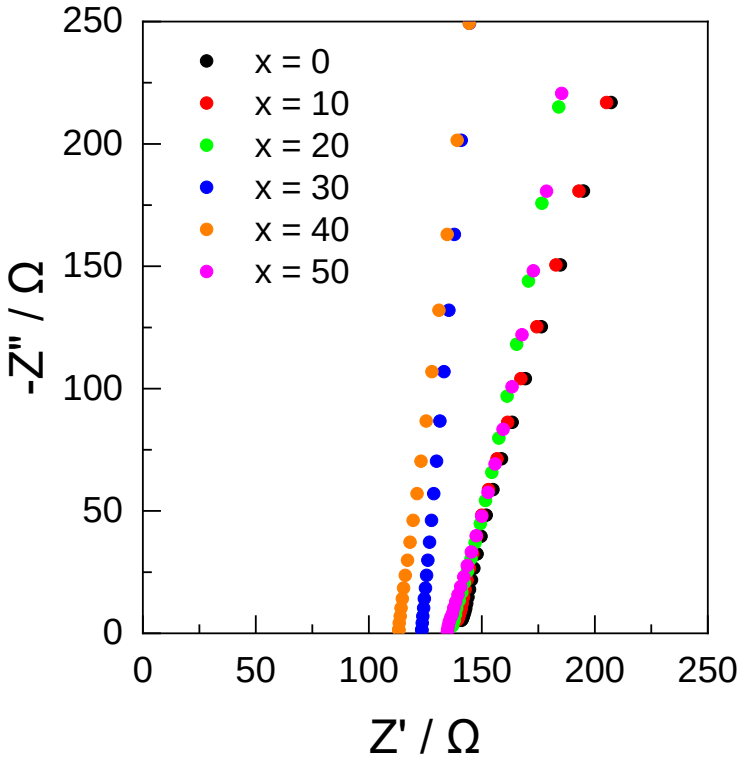

Figure 2. Nyquist plots at 25°C of (100- *x*) Li_3PS_4- *x*LiBr prepared by mechanical milling

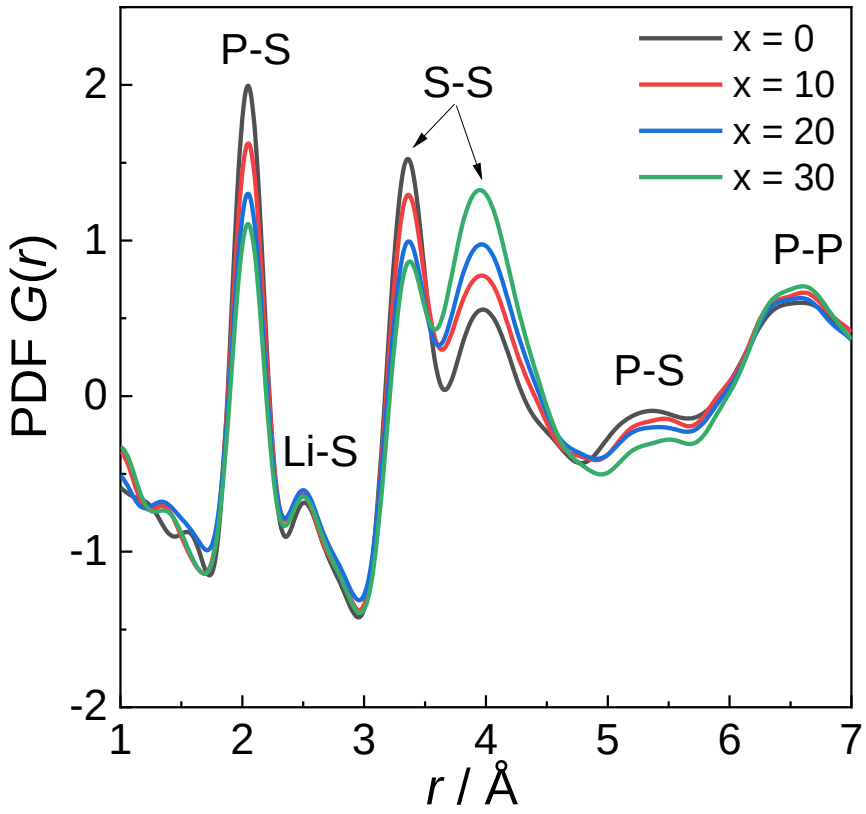

Figure 3. Reduced PDFs of (100−*x*)Li_3PS_4–*x*LiBr prepared via mechanical milling.

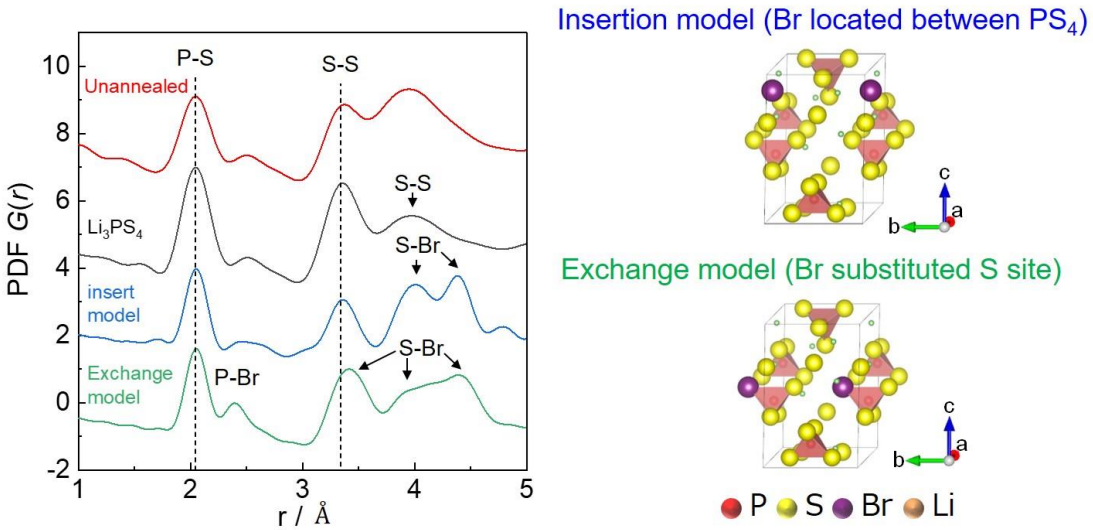

Figure 4. Reduced PDF, G(r), of Li_3PS_4 and 70 Li_3PS_4-30LiBr with simulated PDF obtained using Bromine ion inserted (blue line) and exchanged models (green).

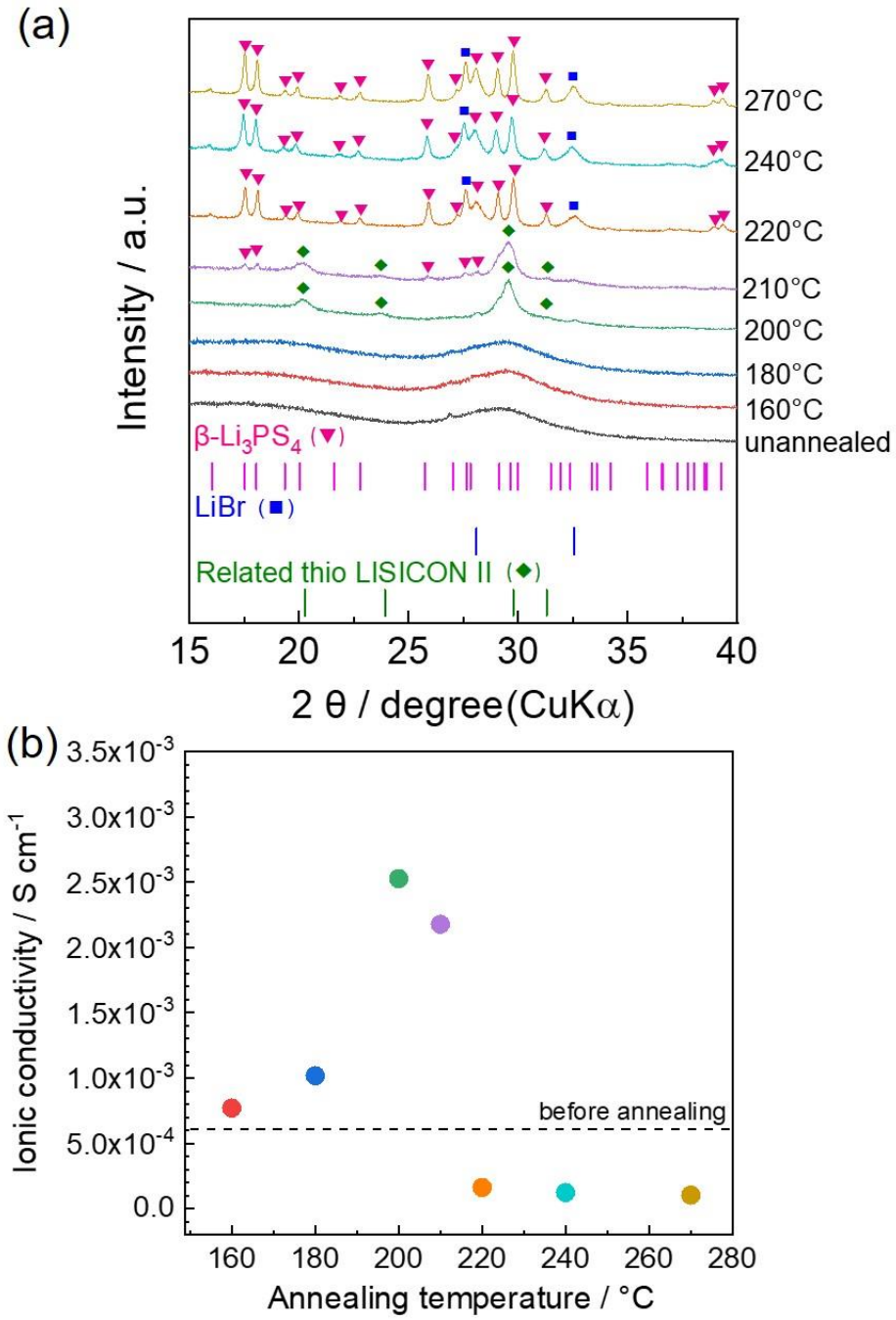

Figure 5. (a) XRD patterns of $70Li_3PS_4$-30LiBr before and after annealing at each temperature for 2 h and (b) ionic conductivities at 25 ºC. Related thio-LISICON II structure is the crystal structure of the oxide LISICON II in which oxide ions are replaced with sulfide ions, and the crystal structure has not been clearly determined because the crystallinity of thio-LISICON is lower than that of oxide LISICON due to larger polarizability of sulfide ion than oxide ions[28-30].

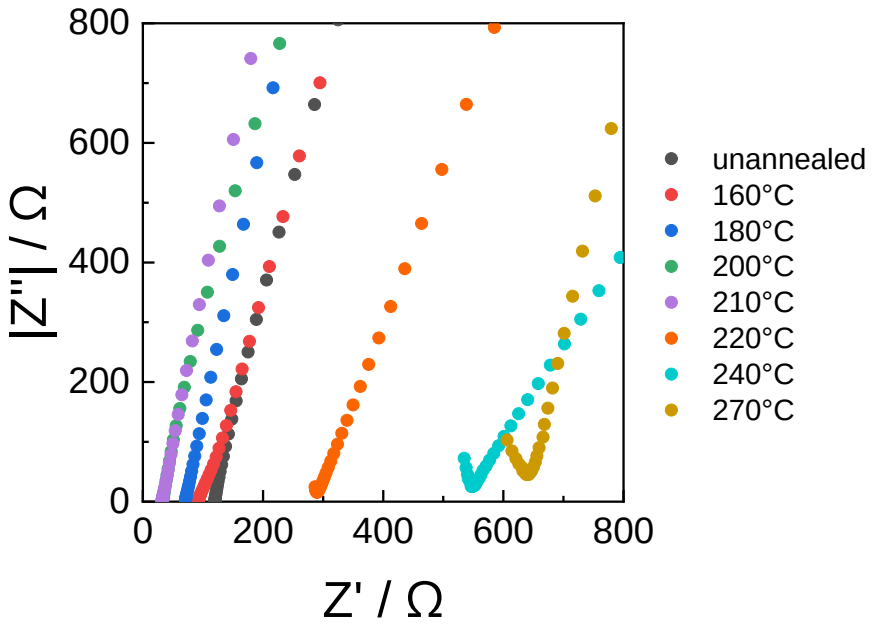

Figure 6. Nyquist plots at 25°C of $70Li_3PS_4$-30LiBr before and after annealing at various temperature.

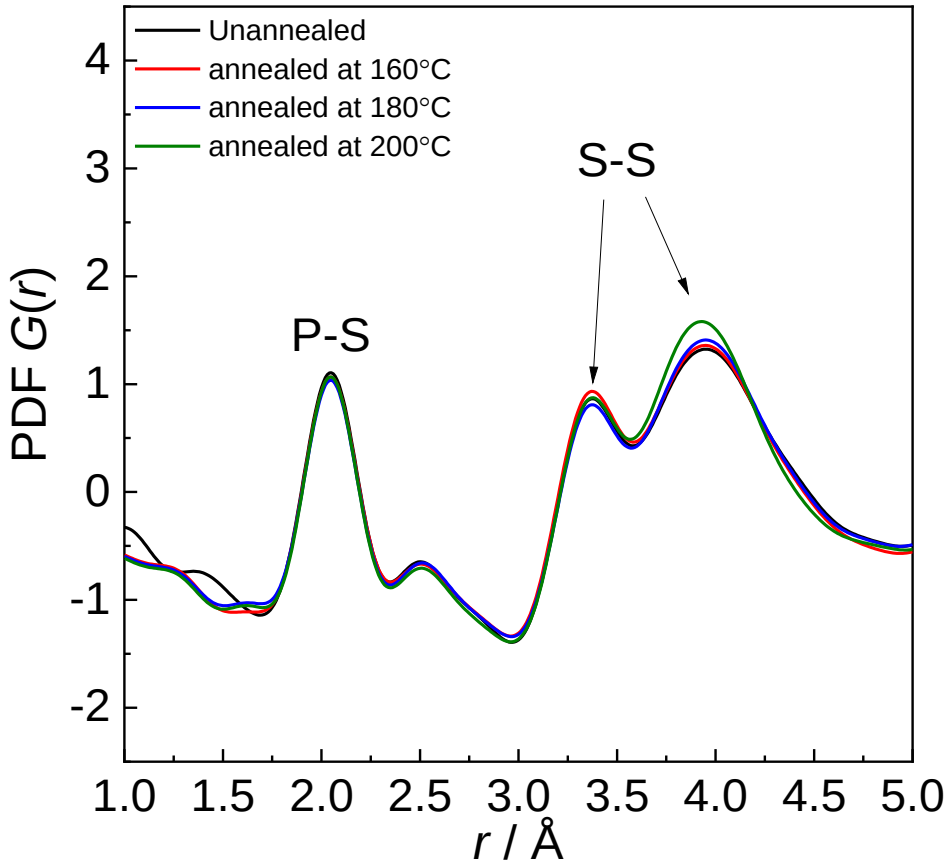

Figure 7. PDF analysis for annealed $70Li_3PS_4$–30LiBr at 160, 180, and 200 °C in comparison with unannealed $70Li_3PS_4$–30LiBr.

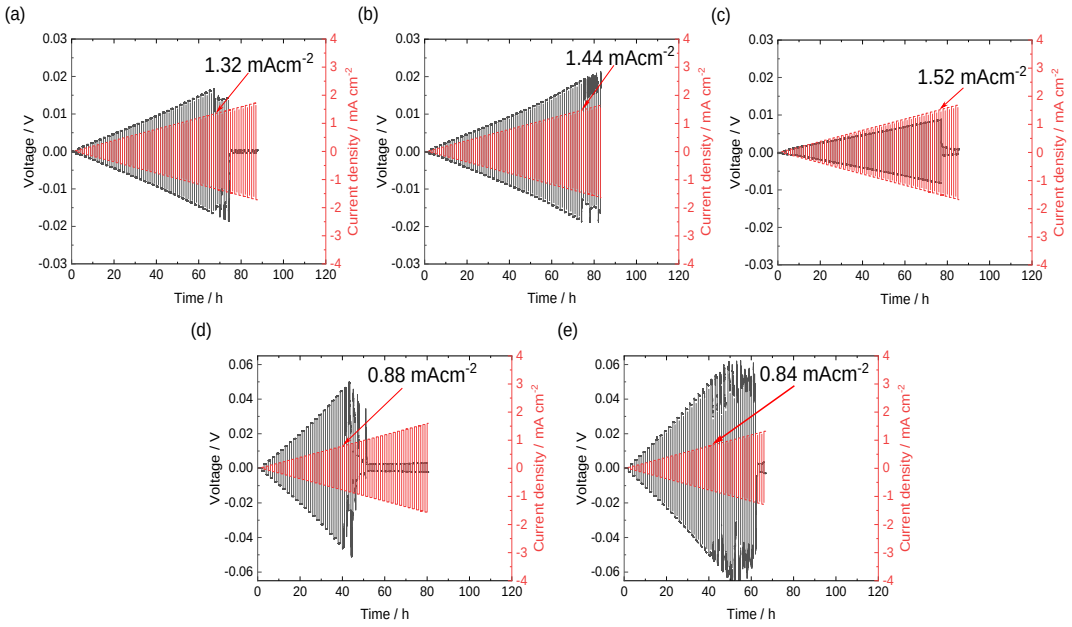

Figure 8. Galvanostatic cycling test of 70 Li_3PS_4-30 LiBr (a) unannealed and after annealed at (b) 180°C, (c) 200°C, (d) 240°C and (e) 270°C, respectively.

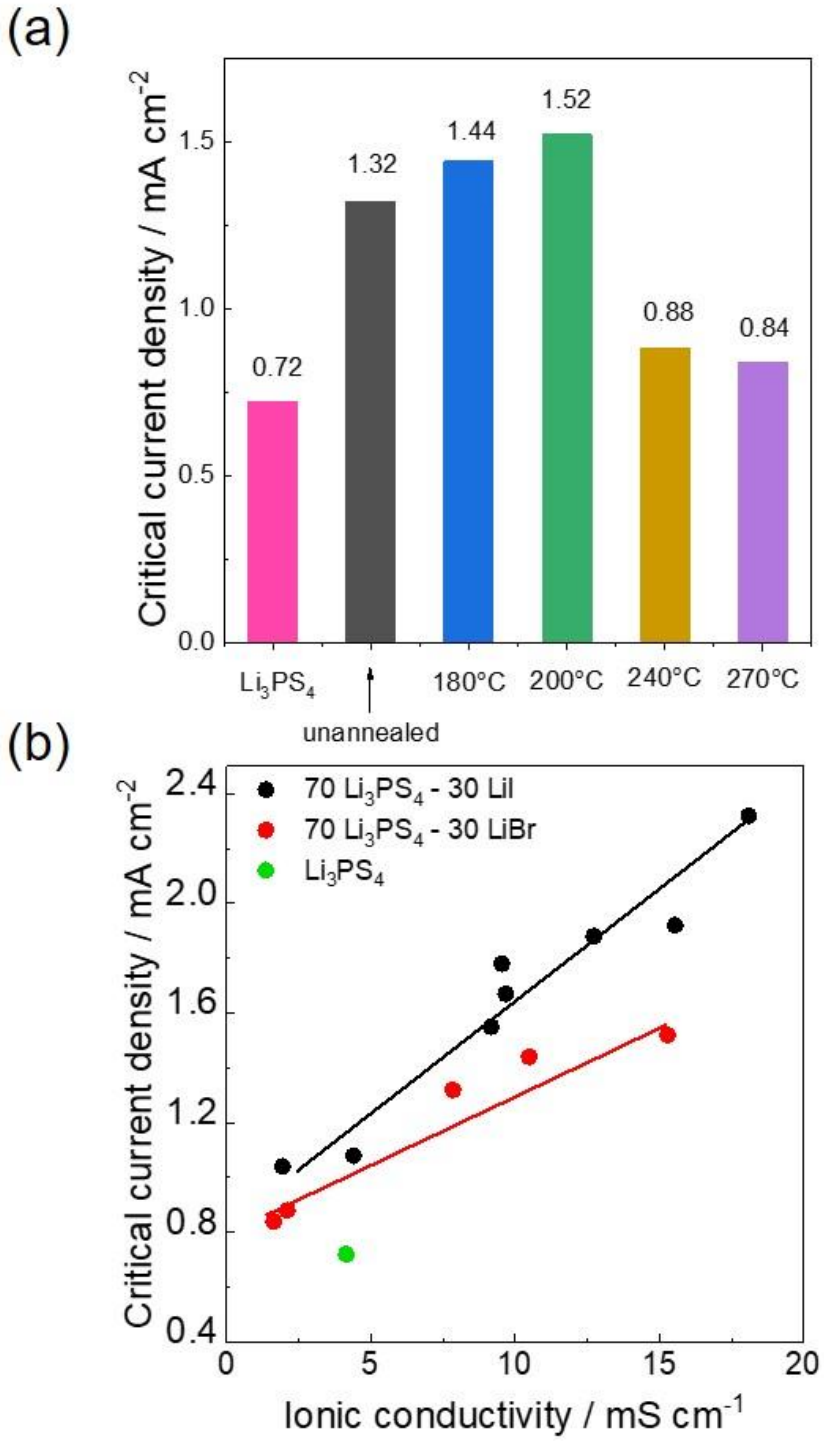

Figure 9. CCDs of Li_3PS_4 and $70Li_3PS_4$–$30LiBr$ unannealed and after being annealed at 180, 200, 240, and 270 °C (a). Correlations between the ionic conductivity at 100 °C and the CCD of Li_3PS_4, LiI-doped Li_3PS_4, and LiBr-doped Li_3PS_4 before annealing and after annealing at various temperatures (b).

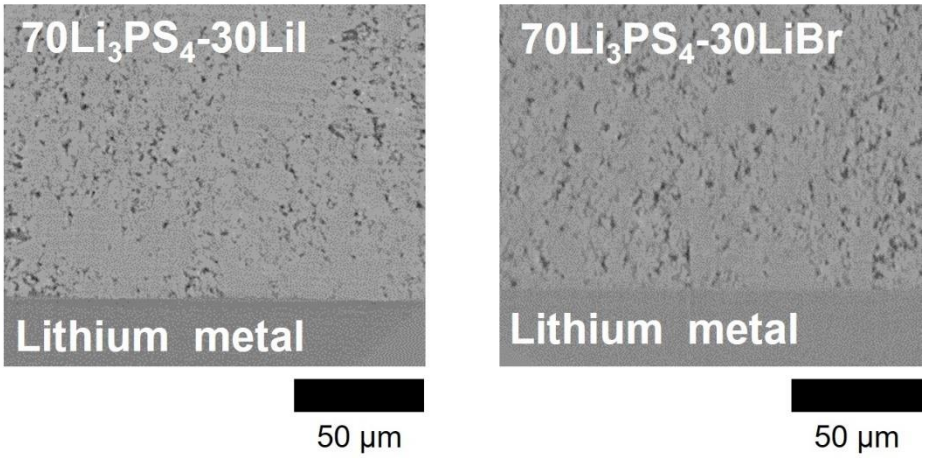

Figure 10. Interface morphology (X-Y direction) obtained from X-ray CT measurement before Galvano cycling test.

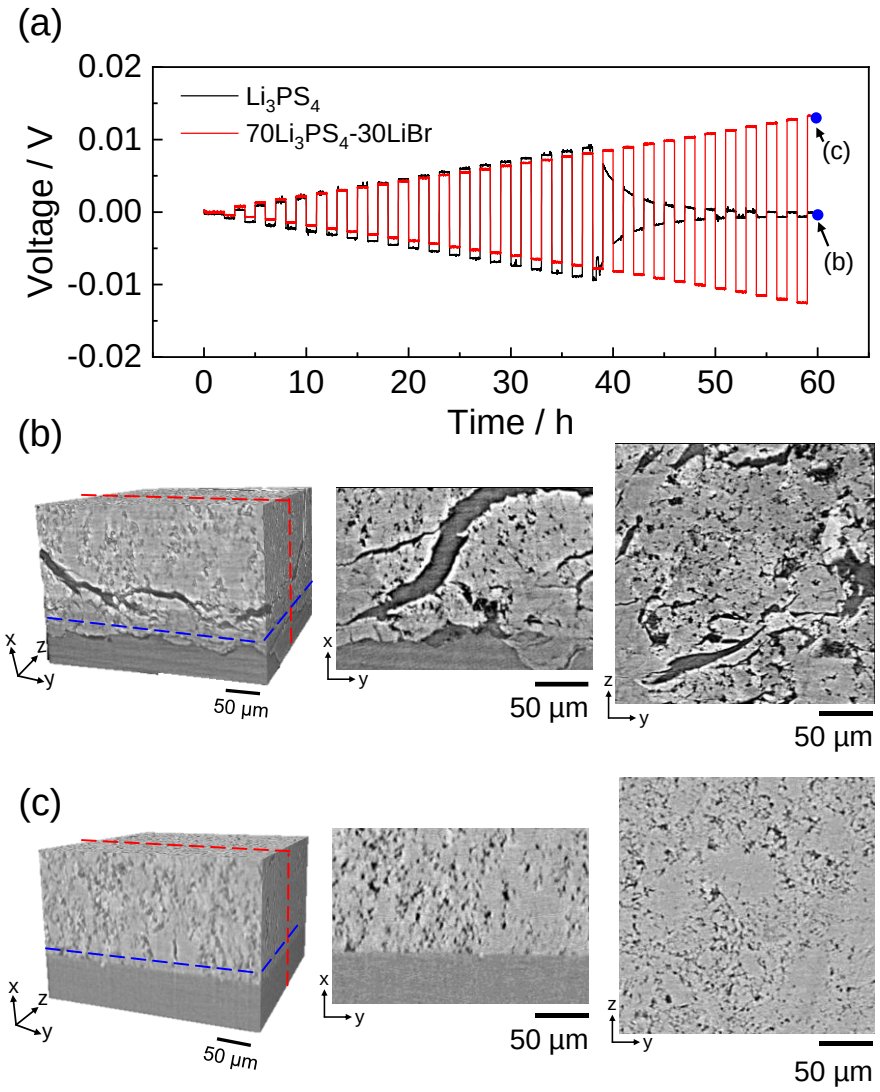

Figure 11. Galvanostatic cycling test results for Li_3PS_4 and $70Li_3PS_4$–$30LiBr$ using Li/solid electrolyte/Li cells under the same conditions. The black line represents Li_3PS_4 and the red line represents unannealed $70Li_3PS_4$–$30LiBr$. Transmission images of (b) Li_3PS_4 and (c) $70Li_3PS_4$–$30LiBr$ after the galvanostatic cycling tests.

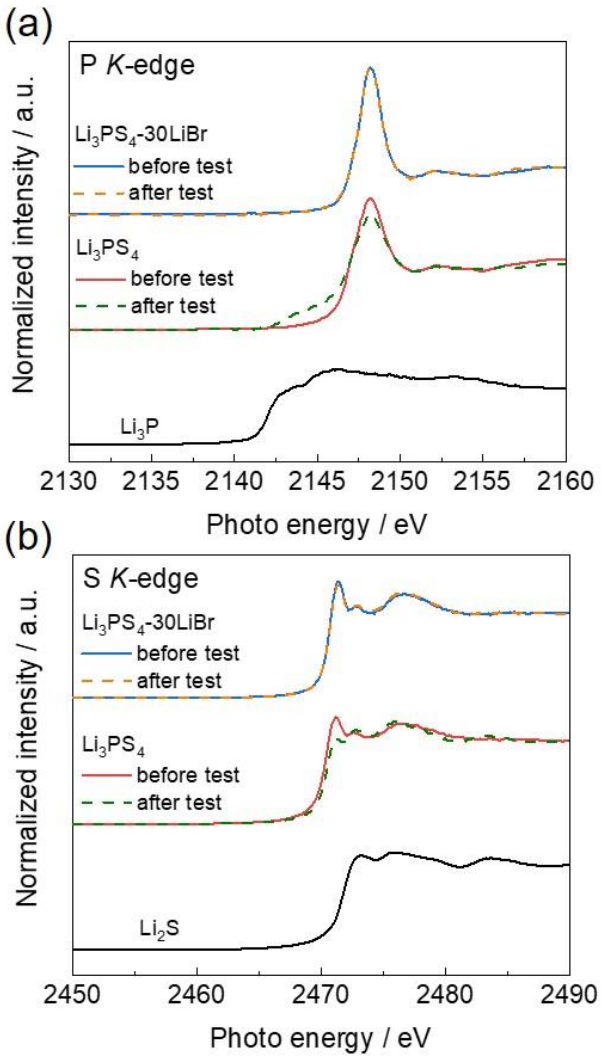

Figure 12. (a) P *K*-edge and (b) S *K*-edge X-ray absorption near edge structure (XANES) difference spectra of Li_3PS_4 and $70Li_3PS_4$–30LiBr before and after the galvanostatic cycling tests.

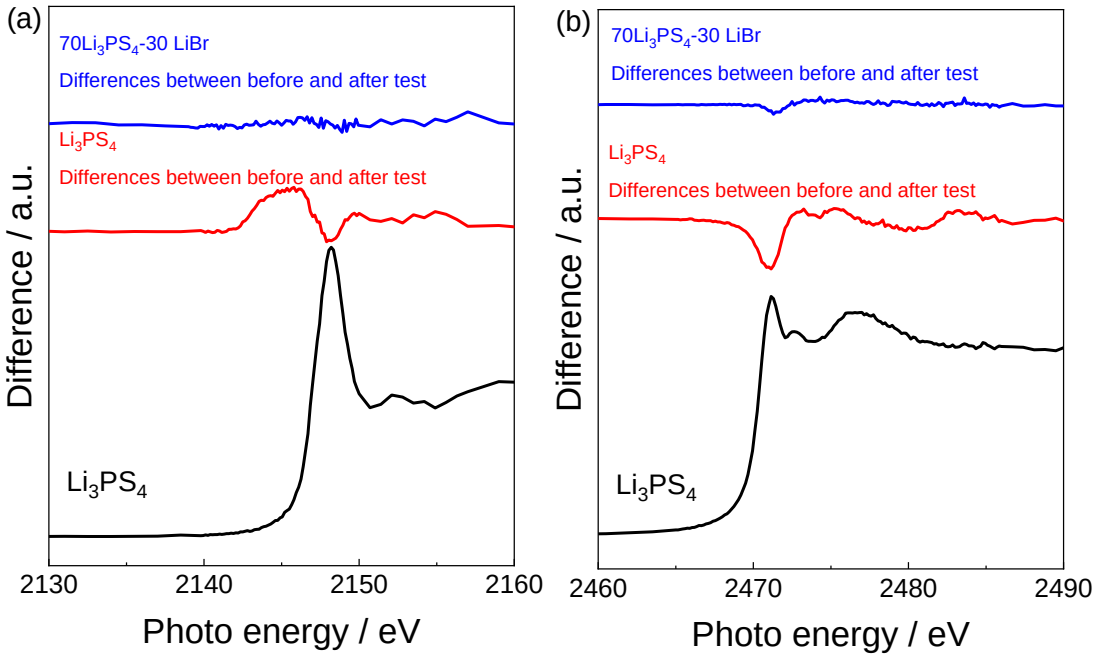

Figure 13. (a) P *K*-edge and (b) S *K*-edge XANES difference spectra of Li_3PS_4 and $70Li_3PS_4$-30LiBr before and after the galvanostatic cycling tests in **Figure 12**

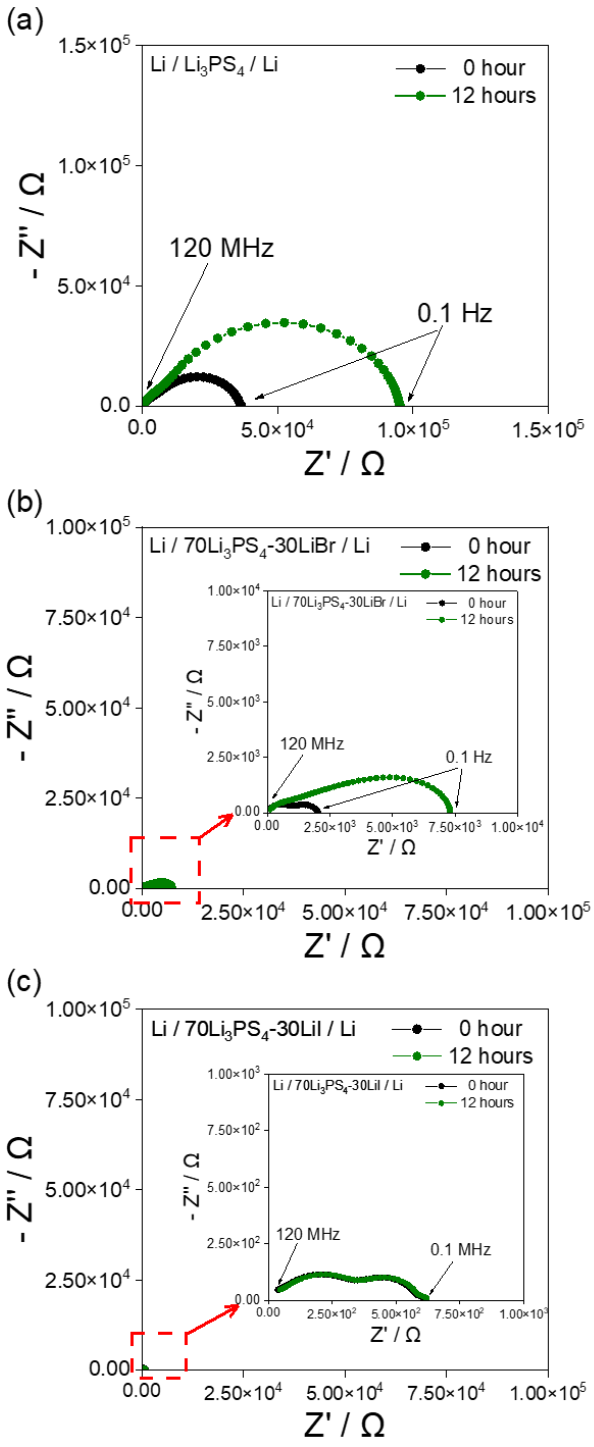

Figure 14. Nyquist plots for before (0 hour) and after (12 hours) at 100°C corresponding to Li_3PS_4(a), LiBr-Li_3PS_4(b), and LiI-Li_3PS_4, respectively.

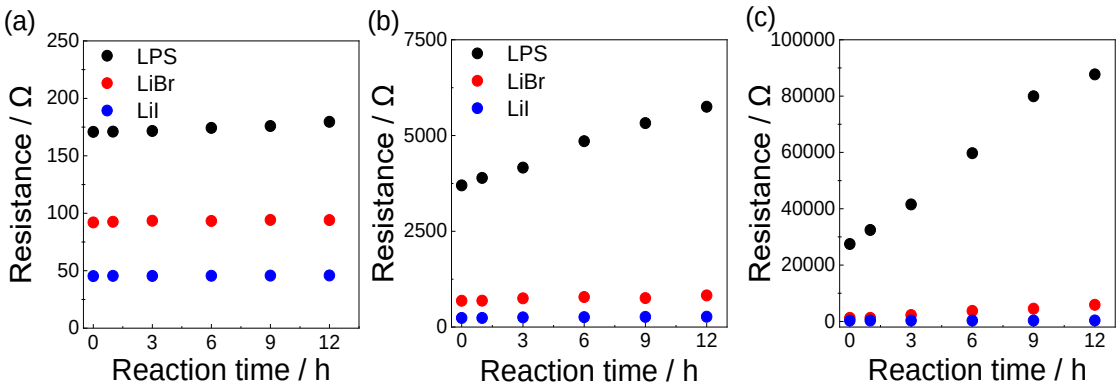

Figure 15. Obtained resistance values for the bulk (a), interphase (SEI) (b), and grain boundary (c) based on Nyquist plots

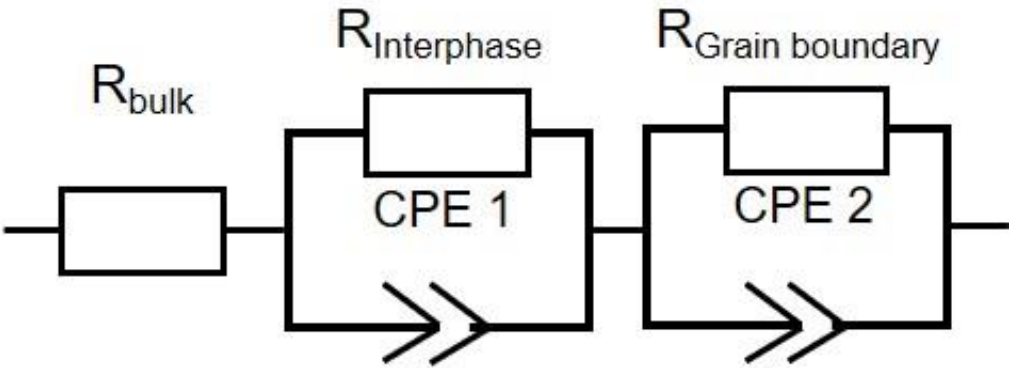

Figure 16. Applied circuit model based on Ref.30

Table 1. The fitted parameter results corresponding to 0 and 24 hours for each Li symmetrical cell with bare Li_3PS_4, and LiI, LiBr doped Li_3PS_4

	Li_3PS_4		$30LiBr\text{-}70Li_3PS_4$		$30LiI\text{-}70Li_3PS_4$	
	0 hour	12 hours	0 hour	12 hours	0 hour	12 hours
R_{bulk}	171.0	188.8	92.56	94.032	46.255	47.04
$R_{Interphase}$ / Ω	3698	5473	687.4	838.6	237.4	248
CPE 1	5.07×10^{-11}	5.43×10^{-11}	1.10×10^{-11}	3.31×10^{-10}	8.61×10^{-11}	1.48×10^{-9}
P1	0.891	0.878	0.996	0.849	0.955	0.882
Capacitance / F	7.61×10^{-12}	5.83×10^{-12}	1.012×10^{-11}	2.23×10^{-11}	3.73×10^{-11}	6.782×10^{-11}
$R_{Grain\ boundary}$ / Ω	27472	82214	1258	5819	280.9	312
CPE 1	3.97×10^{-10}	2.60×10^{-10}	4.53×10^{-8}	1.65×10^{-7}	1.43×10^{-7}	3.33×10^{-7}
P1	0.817	0.878	0.672	0.582	0.696	0.670
Capacitance / F	3.18×10^{-11}	2.94×10^{-11}	3.84×10^{-10}	1.11×10^{-9}	1.73×10^{-9}	3.61×10^{-9}

Chapter 4. High Rate Capability of Graphite Anode by Lithium Iodide Surface Modification for All-Solid-State Batteries

All-solid-state batteries (ASSBs) have been attracting attention as a potential paradigm for batteries in the future as they are safer, because they do not leak and are stable at high temperatures compared to lithium-ion batteries (LIBs) that use liquid electrolytes; further, the use of a bipolar structure is expected to improve energy density. For ASSBs, graphite is one of the most promising practical anode materials because of its superior power density in LIBs. However, the power density of ASSBs is unsatisfactory for practical applications, and is lower than that of LIBs. One reason for this is the slow lithium-ion transport at the interface between the graphite anode and solid electrolyte. Because of the low redox potential for lithium-ion intercalation into graphite (close to the lithium reduction potential), sulfide solid electrolytes undergo reductive decomposition, which impedes lithium-ion transport at the interface with graphite. To address this problem, we attempted to coat LiI, which is stable at the lithium deposition potential, directly onto the graphite surface, and examined the effect on the sulfide solid electrolyte and electrochemical performance. The electrochemical measurements showed that the graphite composite without LiI showed a discharge capacity of 248 mAhg−1, while that with 5 wt% LiI showed a relatively high discharge capacity of approximately 348 $mAhg^{-1}$. Impedance spectroscopy and S and P *K*-edge X-ray absorption spectroscopy indicated that the LiI-coated graphite composites displayed stable interface behavior, in contrast to the uncoated graphite composite, after the lithiation process.

4.1. Introduction

Lithium-ion secondary batteries (LIBs) have been used in a variety of electronic devices, and are also being considered to utilize large power sources such as those for electric vehicle[1]. However, the existing LIBs are not able to guarantee its safety due to flammable organic liquid as an electrolyte, which is serious problem for the large scale

utilization[1,2]. All solid-state batteries (ASSBs), in which non-flammable solid electrolytes are used, have been receiving much attention because they complement the safety problem of LIBs. In particular, the ASSBs using sulfide solid electrolyte such as Li_3PS_4, $Li_{10}GeP_2S_{12}$, and Li_6PS_5X (X=Cl, Br), had been a lot of attentions due to its high ionic conductivity, relatively better wettability than oxide systems[2–5].

For the application of these attractive sulfide electrolytes, various anode materials, such as Si[6,7], Li met-al[8], and graphite[9,10], have been investigated. Si anodes have the advantages of low potential (0.4 V vs. Li/Li^+) and high theoretical capacity (4200 $mAhg^{-1}$), but suffer from volume expansion/contraction during charging/discharging[6]. Li metal also has the advantages of low potential (−3.045 V vs. standard hydrogen electrode) and high theoretical capacity (3860 $mAhg^{-1}$), but dendrite formation occurs during charging and discharging[8]. Conversely, for the immediate practical application of ASSBs, although graphite anodes have lower theoretical capacity (372 $mAhg^{-1}$)[11], they are suitable candidates because of their proven high rate performance and cyclability in LIBs. However, graphite anodes have not shown the same excellent electrochemical performances in ASSB systems as they have in liquid electrolyte systems, owing to their large polarization. The origins of this polarization have been reported to be (1) contact resistance between the graphite and sulfide SE[12–14] and (2) reductive decomposition of the sulfide SE on the graphite surface at the lithiation potential[14,15]. Although the contact resistance can be reduced by con-trolling the particle size of the sulfide SE[14], the decom-position reaction on the graphite surface might be accelerated because of the good interface contact. According to previous studies, most sulfide electrolytes thermodynamically undergo reductive decomposition at the low potential at which lithium ion (de)intercalation in the graphite anode occurs[17–20]. It has been reported that halogen-doped electrolytes are stable during the charge and discharge processes of graphite[15]. Even if the lithium halide doped solid electrolytes have an effect on the suppression for reductive decomposition at low potential window[14], there is the limitation of solid electrolyte selection. For example, when using an electrolyte with high ionic conductivity, but low reductive stability, such as $Li_{10}GeP_2S_{12}$[19], it is desirable to suppress the electrolyte decomposition by modifying the graphite surface. Therefore, direct coating

on the surface of active material would be promising strategy for the compatibility of various solid electrolytes.

In this study, we demonstrate a simple coating process by liquid phase on the graphite surface with lithium iodide (LiI) as a coating agent, which has not only high reductive stability but also good compaction between particle and particle due to its own softness[22-25]. The graphite was successfully coated with LiI *via* the simple wet chemical process, which is characterized by scanning electron microscopy with energy dispersive spectroscopy (SEM/EDS) and Raman spectroscopy. Then, we analyzed the effect of the LiI coating on the electrochemical performance of the graphite anode combination with the Li_3PS_4 that is decomposed at the lithiation potential of the graphite. The optimized LiI-coated graphite anode shows higher discharge capacity (348 $mAhg^{-1}$) than uncoated graphite (248 $mAhg^{-1}$) at 0.05 C rate and superior C-rate performance (310 $mAhg^{-1}$ at 0.1 C rate) to non-coated graphite (162 $mAhg^{-1}$ at 0.1 C rate). Electrochemical impedance spectroscopy (EIS) and X-ray absorption spectroscopy (XAS) clearly showed the interfacial resistance attributed to the contact between the graphite and sulfide electrolyte, and the decomposition products of sulfide solid electrolyte was reduced by the LiI-coating, resulting in the improvement of the power density of the graphite.

4.2. Experimental section

4.2.1. Preparation of Li_3PS_4 and LiI coated graphite *via* liquid phase

The LiI coated graphite was prepared through the wet chemical process. Different weight percent of LiI (1, 3, 5, and 7 wt%, Aldrich, 99.99%) for graphite powder (CGB-10, Nippon Graphite Industries, Ltd) was firstly dissolved in acetonitrile, then the graphite powder was added into the LiI dissolved solution and stirred for 24 hours. The mixture of LiI and graphite was dried to remove remained acetonitrile on 70 °C for 12 hours. The Li_3PS_4 as the electrolyte was synthesized by ball milling of the 3:1 molar ratio of Li_2S (Aldrich, 99%) and P_2S_5 (Aldrich, 99.9%) with zirconia balls for 15 hours at 600 rpm.

4.2.2. Material characterization

The crystal structure of prepared LiI-coated graphite powders was measured by an X-ray diffraction (XRD) apparatus, RINT–Ultima III (Rigaku) with CuKα radiation source. The XRD measurements were performed without sample air exposure. Scanning electron microscopy (SEM) images and energy dispersive X-ray spectroscopy (EDX) profiles for the LiI–coated graphite powders were collected using a SU8220 (Hitachi High-Technologies) system in order to observe the microstructure of each material by using SU8220 (Hitachi High-Technologies). The XAS spectra of the S *K*–edge and P *K*–edge of prepared composite materials was recorded at the BL6N1 beamline of the Aichi Synchrotron Radiation Center. The Raman spectra were collected by a DXR3 Smart Raman spectrometer (Thermo Fisher Scientific) using a 514 nm diode-pumped solid-state laser at room temperature. All the electrolytes were sealed in glass vessels in an Ar-filled glove box and measured between 50 and 200 cm^{-1} without air exposure.

4.2.3. Electrochemical measurements

Electrochemical measurements were performed by using a two-electrode cell. The graphite composite electrodes were prepared by mixing LiI-coated graphite and Li_3PS_4, in which the weight ratio between the LiI-coated graphite and Li_3PS_4 was 60 wt% : 40 wt%. The Li_3PS_4 with 100 mg were placed in a polycarbonate tube with a diameter of 10 mm and pressed to form the solid electrolyte (SE) layer, and then the graphite composite with 10 mg was added on one side of the SE layer and pressed at 360 MPa. A Li–In alloy was placed on the another of the SE layer and pressed at 10 MPa to prepare for a pellet with a three-layers (Li-In alloy / solid electrolyte / graphite composite). The Galvano static cycle test was conducted with cut-off voltages of - 0.62 – 1.0 V vs. Li-In/Li^+ (0.0 V – 1.62 V vs. Li/Li^+)[16] for charge and discharge under the 3 cycles with different current densities of 0.13, 0.26, 0.51, and 0.76 $mAcm^{-2}$ at 25 °C. Furthermore, the cyclability test was conducted under 0.26 $mAcm^{-2}$. To measure the resistance, change during first lithiation process (first charge), an alternative current-electrochemical impedance spectroscopy (AC-EIS) was performed. The EIS spectra were recorded by Biologic VP-300 with the AC amplitude of 50 mV in the frequency ranging from 7 MHz to 100 Hz.

4.3. Results and discussion

The amorphous structure and ionic conductivity of 5.0×10^{-4} Scm^{-1} of the synthesized Li_3PS_4 were similar to those in previous reports[27], which were confirmed using XRD and EIS (Figure 1). The crystal structure of the LiI-coated graphite was examined using XRD (Figure 2). For all samples, all peaks are attributed to the graphite in space group $P6_3/mmc$[21,28]. The lattice parameters of the LiI-coated graphite estimated from the XRD patterns did not change as the amount of LiI increased, indicating that LiI was not incorporated into the graphite structure (Figure 3). The absence of LiI peaks in the XRD patterns implies that significantly small amount of LiI exists on the surface of the graphite, which will be discussed later with the Raman results. The morphology of the LiI-coated graphite was examined using SEM-EDX (Figure 4). As the amount of LiI increased from 0 to 5 wt%, the amount of iodide on graphite increased, while the morphology was maintained. However, 7 wt% LiI-coated graphite formed aggregates, containing small white particles, and had a morphology that was significantly different from those of the other samples. This might be attributed to the compaction effect of excess LiI[23]. Unfortunately, it was not possible to confirm whether LiI was coated at the edge or on the plane of the graphite through SEM. The Raman measurements were performed to detect LiI species on the graphite surface. In the Raman spectra (Figure 5), extremely small peaks, which have been observed for LiI and crystalline alkali metal iodide compounds[29], were observed at 50 and 200 cm^{-1} for 7 wt% LiI-coated graphite, but not for 0–5 wt% LiI-coated graphite because the amount of LiI on the graphite surface may be excessively small for detection.

The electrochemical performances of the LiI-coated graphite samples were evaluated, and the results are shown in Figures 6, 7, and 8. The charge and discharge performance of each sample was determined from its first charge and discharge curves (Figure 6(a)), and the dQ/dV plots obtained from Figure 6(a) are shown in Figure 8. After the first discharge, the uncoated graphite sample showed a discharge capacity of 248 $mAhg^{-1}$, at which the Coulombic efficiency was 90%, with four plateaus at approximately −0.62, −0.56, −0.52, and −0.43 V. These plateaus indicate the formation of a graphite intercalation compound with stages I, II, III, and IV[28]. Compared to the uncoated graphite sample, the LiI-coated graphite samples showed higher discharge capacities (252–348

$mAhg^{-1}$) and Coulombic efficiencies (96–98%) along with lower polarization at 1–5 wt% LiI (Figures 6(a) and 7). However, increasing the LiI content to 7 wt% decreased the discharge capacity (271 $mAhg^{-1}$) and Coulombic efficiency (97%), and increased the polarization. Furthermore, both rate performance and cyclability tests were performed (Figures 6(b) and (c)). Compared to the uncoated graphite sample, the 1–5 wt% LiI-coated graphite samples showed higher discharge capacities at a high current density (Figure 6(c)). However, increasing the amount of LiI to 7 wt% decreased the discharge capacity. This might be attributed to the excess aggregated crystalline LiI, as shown in Figures 3(i), 3(j), and 5. A detailed explanation for 7 wt% LiI-coated graphite is provided later. The relatively high discharge capacity of LiI-coated graphite remained for 30 cycles. These results show that the LiI coating improved the electrochemical performance of the graphite anode.

To clarify the mechanism of the improvement, we analyzed the interfacial resistance between the LiI-coated graphite and Li_3PS_4 sulfide SE during the first charge process using AC-EIS measurements. The Nyquist plots, fitting results obtained using a previously reported equivalent circuit model[16,30], and obtained interfacial resistances are shown in Figures 9, 10, and 11 and Table 1. As shown in Figure 9, the interfacial resistance of the uncoated graphite increased gradually during the middle stage of the charging process, and then, increased significantly toward the end. The interfacial resistances of the graphite coated with 1–5 wt% LiI at the early stage of charging decreased with increasing amount of LiI, and remained relatively constant during subsequent charge processes. In contrast, although the interfacial resistance of the 7 wt% LiI-coated graphite did not increase significantly during the first charge process, it was higher than those of the 3 and 5 wt% LiI-coated graphite at the early stage of charging. The decrease in the resistance at the early stage of charging for the 0–5 wt% LiI-coated graphite might be due to the good contact between the LiI and Li_3PS_4 SE[31]. However, the increase in the resistance at the early stage of charging for the 7 wt% LiI-coated graphite might be caused by the large amount of LiI with low ionic conductivity[23,25] (approximately 10^{-7} Scm^{-1}) based on the Raman spectroscopy results (Figure 5) and the aggregation of the graphite particles (Figure 4). This implies that the small amount of LiI provided a smooth path for the lithium ions between the graphite and electrolyte owing

to its ductility, which led to soft contact, while large amount of LiI on the graphite surface would hinder the mobility of lithium ions at the interface because of the low ionic conductivtiy[23, 25]. The increase in the resistance of the uncoated graphite could be due to a decrease in the electrochemically active surface area, caused by the reductive decomposition of Li_3PS_4, because it is theoretically unstable at the potential at which the intercalation of lithium ions into graphite occurs[19]. The LiI coating suppresses Li_3PS_4 decomposition because LiI is thermodynamically stable at the potential at which Li deposition/stripping occurs[19], thereby preventing increases of the interfacial resistance during the charging process. These results were in accordance with the electrochemical performance results.

Moreover, to investigate the effect of LiI coating for the short circuit caused by Li plating on graphite, we demonstrated a lithium deposition test, in which the cell voltage during charging is under the voltage of Li deposition, for the Li_3PS_4/uncoated graphite and the Li_3PS_4/5 wt% LiI coated graphite as shown in Figure 12. A short circuit behavior was observed in the uncoated graphite composite before providing the theoretical capacity (372 mAh g^{-1}) whereas it was observed in the 5 wt% LiI coated graphite after the theoretical capacity. This is probably because the decomposition of Li_3PS_4 on uncoated graphite increase the polarization and accelerate Li plating, whereas in LiI-coated graphite, the decomposition of Li_3PS_4 is suppressed by LiI, which suppresses the increase of the polarization and Li plating. This result indicates that LiI coating is effective for suppressing Li plating on graphite.

To examine the reductive decomposition of the Li_3PS_4 sulfide electrolyte during the first charge process, we performed P and S *K*-edge XAS measurements for the uncoated and 5 wt% LiI-coated graphite, which showed the best electrochemical performance. In the P *K*-edge XAS spectrum of the uncoated graphite, the peak intensity at approximately 2148 eV decreased, while a shoulder peak attributed to Li_3P was observed at approximately 2145 eV after full charge[26] (Figure 13(b)). In the S *K*-edge XAS spectrum of the uncoated graphite, the peak intensity at approximately 2471 eV decreased, while a peak attributed to Li_2S was observed at approximately 2472 eV after full charge. These results indicate that the Li_3PS_4 sulfide SE undergoes reductive decomposition during the charging process of the graphite anode[26]. In contrast, in the P

and S *K*-edge XAS spectra of the 5 wt% LiI-coated graphite, slight changes were observed after full charge. These results indicate that the LiI coating inhibited the reductive decomposition of the Li_3PS_4 sulfide SE.

Further, in order to examine the morphological change of the uncoated graphite and LiI coated graphite during first charging process, we conducted the X-ray computed tomography for the uncoated graphite and 5 wt% LiI coated graphite powders (Figure 14) and the uncoated graphite and 5 wt% LiI coated graphite composite after charging process (Figure 15). In the CT images, voids were observed for the both graphite particles (Figure 14). Compared to the uncoated graphite, the color of the surface of 5 wt% LiI coated graphite is bright, which is attributed to LiI because of the large absorption coefficient of X-ray, indicating that LiI covered the surface of graphite. In both graphites, voids were observed inside the graphite particles, and the LiI coating layer was limited to the graphite surface, indicating that LiI did not form in the voids inside the graphite particles. Therefore, the LiI coating might be effective to suppress an introduction of solid electrolyte into graphite anode during preparing composite electrode with solid electrolyte. In the CT images of the composites after charging process, a large dark region, in which X-ray absorption coefficient is small, was observed along the interface between Li_3PS_4 and graphite in Figure 15(a). This region may be attributed to decomposition products of Li_3PS_4 and/or formation of void associated with it, which in any case cause to poor lithium diffusion in the composite electrode. In contrast, the dark region along the interface between Li_3PS_4 and LiI coated graphite was not observed in the LiI 5wt% coated graphite composite (Figure 15(b)). These results indicate that the good contact between graphite and Li_3PS_4 is maintained after lithiation in the 5wt% LiI coated graphite composite.

Figure 16 was prepared after combining the above results. In the case of the uncoated graphite, because the lithium-ion intercalation potential is lower than the reduction limit of Li_3PS_4, the Li_3PS_4 around a graphite particle was reductively decomposed to Li_2S and Li_3P during the first charge process, similar to the interfacial reaction between the Li metal and sulfide SE. The lithium-ion conductivity of Li_2S is poor (approximately 10^{-9} Scm^{-1})[32], which increase the interfacial resistance between the graphite and Li_3PS_4. However, in the case of the LiI-coated graphite, the reductive

decomposition of Li_3PS_4 was suppressed, resulting in high power density. Finally, we demonstrate the performance of the full cells of 1 wt% $LiNbO_2$ coated $LiNi_{1/3}Co_{1/3}Mn_{1/3}O_2$ (NMC)// Li_3PS_4//uncoated graphite and NMC// Li_3PS_4//5 wt % LiI coated graphite as shown in Figure 17. The full cell with LiI 5wt% coated graphite composite showed lower polarization, lower irreversible capacity and higher discharge capacity during first cycling, compared to the full cell with uncoated graphite. Then, the full cell with LiI 5wt% coated graphite composite showed lower polarization and higher discharge capacity during second cycling compared to the full cell with uncoated graphite. These results clearly proved that suppression of reductive decomposition of Li_3PS_4 on graphite by LiI coating is effective to improve the performance of a full cell as well as a half cell. Moreover, we investigated the compatibility of LiI coated graphite for another solid electrolyte as shown in Figure 18. Under the Li_6PS_5Cl solid electrolyte system, the LiI 5wt% coated graphite composite demonstrated superior electrochemical performance than that of uncoated graphite composite. It is attributed to the effect of suppression of reductive decomposition of solid electrolyte by LiI on the graphite surface. Moreover, due to its higher ionic conductivity (1.2×10^{-3} Scm^{-1}) than that of Li_3PS_4 (5.0×10^{-4} Scm^{-1}), rate performance was significantly improved. This study revealed that coating a graphite surface with LiI could suppress the decomposition of sulfide SEs and improve the power density of ASSBs.

4.4. Conclusion

LiI-coated graphite was fabricated using a simple liquid-phase process. LiI was well dispersed on the graphite surface at 1–5 wt%, but not at 7 wt%. The graphite coated with 7 wt% LiI had an aggregated morphology, where large amount of LiI exists on the surface. Among the LiI-coated graphite samples, that with 5 wt% LiI showed the highest discharge capacity (348 $mAhg^{-1}$) with superior C-rate performance, while uncoated graphite showed a discharge capacity of 248 $mAhg^{-1}$. To understand the origin of the improved electrochemical properties, we conducted EIS during the first charge process. Because Li_3PS_4 is theoretically un-stable at the intercalation potential for lithium ions into graphite, the interfacial resistance increased, but gradually decreased with the increasing amount

of LiI coating. Furthermore, XAS results clearly show that Li_3PS_4 in the uncoated graphite composite decomposes into Li_2S and Li_3P, while the 5 wt% LiI-coated graphite composite was stable after lithiation and exhibited the highest discharge capacity (348 $mAhg^{-1}$). Our findings suggest that LiI can suppress the decomposition of a sulfide SE in a composite, leading to superior electrochemical performance, and that this coated graphite composite is compatible with most sulfide SEs that de-compose at low reduction potentials.

Reference

1. Sung-wook, K.; Dong-Hwa, S.; Xiaohua, M.; Gebrand, C.; Kisuk K. Electrode Materials for Rechargeable Sodium–Ion Batteries: Potential Alternatives to current Lithium–Ion Batteries, *Adv. Energy Mater.*, **2012**, 2, 710–721.
2. Yanhan, Y.; Qu, W.; Yanhua C.; Yongchang, C.; Siqi, S.; Ru-Zhi, W.; Hui, Y. Elastic Properties, Defect Thermodynamics, Electrochemical Window, Phase Stability, and Li^+ Mobility of Li_3PS_4: Insight from First-Principles Calculations, *ACS Appl. Mater. Interfaces*, **2016**, 6, 38, 25229–25242.
3. Peng-Jie, L.; Bo-Sheng, Z.; Lian-Qi, Z.; Ning, X.; Meng-Tao, W.; Xue-Ping, H. Inorganic sulfide solid electrolytes for all-solid-state lithium secondary batteries, *J. Mater. Chem. A.*, **2019**, 7, 20540–20557.
4. Yong-Gun, L.; Satoshi, F.; Changhoon, J.; Naoki, S.; Nobuyuki, Y.; Ryo, O.; Dong-Su, K.; Tomoyuki, S.; Toshinori, S.; Saebom, R.; Jun Hwan, K.; Taku, W.; Yongsin, P., Yuichi, A., Dongmin, I.; In Taek, H. High-energy long-cycling all-solid-state lithium metal batteries enabled by silver-carbon composite anode, *Nat. Energy*, **2020**, 5, 299–308.
5. Atsushi, S.; Tomonari, T.; Hironori, K. Electrode morphology in all-solid-state lithium secondary batteries consisting of $LiNi_{1/3}Co_{1/3}Ni_{1/3}O_2$ and Li_2S-P_2S_5 solid electrolyte, *Solid State Ionics*, **2016**, 285, 112–117.
6. Reona, M.; Narumi, O.; Tsuyoshi, O.; Isao, S.; Kazunori, T. An amorphous Si film anode for all-solid-state lithium batteries, *J. Power source*, **2014**, 272, 541–545.

7. Rinlee, C.; Naoki, S.; Tsuyoshi, O.; Minoru, O.; Kazutaka, M.; Takayoshi, K.; Kazunori, T. High performance silicon–based anodes in solid–state lithium batteries, *Energy Environ. Sci.*, **2014**, 7, 662–666.
8. Cheng, W.; Xiaolin, S.; Li, Y.; Depeng, S.; Yue, W.; Takeo, O.; Futoshi, M.; Jianfei, W. In Situ Ion–Conducting Protective Layer Strategy to Stable Lithium Metal Anode for All–Solid–State Sulfide–Based Lithium Metal Batteries, *Adv. Mater. Interfaces*, **2021**, 8, 2001698–2001708.
9. Kazunori, T.; Taro, I.; Akihisa, K.; Hideki, S.; Shigeo, K.; Mamoru, W.; Masahiro, M.; Ryoji, K. Solid-state lithium battery with graphite anode, *Solid State Ionics*, **2003**, 158, 269 – 274.
10. Yoshikatsu, S.; Kazunori, T.; Bong Chull, K.; Lianqi, Z.; Narumi, O.; Hiroyuki, W.; Minoru, O.; Takayoshi, S. Synthesis of phosphorous sulfide solid electrolyte and all-solid-state lithium batteries with graphite electrode, *Solid State Ionics*, **2005**, 176, 2389–2293.
11. Charles, C.; Wenzhi, L. A review of application of carbon nanotubes for lithium ion battery anode material, *J. Power Sources*, **2012**, 208, 74–85.
12. Misae, O.; Hiroe, K.; Atsushi, S.; Masahiro, T.; Akitoshi, H. *Operando* Confocal Microscopy for Dynamic Changes of Li^+ Ion Conduction Path in Graphite Electrode Layers of All-Solid-State Batteries, *J. Phys. Chem. Lett.* **2020**, 11, 990 –904.
13. Misae, O.; Atsushi, S.; Akitoshi, H.; Masahiro, T. Optical microscopic observation of graphite composite negative electrodes in all-solid-state lithium batteries, *Solid State Ionics*, **2018**, 323, 123–129.

14. Laura, H.; Franziska, J.; Camelia, B.; Thomas, H.; Claire, V.; Vincent, P.; Christian, J.; Mario, K.; Petr, N. Study of Graphite Cycling in Sulfide Solid Electrolytes, *J. Electrochem. Soc.*, **2020**, 167, 110558–1105568.
15. Laura, H.; Camelia, B.; Thomas, H.; Federica, M.; Christian, S.; Vincent, P.; Christian, J.; Claire, V.; Mario, K.; Petr, N. Performance-limiting factors of graphite in sulfide-based all-solid-state lithium-ion batteries, *Electrochem. Acta*, **2021**, 389, 138735-138745.
16. Giovanna, M.; Akiko, T.; Naoki, S.; Tomoyuki, T.; Yuichi, A.; Maria, N. Improvement of Graphite Interfacial Stability in All-Solid-State Cells Adopting Sulfide Glassy Electrolytes, *ChemElectroChem*, **2021**, 8, 689–696.
17. Dave, A.; Holger, H.; Peter, L.; Filippo, M.; Barbara, S. Future high-energy density anode materials from an automotive application perspective, *J. Mater. Chem. A*, **2017**, 5, 17174–17198.
18. Sivakkumar, S. R.; Nerkar, J. Y.; Pandolfo A.G. Rate capability of graphite materials as negative electrodes in lithium-ion capacitors, *Electrochem. Acta*, **2015**, 55, 3330–3335.
19. Yizhou, Z.; Xingfeng, H.; Yifei, M. Origin of Outstanding Stability in the Lithium Solid Electrolyte Materials: Insight from thermodynamic Analyses Based on First-Principles Calculations, *ACS Appl. Mater. Interfaces*, **2015**, 7, 23685–23693.
20. Misae, O.; Motoshi, S.; Chie, H.; Hiroe, K.; Yoshihiro, T.; Koichiro, I.; Atsushi, S.; Masahiro, T.; Akitoshi, H. Visualization and control of Chemically induced Crack Formation All-Solid-State Lithium-Metal Batteries with Sulfide Electrolyte, *ACS Appl. Mater. Interfaces*, **2021**, 13, 4, 5000–5007.

21. Fei, D.; Wu, X.; Daiwon, C.; Wei, W.; Xiaolin, L.; Mark, E.; Xilin, C.; Zhenguo, Y.; Ji–Guang, Z. Enhanced performance of graphite anode materials by AlF_3 coating for lithium-ion batteries, *J. Mater. Chem. A*, **2012**, 22, 12745–12751.
22. Dae Sik, K.; Yeong Eun, K.; Hansu, K. Improved fast charging capability of graphite anodes via amorphous Al_2O_3 coating for high power lithium ion batteries, *J. Power Sources*, **2019**, 422, 18–24.
23. Atsutaka, K.; Mirai, Y.; Atsushi, S.; Akitoshi, H.; Masahiro, T. Mechanical Properties of Li_2S-P_2S_5 glasses with Lithium Halide and Application in All-Solid-State Batteries, *ACS Appl. Energy Mater.*, **2018**, 1, 1002–1007.
24. Seon–Joo, C.; Sun–Hwa, C.; Anh, B.; You–Jin, L.; Sang–Min, L.; Heon–Cheol, S.; Yoon–Cheol, H. LiI-Doped Sulfide Solid Electrolyte: Enabling a High-Capacity Slurry-Cast Electrode by Low-Temperature Post-Sintering for Practical All-Solid-State Lithium Batteries, *ACS Appl. Mater. Interfaces*, **2018**, 10, 31404–31412.
25. Ysbrand, H. THE IONIC CONDUCTIVITY OF Li–HALIDE CRYSTALS, *Recl. Trav. Chim. Pays-Bas.*, **1950**, 69, 1471–1480
26. Masakuni, T.; Toshiki, W.; Kentaro, Y.; Koji, O.; Atsushi, S.; Takuya, K.; Seunghoon, Y.; Koji, N.; Tomoki, U.; Masao, K.; Akitoshi, H.; Masahiro, T.; Yoshiharu, U.; Investigation of the Suppression of Dendritic Lithium Growth with a Lithium-Iodide-Containing Solid Electrolyte, *Chem. Mater.*, **2021**, 33, 4907–4914.
27. Kentaro, Y.; Seunghoon, Y.; Masakuni, T.; Koji, O.; Tomoki, U.; Toshiki, W.; Atsushi, S.; Akitoshi, H.; Masahiro, T.; Hiroyuki, M.; Atsunori, M.; Yoshiharu, U. High Ionic Conductivity of Liquid-Phase-Synthesized Li_3PS_4 Solid Electrolyte, Comparable to That of Obtained via Ball Milling, *ACS Appl. Energy Mater.*, **2021**, 4, 2275–2281.

28. Annadanesh, S.; Venroy, W.; Daniel, A.; Egwu, K.; Jeffrey, R.; Richard, J.; Junsheng, Z.; Jim, Z. Investigation of Pre-lithiation in Graphite and Hard-Carbon Anodes Using Different Lithium Source Structure, *J. Electrochem. Soc.*, **2017**, 164, 3914–3924.
29. Rita, C.; Eric, P.; Lucie, G.; Pierre, F.; Jean, B.; Delphine, V.; Daniel, N. Iodine solubility and speciation in glasses, *Sci. Rep.*, **2019**, 9, 7758–7771.
30. John, I.; Derek, S.; Anthony, W. Electroceramics: Characterization by Impedance Spectroscopy, *Adv. Mater.*, **1990**, 2, 132–138.
31. Yushi, F.; Yusuke, K.; Takeaki, I.; Takuya, K.; Atsuhi, S.; Masahiro, T.; Akitoshi, H. Amorphous Li_2O-LiI Solid Electrolytes compatible to Li Metal, *Electrochemistry*, **2021**, 89, 334–336.
32. Altorfer, F.; Bührer, W.; Anderson, I.; Scharpf, O.; Bill, H.; Pierre, C.; H. Smith. Lithium diffusion in the superionic conductor Li_2S, *Phys.B.*, **1992**, 180, 795–797

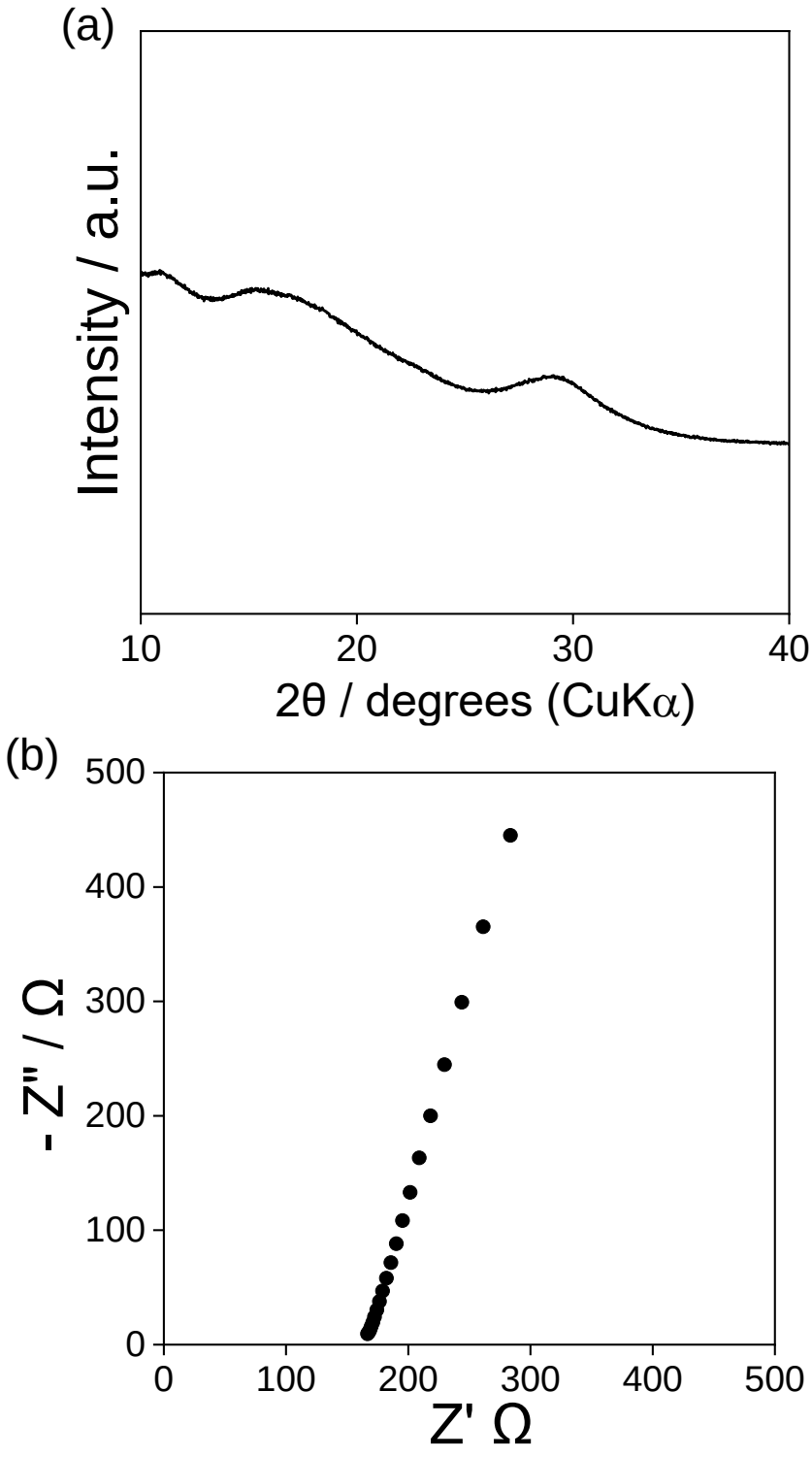

Figure 1. XRD patterns (a) and Nyquist plot (b) for prepared Li_3PS_4.

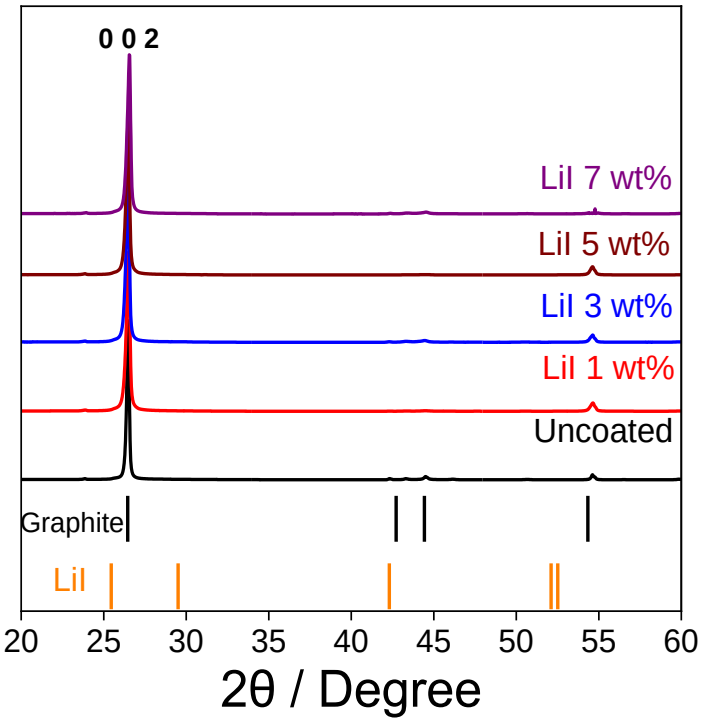

Figure 2. X-ray diffraction for the graphite and coated graphite powers according to LiI 0, 1, 3, 5, and 7 wt%.

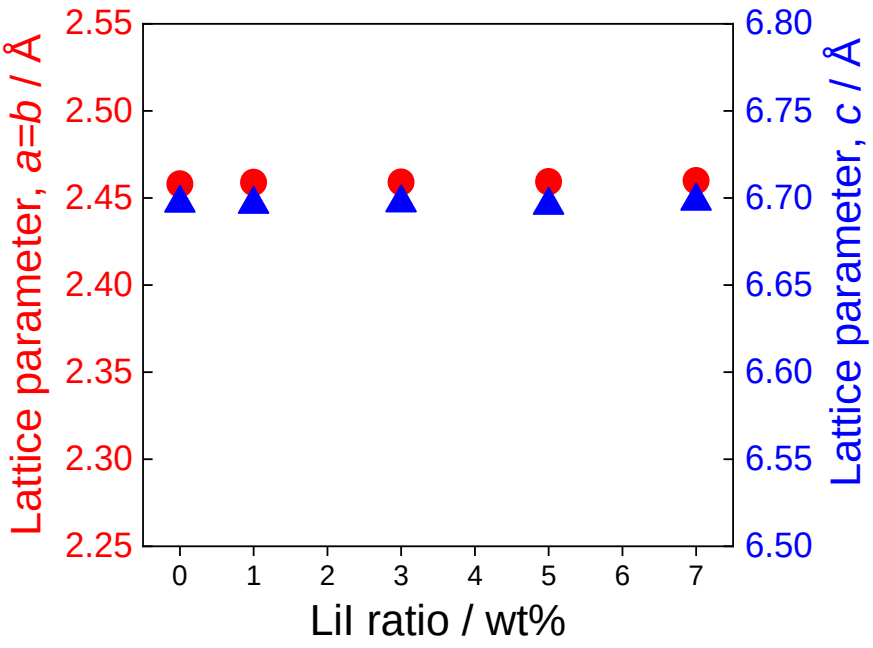

Figure 3. Rietveld refinement results, based on measured XRD patterns, for the lattice parameter, Å, of the graphite powders with Lithium iodide contents.

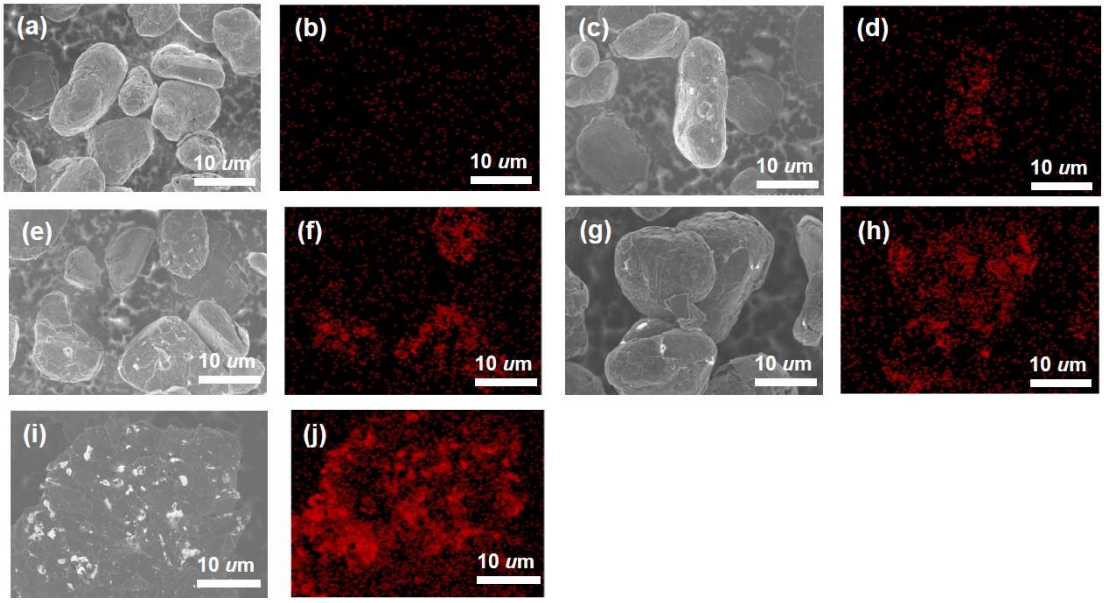

Figure 4. SEM and EDX mapping images for the graphite composites: (a-b) uncoated, (c-d) 1 wt%, (e-f) 3 wt%, (g-h) 5 wt%, and (i-j) 7 wt% coated graphite morphology.

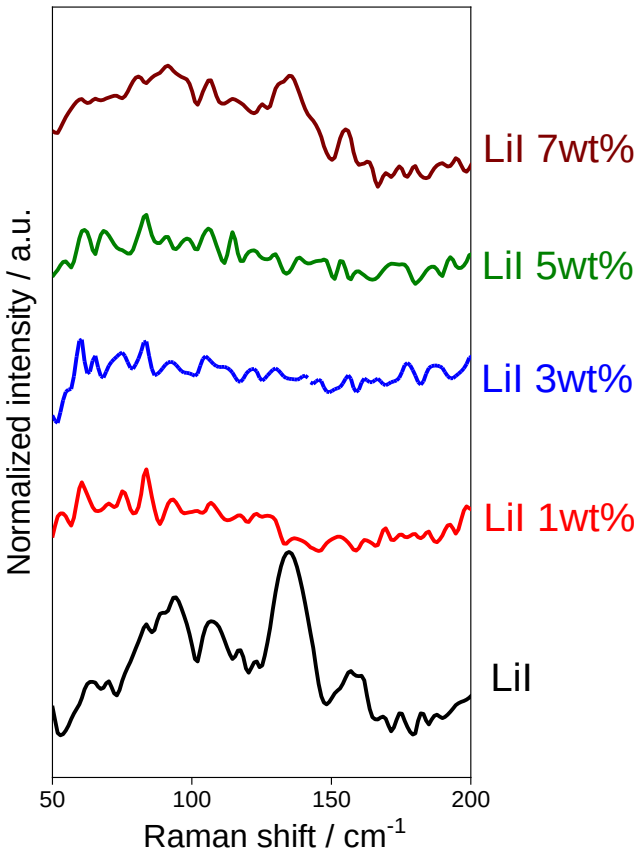

Figure 5. Raman spectra in the range from 50 to 200 cm^{-1} corresponding to crystalline lithium iodide.

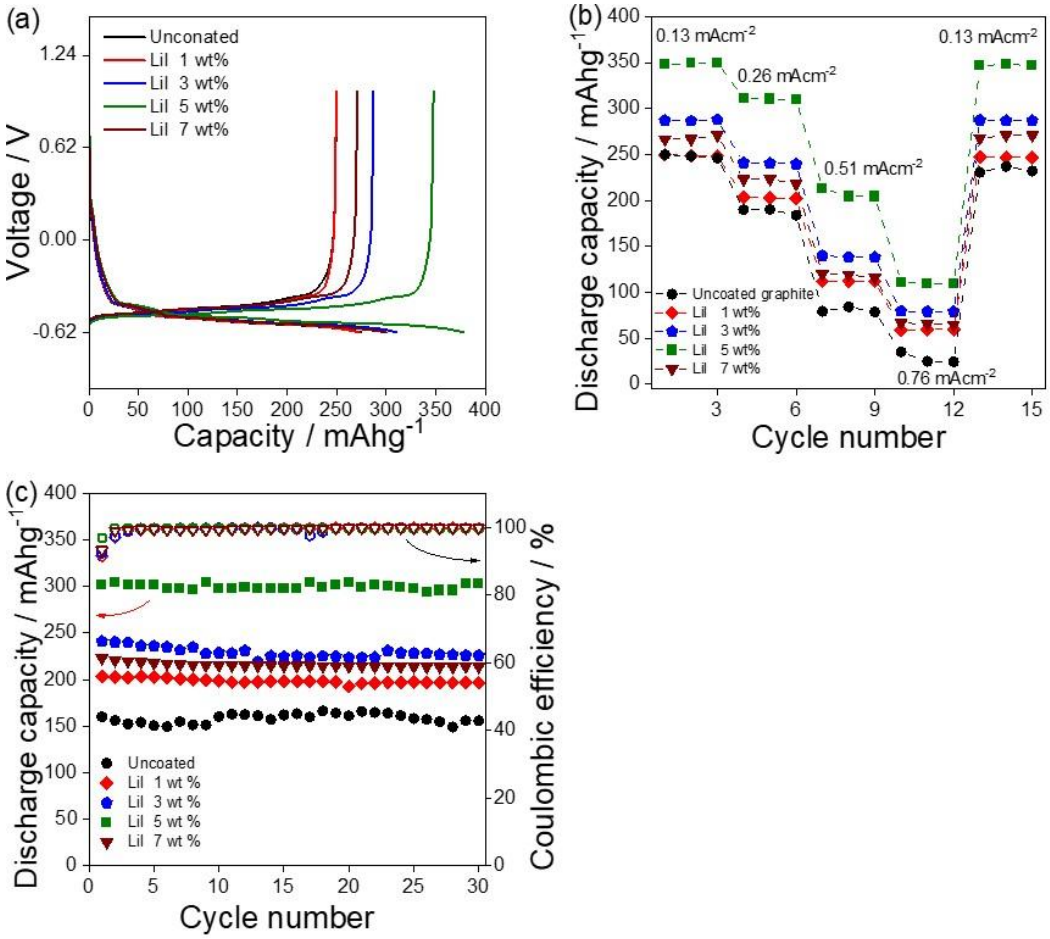

Figure 6. First charge-discharge profiles under 0.13 $mAcm^{-2}$ for each graphite composite (a), Rate performance at each current density (b), Cyclability and coulombic efficiency under 0.26 $mAcm^{-2}$ at 25 °C (c).

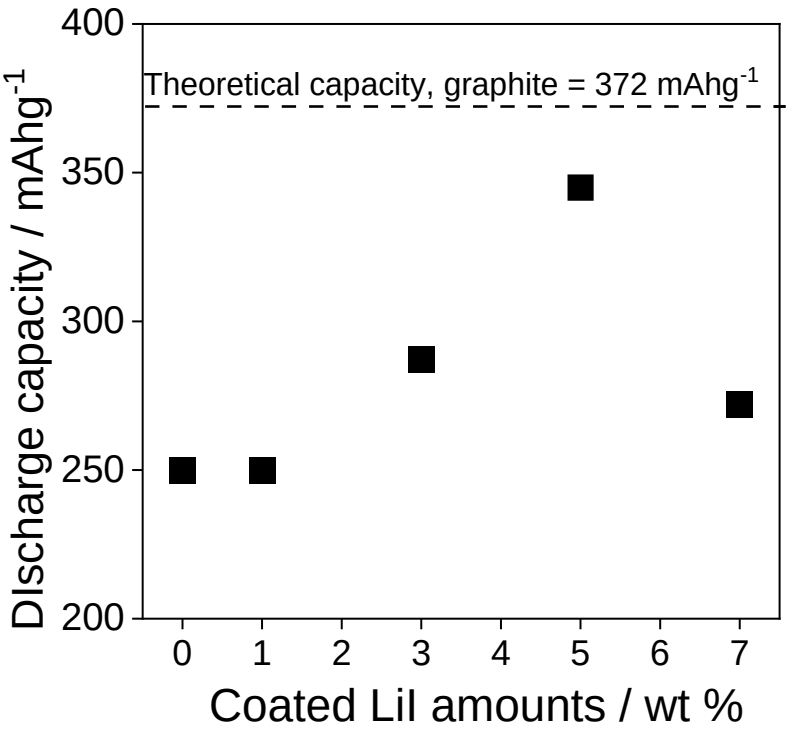

Figure 7. First discharge capacity for the LiI coated graphites under the current density of 0.13 $mAcm^{-2}$ at 25 °C.

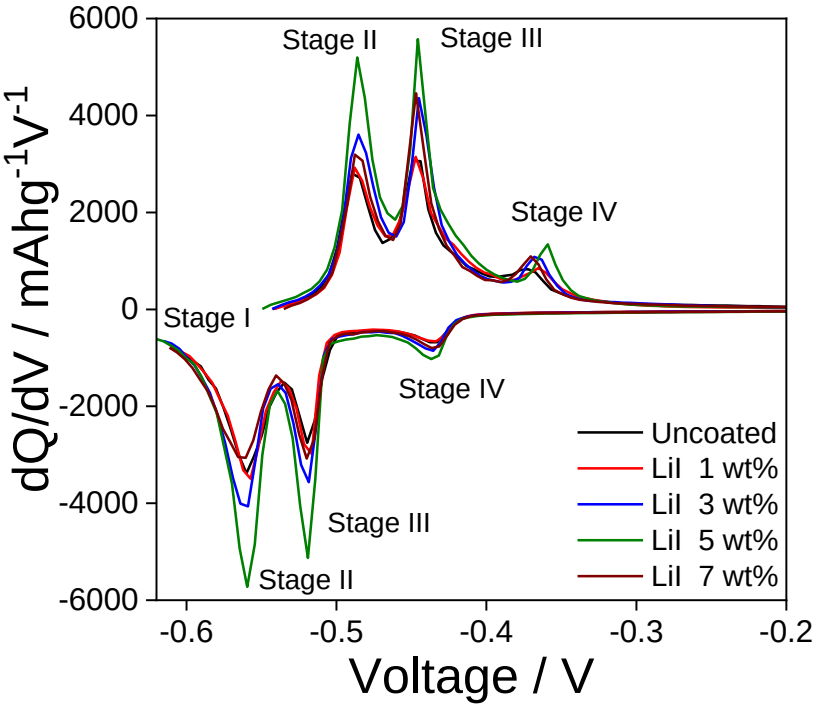

Figure 8. Total scale dQ/dV plots corresponding to 1st charge and discharge of each graphite composite with LiI amounts under the current density of 0.13mAcm^{-2} at 25 °C.

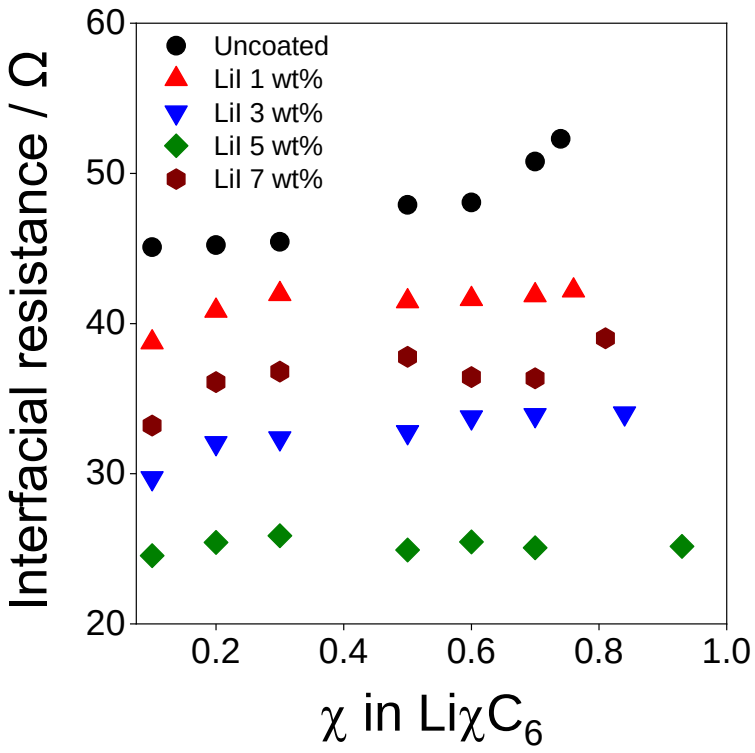

Figure 9. Interface resistance behaviors of uncoated and LiI-coated graphite during first lithiation process.

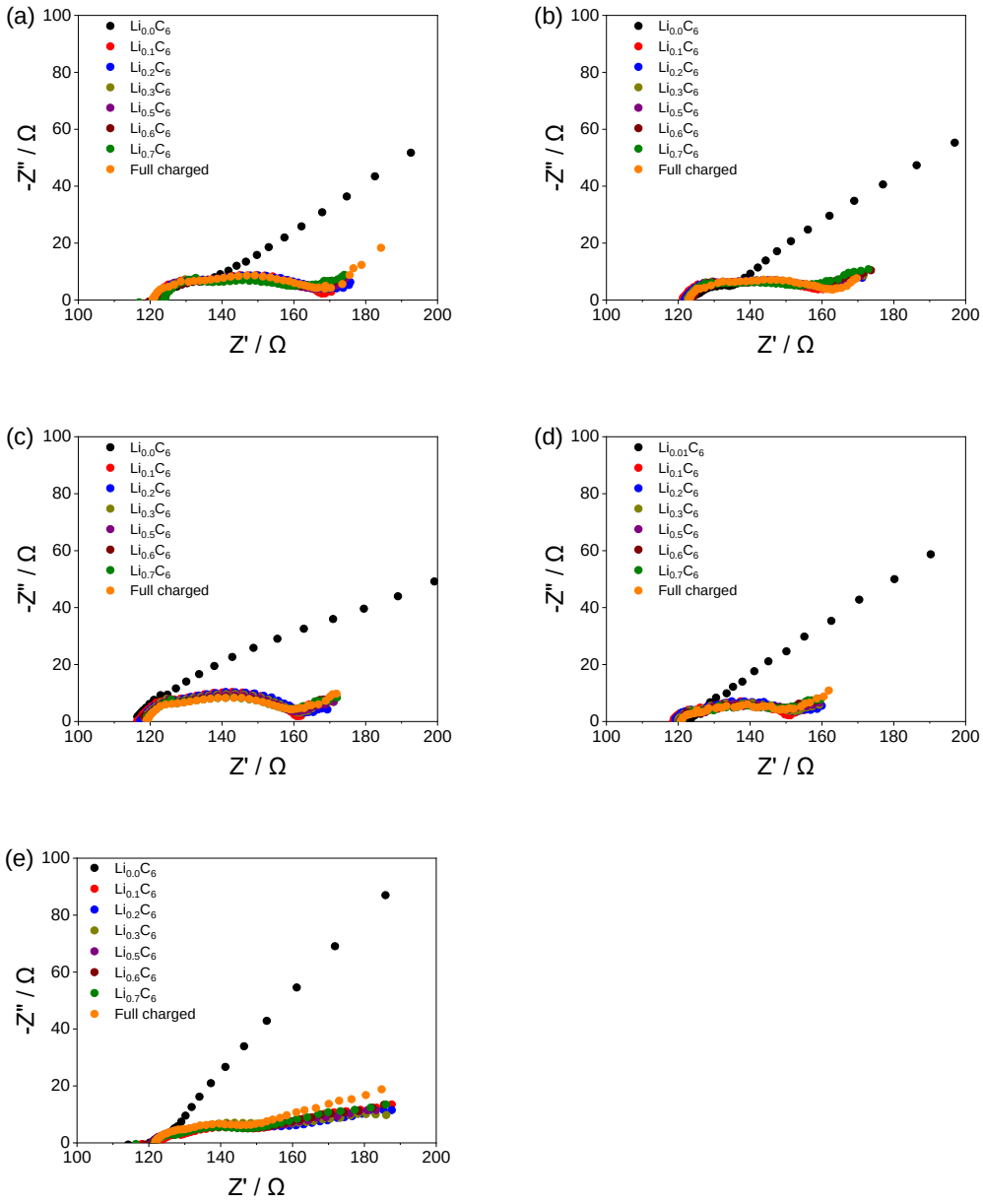

Figure 10. Nyquist plot behaviors during each lithiation process under 0.10 $mAcm^{-2}$ (0.05 C) at 25 °C, (a) Uncoated, (b) LiI 1 wt%, (c) LiI 3 wt%, (d) LiI 5 wt%, and (e) LiI 7 wt%.

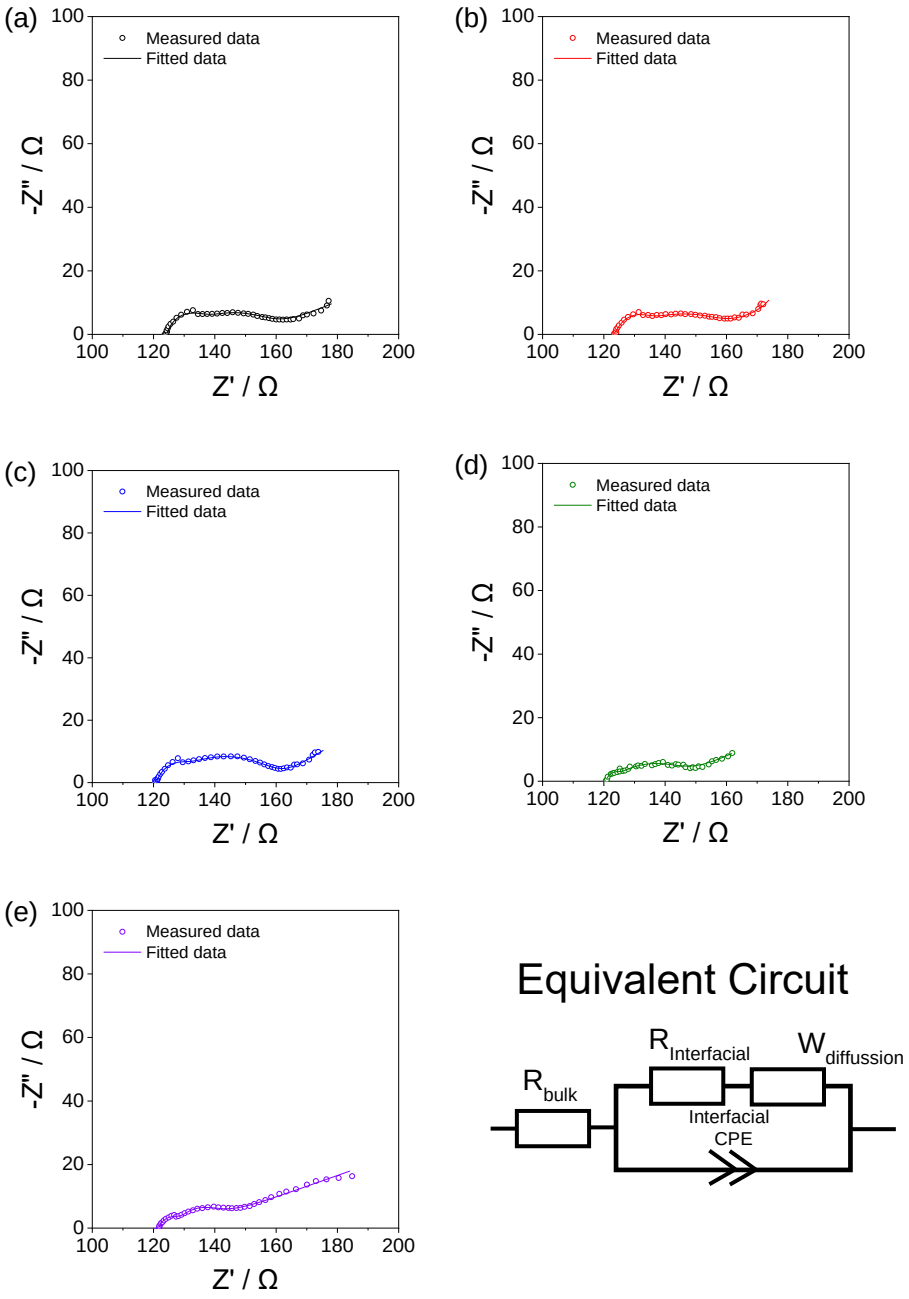

Figure 11. Fitted results for the uncoated (a) LiI 1 wt%, (b) LiI 3 wt%, (c) LiI 5 wt%, (d), and LiI 7 wt% (e) based on equivalent circuit model.

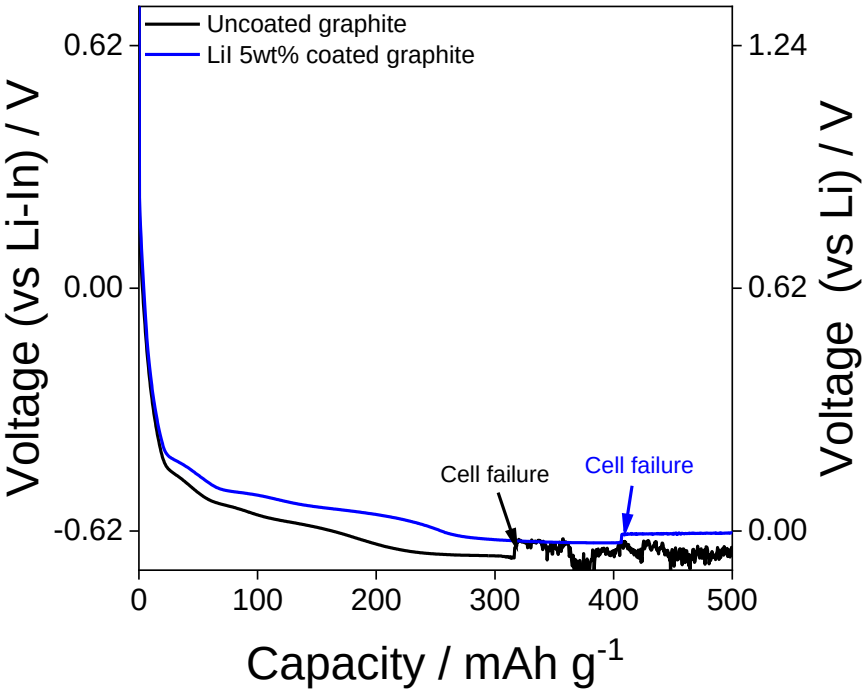

Figure 12. Voltage profiles of Li deposition for uncoated graphite composite (Black line) and LiI 5wt% coated graphite composite (blue line) under 0.23 $mAcm^{-2}$ at 25 ºC.

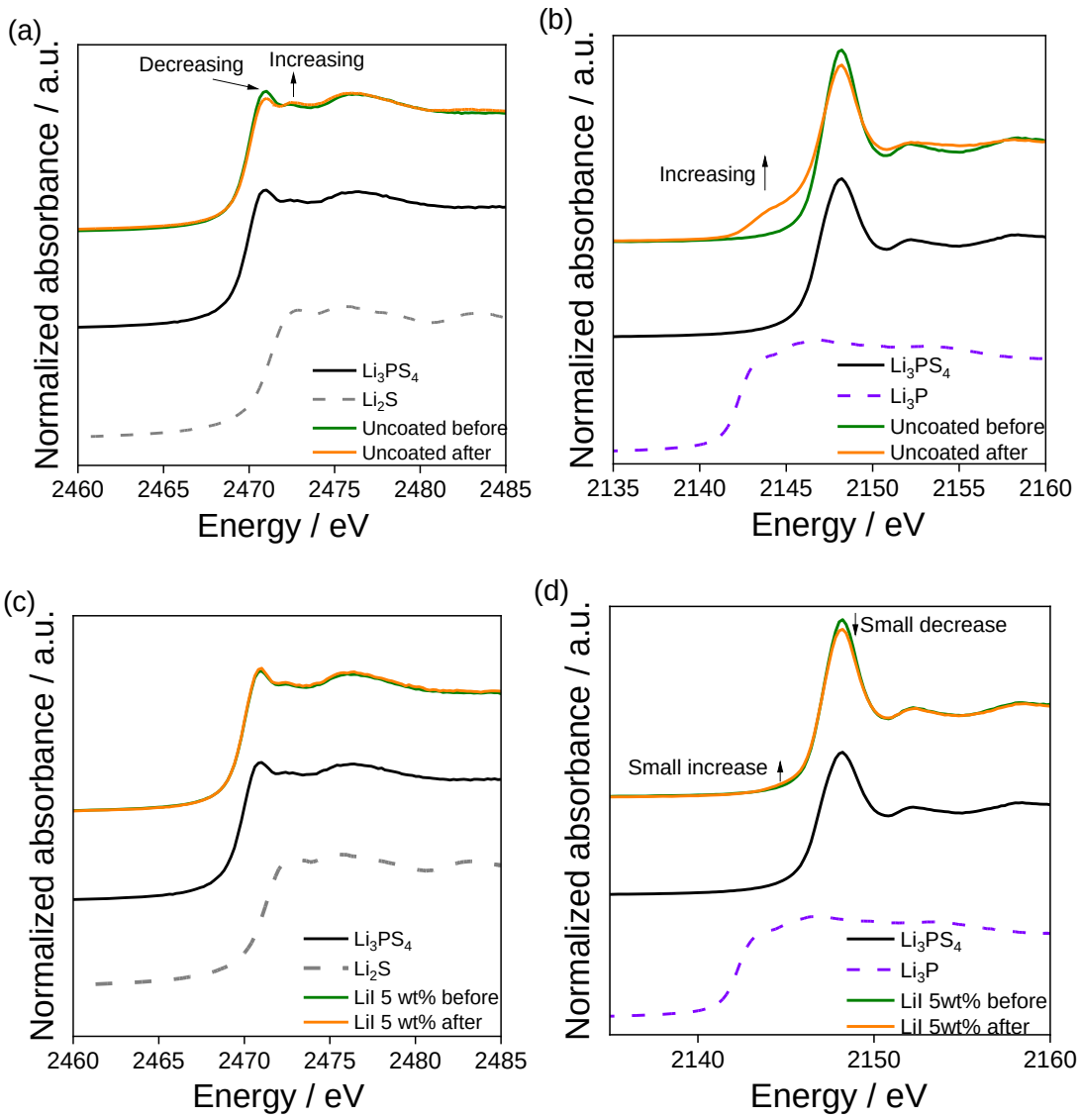

Figure 13. S, P K edge for uncoated graphite composite (a – b) and LiI 5wt% coated graphite composite (c-d) before and after the lithiation.

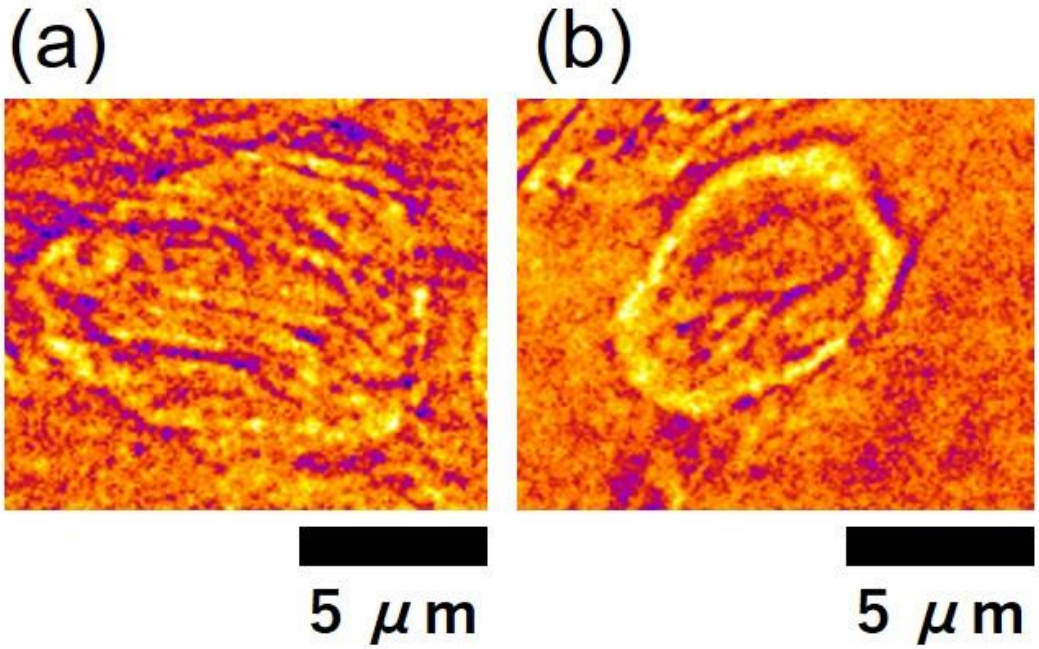

Figure 14. X-ray computed tomography images for (a) uncoated graphite and (b) LiI 5 wt% coated graphite. The X-ray CT measurements were carried out at BL20XU on the SPring-8 using a transmission X-ray microscope with 30 keV of a monochromatic X-ray beam. The X-ray beam was focused onto the sample using an elliptical glass capillary and the images were projected onto a scintillator using a Fresnel zone plate. The images were also recorded using a charge-coupled device camera (2048 × 2048 pixels). The image with a voxel size of 32 nm and a 65 × 65 μm^2 field of view was measured. 1800 radiographs were collected using an exposure time of 500 ms during 180° rotation.

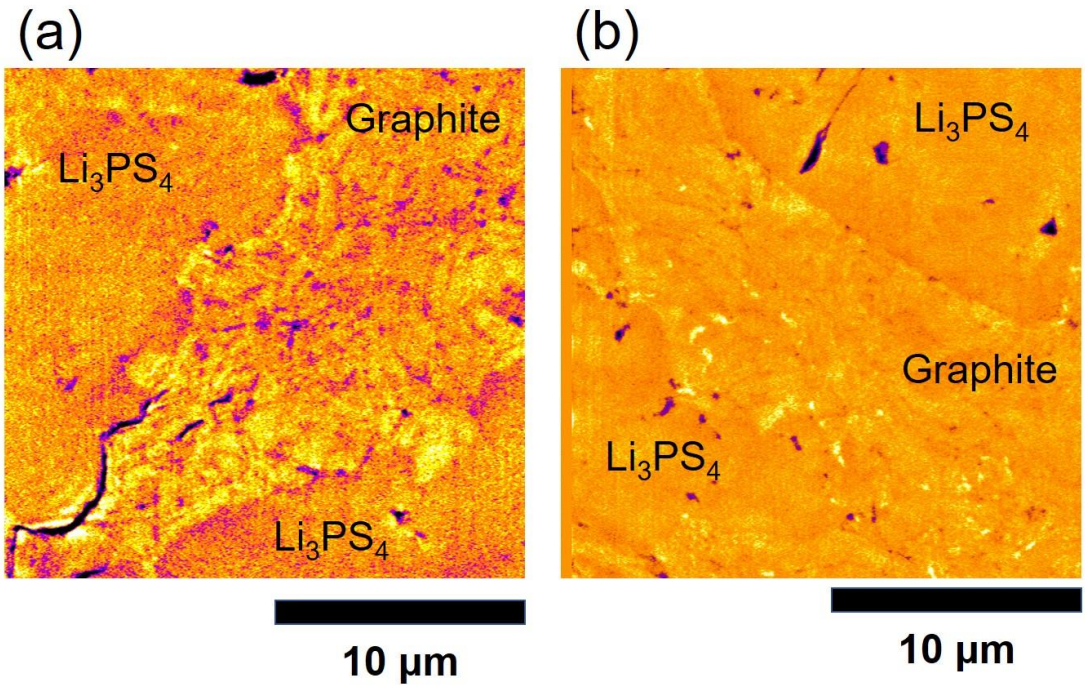

Figure 15. X-ray CT images for (a) uncoated graphite composite and (b) LiI 5wt% coated graphite composite after first charging. A large dark region, in which X-ray absorption coefficient is small, was observed along the interface between Li_3PS_4 and graphite in (a). This region may be attributed to decomposition products of Li_3PS_4 and/or formation of void associated with it, which in any case cause to poor lithium diffusion in the composite electrode. In contrast, the dark region along the interface between Li_3PS_4 and LiI coated graphite was not observed in the LiI 5wt% coated graphite composite (Figure 15(b)).

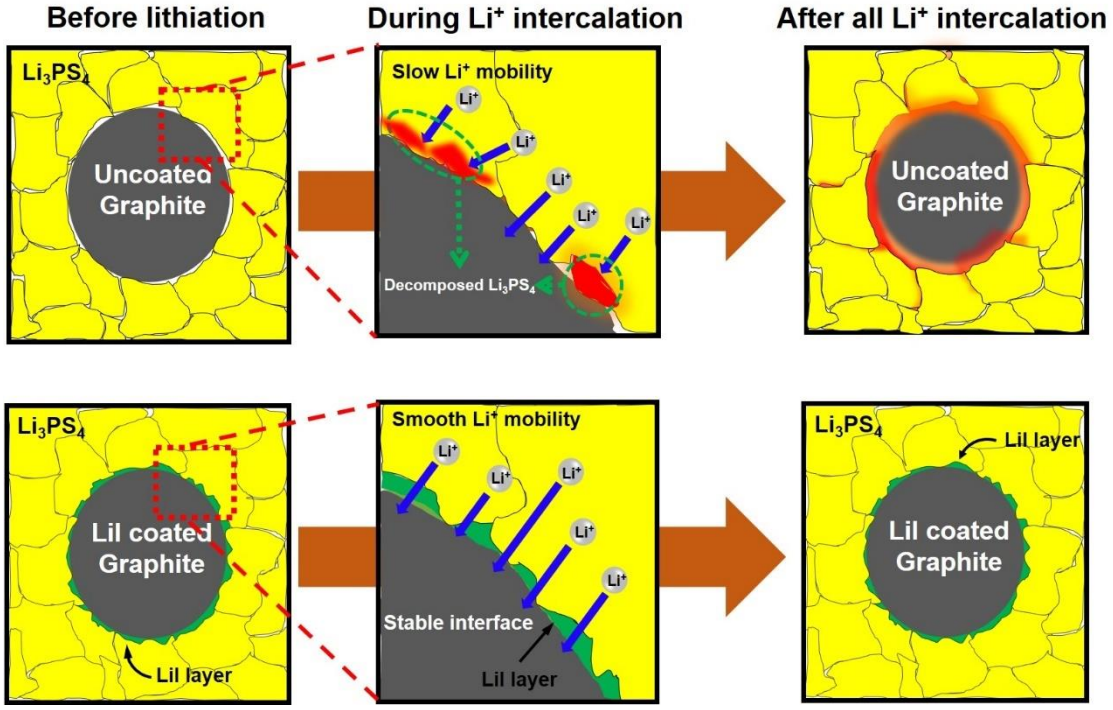

Figure 16. Schematics for the LiI coating effect on the graphite surface. It demonstrates that the suppression effect of LiI coating on the graphite surface, in which the Li_3PS_4 around graphite particles in the composite is begun to be decomposed but, it is suppressed that the decomposition of Li_3PS_4 at LiI (green) coated graphite composite when the lithiation process was started.

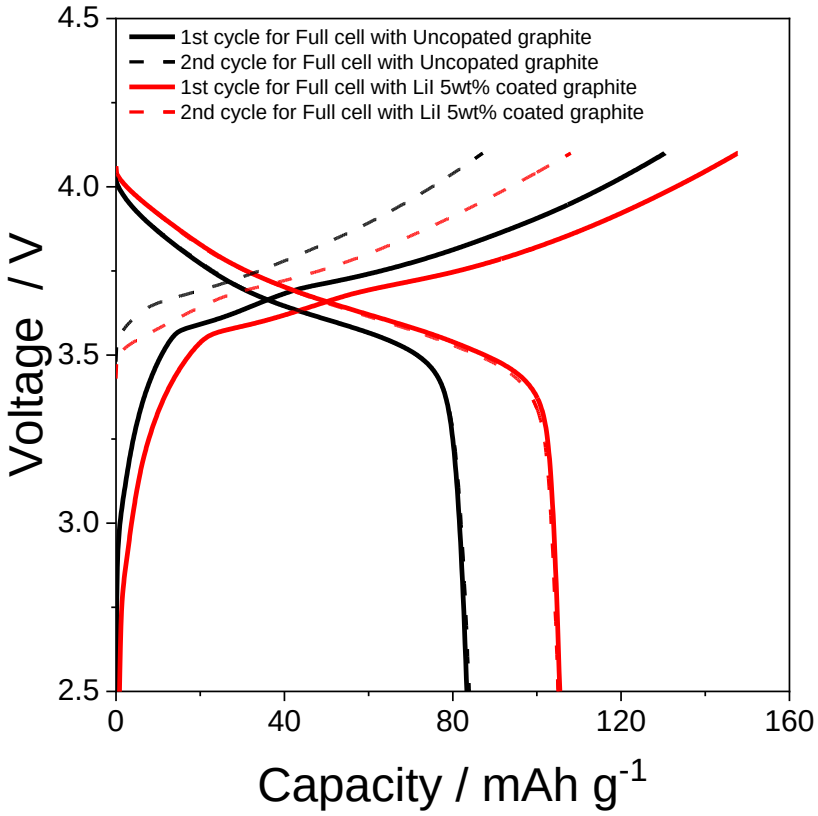

Figure 17. First cycle charge discharge of full cells corresponding to the uncoated graphite and LiI 5 wt% coated graphite under 0.05 C at 25 ºC, in which the cell operation was conducted under the 0.05C and cut off voltage was 2.5 to 4.1 V. A cathode composite electrode was prepared by mixing with 1 wt% $LiNbO_2$ coated $LiNi_{1/3}Co_{1/3}Mn_{1/3}O_2$ (NMC) and Li_3PS_4 (LPS) and in the ratio of 70 wt% : 30 wt%.

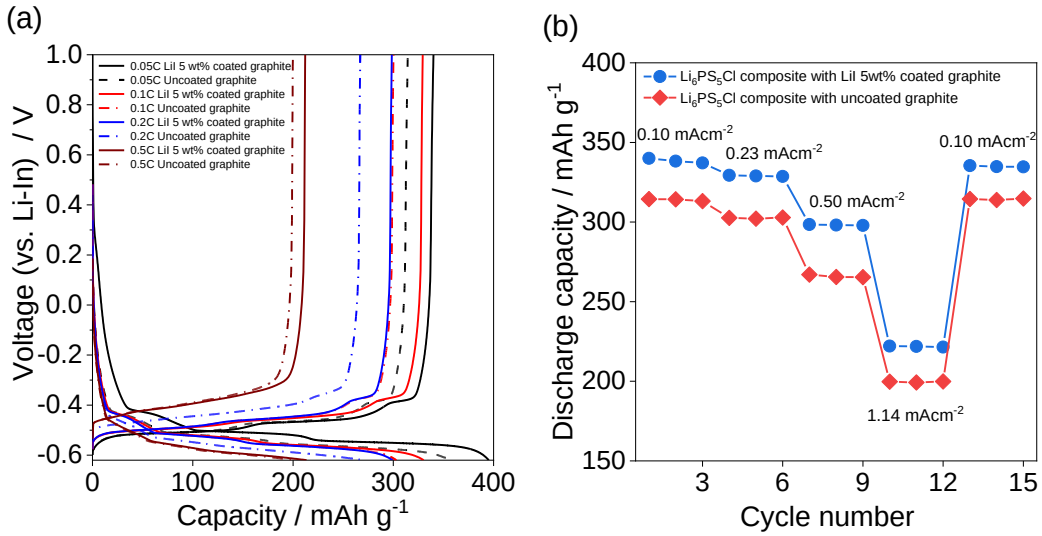

Figure 18. (a) First cycle charge-discharge for LiI 5wt% coated graphite composite with Li_6PS_5Cl, and (b) Rate performance compared with that with Li_3PS_4.

Table 1. Impedance parameters for each sample according LiI coating amounts based on the fitting process with obtained Nyquist plots

Uncoated	$Li_{0.1}C_6$	$Li_{0.2}C_6$	$Li_{0.3}C_6$	$Li_{0.5}C_6$	$Li_{0.6}C_6$	$Li_{0.7}C_6$	$Li_{0.75}C_6$
R_{bulk} / Ω	123.1	123.2	122.1	124.1	125.9	125.5	125.6
$R_{interfacial}$ / Ω	45.09	45.22	45.44	47.09	48.06	50.79	52.3
CPE–T	0.000164	0.000133	0.000277	0.00377	0.00504	0.00529	0.00738
CPE–P	0.536	0.556	0.486	0.461	0.433	0.430	0.397
Capacitance / F	2.35×10^{-6}	2.26×10^{-6}	2.69×10^{-6}	3.42×10^{-6}	3.89×10^{-6}	4.38×10^{-6}	5.25×10^{-6}
W-R	31.33	34.33	32.79	31.39	32.12	34.97	38.9
W-T	32.8	30.6	31.5	27.43	32.3	30.0	29.5
W-P	0.5	0.5	0.5	0.5	0.5	0.5	0.5

LiI 1 wt%	$Li_{0.1}C_6$	$Li_{0.2}C_6$	$Li_{0.3}C_6$	$Li_{0.5}C_6$	$Li_{0.6}C_6$	$Li_{0.7}C_6$	$Li_{0.76}C_6$
R_{bulk} / Ω	121.2	121.6	122.1	122.9	123.5	124.5	125.2
$R_{interfacial}$ / Ω	38.75	40.85	41.96	41.48	41.63	41.88	42.20
CPE–T	0.00301	0.00342	0.00378	0.00392	0.00414	0.00396	0.00327
CPE–P	0.515	0.501	0.486	0.479	0.470	0.473	0.496
Capacitance / F	4.59×10^{-6}	4.87×10^{-6}	4.72×10^{-6}	4.45×10^{-6}	4.26×10^{-6}	4.12×10^{-6}	4.18×10^{-6}
W-R	33.9	31.6	27.7	29.5	29.2	34.2	36.0
W-T	28.7	20.7	25.7	25.9	25.8	27.4	28.5
W-P	0.5	0.5	0.5	0.5	0.5	0.5	0.5

LiI 3 wt%	$Li_{0.1}C_6$	$Li_{0.2}C_6$	$Li_{0.3}C_6$	$Li_{0.5}C_6$	$Li_{0.6}C_6$	$Li_{0.7}C_6$	$Li_{0.84}C_6$
R_{bulk} / Ω	120.1	120.2	117.3	118.5	119.8	121.1	122.5
$R_{interfacial}$ / Ω	29.71	32.04	32.36	32.77	33.76	33.90	34.02
CPE–T	0.000480	0.000565	0.000479	0.000377	0.000443	0.000376	0.000349
CPE–P	0.442	0.431	0.449	0.461	0.455	0.472	0.478
Capacitance / F	2.26×10^{-6}	2.82×10^{-6}	2.86×10^{-6}	2.20×10^{-6}	2.86×10^{-6}	2.84×10^{-6}	2.75×10^{-6}
W-R	24.5	24.6	23.9	25.3	25.9	29.5	31.4
W-T	13.4	12.7	12.1	12.4	13.0	13.9	13.8
W-P	0.5	0.5	0.5	0.5	0.5	0.5	0.5

LiI 5 wt%	$Li_{0.1}C_6$	$Li_{0.2}C_6$	$Li_{0.3}C_6$	$Li_{0.5}C_6$	$Li_{0.6}C_6$	$Li_{0.7}C_6$	$Li_{0.96}C_6$
R_{bulk} / Ω	118.2	119.3	119.1	119.9	119.1	119.7	120.3
$R_{interfacial}$ / Ω	24.54	25.43	25.87	24.92	25.45	25.07	25.16
CPE–T	0.00131	0.00172	0.00169	0.00226	0.00270	0.00293	0.00187
CPE–P	0.442	0.402	0.402	0.366	0.344	0.333	0.387
Capacitance / F	1.70×10^{-5}	1.63×10^{-5}	1.60×10^{-5}	1.52×10^{-5}	1.64×10^{-5}	1.59×10^{-5}	1.49×10^{-5}
W-R	23.3	20.9	24.0	26.1	23.5	26.5	28.4
W-T	9.63	9.01	8.5	7.56	7.27	6.61	6.84
W-P	0.5	0.5	0.5	0.5	0.5	0.5	0.5

LiI 7 wt%	$Li_{0.1}C_6$	$Li_{0.2}C_6$	$Li_{0.3}C_6$	$Li_{0.5}C_6$	$Li_{0.6}C_6$	$Li_{0.7}C_6$	$Li_{0.81}C_6$
R_{bulk} / Ω	119.7	120.2	120.6	121.8	122.0	122.8	123.5
$R_{interfacial}$ / Ω	33.2	36.1	36.8	37.8	36.4	36.4	39.0
CPE-T	0.000890	0.000753	0.000992	0.00123	0.00165	0.00164	0.00213
P	0.441	0.482	0.435	0.400	0.396	0.383	0.329
Capacitance / F	1.03×10^{-5}	1.56×10^{-5}	1.34×10^{-5}	1.24×10^{-5}	2.47×10^{-5}	1.06×10^{-5}	1.33×10^{-5}
W-R	109.5	104.2	94.96	102	99.31	102.4	97.62
W-T	14.4	13.8	14.9	15.5	15.8	14.4	17.9
W-P	0.5	0.5	0.5	0.5	0.5	0.5	0.5

Chapter 5. Internal Phenomena of Graphite Composite Anode for All-Solid-State Batteries *via Operando* X-ray Computed Tomography

Recently, all-solid-state batteries (ASSBs) equipped with inorganic solid electrolyte have been a lot of attention as next generation batteries due to its safety and theoretically high energy and power density. In order to utilize these advantages of ASSBs, graphite anode is real solution due to its proven performance in lithium-ion batteries. Therefore, the electrochemical reaction should be homogeneously formed inside the graphite composite anode. Unfortunately, it is not free from inhomogeneous reaction distribution originated from either poor contact between solid electrolyte and graphite or reductive decomposition of solid electrolyte inside graphite composite anode. Moreover, these attribute to the lithium deposition, leading to degradation of battery performance. However, the mechanism of lithium dendrite generation and growth on graphite composite anode has not been clarified, and guidelines for suppressing them have not been established. In this study, the behavior of lithium dendrite inside graphite composite anode was clarified in relation to origin and growth process by *Operando* X-ray computed tomography.

5.1. Introduction

Among the various eco-friendly vehicles being developed, the expectation and possibility of electric vehicles (EVs) operated with electricity is the greatest[1-3]. Although EVs equipped with lithium-ion batteries (LIBs) are currently in operation, it is difficult to replace vehicles operated by gasoline with the performance of LIBs, which are currently limited instability and energy / power density[3-5]. In particular, concerns about LIB's stability limit the development of long-distance and fast charging of EVs. To overcome and replace these limitations of LIB, All-solid-state batteries (ASSBs), which are replaced from organic liquid electrolyte to inorganic sulfide solid electrolyte, have been attracting attention as next-generation batteries with more improved performance

and safety than those of LIBs. Unlike organic liquid electrolytes, which have high risk of ignition, inorganic sulfide solid electrolytes are substitute in terms of safety because there is basically no risk of ignition[6].

However, solving the safety concerning does not mean that ASSB can be directly applied to EVs. The current level of ASSBs is poor in terms of the power density even more than existing LIBs[6-9], still remained a challenge to be solved. Thus, improvement of the power density is very important for ASSB's commercialization. In this regard, the choice of appropriate electrode materials is definitely a clue to solving problems. So far, sulfide solid electrolytes with comparable ionic conductivity to that of liquid electrolytes have been discovered, and studied in conjunction with existing cathode electrodes that have been utilized in LIBs[10]. Considerable advanced results have been reported to improve the energy density coupled with existing cathode materials ($LiCoO_2$[11-12], $LiNi_{0.8}Co_{0.1}Mn_{0.1}O_2$[13-14], and Li_2S[15-16]) by modifying the surface modification with Li_2SiO_3[17], Li_3PO_4[18], and $LiNbO_3$[19-20] to suppress the oxidize decomposition of sulfide solid electrolytes while, the knowledge and study on anode materials for ASSBs are just about to start, or at a tardy level than in the case of cathode for ASSB. Even, owing to the initial expectation of lithium dendrite suppression from replacing the solid electrolyte, a suitable anode material candidate for ASSB had not been presented except for lithium metal anode. Although lithium metal is considered an ideal anode for ASSB due to its favorable properties as follows; low potential window (-3.040 *vs SHE*), high theoretical capacity (3,860 $mAhg^{-1}$), and low density (0.534 gcm^{-3})[21], previous studies have been suggested that the ASSB also cannot be free from lithium dendrites and critical reactivity of sulfide solid electrolyte for lithium metal[22-24]. Thus, Li-In alloy, suggested to alleviate the reaction, has been suggested as the anode for ASSBs[22]. However, large volume expansion (500 % compared to pristine state) during battery cycling and lowered operation voltage (0.62 V *vs* $Li\text{-}In/Li^+$) of Li-In alloy are not suitable for the improvement of energy density and duration of ASSBs[22,25-29]. Likewise, the Si receiving a lot of attention as next-generation anode replacing lithium metal has also the similar problem of volume expansion/shrink during battery cycling in spite of its superior advantages such as low potential (0.4 V *vs* Li/Li^+) and high theoretical capacity (4,200 $mAhg^{-1}$)[30-31]. Compared with the fatal problems of the above anode material candidates, graphite is a very promising anode material not only in LIB but also in ASSB. Except for relatively

low capacity (372 $mAhg^{-1}$), its low reduction potential area (0 ~ 0.01 V), superior reversibility, and structural stability during battery cycling are still attractive as the anode electrode[32-38]. Furthermore, the ability of graphite as an anode has been sufficiently demonstrated in LIBs. Therefore, it is most favorable to access among the mentioned promising anode candidates for ASSBs.

To utilize the graphite composite anode for ASSB, high polarization, originated either the contact resistance between graphite and electrolyte or reductive decomposition of electrolyte at reduction potential of graphite[32-39], must be improved. Considerable results have been reported by suppressing the reductive decomposition of sulfide solid electrolyte in previous studies[35,37]. However, the electrochemical performance under relatively high current density was still poor, which was shown regardless of solid electrolyte's species. It implies that various phenomena are occurred during lithiation process. Thus, comprehensive investigations are required to understand the phenomena inside graphite composite electrode during lithiation. Meanwhile, X-ray computed tomography has been utilized to understand the phenomena occurring inside ASSBs using X-ray computed tomography[24,40-42]. This analysis technique has the advantage of not only observation for internal phenomena in real time without destruction of sample but also three-dimensional image of each element such as electrolyte and electrode material. In this study, we demonstrated internal phenomena inside the graphite composite electrode during lithiation with *Operando* X-ray computed tomography.

5.2. Experimental section

5.2.1. Material preparation

The Li_3PS_4 as the electrolyte, the molar ratio of the Li_2S (Aldrich, 99%) and P_2S_5 (Aldrich, 99.9%) was 3:1, was synthesized by mechanical ball milling with 60 g of zirconia balls for 15 hours under 600 RPM. The graphite composite was prepared by mixing with prepared Li_3PS_4 solid electrolyte in the weight ratio of 60 wt% : 40 wt%.

5.2.2. Material Characterization

The graphite and Li_3PS_4 were measured by the XRD with RINT-Ultima III (Rigaku) with CuKα radiation of 1.54056 Å at 40 kV and 40 mA on special holder to obstruct the air from the samples. they were analyzed in the range of 2 theta from 10 to 40 °. The scanning electron microscopy (SEM) images were collected using an SU8220 (Hitachi High-Technologies) to observe the morphology both graphite and Li_3PS_4.

5.2.3. Electrochemical measurement

Prepared graphite composite electrode was measured with 2 kinds of cell. First, basic performance for charge/discharge behavior under different current densities were evaluated with the general two-electrode cell. Li_3PS_4 (100 mg) was placed in a polycarbonate tube with a diameter of 10 mm, and smoothly pressed to make an pellet as a solid electrolyte layer. Then, the graphite composite (10 mg) was added on one side of pellet, and pressed at 360 MPa. Last, an Li-In alloy (Li: 0.2 mm^t, 8pi/ In: 0.3 mm^t, 9pi) was attached and pressed at 10 MPa. Galvanostatic cycle tests were conducted with cut-off voltages of −0.62 to 1.0 V vs. Li–In/Li^+ (0.0–1.62 V vs. Li/Li^+) for charging and discharging over three cycles at C-rate of 0.13, 0.26, 0.51, and 0.76 $mAcm^{-2}$ at 25 °C. The *Operando* cell for the X-ray C.T was fabricated as follows, the Li_3PS_4 (3 mg) was placed in the polycarbonate tube with a diameter of 1.0 mm, and pressed to make a SE layer with 35 cN·m by torque wrench. Then, about 0.1 mg of graphite composite was added on one side of SE layer with 35 cN·m. Last, the Li-In alloy punched with 1.0 mm of diameter was attached on opposite side of SE layer with 10 cN·m.

5.2.4. *Operando* X-ray computed tomography

Prepared *Operando* cell test was focused on the charge process (lithiation process). *Operando* X-ray Computed Tomography was evaluated under 0.5 $mAcm^{-2}$, and collected according to lithiation state as follows, Li_0C_6, $Li_{0.05}C_6$, $Li_{0.1}C_6$, $Li_{0.15}C_6$, $Li_{0.2}C_6$, $Li_{0.4}C_6$, $Li_{0.6}C_6$, and $Li_{0.9}C_6$, corresponding to 0, 18, 37, 56, 74, 149, 23, and 332 $mAhg^{-1}$ on the beamline of BL20XU at Spring-8. On the basis of obtained X-ray CT results, three dimensional images, separated as Li_3PS_4, graphite, and expected lithium dendrite, respectively, were obtained by using dragonfly software.

The X-ray CT measurements were conducted using micro-CT and nano-CT modes. Both modes used a monochromatic X-ray beam with 15 keV. In the micro-CT mode, each

transmission image was acquired with a charge-coupled device camera (2048 × 2048 pixels) through a scintillator plate. Typically, an image with a 1 × 1 mm^2 FOV is measured resulting in a voxel size of 0.49 μm. The micro-CT mode was used to measure the morphological changes in the anode composite electrode due to pressure changes. In the nano-CT mode, the X-ray beam was focused onto the sample using an elliptical glass capillary and the images were projected onto a scintillator using a Fresnel zone plate lens. The images were also recorded using a charge-coupled device camera (2048 × 2048 pixels). The image with a voxel size of 31 nm and a 63 × 63 μm^2 FOV is measured. In order to obtain better contrast from the transmitted image of materials, the image was taken using the Zernike phase contrast method. This mode was utilized to observe the morphology of the spherical type and sheet type graphite. In total, 1800 radiographs were collected using an exposure time of 30 ms (micro-CT mode) or 500 ms (nano-CT mode) during 180° rotation. The images were reconstructed to 3D volume images using a filtered back projection method.

5.3. Results and discussion

Both XRD and SEM were utilized to investigate their structure and morphology. Traditional amorphous phase of Li_3PS_4 and the crystalline graphite structure were demonstrated in Figure 1(a-b) and spherical type particles were observed in both of them with about 10 μm of diameter. An ionic conductivity for Li_3PS_4 was calculated based on Figure 2, was a 5.12 x 10^{-4} Scm^{-1}. With these materials, we fabricated conventional solid-state cell for confirmation of electrochemical property (Figure 3) and deposition test with *Operando* cell demonstrates in Figure 4(a) with cell illustration Figure 4(b), in which each point corresponding to targeted lithium deposition capacity was collected. In Figure 3, graphite composite indicated about 250 $mAhg^{-1}$ of discharge capacity, which is lower than its theoretical capacity. It is attributed to the high polarization by decomposing the Li_3PS_4 at reduction potential of graphite and inhomogeneous reaction distribution[32-33]. After measurement at 0 $mAhg^{-1}$, later points corresponding to 18 mAh g^{-1} ($Li_{0.05}C_6$), 37 mAh g^{-1} ($Li_{0.1}C_6$), 56 $mAhg^{-1}$ ($Li_{0.15}C_6$), 74 mAh g^{-1} ($Li_{0.2}C_6$), 149 mAh g^{-1} ($Li_{0.4}C_6$), 223 mAh g^{-1} ($Li_{0.6}C_6$), and 332 mAh g^{-1} ($Li_{0.9}C_6$) were collected with micro/nano X-ray CT.

First, a voltage of *Operando* cell voltage was increased from 200 mAh g^{-1}, which might be attributed to short circuit by deposited lithium on the graphite. Before describing the lithium deposition behavior, the author explains for the micro / nano X-ray C.T. image (Figure 4(c)) corresponding to 0 mAh g^{-1}. From the top of the image, total micro–X-ray C.T images demonstrate the stainless–steel current collector, graphite composite anode, Li_3PS_4 layer, and Li-In alloy layer. Based on that the elements with high atom number are generally demonstrated with relatively bright color, it was separated for the solid electrolyte and graphite anode in the graphite composite layer, where orange color area is Li_3PS_4 and brown color area is graphite. Then, specific area was collected with enlarged nano X-ray C.T images as shown in Figure 4(d).

First of all, no noticeable change behaviors were observed inside the cell for lithium deposition capacity as shown in Figure 5. It implies that lithium dendrite evolution behavior in the composite anode too low scale to be observe. Thus, it is necessary to utilize the nano X-ray C.T analysis in order to observe the local area in the graphite composite anode, and the author attempted to observe the fixed position for nano X-ray C.T as in Figure 4(d), and Figure 6 and 7 demonstrate obvious evolution behaviors, which were obviously observed at the interface between graphite composite and Li_3PS_4, marked with black dashed quadrangles in Figure 7. Furthermore, enlarged nano X-ray C.T images (Figure 7) clearly demonstrate that different contrast appears from 56 mAh g^{-1} where the interface area contacted between graphite and Li_3PS_4, indicating the decomposition of Li_3PS_4 by low reduction potential of graphite. Later, new filament form was observed and gradually spread out from edge area to outside of graphite. On the other hand, invisible neither obvious crack nor changed contrast is invisible at upstage near the stainless-steel current collector than at near downstage. It implies that lithium dendrite evolution was begun after deposition of the lithium on the graphite at the downstage near the Li_3PS_4 layer because of favorable lithium-ion transportation while, further migration of lithium-ion to depth area near the stainless-steel current collector might be congested by the resistance originated from the decomposed products (Li_2S, Li_3P) that have low ionic conductivity and high electronic conductivity. Additionally, it might be attributed to inhomogeneous reaction distribution inside graphite composite anode as shown in Figure 8. Most of intercalation of lithium ions was formed in the vicinity of the Li_3PS_4 area. 3D

images for graphite composite anode clearly demonstrate the reductive decomposition of Li_3PS_4 inside graphite composite anode, in which there is no reductive decomposition at upstage near the stainless steel as shown in Figure 9. It was confirmed that the range of reductive decomposition also expanded as the reaction continued. This might lead to acceleration of inhomogeneous reaction distribution inside graphite composite. To investigate the lithium dendrite behavior inside graphite composite anode, 3D images were also extracted for graphite and lithium dendrite as shown in Figure 10. In here, three positions corresponding to 0, 74, and 149 mAh g^{-1} are selected to discuss the lithium dendrite behavior because the lithium dendrite behaviors were not progressed at 232 and 332 $mAhg^{-1}$. 3D images demonstrated that the morphology of lithium dendrite is sheet-like shape and the growth of lithium dendrite within the graphite composite anode were begun and concentrated at the edge side of graphite particle, and gradually connected with other edge of graphite particle like net connection.

Through the nano X-ray C.T., the Li_3PS_4 inside the graphite composite anode was decomposed at reduction potential of graphite, and then the lithium dendrite gradually grew from the edge side of graphite particle as lithiation goes by. This was demonstrated with 3 D images in Figure 9 and 10. It is considered as a result by this reaction process was only concentrated on the closely contacted region between the graphite composite electrode and Li_3PS_4 layer, leading to inhomogeneous reaction distribution in Figure 8. Therefore, this study suggests that the homogeneous reaction distribution is preferred inside graphite composite anode, and the morphological change must be minimized to suppress the lithium dendrite formation

5.4. Conclusion

Lithium dendrite evolutions were successfully observed in nano scale for the graphite composite thorough *Operando* X-ray computed tomography technique. X-ray CT images were collected according to the lithium deposition capacity. The micro-scale images could not verify a change behavior in the graphite composite anode, but nano-scale images demonstrated the expected decomposition of Li_3PS_4 in the graphite composite anode and lithium dendrite. Furthermore, the intercalation of lithium ions into

the graphite inside composite anode was mainly concentrated on the part in contact with the Li_3PS_4 layer. Thus, this limited reaction distribution led to the growth of lithium dendrites as shown in three-dimensional images, in which it was confirmed that the lithium dendrites grew at the edge of graphite particles and were connected to the edge of other graphite particle inside the composite anode. This study showed that not only should it be designed so that a uniform reaction distribution can be achieved in composite electrodes, but also that the shape change of graphite should be maintained against pressure.

Reference

1. Mark Skiton, Felix hovsepian, The 4th Industrial Revolution, Springer, **2018**.
2. Kenneth Holmberg, Ali Erdemir, The impact of tribology on energy used and CO2 emission globally and in combustion engine and electric cars, *Tribology International*, **2019**, 132, 389-396.
3. Joris Baars, Teresa Domenech, Raimund Bleischwitz, Hans Eric Melin, Oliver Heidrich, Circular economy strategies for electric vehicle batteries reduce reliance on raw materials, *Nature Sustainability*, **2021**, 4, 71-79.
4. Silvia Bobba, Fabrice Mathieux, Fulvio Ardente, Gian Andrea Blegini, Maria Anna Cusenza, Adreas Podias, Adreas Pfang, Life Cycle Assessment of repurposed electric vehicle batteries: an adapted method based on modelling energy flows, *J. Energy Storage*, **2018**,19, 213-225.
5. Zachary P. Cano, Dustin Banham, Siyu Ye, Andreas Hintennach, Michael Fowler, Zhongwei Chen, Batteris and fuel cells for emerging electric vehicle markets, *Nature Energy*, 2018, 3, 279-289.
6. Davide Castelvecchi, *Nature*, **2021**, 596, 336-339.
7. M. scarfogliero, S. Carmeli, F. Castelli–Dezza, M. Mauri, M. Rossi, G. Marchegiani, E. Rovelli, Lithium-ion batteries for electric vehicles: A review on aging models for vehicle-to-grid services, *2018 International Conference of Electrical and Electronic Technologies for Automotive*, 2018, 1-6.
8. Chengjian Xu, Qiang Dai, Linda Gaines, Mingming Hu, Arnold Tukker, Berhard Steubing, Future material demand for automotive lithium-based batteries, *Commun. Mater.*, **2020**, 1, 1-10.

9. Fanglin Wu, Shan Fang, Matthias Kuenzel, Angelo Mullaliu, Jae-Kwang Kim, Xinpei Gao, Thomas Diemant, Guk Tae Kim, Stefano Passerini, Dual-anion ionic liquid electrolyte enables stable Ni-rich cathodes in lithium-metal batteries, *Joule*, **2021**, 5, 2177-2194.
10. Anja Bielefeld, Dominik A. Weber, Jürgen Janek, Microstructural Modeling of Composite Cathodes for All-Solid-State Batteries, *J.Phys.Chem.C*, **2019**, 123, 1626-1634.
11. Wen Jing, Masaaki Hirayama, Kota Suzuki, Ryoji Kanno, Fabrication and electrochemical properties of a $LiCoO_2$ and $Li_{10}GeP_2S_{12}$ composite electrode for use in all-solid-state batteries, *Solid State Ion.*, **2016**, 285, 136-142.
12. Yuki Kato, Shinya Shiotani, Keisuke Morita, Kota Suzuki, Masaaki Hirayama, Ryoji Kanno, All-Solid-State Batteries with Thick Electrode Configurations, *J.Phys.Chem.Lett.*, **2018**, 9, 607-613.
13. Jun Zhang, Haoyue Zhong, Chao Zheng, Yang Xia, Chu Liang, Hui Huang, Yongping Gan, Xinyong Tao, Wenkui Zhang, All-solid-states batteries with slurry coated $LiNi_{0.8}Co_{0.1}Mn_{0.1}O_2$ composite cathode and Li_6PS_5Cl electrolyte: Effect of binder content, *J.Power Sources*, **2018**, 391, 73-79.
14. Florian Strauss, Timo Bartsch, Lea de Biasi, A-Young Kim, Jürgen Janek, Pascal Hartmann, Torsten Brezesinski, *ACS Energy Lett.*, **2018**, 3, 992-996.
15. Lei Zhou, Muhammad Khurram Tufail, Niaz Ahmad, Tinglu Song, Renjie Chen, Wen Yang, Strong Interfacial Adhesion between the Li_2S cathode and a Functional $Li_7P_{2.9}Ce_{0.2}S_{0.9}Cl_{0.3}$ Solid-State Electrolyte Endowed Long-Term Cycle Stability to All-Solid-State Lithium-Sulfur Batteries, *ACS Appl. Mater. Interfaces*, **2021**, 13, 28270-28280.

16. Hany El-Shinawi, Edmund J. Cussen, Serena A. Corr, A facile synthetic approach to nanostructured Li2S cathodes for rechargeable solid-state Li-S batteries, *Nanoscale*, **2019**, 11, 19297-19300.
17. Atsushi Sakuda, Akitoshi Hayashi, Masahiro Tatsumisago, Interfacial Observation between $LiCoO_2$ Electrode and Li_2S-P_2S_5 Solid Electrolytes of All-Solid-State Lithium Secondary Batteries Using Transmission Electron Microscopy, *Chem.Mater.*, **2010**, 22, 949-956.
18. So Yubuchi, Yusuke Ito, Takuya Matsuyama, Akitoshi Hayashi, Masahiro Tatsumisago, *Solid State Ion.*, **2016**, 285, 79-82.
19. Felix Walther, Florian Strauss, Xiaohan Wu, Boris Mogwitz, Jonas Hertle, Joachim Sann, Marcus Rohnke, Torsten Brezesinski, Jürgen Janek, The Working Principle of a Li_2CO_3/$LiNbO_3$ Coating on NCM for Thiophosphate-Based All-Solid-State Batteries, *Chem. Mater.*, **2021**, 33, 2110-2125.
20. Jun Su Lee, Young Joon Park, Comparison of $LiTaO_3$ and $LiNbO_3$ Surface Layers Prepared by Post- and Precursor-Based Coating Methods for Ni-Rich Cathodes of All-Solid-State Batteries, *ACS Appl. Mater. Interfaces*, **2021**, 13, 38333-38345.
21. Jiangfeng Qian, Wesley A. Henderson, Wu Xu, Priyanka Bhattacharaya, Mark Engelhard, Oleg Borodin, Ji-Guang Zhang, High rate and stable cycling of lithium metal anode, *Nat. Commun.*, **2015**, 6, 6362-6371.
22. Hatzell, K.B.; Chen, X.C.; Cobb, C.L; Dasgupta N.P.; Dixit, M.B; Marbella, L.E.; McDowell. M.T.; Mukherjee, P.P.; Verma, A.; Viswanathan, V.; Westover, A.S.; Zeier, W.G.; Challenges in Lithium Metal Anodes for Solid-State Batteries, *ACS Energy Lett.*, **2020**, 5, 922-934.

23. Liu, H.; Cheng, X.B.; Huang, J.Q.; Yuan, H.; Lu, Y.; Yan, C.; Zhu, G.L.; Xu, R.; Zhao, C.Z.; Hou, L.P.; He, C.; Kaskel, S.; Zhang, Q.; Controlling Dendrite Growth in Solid-State Electrolytes, *ACS Energy Lett.*, **2020**, 5, 833-843.
24. Lewis, J.A.; Cortes, F.J.Q.; Liu, Y.; Miers, J.C.; Verma, A.; Vishinugopi, B.S.; Tippens, J.; Prakash, D.; Marchese, T.S.; Han, S.Y.; Lee, C.; Shetty, P.P.; Lee, H-W.; Shevchenko, P.; Carlo, F.D.; Saldana, C.; Mukherjee, P.P.; McDowell M.T.; Linking void and interphase evolution to electrochemistry in solid state batteries using operando X-ray tomography, *Nature materials*, **2021**, 20, 503-510.
25. Hongyi Li, Takitaro Yamaguchi, Shingo Matsumoto, Hiroaki Hoshikawa, Toshiaki Kumagai, Norihiko L. Okamoto, Tetsu Ichitsubo, Circumventing huge volume strain in alloy anodes of lithium batteries, *Nature materials*, **2020**, 11, 8.
26. Y. Seino, K. Takada, B-C Kim, L. Zhang, N. Ohta, H. Wada, M. Osada, T. Sasaki, Synthesis of phosphorous sulfide solid electrolyte and all-solid-state lithium batteries with graphite electrode, *Solid State Ionics*, **2005**, 176, 2389–2293.
27. Charles las Casas, Wenzhi Li, A review of application of carbon nanotubes for lithium ion battery anode material, *Journal of Power Sources*, **2012**, 208, 74-85.
28. Dave Andre, Holger Hain, Peter Lamp, Filippo Maglia, Barbara Stiazny, Future high-energy density anode materials from an automotive application perspective, *J. Mater. Chem. A*, **2017**,5,17174.
29. Kazunori Takada, Taro Inaba, Akihisa Kajiyama, Hedeki Sasaki, Shigeo Kondo, Mamoru Watanabe, Masahiro Murayama, Ryoji Kanno, Solid-state lithium battery with graphite anode, *Solid State Ion.*, **2003**, 158, 269-274.
30. R. Miyazaki, N. Ohta, T. Ohnishi, I. Sakaguchi, K. Takada, An amorphous Si film anode for all-solid-state lithium batteries, *J. Power source*, **2014**, 272, 541–545.

31. R. B. Cervera, N. Suzuki, T. Ohnishi, M. Osada, K. Mitsushi, T. Kambara, K. Takada, *Energy Environ. Sci.*, **2014**, 7, 662–666.
32. M. Otoyama, H. Kowada, A. Sakuda, M. Tatsumisago, A. Hayashi, *Operando* Confocal Microscopy for Dynamic Changes of Li^+ Ion Conduction Path in Graphite Electrode Layers of All-Solid-State Batteries, *J. Phys. Chem. Lett.* **2020**, 11, 990 –904.
33. M. Otoyama, A. Sakuda, A. Hayashi, M. Tatsumisago, Optical microscopic observation of graphite composite negative electrodes in all-solid-state lithium batteries, *Solid State Ionics*, **2018**, 323, 123–129.
34. L. Höltchi, F. Jud, C. Borca, T. Huthwelker, C. Villevieille, V. Pelé, C. Jordy, M. E. Kazzi, P. Nvák, Study of Graphite Cycling in Sulfide Solid Electrolytes, *J. Electrochem. Soc.*, **2020**, 167, 110558–1105568.
35. L. Höltchi, C. Borca, T. Huthwelker, F. Marone, C. schlepütz, V. Pelé, C. Jordy, C. Villevieille, M. E. Kazzi, P. Nvák, Performance-limiting factors of graphite in sulfide-based all-solid-state lithium-ion batteries, *Electrochem. Acta*, **2021**, 389, 138735-138745.
36. G. Maresca, A. Tsurumaki, N. Suzuki, T. Tsujimura, Y. Aihara, M. A. Navarra, Improvement of Graphite Interfacial Stability in All-Solid-State Cells Adopting Sulfide Glassy Electrolytes, *ChemElectroChem*, **2021**, 8, 689–696.
37. Y. Zhu, X. He, Y. Mo, Origin of Outstanding Stability in the Lithium Solid Electrolyte Materials: Insight from thermodynamic Analyses Based on First-Principles Calculations, *ACS Appl. Mater. Interfaces*, **2015**, 7, 23685–23693.
38. Yuji Yamagishi, Hiromi Morita, Yuki Nomura, Emiko Igaki, Visualizing Lithiation of Graphite Composite Anodes in All-Solid-State Batteries Using

Operando Time-of-Flight Secondary Ion Mass Spectrometry, *J.Phys.Chem.Lett.*, **2021**, 12, 4623-4627.

39. Anton Neumann, Simon Randau, Katharina Becker-Steinberger, Timo Danner, Simon Hein, Ziyang Ning, James Marrow, Felix H. Richter, Jürgen Janek, Amulf Latz, Analysis of Interfacial Effects in All-Solid-State Batteries with Thiophosphate Solid Electrolytes, *ACS Appl. Mater. Interfaces*, **2020**, 12, 9277-9291.
40. Darren H.S. Tan, Abhik Banerjee, Zheng Chen, Ying Shirley Meng, From nanoscale interface characterization to sustainable energy storage using all-solid-state batteries, *Nat. Nanotechnol.*, **2020**, 15, 170-180.
41. Shuai Hao, Josh J. Bailey, Francesco Lacoviello, Junfu Bu, Patrick S. Grant, Dan J. L. Brett, Paul R. Shearing, 3D imaging of Lithium Protrusions in Solid-State Lithium Batteries using X-ray Computed tomography, *Adv.Funct.Mater.*, **2021**, 31, 2007564-2007573.

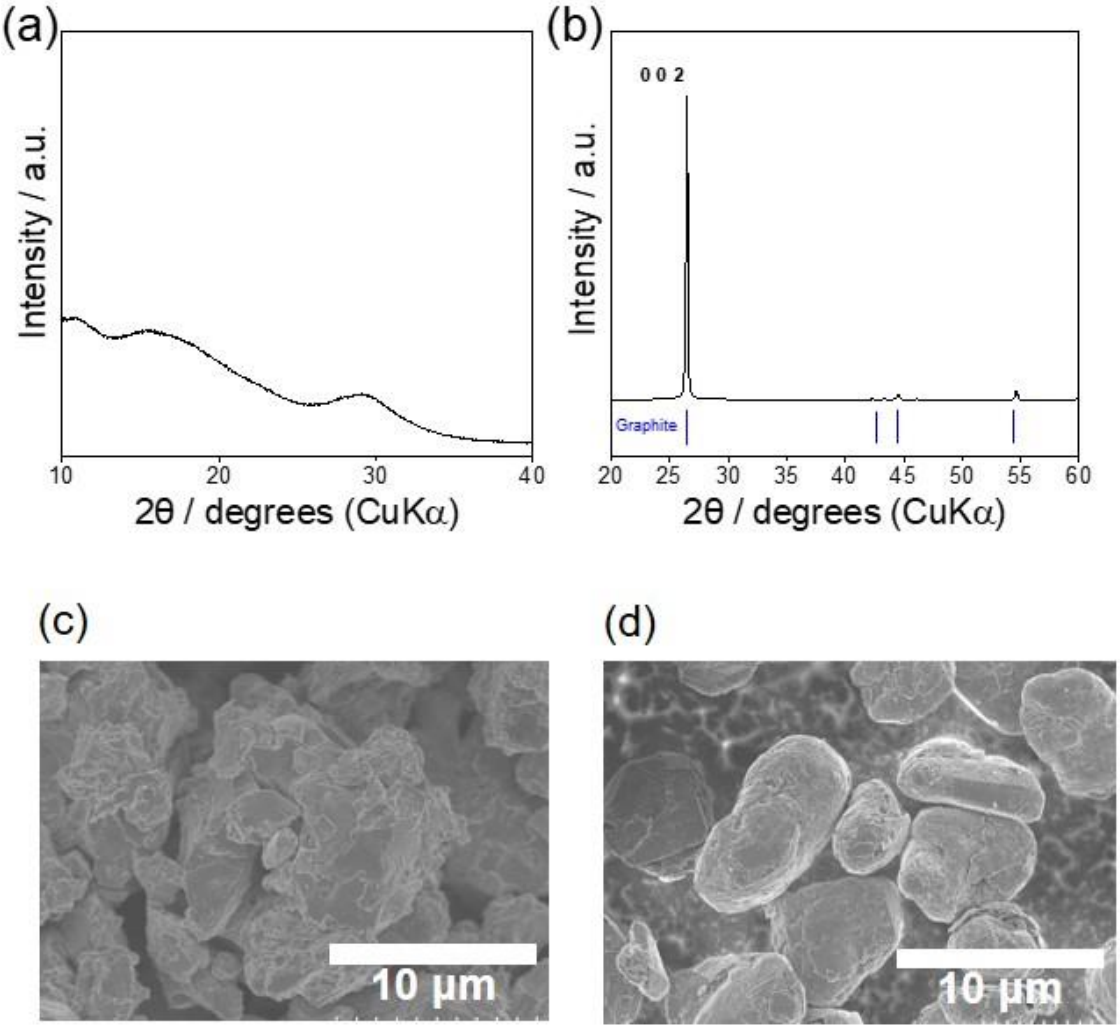

Figure 1. XRD patterns (a – b) and SEM images (c – d) for Li_3PS_4 and graphite

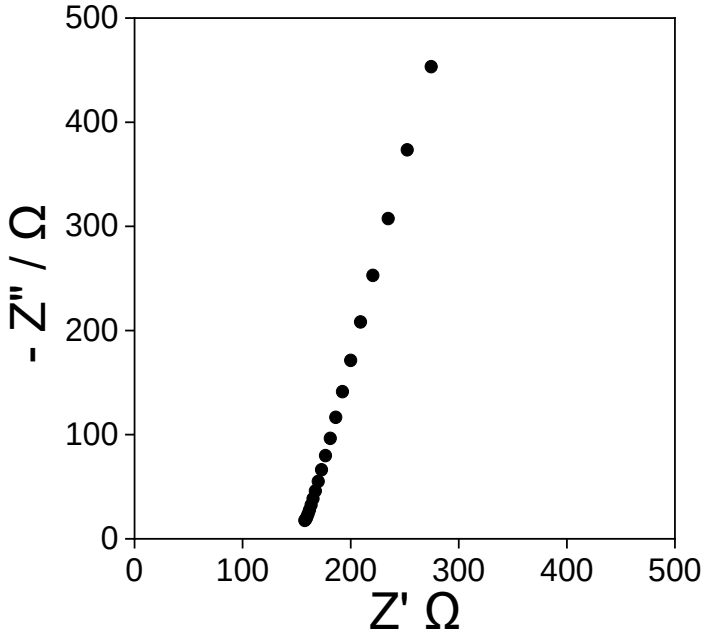

Figure 2. Nyquist plot for Li_3PS_4 as the solid electrolyte.

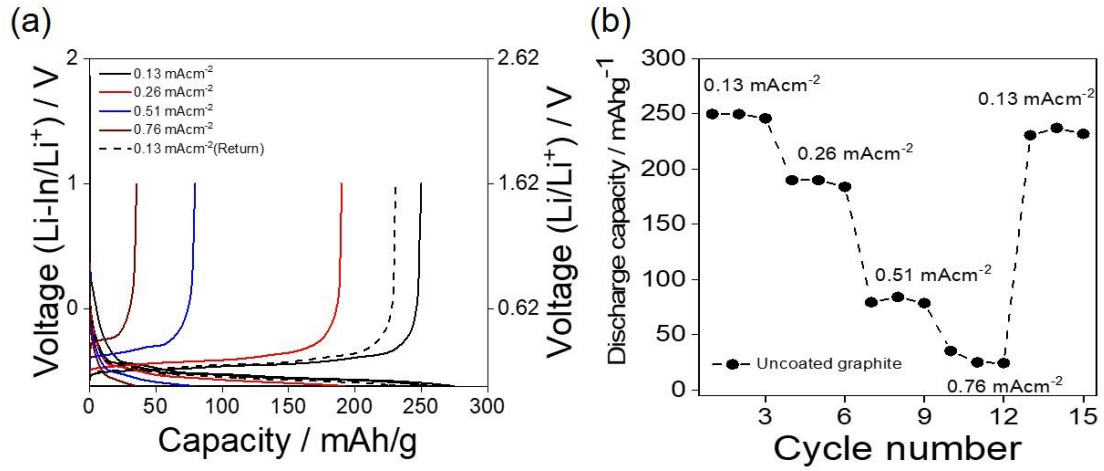

Figure 3. Galvanostatic charge discharge test results and rate performance for normal cell.

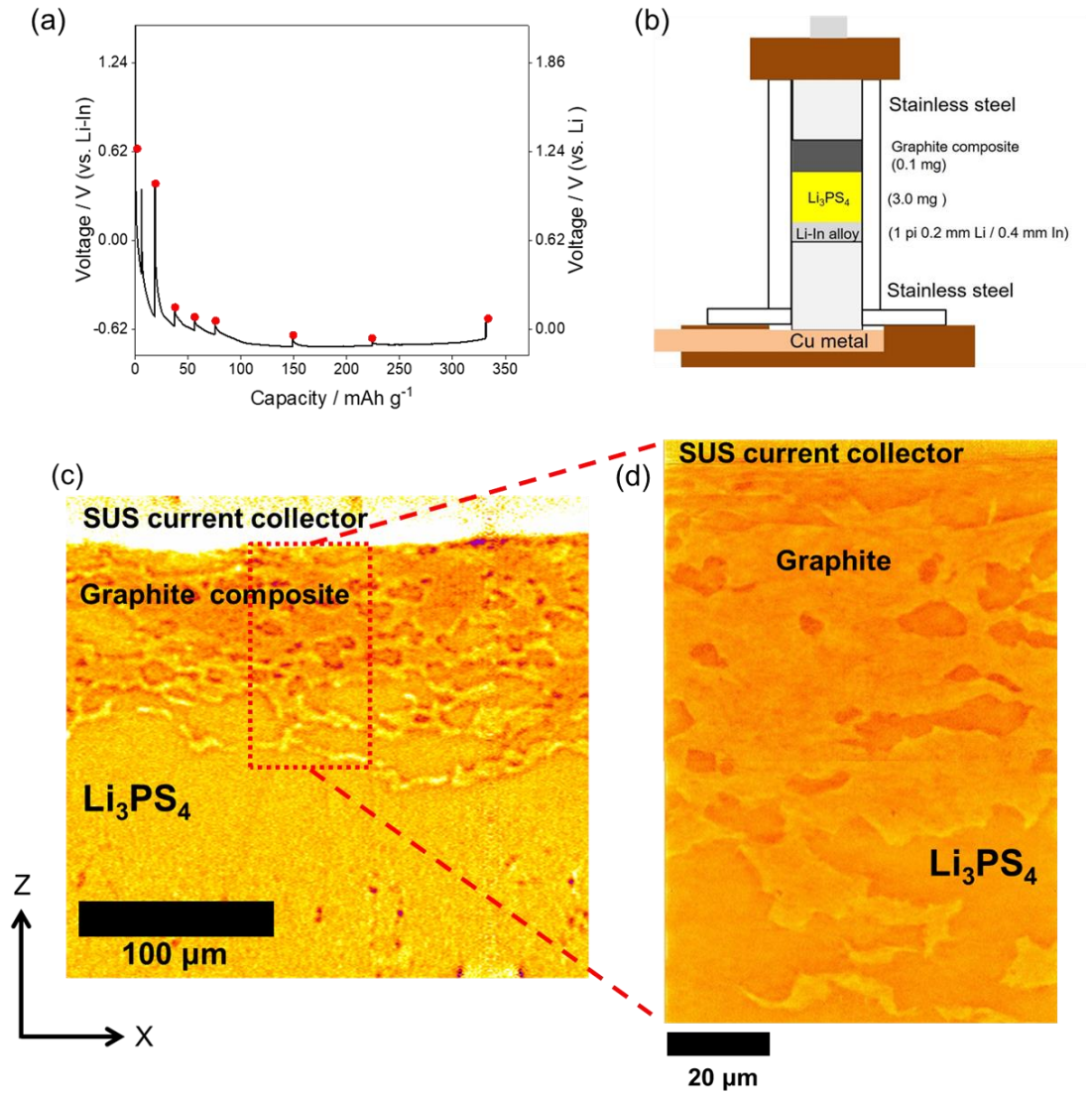

Figure 4. Lithium deposition into graphite composite and each point collected by X-ray C.T under 0.5 $mAcm^{-2}$ at room temperature (a). Schematic illustration of *Operando* cell for X-ray C.T (b). Micro C.T image for 0 $mAhg^{-1}$ and enlarged with nano CT image for red dot box (c).

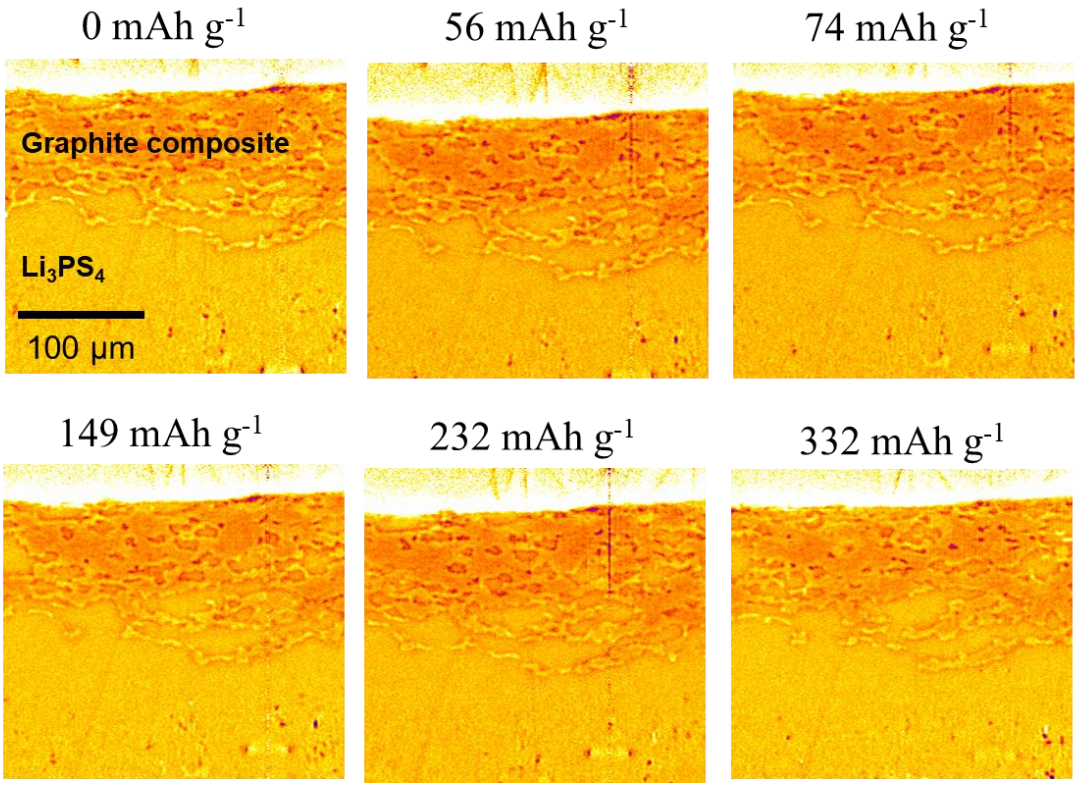

Figure 5. Micro X-ray C.T images corresponding to each lithium deposition capacity.

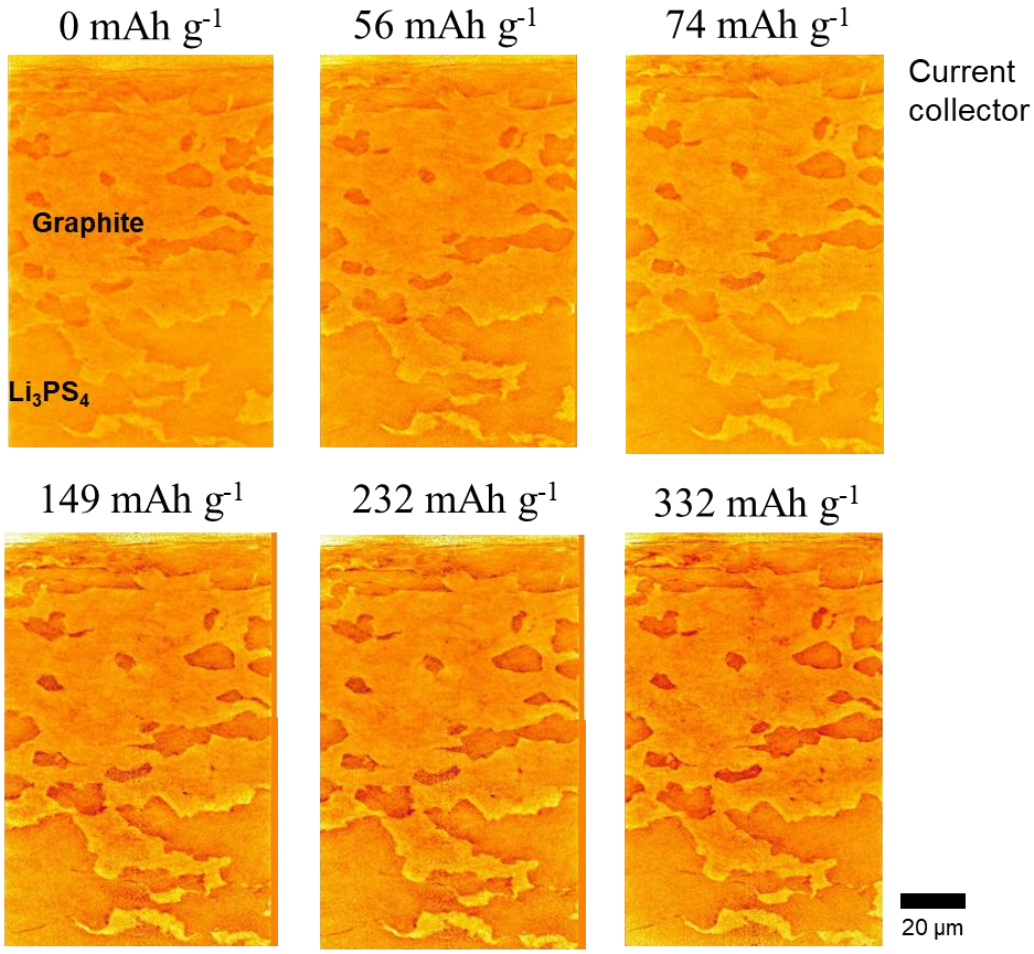

Figure 6. Nano X-ray C.T images corresponding to pre-fixed positions with the lithium deposition capacity. Evolution behavior was highlighted dashed quadrangle in the nano X-ray C.T images.

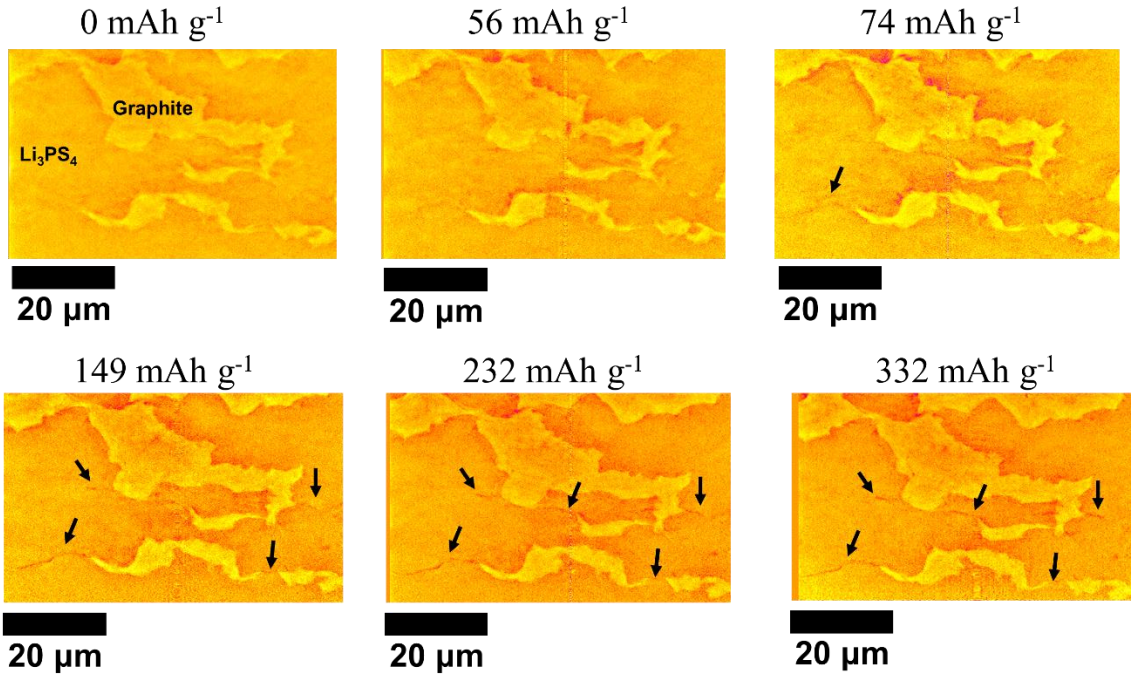

Figure 7. Nano X-ray C.T images for 0, 56, 74, 149, 232, and 332 $mAhg^{-1}$. the arrows were added either changed contrast or new formed position.

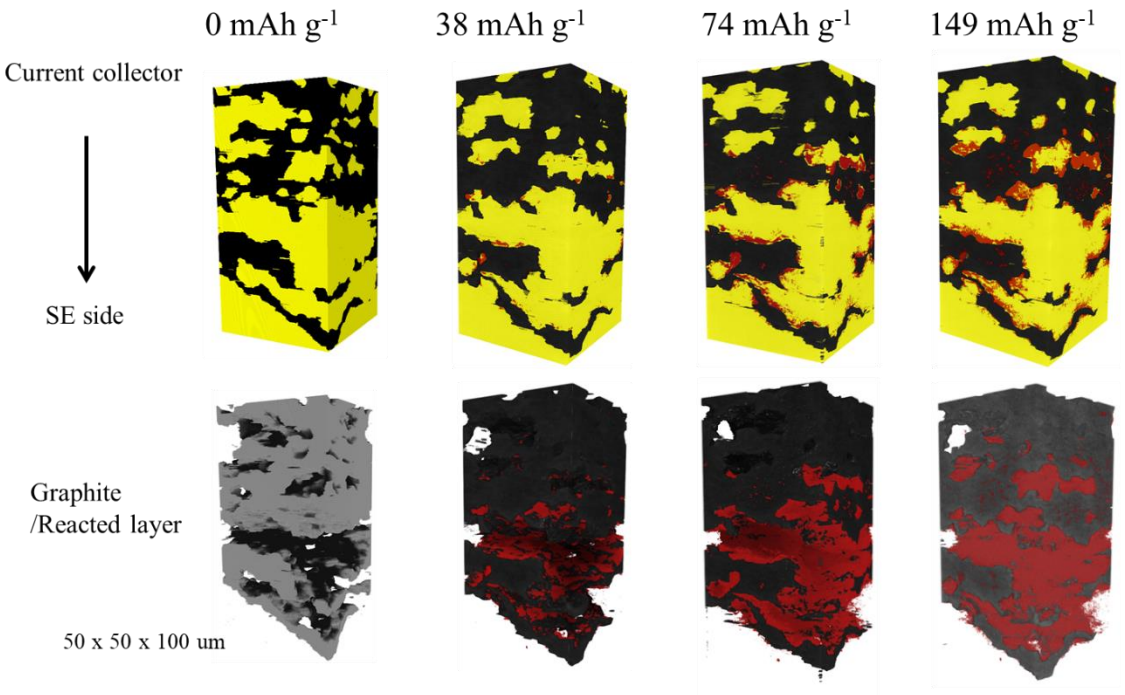

Figure 8. 3–D images extracted from the nano X-ray C.T images at the interface near the Li_3PS_4. Yellow, black, and red colors indicate the Li_3PS_4, graphite, and lithium dendrite, respectively.

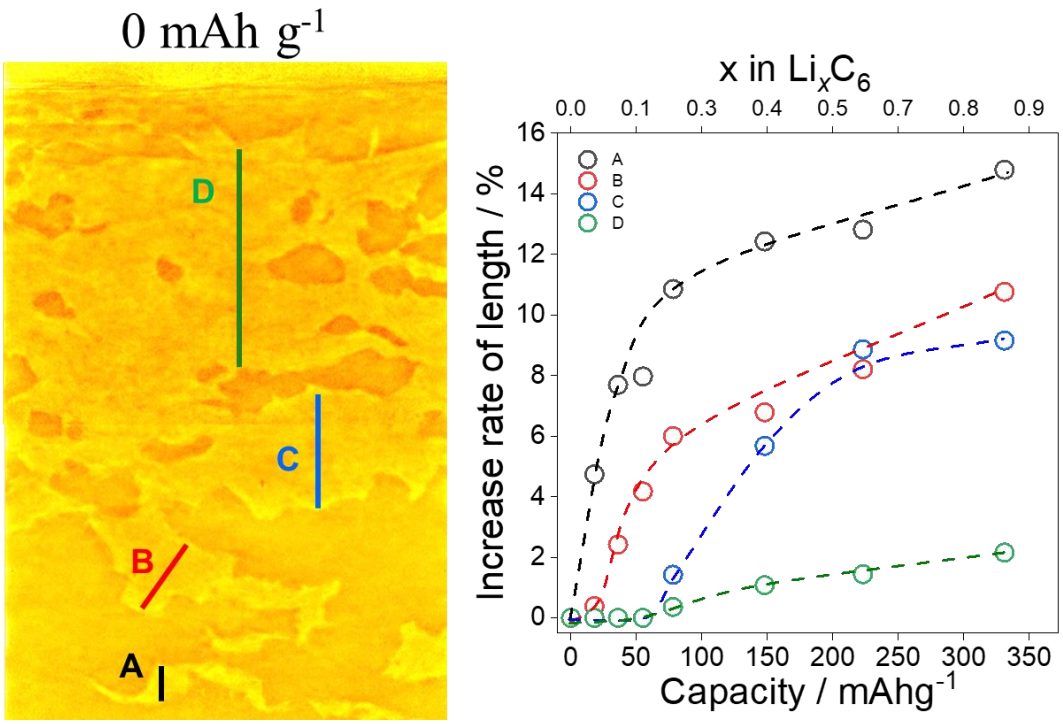

Figure 9. Nano X-ray CT (Left) corresponding to 0 mAh g-1, in which each graphite area was marked with A, B, C, and D, respectively. Expansion progress of graphite in the composite anode with the lithium deposition capacity (right).

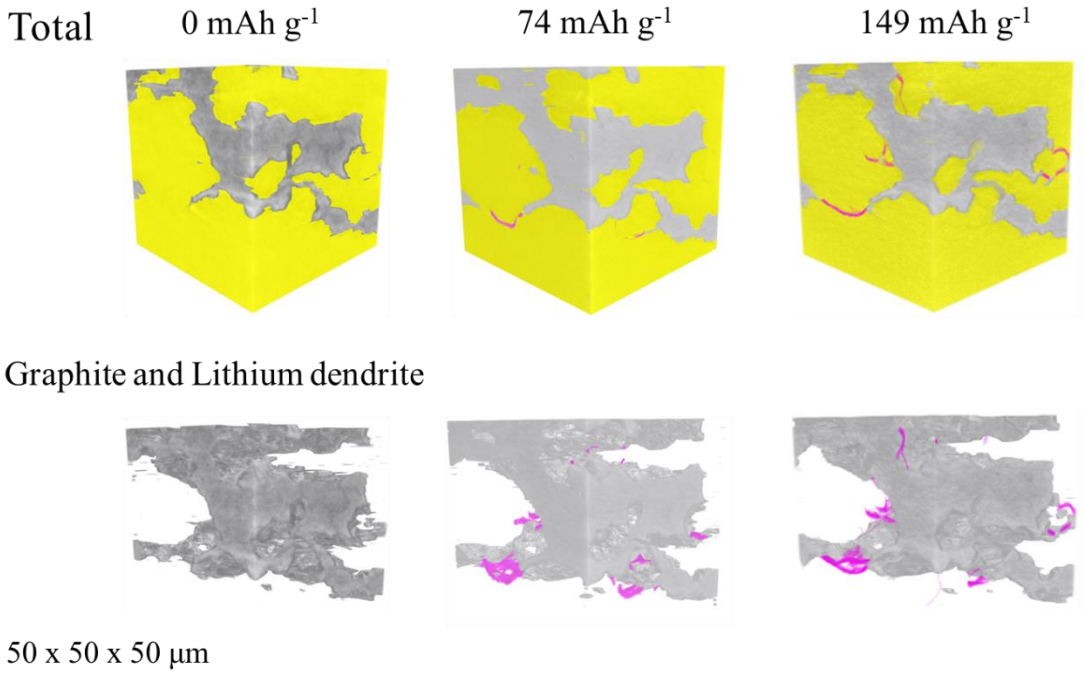

Figure 10. 3–D images extracted from the nano X-ray C.T images for graphite and lithium dendrite inside composite anode.

Chapter 6. Elucidation of Dominant Factors of Ion Transport Resistance in Graphite Composite Anodes for All-Solid–State Batteries using X–ray Computed Tomography

Despite significant progress in all-solid-state batteries (ASSBs), there is chronic problem of poor power density, which is caused by large polarization. It was initially considered due to low ionic conductivity of solid electrolyte but, it was not also a clue to solve this problem as reported in the case of utilizing the solid electrolytes comparable to that of liquid electrolyte. Thus, it is reasonable to suspect the ineffective lithium-ion transport inside the composite electrode for ASSB. It was reported that low tortuosity and high ionic conductivity of solid electrolyte was preferred in solid electrolyte layer in ASSBs while, those were unclear inside composite electrode. To take account for this, it is necessary to investigate not only the solid electrolyte's tortuosity indicating an ionic pathway but also the anisotropy of active material indicating an electrochemical active site through the investigation of the microstructure of composite electrode for ASSB. Furthermore, it is probably expected to differ from its behavior in the electrolyte layer and its behavior in the composite electrode. Thus, in this study, we firstly investigated the behavior of tortuosity change in the composite electrodes by the pressure and graphite's shape using in situ X-ray computed tomography (CT) and elucidate the correlation of electrochemical performance of graphite composite anodes in relation to quantitative data (void ratio, tortuosity of Li_3PS_4) extracted from obtained X-ray CT images. Finally, based on these results, we suggested the condition of the materials, which are solid electrolyte and active material, for effective design to composite electrode for ASSB.

6.1. Introduction

As the usage of a lithium-ion battery (LIBs) has been extended from the small electronic products market to Electric Vehicle market[1–5], a lot of related studies have been

focused on the improvement of high energy density and power density of the existing LIBs[1,6–8]. Unfortunately, there was one concern related to the safety, originated from the organic liquid electrolyte with flammability in LIBs[4–6]. Therefore, as the demand for a battery with great safety is required first, a type of battery replaced liquid with solid, that is, all-solid-state batteries (ASSBs) have been receiving great attention as alternatives to existing LIBs[3]. Moreover, these make the ASSBs could accomplish the excellent performances more than those of LIBs[3]. The studies for ASSB have been progressed from discovering and developing a variety of solid electrolyte candidates to implementing them in the form of solid-state cells with active materials[7,9–15]. At present, ASSBs with sulfide-based solid electrolytes have been receiving attention due to not only their high ionic conductivity than other types of solid electrolyte but also favorable ductility toward the interface with active materials[16–22]. However, there is critical problem that large polarization is often observed in practice. Although the ASSBs have theoretically high power density. It has been considered as poor contact of solid phase between the solid electrolyte and active material[23–27].

Unlike the interface environment between liquid phase as the liquid electrolyte and solid phase including active material and conductive carbon in composite electrode for LIBs, Numerous interfacial problems have been identified between solid phase and solid phase in for composite electrode for ASSBs[9,12–17]. In the void or pore phase inside the composite electrode for LIBs[5], the liquid electrolyte is naturally filled to allow lithium ions to transport whereas, in the case of the composite electrode for ASSBs, the lithium-ion transport is blocked at there, leading to inhomogeneous reaction distribution in composite electrode due to the difference of transport between electron and lithium ion when C-rate was increased[13,28–31]. These previous studies on the composite electrode had initially revealed that this ion transport resistance might be caused by low ionic conductivity of solid electrolyte, leading to an ineffective lithium–ion transport inside the composite electrode. However, current studies utilized with superior solid electrolyte, which has equivalent ionic conductivity to liquid electrolyte, has not also demonstrated any equal results to that of liquid electrolyte for existing LIBs even if they are applied to composite electrode for solid-state cells[30–31]. Therefore, it was suspected from different ion transport resistance in the composite electrode, might be caused by the solid electrolyte's tortuosity indicating the ion pathway inside the composite electrode and the

anisotropy of active material indicating the electrochemically active site[24,32–37]. While the correlations of solid electrolyte's tortuosity with lithium–ion transport of the solid electrolyte layer in ASSB were reported through the X-ray computed tomography (CT), in which low tortuosity was formed with high pressure and few void phases. the internal structure of the solid electrolyte when applied to pressure[25] but also the tortuosity and voids effect[26] were identified. However, it is limited only to solid electrolyte layer itself, and variables for lithium–ion transport that may occur in the composite electrode combined with the active material were not compressively investigated. So far, regarding the tortuosity of the solid electrolyte inside the composite electrode, it has been conventionally obtained either by electrochemical measurements or by computational modeling[24–25,32,37]. These indirect methods are comparatively quick and can be scaled to describe local phenomena, but it could not include information on real morphological or directional changes in components such as either the solid electrolyte or the active material in the composite electrode that occurs when actual pressure is applied. On the contrary, directly observed microstructural data from X-ray computed tomography (CT)[38] can provide useful insight into local transport tortuosity as well as help to find the bottlenecks to lithium-ion transports[25–26]. However, studies on these were applied only to the solid electrolyte as an electrolyte layer, to the best of our knowledge, there are no cases of application to composite electrodes for ASSBs.

In this study, the Li_3PS_4 was used as the model material of solid electrolyte, and spherical and sheet graphite anodes were used as active material models to compare the effect on the anisotropy in the composite anode under the pressures (0 to 160 MPa) as the variable factor, and we firstly demonstrated the morphological change of Li_3PS_4 and each graphite in form of composite anode with the applied pressure in real time through the in situ X-ray computed tomography (CT). based on obtained directly observed morphological information, real quantitative data such as tortuosity of Li_3PS_4 and anisotropic change of graphite in the composite anodes was extracted through three-dimensional imaging. Last, the correlation with electrochemical performance was discussed with quantitative data.

6.2. Experimental section

6.2.1 Material Preparation

A Li_3PS_4 was prepared using ball-milling (Pulverisette 7; Fritsch). The raw materials of Li_2S (Aldrich, 99.99%) and P_2S_5 (Aldrich, 99%) powders were mixed for 10 min in an agate mortar. the mixture of raw materials was put into the zirconia pot with zirconia balls, and then ball-milled under 600 RPM for 15 hours. The graphite composite anodes were prepared by mixing each graphite powders with spherical and sheet type (product names are CGB–10 and UP–20, Nippon Graphite Industries, Ltd.) with Li_3PS_4, in which the ratio between solid electrolyte and graphite was fixed in 60: 40 wt%, mixed for 1hour in the mortar.

6.2.2 Electrochemical measurements

The electrochemical properties for each graphite were measured with CR2032 coin cells to obtain the reference performance regardless of the microstructural impact in the electrode. This coin cell composed of the lithium metal electrode, a polypropylene separator, each graphite electrode, and an electrolyte of 1M $LiPF_6$ in Ethyl carbonate/Dimethyl carbonate (EC/DMC_3:7 by volume). The graphite electrodes were prepared by mixing 80 wt% graphite powders with 10 wt% of carbon blacks as a conductor and 10 wt% Polyvinylidene fluoride (PVDF) as a binder in a 1-methyl-2-pyrrolidinone solvent, and then casted in the about 20 μm thickness using doctor blade. All coin cells were assembled in an argon-filled glove box. The galvanostatic cycle test was conducted in the voltage range of 0.01 to 1.5 V (vs. Li) for charge and discharge over three cycles at current density (0.13, 0.26, 0.51, and 0.76 $mAcm^{-2}$) at 25 ºC. In different way, solid state cells were prepared to investigate the electrochemical performance for the impact of microstructure in composite electrode using a two–electrode cell by pressing. The Li_3PS_4 with 120 mg was placed in a polycarbonate tube with a diameter of 10 mm, and slightly pressed to form the solid electrolyte layer. An Li–In alloy was placed on one side of the solid electrolyte layer, and pressed at 10 MPa, and prepared graphite composite powder was added to opposite side, and pressed from 10 to 160 MPa. Galvanostatic cycle tests were conducted in the voltage range of -0.62 to 1.0 V (vs. Li-In) for charge and discharge over three cycles at current density (0.13, 0.26, 0.51, and

0.76 $mAcm^{-2}$) at 25 ºC. Furthermore, ionic conductivity was measured for Li_3PS_4 using alternating current–EIS (AC–EIS). The EIS results were recorded using VP 300 with AC amplitude of 50 mV in the frequency range of 7.0 MHz to 100 Hz.

6.2.3 Material Characterization

X-ray diffraction was conducted with RINT-Ultima III (Rigaku) with CuKα radiation of 1.54056 Å at 40 kV and 40 mA. All materials were analyzed in the range of 2 theta from 10 to 50 °. Raman spectra were collected using a DXR3 (Thermo scientific) device with 532 nm laser. All samples were prepared on a special holder fabricated to prevent the reaction of the compounds with air in the glove box. SEM measurements were performed using a SU8220 (Hitachi High-Technologies) system in order to observe the microstructure of each material.

6.2.4 in-situ X-ray Computed tomography (CT)

X-ray CT was utilized to investigate the morphology in the composite electrode for ASSBs, and conducted at BL20XU on the SPring-8. In addition, an in–situ cell was assembled for the X-ray CT measurements. Assembling process is as follows, each solid electrolyte (~ 1 mg) was placed in the polycarbonate tube with a diameter of 1.0 mm, and pressed to make a SE layer using stainless steel bar with 1.0 mm diameter with 20 cN·m by a torque wrench. Then, about 0.1 mg of composite graphite anode powder was added on one side of SE layer and compressed with the pressure as follows, 0, 40, 80, 120, and 160 MPa. At each pressure, X-ray CT images for change behavior with the pressure were collected in micro scale.

The X-ray CT measurements were carried out at BL20XU on the SPring-8 using micro-CT and nano-CT modes. Both modes used a monochromatic X-ray beam with 15 keV. In the micro-CT mode, each transmission image was acquired with a charge-coupled device camera (2048 × 2048 pixels) through a scintillator plate. Typically, an image with a 1 × 1 mm^2 FOV is measured resulting in a voxel size of 0.49 μm. The micro-CT mode was used to measure the morphological changes in the anode composite electrode due to pressure changes. In the nano-CT mode, the X-ray beam was focused onto the sample using an elliptical glass capillary and the images were projected onto a scintillator using a Fresnel zone plate lens. The images were also recorded using a charge-coupled device

camera (2048 × 2048 pixels). The image with a voxel size of 31 nm and a 63 × 63 μm^2 FOV is measured. In order to obtain better contrast from the transmitted image of materials, the image was taken using the Zernike phase contrast method. This mode was utilized to observe the morphology of the spherical type and sheet type graphite. In total, 1800 radiographs were collected using an exposure time of 30 ms (micro-CT mode) or 500 ms (nano-CT mode) during 180° rotation. The images were reconstructed to 3D volume images using a filtered back projection method.

The reconstructed gray-scale images were segmented into three regions, void, graphite, and Li_3PS_4, using an opensource software ImageJ. First, to reduce image noise, 3Dmedian filter with radius of 3 pixels was applied. Then, dark areas of the images were isolated as voids. Next, the threshold value for segmentation of Li_3PS_4 and graphite was set so that the volume ratio of Li_3PS_4 and graphite in the stocking volume would match. The tortuosity of Li_3PS_4 at each pressure of the two types of graphite was calculated using a commercial software Dragonfly (Object Research Systems Inc., Canada). Dragonfly has the ability to compute a 3D path network of segmented regions and calculate the tortuosity. From this function, the 3D path network of the Li_3PS_4 was calculated and the calculated network is shown in Figure S11. The tortuosity (τ) is expressed as an equation below.

$$\tau = \frac{L_e}{L_s} \qquad (1)$$

where τ, L_s, and L_e indicate the tortuosity of electrode, the linear distance between the two points of one path, and the length along a serpentine path between two points of the path, respectively. From this 3D network, the tortuosity of all paths in the electrode thickness direction were calculated and the average value was used as the tortuosity. The above calculations were adapted for two types of graphite at pressures from 40 to 160 MPa to calculate the tortuosity. 3D rendering images of each figure were also created by Dragonfly.

6.3. Results and discussion

First of all, the morphology, structure, and electrochemical performance for spherical and sheet graphite as anode material were investigated through the SEM, XRD, X-ray CT and electrochemical performance. Both morphological information for both spherical and sheet graphite was observed through the SEM and X-ray CT in Figure S1, in which roughly spherical shape of graphite (Figure 1(a)) and plate shape graphite (Figure 1(b)) were demonstrated and the observed particle sizes corresponding to spherical and sheet graphite are 10 and 20 μm, respectively. Figure 1(c) and (d) demonstrated the cross section (Z – Y plane) of X-ray CT images, from which the anisotropy for spherical and sheet graphite was also projected to the 3D images according to remarked redline as shown in Figure 2. In the case of spherical graphite in Figure 2(a), the electrochemically active site is widely distributed while, it is limited at only edge plane because the basal plane is not active site in sheet graphite (Figure 2(b)). The crystal structure for each graphite was demonstrated by XRD analysis (Figure 3). Typical graphite peak [002] was confirmed at 27º with the space group $P6_3/mmc$[30], demonstrating equal structures each other. Additional data for the properties such as average diameter of particle (D_{50}), apparent density, and specific surface area were summarized in Table 1, provided from Nippon graphite L&C. The results for structural information and ionic conductivity for Li_3PS_4 as model solid electrolyte are demonstrated in Figure 4. Conventional amorphous phase was confirmed through the XRD in Figure 4(a), and Raman spectra (Figure 4(b) demonstrated the peak at around 426 cm^{-1}, indicating PS_4^{3-} anion. The Arrhenius plots (Figure 4(c)) was obtained by measuring the ionic conductivity through AC impedance with the temperature, and the ionic conductivity at 25 ºC was calculated as 5.13 x 10^{-4} Scm^{-1}. Figure 4(d) demonstrates the inhomogeneous particle shape and size of Li_3PS_4 prepared by ball milling. These are also in agreement with previous studies. To investigate the intrinsic electrochemical performance of each graphite regardless of reaction distribution, all graphite composite anodes were fabricated with thin thickness (20 μm), which was evaluated with the Galvano cycle test with the coin cell as shown in Figure 5. Conventional SEI formation behaviors, attributed to the formation of Li_2CO_3 and $(CH_2OO_2Li)_2$, were observed in both graphite at first cycle[39–40], and equal level of charge discharge capacities were confirmed regardless of graphite

anisotropy at all current densities. This result clearly implies that each graphite has equal electrochemical performance, provided that environment for smooth ionic path can be formed inside the composite electrode.

In order to investigate the solid system for two types of graphite, electrochemical measurements were conducted with the pressure and the results demonstrated with Figure 6 and 7. Unlike the liquid system, the distinct difference for electrochemical performance was clearly demonstrated in the solid–state cells employed with each graphite composite anode, which was consisted of spherical graphite and sheet graphite in Figure 6. In general, spherical graphite composite anode showed better discharge capacity than that of sheet graphite composite anode. Compared to spherical graphite with the electrochemical active site being widely distributed, sheet graphite might be only limited to near the edge as the path of lithium intercalation/deintercalation during cycling as shown in Figure 2. The charge/discharge curves and discharge capacities for the pressure at first cycle are demonstrated in Figure 6(a–b). In rate performance (Figure 7(a–b), The higher current density was applied, the lower discharge capacity was confirmed. Except for anisotropic difference between these two types of graphite, this poor electrochemical performance of all graphite composite anodes is might be attributed to large polarization by the interface resistance between solid electrolyte and graphite, according to previous studies[41-44]. In there, the charge transfer resistance would be induced between sulfide solid electrolytes and carbon–based materials by low ionic conductivity of Li_3PS_4. However, as recent studies showed that the interfacial resistance between the sulfide solid electrolyte and either graphene or graphite[45–47], it might be also considered to be subtle in these studies. Therefore, we considered that not only relatively low ionic conductivity of Li_3PS_4 but also thick composite anode over about 100 μm as the cause of poor electrochemical performance in spite of homogeneously distributed spherical graphite and Li_3PS_4 in the composite anode layer as shown in Figure 8. Moreover, considering the improved discharge capacity by higher ionic conductivity than that of Li_3PS_4[30,43,47], it suggested that relatively low ionic conductivity of Li_3PS_4 had an effect to ineffective lithium–ion transport as well as inhomogeneous electrode reaction originated from the transport difference between ion and electron. However, it is difficult to explain dramatical degradation of rate performance in Figure 7(a) and (b) by only low ionic conductivity of

Li_3PS_4. because it is expected that the contact between solid electrolyte and active material would be better when the pressure increases, leading to the decrease of void and pore phase in the composite electrode. To further investigate the correlation with the poor rate performance of graphite composite anodes, we conducted to measure the X-ray CT to obtain morphological change of Li_3PS_4 and each graphite in the composite anode with the applied pressures.

The 3D images of the graphite composite anodes with the pressure at 40, 80, 120, and 160 MPa are demonstrated in the volume scale of 200 x 200 x 200 μm^3 based on measured X-ray CT images in Figure 9 and 10. Through these 3D images, significantly reduced voids are observed in spherical graphite composite anode in Figure 9 rather than in sheet graphite composite anode in Figure 10. The quantitative data for void volume ratio was summarized with Table 2. It clearly demonstrated that the void phase could be reduced by the pressure and explained the reason for higher discharge capacity of spherical graphite composite anode with lower void ratio than that of sheet graphite. It was demonstrated that the reduced void volume ratio inside the composite anode influenced the improved efficiency of lithium–ion transport, leading to the enhanced electrochemical performance, at low pressure ranges (40 and 80 MPa) but, there was no impact on relatively high pressure from 120 to 160 MPa as shown in Figure 11(a) and (b), in which no enhance of discharge capacity for graphite composite anodes was demonstrated. This result suggests that there is other factor to influence the lithium–ion transport inside the composite anode at high pressure range. To investigate the behavior of lithium–ion transport inside graphite composite anodes, each tortuosity of Li_3PS_4 in the composite anodes was calculated and compared with the discharge capacities as shown in Figure 11(c), (d), and Table 3. The tortuosity of Li_3PS_4 in the spherical graphite composite anode was formed about 1.51, 1.53, 1.62, and 1.72, corresponding to 40, 80, 120, and 160 MPa, respectively. In the case of sheet graphite composite anode, it was confirmed as 1.54, 1.63, 1.71, and 1.80, corresponding to 40, 80, 120, and 160 MPa, respectively. Low tortuosity of Li_3PS_4 implies the ability to provide a short distance of lithium-ion transport inside the composite anode according to the equation (1) as shown in Figure 12. Therefore, it could provide better lithium–ion transport with higher discharge capacity in spherical graphite composite anode than that of sheet graphite

composite anode. However, in the end, the increase in tortuosity of Li_3PS_4 in the composite anode adversely affected the lithium–ion transports, which led to poor electrochemical performance. Moreover, we have one question as to why tortuosity of Li_3PS_4 increases with the pressure. In previous study[25], although it relates only to a solid electrolyte layer, when a high pressure is applied to the solid electrolyte powder, the tortuosity was lowered and the lithium–ion transport is facilitated, thereby increasing ionic conductivity. However, the opposite phenomenon was observed in the composite anodes, implying another variable.

To further identify this cause, we observed internal morphology of graphite composite anodes by enlarging the 3D images as shown in Figure 13. In here, it obviously demonstrated that anisotropic difference of graphite and the shape of Li_3PS_4 between spherical type and sheet type was not observed due to deformed morphology. In general, the Li_3PS_4 might be formed along with the shape of graphite because the it was formed along with each graphite shape at 0 MPa as shown in Figure 14. However, it was observed that spherical graphite in the composite anode tend to be orientated from the Z-direction to X-Y plane, leading the distorted shape of spherical graphite into sheet-like shapes in enlarged 3D images (Figure 13). Moreover, it was already changed from 40 MPa, from which the anisotropy of graphite in both graphite composite anodes was not significantly different. Thus, this anisotropic change of spherical graphite into sheet-like shape might be led to low and constant discharge capacity as the pressure increase. Furthermore, it might be unfavorable in the context of lithium–ion transport in the solid system unlike liquid system, and this character might be also attributed to relatively low shear modulus of graphite (5.0 GPa)[54] and Li_3PS_4 (5.9 GPa)[55]. This result indicates sufficient durability of either solid electrolyte or active material will be preferred against the pressure.

Based on this study, we found the factors affecting the increase of tortuosity of solid electrolyte inside the composite electrode for the pressure, and suggest the ideal condition of materials for designing the composite electrode for ASSBs. (1) High ionic conductivity of solid electrolyte; the high ionic conductivity can lead to improved electrochemical performance with low polarization, (2) Fine particle size of solid electrolyte to alleviate the tortuosity in the composite electrode, and (3) Active materials with large surface area and sufficient durability against pressure; electrochemically active site of active material

should be larger, and the anisotropy should be maintained regardless of the pressure. and mentioned 3 kinds of condition should be considered to design of the composite electrode for ASSBs.

6.4. Conclusion

Two kinds of graphite both spherical type and sheet type were fabricated with the composite anode, including the Li_3PS_4. Unlike the liquid system, obvious difference was clearly confirmed between spherical and sheet graphite composite anodes, in which spherical graphite composite anode demonstrated better discharge capacity, with large polarization. It was attributed to thick composite electrode and low ionic conductivity of Li_3PS_4. In addition, we described the main factors to determine this poor electrochemical performance in the composite electrode. At low pressures (40, 80 MPa), the void ratio inside the composite anode had affected to the improvement of electrochemical performance but, it was no effect at high pressure range. This result indicated that it might be the limitation to improve the electrochemical performance of these graphite composite anodes from the high pressure. Despite high pressure, the tortuosity of Li_3PS_4 was increased inside composite anodes, indicating longer lithium–ion path based on that the extracted tortuosity values through X-ray CT images. It was originated from anisotropic change of graphite and flexible property of Li_3PS_4 for the pressure. Finally, for efficient design of composite electrode for ASSB, we suggest that preferential condition of materials to design the composite electrode for ASSBs. (1) High ionic conductivity of solid electrolyte, (2) Active materials with large surface area and sufficient durability against pressure, and (3) Low tortuosity of solid electrolyte should be considered to design of the composite electrode for ASSBs.

Reference

1. Mark S.; Felix H., The 4th Industrial Revolution, Springer, **2018**.
2. Kenneth H.; Ali E., The impact of tribology on energy used and CO2 emission globally and in combustion engine and electric cars, *Tribology International*, **2019**, 132, 389-396.
3. Joris B.; Teresa D.; Raimund B.; Hans E. M., Oliver Heidrich, Circular economy strategies for electric vehicle batteries reduce reliance on raw materials, *Nature Sustainability*, **2021**, 4, 71-79.
4. Silvia B.; Fabrice M.; Fulvio A.; Gian A. B.; Maria A. C.; Adreas P.; Adreas P., Life Cycle Assessment of repurposed electric vehicle batteries: an adapted method based on modelling energy flows, *J. Energy Storage*, **2018**,19, 213-225.
5. S. W. Kang, D. H. Seo, X. Ma, G. Ceder, K. Kang, Electrode Materials for Rechargeable Sodium–Ion Batteries: Potential Alternatives to current Lithium–Ion Batteries, *Adv. Energy Mater.*, **2012**, 2, 710–721.
6. Zachary P. C.; Dustin B.; Siyu Y.; Andreas H.; Michael F.; Zhongwei C. Batteries and fuel cells for emerging electric vehicle markets, *Nature Energy*, 2018, 3, 279-289.
7. Y.G. Lee, S. Fujiki, C.H. Jung, N. Suzuki, N. Yashiro, R. Omoda, D. S. Ko, T. Shiatsuchi, T. Sugimoto, S.B. Ryu, J. H. Ku, T. Watanabe, Y.S. Park, Y. Aihara, D.M. Im, I. T. Han, High-energy long-cycling all-solid-state lithium metal batteries enabled by silver-carbon composite anode, *Nat. Energy*, **2020**, 5, 299–308.
8. Chengjian Xu, Qiang Dai, Linda Gaines, Mingming Hu, Arnold Tukker, Berhard Steubing, Future material demand for automotive lithium-based batteries, *Commun. Mater.*, **2020**, 1, 1-10.
9. Atsushi, S.; T. Takeuchi, H. Kobayashi, Electrode morphology in all-solid-state lithium secondary batteries consisting of $LiNi_{1/3}Co_{1/3}Ni_{1/3}O_2$ and Li_2S-P_2S_5 solid electrolyte, *Solid State Ionics*, **2016**, 285, 112–117.
10. C. Wang, X. Sun, L, Yang, D. Song, Y. Wu, T. Ohsaka, F. Matsumoto, J. Wu, In Situ Ion–Conducting Protective Layer Strategy to Stable Lithium Metal Anode

for All–Solid–State Sulfide–Based Lithium Metal Batteries, *Adv. Mater. Interfaces,* **2021**, 8, 2001698–2001708.

11. Anja B.; Dominik A. W.; Jürgen J. Microstructural Modeling of Composite Cathodes for All-Solid-State Batteries, *J.Phys.Chem.C,* **2019**, 123, 1626-1634.
12. Wen J.; Masaaki H.; Kota S.; Ryoji K. Fabrication and electrochemical properties of a $LiCoO_2$ and $Li_{10}GeP_2S_{12}$ composite electrode for use in all-solid-state batteries, *Solid State Ion.*, **2016**, 285, 136-142.
13. Yuki K.; Shinya S.; Keisuke M.; Kota S.; Masaaki H.; Ryoji K. All-Solid-State Batteries with Thick Electrode Configurations, *J.Phys.Chem.Lett.*, **2018**, 9, 607-613.
14. Jun Z.; Haoyue Z.; Chao Z.; Yang X.; Chu L.; Hui H.; Yongping G.; Xinyong T.; Wenkui Z. All-solid-states batteries with slurry coated $LiNi_{0.8}Co_{0.1}Mn_{0.1}O_2$ composite cathode and Li_6PS_5Cl electrolyte: Effect of binder content, *J.Power Sources,* **2018**, 391, 73-79.
15. Florian S.; Timo B.; Lea de. B.; A-Young K.; Jürgen J.; Pascal H.; Torsten B. Impact of Cathode Material Particle Size on the Capacity of Bulk Type All Solid State Batteries, *ACS Energy Lett.*, **2018**, 3, 992-996.
16. Y. Yang, Q. Wu, Y. Cui, Y. Chen, S. Shi, R. Z. Wang, H. Yan, Elastic Properties, Defect Thermodynamics, Electrochemical Window, Phase Stability, and Li^+ Mobility of Li_3PS_4: Insight from First-Principles Calculations, *ACS Appl. Mater. Interfaces,* **2016**, 6, 38, 25229–25242.
17. Tatsumisago, M.; Nagao, M.; Hayashi, A., Recent development of sulfide solid electrolytes and interfacial modification for all-solid-state rechargeable lithium batteries. *J. Asian Ceram. Soc.* **2013,** *1* (1), 17-25.
18. Inaguma, Y.; Liquan, C.; Itoh, M.; Nakamura, T.; Uchida, T.; Ikuta, H.; Wakihara, M., High ionic conductivity in lithium lanthanum titanate. *Solid State Commun.* **1993,** *86* (10), 689-693.
19. Murugan, R.; Thangadurai, V.; Weppner, W., Fast Lithium Ion Conduction in Garnet-Type $Li_7La_3Zr_2O_{12}$. *Angew. Chem., Int. Ed.* **2007,** *46* (41), 7778-7781.
20. Yao, P.; Yu, H.; Ding, Z.; Liu, Y.; Lu, J.; Lavorgna, M.; Wu, J.; Liu, X., Review on Polymer-Based Composite Electrolytes for Lithium Batteries, *Front. Chem.*, **2019**.

21. Park, S.; Han, A.; Shin, J., Kim, Kim., Influence of crystallinity on ion conductivity of PEO-based solid electrolytes for lithium batteries, *Macromol. Res.*, **2010**, 18, 336-340.
22. Joonam, P.; Dohwa, Kim.; Williams A, A.; Jihun, S.; Kyung Teak, B.; Kang Teak, L.; Jimin, O.; Ju Young, K.; Young-Gi, L.; Myung-Hyun, R.; Young Min, L., Electrode design methodology for all-solid-state batteries: 3D structural analysis and performance prediction, *Energy Storage Materials*, **2019**, 19, 124-129.
23. Lotsch, B. V.; Maier, J. Relevance of Solid Electrolytes for Lithium-Based Batteries: A Realistic View. *J. Electrochem*. 2017, 38, 128-141
24. Han, F.; Zhu, Y.; He, X.; Mo. Y.; Wang, C. Electrochemical stability of $Li_{10}GeP_2S_{12}$ and $LI_7La_3Zr_2O_{12}$ Solid Electrolytes. *Adv. Energy Mater*. **2016**, 6, 1501590
25. Wang, J.; Guo, Z.; Xiong, S. Characterization of the Morphology of Primary Silicon Particles using Synchrotron X-Ray Tomography. *Mater. Charact*. **2017**, 123, 354-359
26. Wang, Z.; Santhanagopalan, D.; Zhang, W.; Wang, F.; Xin, H. L.; He, K.; Li, J.; Dudney, N.; Meng, Y. S. In situ STEM-EELS Observation of Nanoscale Interfacial Phenomena in All-Solid State Batteries. *Nano Lett*. **2016**, 16, 3760-3767
27. Ohta, N.; Takada, K.; Sakaguchi, I.; Zhang, L.; Ma, R.; Fukuda, K.; Osada, M.; Sasaki, T. $LiNbO_3$-Coated $LiCoO_2$ as Cathode Material for All Solid-State Lithium Secondary Batteries. *Electrochem. Cmmun.* **2007**, 9, 1486-1490
28. Takada, K.; Nakano, S.; Inada, T.; Kajiyama, A.; Sasaki, H.; Kondo, S.; Watanabe, M.; Compatibility of Lithium Ion Conductive Sulfide Glass with Carbon-Lithium Electrode. *J. Electrochem. Soc.* **2003**, 150, 274-277
29. Banerjee, A.; Wang, X.; Fang, C.; Wu, E.A.; Meng, Y.S.; Interfaces and Interphases in All Solid State Batteries with Inorganic Solid Electrolytes, *Chem. Rev.,* **2020**, 120, 6878-6933.
30. Lagadec, M. F.; Ebner, M.; Zahn, R.; Wood, V. Technique for Visualization and Quantification of Lithium-Ion Battery Separator Microstructure. *J. Electrochem. Soc.* **2016**, 163, 992-994

31. Lagadec, M. F.; Zahn, R.; Wood, V. Designing Polyolefin Separator to Minimize the Impact of Local Compressive Stresses on Lithium Ion Battery Performance. *J. Electrochem. Soc*. **2018**, 8, 32637-32642
32. Zahn, R.; Lagadec, M. F.; Hess, M.; Wood, V. Improving Ionic conductivity and Lithium Ion Transference Number in Lithium Ion Battery Separators. *ACS Appl. Mater. Interfaces*, **2016**, 8, 32637-32642
33. Hlushkou, D.; Reising, A. E.; Kaiser, N.; Spannenberger, S.; Schlabach, S.; Kato, Y.; Roling, B.; Tallarek, U. The Influence of Void Space on Ion Transport in a Composite Cathode for All-Solid-State Batteries. *J. Power Sources*, **2018**, 396, 363-370
34. Yuta, K.; Mahunnop, F.; Takashi, N.; Toyoki, O.; Nozomu, I,; Oki, S.; Kiyofumi, N.; Tomoya, U.; Mizuki, T.; Yoshiharu, U.; Koji, A. Influence of Active Material Loading on Electrochemical Ractions in Composite Solid-State Battery Electrode Revealed by *Operando* 3D CT-XANES Imaging, *ACS Appl. Energy Mater*. **2020**, 3, 7782-7793
35. Andrew, L. D.; Vishwas, G.; Daniel, W. L.; Mark, N. M.; Eric, K.; John, L.; Katsuyo, T.; Neil, P. D. Rate Limitations in Composite Solid-State Battery Electrodes: Revealing Heteroneity with *Operando* Microscopy, *ACS Energy Lett*. **2021**, 6, 2993-3003
36. Dixit, M.B.; Regala, M.; Shen, F.; Xiao, X.; Hatzell, K.B.; Tortuosity Effect in Garnet Type $Li_7La_3Zr_2O_{12}$ Solid Electrolytes, *ACS Appl. Mater. Interfaces*, **2019**, 11, 2022-2030
37. Linus, F.; Jan. F. S.; Thomas, L.; Laura, H.; Arno, K. Effect of Microstructure on the Ionic Conductivity of an All Solid–State Battery Electrode, *J. Electrochem. Soc*. **2019**, 166, 318-328
38. Ebner. M.; Chung, D.W., Garcia E.; Wood, V., Tortuosity Anisotropic in Lithium Ion Battery Electrodes, *Adv, Energy Mater.*, **2014**, 4, 1301278-1301284.
39. Francois, L. E.; Usseglio, V.; Donal P. F.; Andrew, C.; Thomas M. M. H.; Daniel, A.; Paul, S.; Kandler, S. Quantitative Relationship Between Pore Tortuosity, Pore Topology, and Solid Particle Morphology Using a Novel Discrete Particle Size Algorithm, *J. Electrochem. Soc*. **2020**, 167, 100513

40. Xuekun, L.; Antonio, B.; Donal, P. F.; Chun, T.; Sohrab, R. D.; Julia, S. W.; Kieran, B. O.; Thomas, M. M. H.; Gareth, H.; Emma, K.; Dan, J. L. B.; Paul, R.S. 3D microstructure design of lithium-ion battery electrodes assisted by X-ray nano-computed tomography and modeling, *Nature Commun.*, **2020**, 11, 2079
41. Sungjun, C.; Minjae, J.; Junsung, A.; Wo Dum, J.; Sung Min, C.; Ji-Su, K.; Jaemin, L.; Young-Jun, J.; Hun-Gi, J.; Jong-Ho, L.; Byoung-In, S.; Hyoungchul, K. Quantitative Analysis of Microstructures and Reaction Interfaces on Composite Cathodes in All-Solid-State Batteries Using a Three-Dimensional Reconstruction Technique, *ACS Appl. Mater. Interfaces*, **2018**,10, 23740-23747
42. Hamann, T.; Zhang, L.; Gong, Y.; Godbey, F.; Gritton, J.; McOwen, D.; Hitz, G.; Wachsman, E.; The Effect of Construction Factor and Geometric Tortuosity on Li Ion Transport in Porous Solid State Li Ion Electrolytes, *Adv. Funct. Mater.*, **2020**, 30, 1910362-1910377
43. Buqa, H.; Goers, D.; Holzapfal, M.; Spahr, M.E.; Novac, P.; High Rate Capability of Graphite Negative Electrodes for Lithium Ion Batteries, *Journal of The Electrochemical Society*, **2005**, 152, 474-481
44. A. Shellikeri, V. Watson, D. Adams, E. E. Kalu, J. A. Read, T. R. Jow, J. S. Zheng, J. P. Zheng, Investigation of Pre-lithiation in Graphite and Hard-Carbon Anodes Using Different Lithium Source Structure, *J. Electrochem. Soc.*, **2017**, 164, 3914–3924
45. Misae, O.; Hiroe, K.; Atsushi, S.; Masahiro, T.; Akitoshi, H. *Operando* Confocal Microscopy for Dynamic Changes of Li^+ Ion Conduction Path in Graphite Electrode Layers of All-Solid-State Batteries, *J. Phys. Chem. Lett.* **2020**, 11, 990 –904.
46. Misae, O.; Atsushi, S.; Akitoshi, H.; Masahiro, T. Optical microscopic observation of graphite composite negative electrodes in all-solid-state lithium batteries, *Solid State Ionics*, **2018**, 323, 123–129.
47. Laura, H.; Franziska, J.; Camelia, B.; Thomas, H.; Claire, V.; Vincent, P.; Christian, J.; Mario, K.; Petr, N. Study of Graphite Cycling in Sulfide Solid Electrolytes, *J. Electrochem. Soc.*, **2020**, 167, 110558–1105568.
48. Laura, H.; Camelia, B.; Thomas, H.; Federica, M.; Christian, S.; Vincent, P.; Christian, J.; Claire, V.; Mario, K.; Petr, N. Performance-limiting factors of

graphite in sulfide-based all-solid-state lithium-ion batteries, *Electrochem. Acta*, **2021**, 389, 138735-138745.

49. Xiao, J.; Singyuk, H.; Pengfei, W.; Xinzi, H.; Nan, Piao, Ji, C.; Xiulin, F,; Chuncheng W. Solid-State Electrolyte Design for Lithium Dendrite Suppression, *Adv. Mater.*, **2020**, 32, 2002741-2002750
50. Nan W.; Yutao, L.; Andrei, D.; Wei, L; Henghui, X.; Biyi X.; Nicholas, S. G.; Zhiming C.; Haibo, J.; John. B. G. In Situ Formation of Li_3P Layer Enables Fast Li^+ Conduction across Li/Solid Polymer Electrolyte Interface, *Adv. Funct. Mater*. **2020**, 30, 2000831-2000837
51. Ruochen, X.; Zhang, W.; Shenzhao, Z.; Xiuli, W.; Wan, X.; Xinhui, X.; Xioahua, H.; Jiangping, T. Construction of All-Solid-State Batteries based on a Sulfur-Graphene Composite and $Li_{9.54}Si_{1.74}P_{1.44}S_{11.7}Cl_{0.3}$ Solid Electrolyte, *Chem. Eur. J.*, **2017**, 23, 13950-13956
52. Jianwei, L.; Yuanyuan, L.; Jun, C.; Qing S.; Linna, D.; Xiangkun, N.; Lina, C.; Guifang, H.; Lijie, C. A graphene oxide coated sulfide-based solid electrolyte for dendrite-free lithium metal batteries, *Carbon*, **2021**, 177, 52–59
53. Giovanna, M.; Akiko, T.; Naoki, S.; Tomoyuki, T.; Yuichi A.; Maria, A. N. Improvement of Graphite interfacial Stability in All-Solid-State Cells Adopting Sulfide Glassy Electrolytes, *ChemElectroChem*, **2021**, 8, 689-696
54. Grimsditch, M. Shear elastic modulus of graphite, *J. Phys. C: Solid State Phys.*, **1983**, 16, 143-144
55. Sakuda, A.; Hayashi, A.; Takigawa, Y.; Higashi, K.; Tatsumisago, M. Evaluation of Elastic Modulus of Li_2S-P_2S_5 Glassy Solid Electrolyte by Ultrasonic Sound Velocity Measurement and Compression Test, *J. Ceram. Soc. Jpn*. **2013**, 121, 946-949

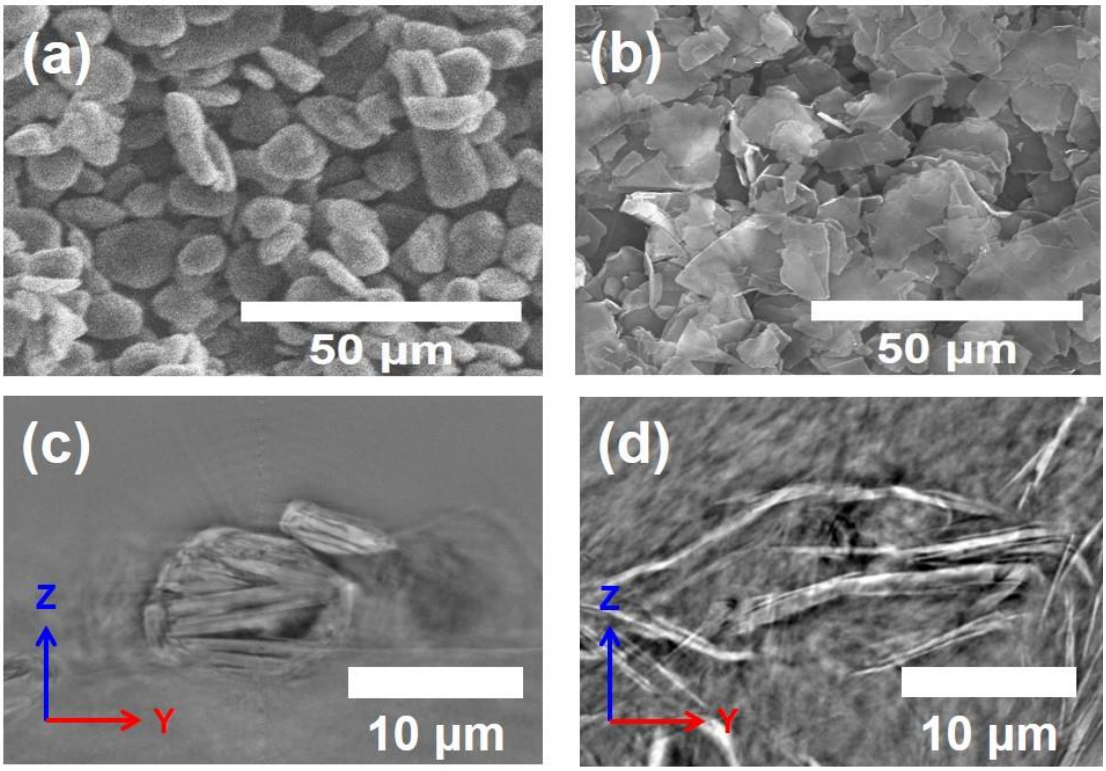

Figure 1. Morphology observed by SEM and X-ray CT for the spherical graphite (a – c) and sheet graphite (b – d).

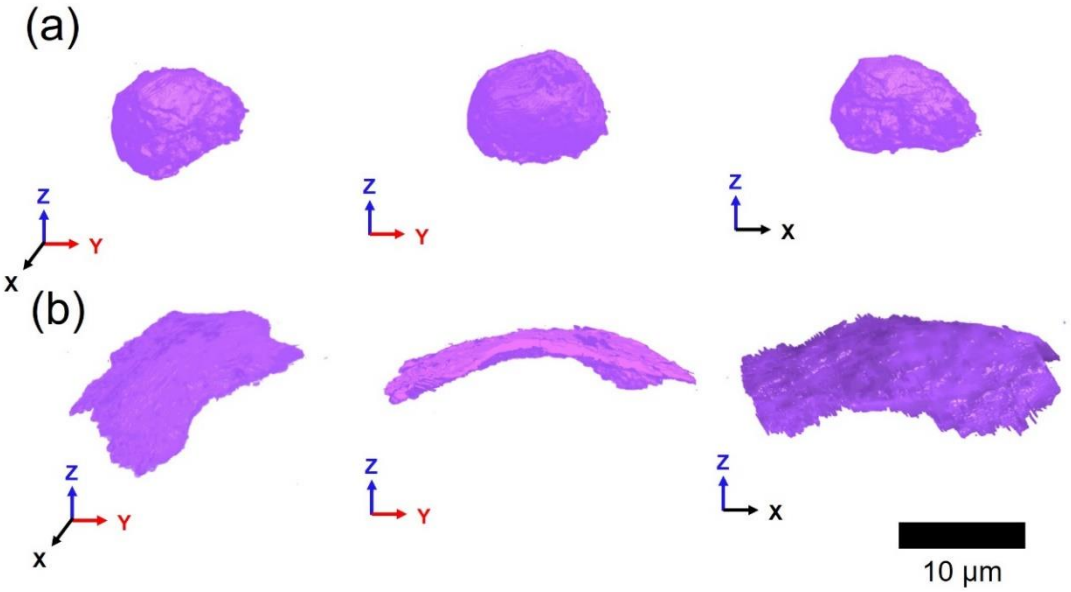

Figure 2. Morphology observed by X-ray CT for the spherical graphite (a) and sheet graphite (b).

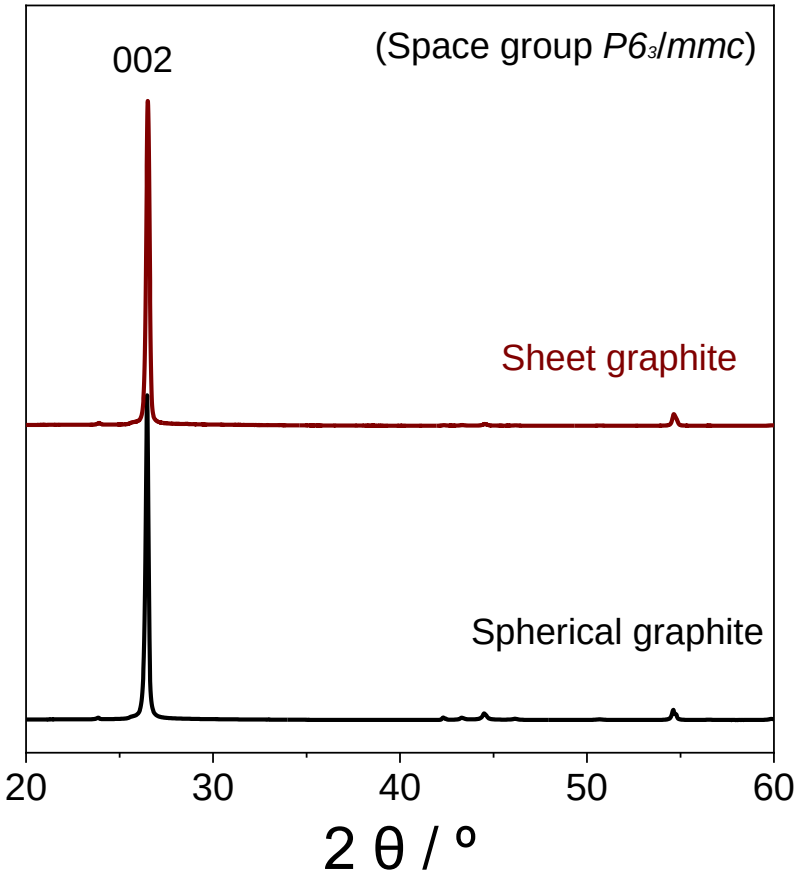

Figure 3. X-ray diffraction pattens corresponding to the spherical graphite (black) and sheet graphite (brown).

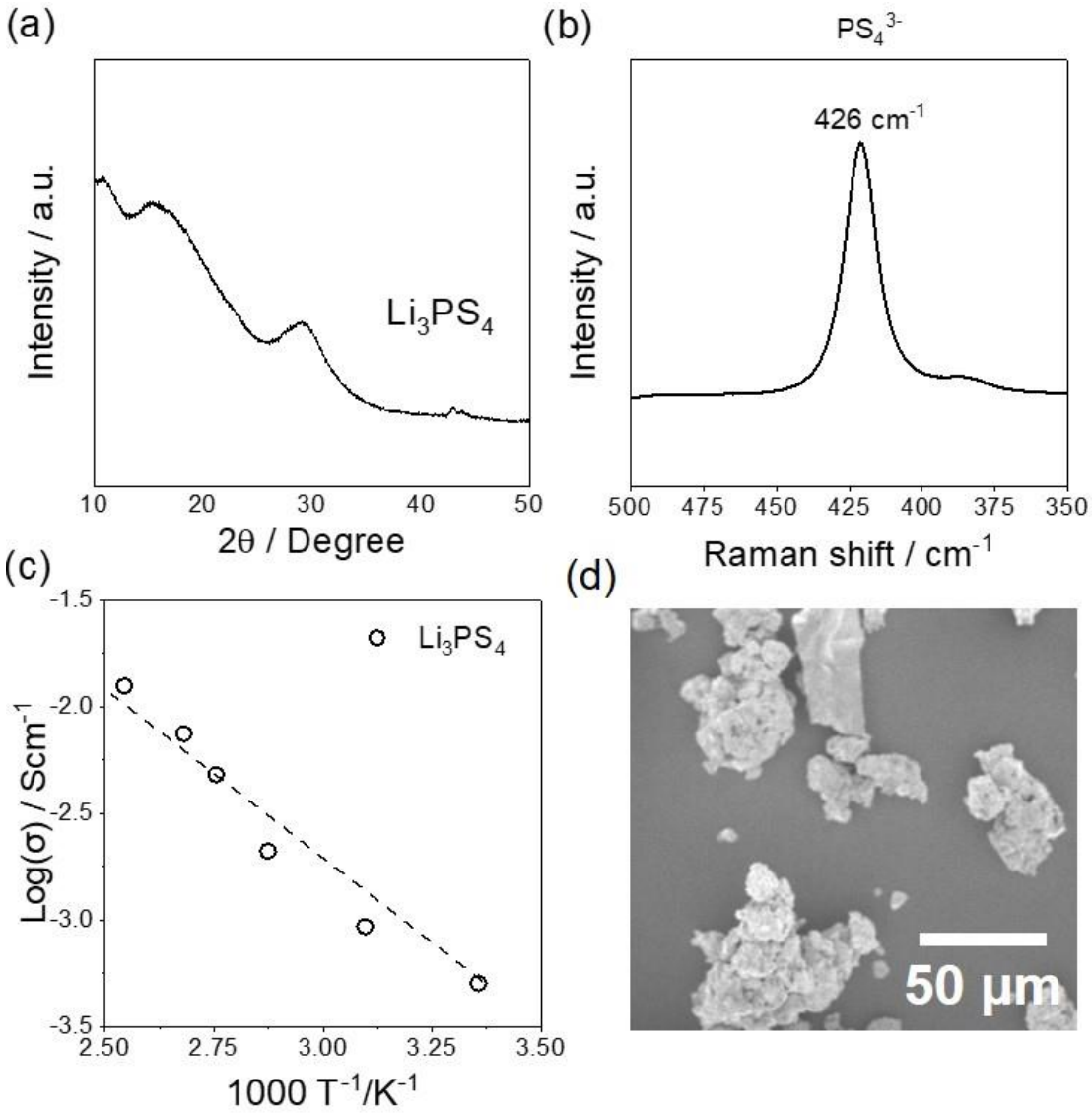

Figure 4. X-ray diffraction pattern (a), Raman spectra (b), Arrhenius plot (c), and SEM images for Li_3PS_4 prepared by ball milling.

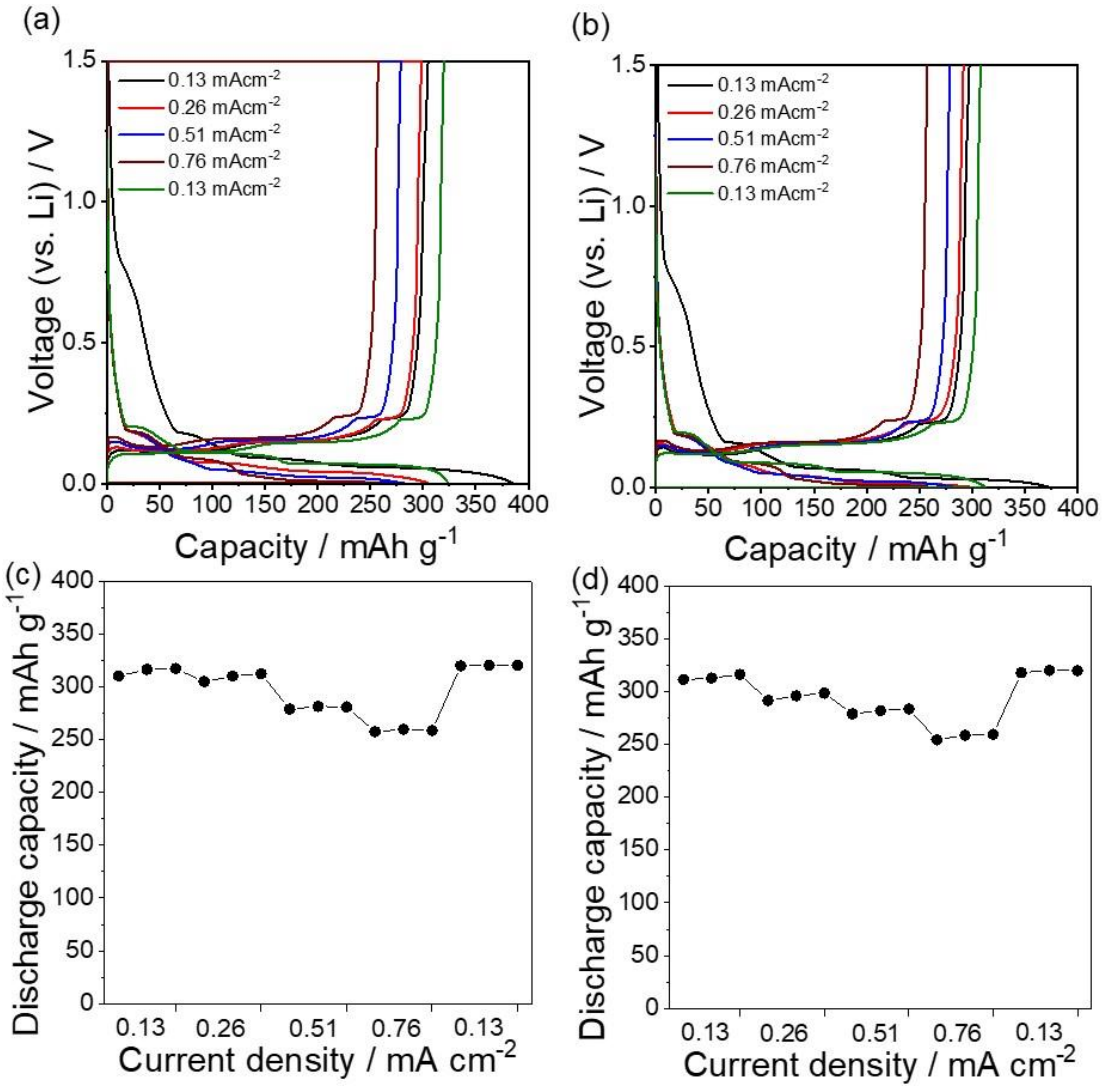

Figure 5. Electrochemical performance for each graphite in the liquid electrolyte system. First charge discharge curves at each current density of spherical graphite (a) and sheet graphite (b). Rate performances at each current density of spherical graphite (c) and sheet graphite (d).

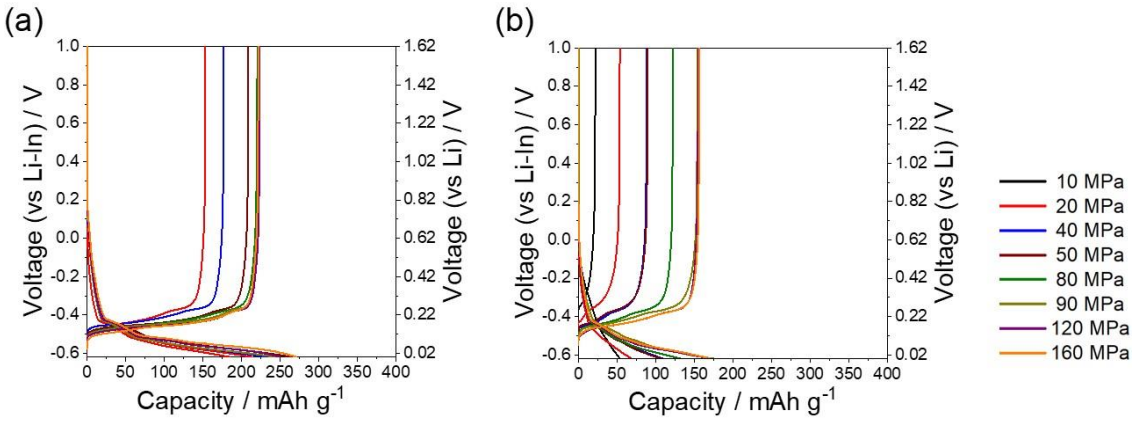

Figure 6. First charge and discharge curves corresponding to each pressure under the 0.13 $mAcm^{-2}$ at 25 ºC.

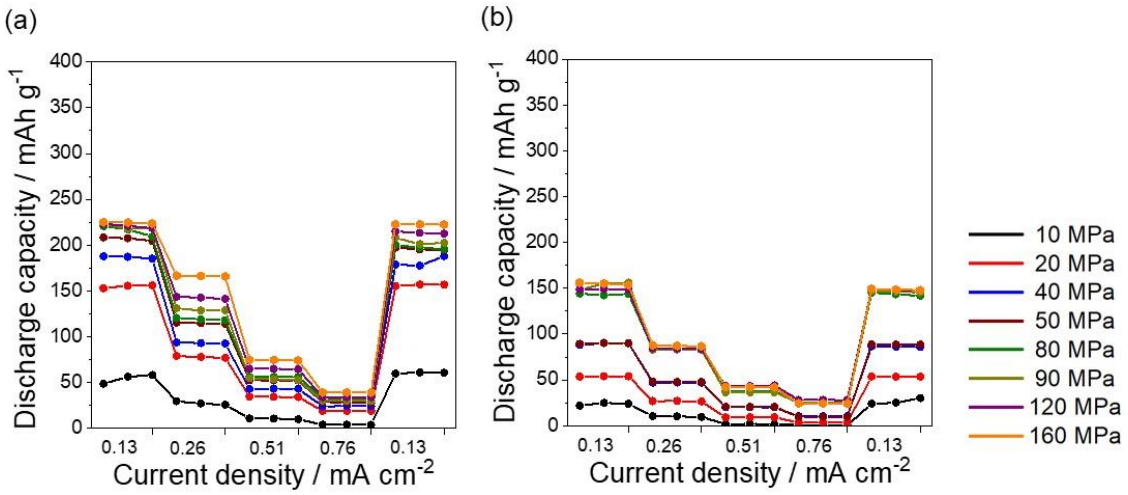

Figure 7. Rate performance for the spherical graphite composite (a) and sheet graphite composite (b) at 25 ºC.

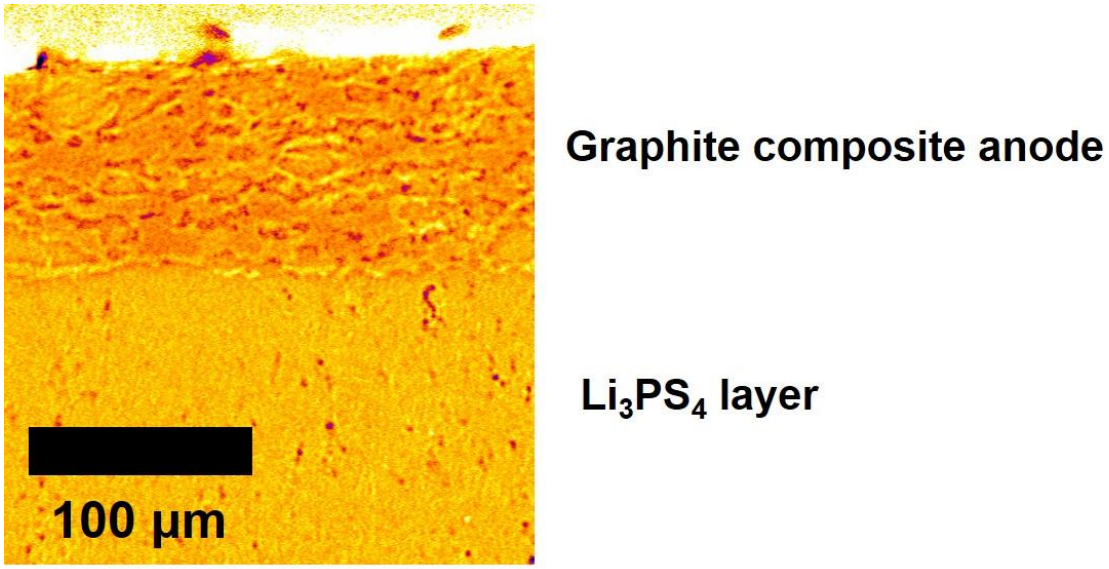

Figure 8. X-ray C.T images for cross section of spherical graphite composite anode.

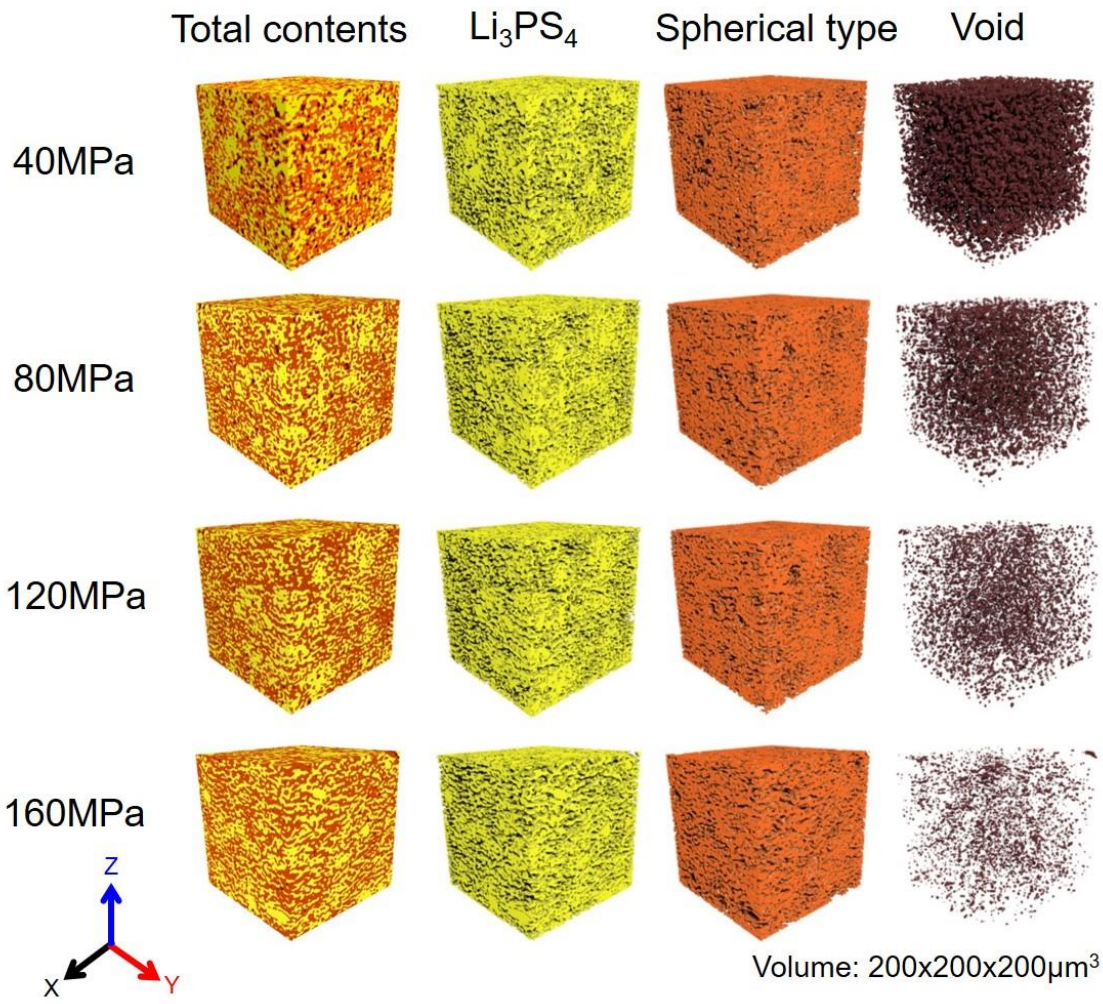

Figure 9. Three dimensional images of spherical graphite composite for each pressure.

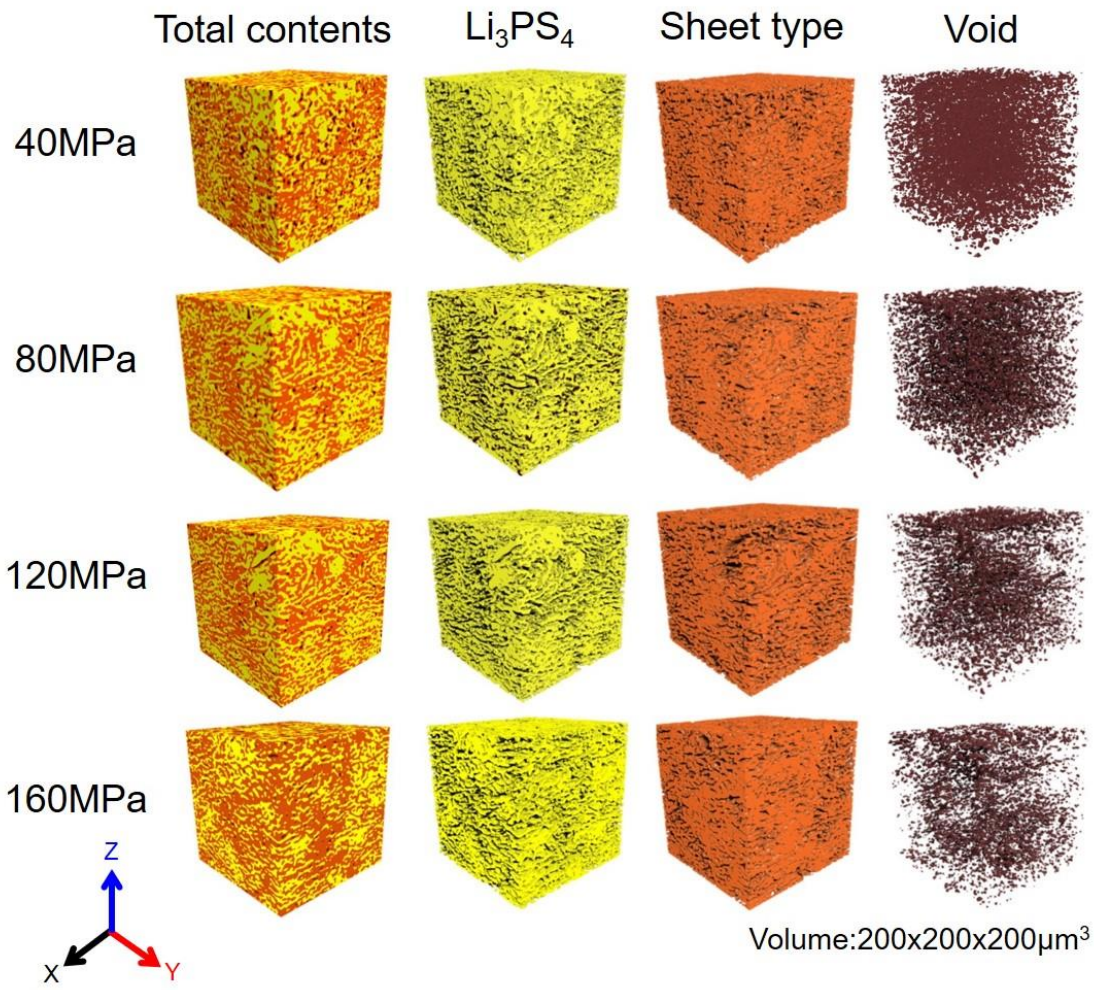

Figure 10. Three dimensional images of sheet graphite composite for each pressure.

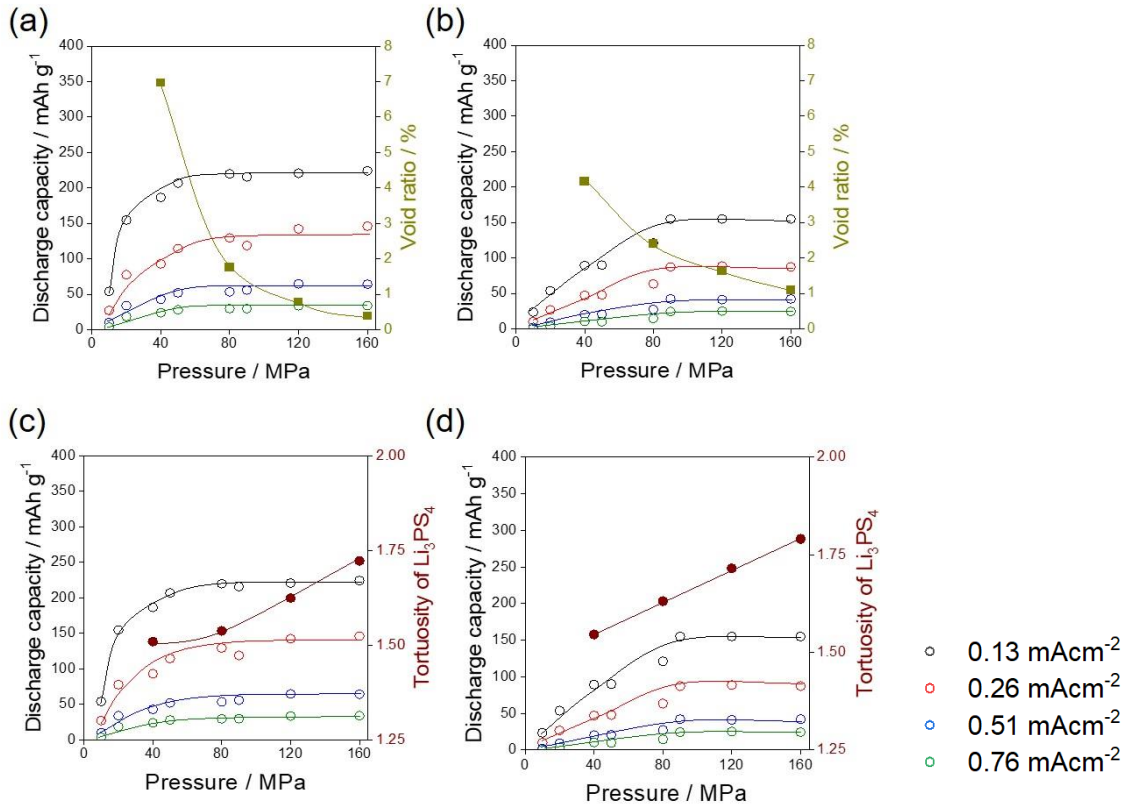

Figure 11. Correlation of discharge capacity with void ratio in the composite anode of spherical graphite (a) and sheet graphite (b). correlation of discharge capacity with tortuosity of Li_3PS_4 in the composite electrode of spherical graphite (c) and sheet graphite (d).

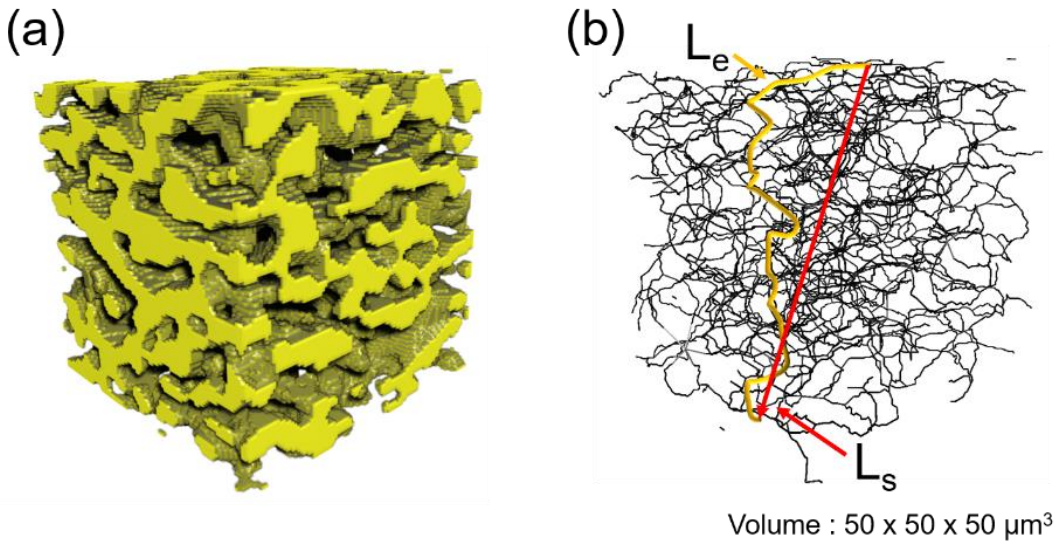

Figure 12. 3D rendering image of segmented Li_3PS_4 in the composite electrode (a) and 3D path network (b). A red line is the linear distance between the two points of one path and an orange line is the length along a serpentine path between two points of the path.

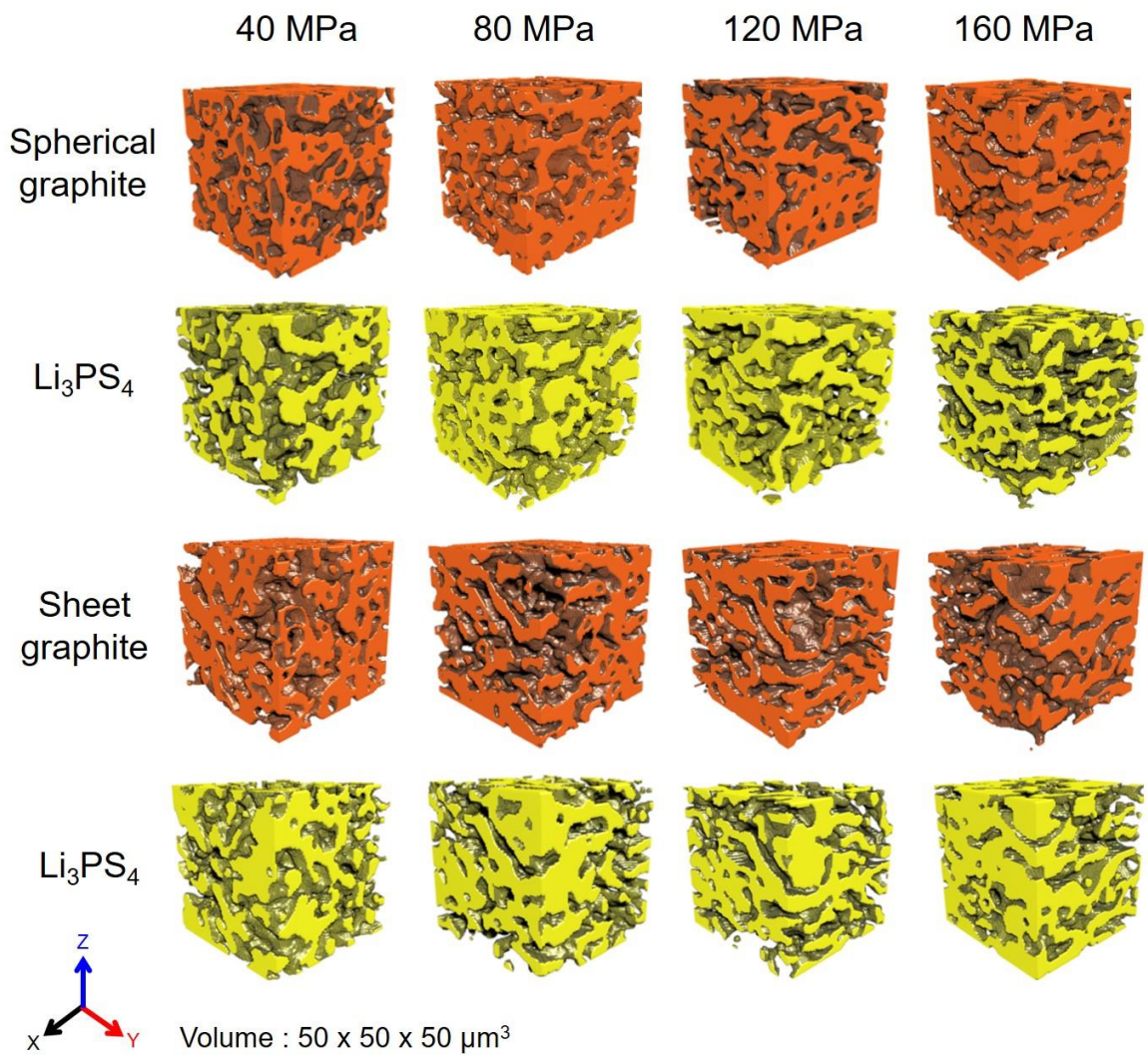

Figure 13. Enlarged three dimensional images based on the measured X-ray CT results Figure 9, 10.

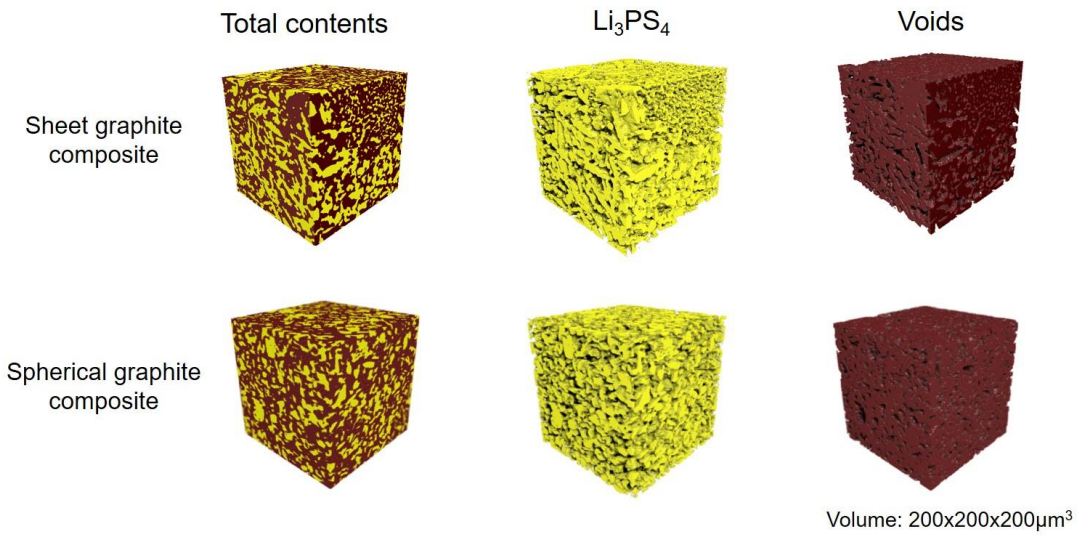

Figure 14. Three dimensional images for each composite electrode at 0 MPa. In here, the contrast of void and graphite at 0 MPa was too subtle to be separated because the contrast difference between the graphite and void in the composite electrode at 0 MPa could not be separated due to the poor X-ray absorption coefficient environment

Table 1. Properties for spherical graphite and sheet graphite

Properties	Spherical graphite	Sheet graphite
Diameter of particle (μm)	10.32	19.33
Apparent density (gcm^{-3})	0.46	0.12
Specific surface area (m^2g^{-1})	8.59	5.12

Table 2. Extracted void volume ratio (%) based on three dimensional images in Figure S9, 10

Pressure (MPa)	Spherical graphite composite	Sheet graphite composite
	Void ratio %	Void ratio %
40	7.00	4.16
80	1.75	2.41
120	0.78	1.62
160	0.38	1.08

Table 3. Extracted Li_3PS_4's tortuosity values based on three dimensional images in Figure S9, 10

Pressure (MPa)	Spherical graphite composite	Sheet graphite composite
	Tortuosity	Tortuosity
40	1.51	1.54
80	1.53	1.63
120	1.62	1.71
160	1.72	1.80

Chapter 7. General conclusions

ASSBs are a promising alternative that replaces the position of LIBs. However, it has been suffered from inefficient synthesis and poor performance that is not comparable to that as much as that of LIBs. In order to solve the inefficient synthesis approach, liquid phase synthesis was suggested due to its bulk scale, low-cost, and controllable particle size targeted for high energy density. However, both the origin of low ionic conductivity and the correlation with used solvent were unclear. Furthermore, the Various origins for the poor performance of ASSBs have been investigated and considerable reasons are originated from the interfacial problems. To commercialize the ASSBs, aforementioned problems must be fully understood. Therefore, in this work, various perspectives were investigated and identified through the advanced analysis techniques.

In Chapter 1, the faced environmental problems and their solution strategies were described with the importance for developing alternative energy sources and promising devices to reduce CO_2 emission. All solid−state battery was introduced with representative solid electrolytes developed so far, and both the challenges to commercialize this battery and the fundamental origin of problem that was not able to be commercialized were reviewed. The approach and strategies of us were described.

In Chapter 2, the correlation of the ionic conductivity and crystallinity of liquid phase synthesized Li_3PS_4 with the acetate system solvent properties. Through the PDF analysis, the lower polarity of solvent was the lower crystallinity and higher ionic conductivity of Li_3PS_4 were identified after liquid phase synthesis. The highest ionic conductivity as 5.09×10^{-4} Scm^{-1} was obtained when butyl acetate with 2.1 polarity was used as solvent. Based on this result, the polarity of solvent affects to the formation of crystalline phase of Li_3PS_4 in the liquid media.

In Chapter 3, the lithium dendrite suppression ability and improved ionic conductivity were investigated about the Li_3PS_4 doped by lithium halides before/after the annealing. PDF analysis revealed the structural information related to the behavior of ionic conductivity and phase dynamics during the annealing. Interfacial information for decomposed products Li_2S and Li_3P and cracks were demonstrated by the XAS and X-

ray CT. Main factor determining CCD property obtained from interfacial resistances by high frequency EIS measurements. These results indicated that lithium dendrite suppression is due to the improvement of the ionic conductivity and the ionic conductivity of the stable interfacial layer between the solid electrolyte and lithium metal.

In Chapter 4, LiI coated graphite was successfully prepared by simple liquid phase synthesis. SEM-EDX demonstrated well dispersed LiI on the surface of graphite from 1 to 5 wt%. In here, Coated LiI was existed as amorphous phase. Among the LiI-coated graphite samples, that with 5 wt% LiI showed the highest discharge capacity (348 $mAhg^{-1}$) with superior C-rate performance, while uncoated graphite showed a discharge capacity of 248 $mAhg^{-1}$. The interfacial resistance increased, but gradually decreased with the increasing amount of LiI coating. Furthermore, XAS results clearly show that Li_3PS_4 in the uncoated graphite composite decomposes into Li_2S and Li_3P, while the 5 wt% LiI–coated graphite composite was stable after lithiation.

In Chapter 5, Lithium filament evolutions were successfully observed inside the graphite composite thorough *Operando* X-ray computed tomography. In the composite electrode, the Li_3PS_4 near the graphite area was decomposed, from which the growth of lithium filament was generated from the edge side of graphite. After that, as the cell voltage rises, the void layer was formed. In there, not only deepen lithium filaments but also the broken graphite morphology was observed. It was considered that the diffusion of lithium–ions inside the graphite composite was non uniform at relatively high current density, concentrating only in a specific region. Finally, this concentrated area was responsible for lithium filament growth as well as delamination of the graphite layer.

In Chapter 6, the graphite composite anodes were investigated to understand and identify a factor for lithium ion transportation using in-situ X-ray computed tomography. Two kinds of graphite both spherical type (CGB−10) and sheet type (UP−20) were fabricated with the composite anodes including the Li_3PS_4, and the factors that affect electrochemical performance due to the anisotropy of solid electrolytes and active materials. Overall, the composite anode containing CGB−10 showed better electrochemical performances due to its large surface area. In addition, micro-scale X-ray computed tomography has confirmed that physical changes occurring inside the

composite electrode when pressure is applied have a significant impact on electrochemical performance. For efficient design of all solid−state battery, the active material and the solid electrolyte with a large surface part are preferred, and optimization of pressure applied to a composite electrode is required.

List of publications

1. Yamamoto, K.*; **Yang S.;** (**co-1st author**); Takahashi, M.; Ohara, K.; Uchiyama, T.; Watanabe, T.; Sakuda, A.; Hayashi, A.; Tatsumisago, M.; Muto, H.; Matsuda, A.; Uchimoto, Y., High Ionic Conductivity of Liquid-Phase-Synthesized Li_3PS_4 Solid Electrolyte, Comparable to That Obtained via Ball Milling, *ACS Appl. Energy Mater.*, **2021**, 4, 2275-2281 (**Chapter 2**)
2. **Yang S.;** Takahashi, M.; Yamamoto, K.*; Ohara, K.; Watanabe, T.; Uchiyama, T.; Takami, T.; Sakuda, A.; Hayashi, A.; Tatsumisago, M.; Uchimoto, Y., Studies on the inhibition of lithium dendrite formation in sulfide solid electrolytes doped with LiX (X = Br, I), *Solid State Ionics*, **2022**, 377, 115869 (**Chapter 3**)
3. **Yang S.;** Yamamoto, K.*; Mei, X.; Sakuda, A.; Uchiyama, T.; Watanabe, T.; Takami, T.; Hayashi, A.; Tatsumisago, M.; Uchimoto, Y., High Rate Capability from a Graphite Anode through Surface Modification with Lithium Iodide for All-Solid-State Batteries, *ACS Appl. Energy Mater.*, **2022**, 5, 667-673 (**Chapter 4**)
4. Takahashi, M.; **Yang S.;** (**co-1st author**), Yamamoto, K.*; Ohara, K.; Phuc, H. H. N.; Watanabe, T.; Uchiyama, T.; Sakuda, A.; Hayashi, A.; Tatsumisago, M.; Muto, H.; Matsuda, A.; Uchimoto, Y., Improvement of lithium ionic conductivity of Li_3PS_4 through suppression of crystallization using low-boiling point solvent in liquid-phase synthesis, *Solid State Ionics*, **2021**, 361, 115568
5. Yamamoto, K.*; Takahashi, M.; Ohara, K.; Phuc, H. H. N.; **Yang S.;** Watanabe, T.; T.; Uchiyama, T.; Sakuda, A.; Hayashi, A.; Tatsumisago, M.; Muto, H.; Matsuda, A.; Uchimoto, Y., Synthesis of Sulfide Solid Electrolytes through the Liquid Phase: Optimization of the Preparation Conditions, *ACS Omega*, **2020**, 5, 26287-26294
6. Takahashi, M.; Watanabe, T.; Yamamoto, K.; Ohara, K.; Sakuda, A.; Kimura, T.; **Yang, S.**; Nakanishi, K.; Uchiyama, T.; Kimura, M.; Hayashi, A.; Tatsumisago, M.; Uchimoto, Y.; Investigation of the Suppression of Dendritic Lithium Growth with a Lithium-Iodide-Containing Solid Electrolyte, *Chem. Mater.*, **2021**, 33, 4907-4917

Acknowledgements

The studies in this doctoral thesis have been conducted at graduate school of human and environmental studies, Kyoto university.

First of all, I would really like to appreciate to Prof. Yoshiharu Uchimoto, who gave me a great opportunity in my life, for his guidance and advice for my research activity and this thesis content. Without his attribution to this thesis, it could never be accomplished like present form.

Special thanks are expressed to Prof. Kentaro Yamamoto for his useful comments and discussions about electrochemical theory and material science. Furthermore, I want to express our lab instructors, Prof. Toshiki Watanabe, Prof. Tomoki Uchiyama, Prof. Toshiyuki Matsunaga, and Prof. Takami Tsuyoshi for precious comment and advices.

I am also grateful to Dr. Koji Ohara and Dr. Takahashi for their advices on the pair distribution function analysis to analyze my materials

I would like to thank to all the members of Uchimoto lab for their helps, discussions and encouragement throughout this study. I will never forget our memory forever and hope all to accomplish things that you want.!

I would like to thank to my previous supervisor Dr. Ho−sung Kim, lab members, and co-workers who have been still giving an unchangeable support to me in Korea.

Finally, I would like to appreciate my parents for their dedication, and my brother and sister, All I love you.

Seunghoon Yang

\

※著作権等

1. High Ionic Conductivity of Liquid-Phase-Synthesized Li_3PS_4 Solid Electrolyte, Comparable to That Obtained via Ball Milling

Kentaro Yamamoto[*1], Seunghoon Yang[1], Masakuni Takahashi, Koji Ohara, Tomoki Uchiyama, Toshiki Watanabe, Atsushi Sakuda, Akitoshi Hayashi, Masahiro Tatstumisago, Hiroyuki Muto, Atsunori Matsuda, and Yoshiharu Uchimoto

ACS Applied energy materials, 2021, 3. 2275-2281

DOI: 10.1021/aceaem.Oc027771

2. Studies on the inhibition of lithium dendrite formation in sulfide solid electrolytes doped with LiX (X = Br, I)

Seunghoon Yang[1], Masakuni Takahashi[1], Kentaro Yamamoto, Koji Ohara, Toshiki Watanabe, Tomoki Uchiyama, Tsuyoshi Takami, Atsushi Sakuda, Akitoshi Hayashi, Masahiro Tatsumisago, and Yoshiharu Uchimoto

Solid State Ionics, 2022, 377, 115869

DOI: 10.1016/j.ssi.2022.115869

3. High Rate Capability from a Graphite Anode through Surface Modification with Lithium Iodide for All-Solid-State Batteries

Seunghoon Yang[1], Kentaro Yamamoto, Xiaohan Mei, Atsushi Sakuda, Tomoki Uchiyama, Toshiki Watanabe, Tsuyoshi Takami, Akitoshi Hayashi, Masahiro Tatsumisago, and Yoshiharu Uchimoto

ACS Applied energy materials, 2022, 5, 667-673

DOI : 10.1021/acsaem.1c03166